

## 11. REAL-TIME SUPPRESSANT CONCENTRATION MEASUREMENT

William M. Pitts, George W. Mulholland, Brett D. Breuel,  
Erik L. Johnsson, Steve Chung, Richard H. Harris  
Building and Fire Research Laboratory

David E. Hess  
Chemical Science and Technology Laboratory

### Contents

	Page
<b>11. REAL-TIME SUPPRESSANT CONCENTRATION MEASUREMENT</b>	<b>319</b>
11.1 Introduction	322
11.2 Development and Testing of a Combined Aspirated Hot-Film and Cold-Wire Probe	324
11.2.1 Background	324
11.2.1.1 Hot-Film Anemometry	324
11.2.1.2 Hot-Film Sensitivity to Composition	326
11.2.2 Design Considerations	334
11.2.3 Combined Aspirated Hot-Film/Cold-Wire Probe Electronics and Operation	337
11.2.4 Calibration System	341
11.2.4.1 Test Section	341
11.2.4.2 Mixing Chamber	343
11.2.4.3 Mass-Flow Controllers	343
11.2.4.4 Thermal Bath and Heat-Transfer Coil	350
11.2.4.5 Data Acquisition and Control	351
11.2.4.6 Calibration Procedures	354
11.2.5 Calibration Results and Probe Characterization	355
11.2.5.1 Calibration Results	355
11.2.5.2 Characterization of Probe Response to Velocity Fluctuations	361
11.2.5.3 Estimation of Uncertainty in Concentration Measurements Introduced by Probe Sensitivity to Turbulent Fluctuations	367
11.2.6 Aspirated Hot-Film Concentration Measurements During Releases of Pressurized Agents	370
11.2.6.1 Experimental System and Data Analysis for Concentration Measurement	370
11.2.6.2 Measurement of Halon 1301 Concentration Following Release From a Pressurized Vessel into an Open Room	372
11.2.6.3 Attempt to Measure Halon 1301 Concentration Following Release From Pressurized Vessels into a Simulated Dry Bay	382
11.2.6.4 Measurement of Halon 1301 Concentration Following Release Into a Turbulent Spray-Flame Burner	391
11.2.7 Summary and Recommendations	399

11.3	Evaluation of Infrared Sensing For Rapid Measurement of Halon Replacement	
	Chemicals	401
11.3.1	Background	401
11.3.2	Description of FEAS	401
11.3.2.1	Phenomenology of a Pyroelectric Sensor	403
11.3.2.2	Heat Transfer for a Pyroelectric Sensor	403
11.3.2.3	Response to a Gaussian Thermal Pulse	405
11.3.2.4	A Periodic Source Intensity	406
11.3.2.5	Characterization of FEAS Performance	408
11.3.3	Description of An Improved <u>D</u> ifferential <u>I</u> nfrared <u>R</u> apid <u>A</u> gent <u>C</u> oncentration <u>S</u> ensor (DIRRACS)	410
11.3.3.1	Design Improvements	410
11.3.3.2	Instrument Design	414
11.3.4	Theory of Operation	418
11.3.5	Data Acquisition	428
11.3.6	Temporal and Spatial Resolution	433
11.3.7	Signal-to-Noise Behavior	434
11.3.8	Instrument Calibration	435
11.3.9	Field Testing of DIRRACS	445
11.3.9.1	Dry-Bay Testing at Wright Patterson AFB	445
11.3.9.2	Testing in the Turbulent Spray Burner Facility at NIST	450
11.3.10	Summary and Recommendations	456
11.4	Review of Statham and Halonyzer Extinguishing-Agent Concentration Recorders	457
11.5	Literature Search For Additional Diagnostics for High-Speed Alternative-Agent Concentration Measurement	465
11.5.1	Introduction	469
11.5.2	"Standard" Chemical-Analysis Techniques	470
11.5.2.1	Gas-Solid and Gas-Liquid Chromatography	470
11.5.2.2	Mass Spectrometry	470
11.5.2.3	Standard Optical Absorption Techniques	472
11.5.3	Fiber-Optic-Based Measurements of Concentration	475
11.5.3.1	Introduction To Fiber Optics	475
11.5.3.2	Spatially Resolved Absorption Concentration Measurements Using Fiber Optics	477
11.5.3.3	Other Fiber-Optic-Based Concentration Measurement Approaches	485
11.5.4	Additional Optical-Based Techniques	486
11.5.4.1	Raman Spectroscopy	486
11.5.4.2	Coherent Anti-Stokes Raman Spectroscopy (CARS)	487
11.5.4.3	Rayleigh Light Scattering	488
11.5.4.4	Fluorescence Concentration Measurements	489
11.5.4.5	Mie Scattering Concentration Measurements	490
11.5.4.6	Specialized Concentration Measurements Based on Optical Absorption	495
11.5.4.7	Optical Speckle Technique	495
11.5.4.8	Miniature Mach-Zehnder Interferometer	497
11.5.5	Acoustic Absorption	497
11.5.6	Summary and Recommendations	503
11.6	Acknowledgments	505
11.7	References	505

Appendix A. FORTRAN Program NOZZLE.FOR to Estimate Volume-Flow Rates of Agents and Air Extracted By Aspirating Hot-Film Probe .....	513
Appendix B. FORTRAN Program COIL.FOR to Estimate Length of Pipe Required For Laminar and Turbulent Flows in Pipes to Achieve Pipe-Wall Temperature ....	522
Appendix C. Electrical Connections of Interface Boards and Components of Flow Calibration System .....	529
Appendix D. Workbench PC Icon-Based Worksheet ACTRL3.WBB for Controlling Calibration System, Digitizing Voltages During Calibrations, and Storing Results to Files .....	531
Appendix E. Workbench PC Computer-Control Panel for Calibration System. Panel Is Controlled By worksheet ACTRL3.WBB Shown in Appendix D .....	538
Appendix F. Detailed Operating Procedures for Calibration of Combined Aspirated Hot-Film/Cold-Wire Probe .....	539
Appendix G. Workbench PC Icon-Based Worksheet SHOT.WBB for Triggering Data Acquisition, Digitizing Hot-Film and Cold-Wire Voltages and Output of DIRRACS, and Storing Results to Files .....	543
Appendix H. FORTRAN Program SURFFIT.FOR to Calculate Least Squares Fit to Surface of Order m Representing Agent Concentration. Surface is Fit of Agent Concentrations As Function of Temperature and Aspirated Hot-Film Voltage ..	544
Appendix I. FORTRAN Program CONCEN.FOR Used to Calculate Time Records of Concentration and Temperature From Digitized Records of Cold-Wire and Aspirated Hot-Film Voltages .....	566
Appendix J. Components of DIRRACS .....	572
Appendix K. Infrared Detector Model .....	574
Appendix L. DIRRACS Data Reduction Program .....	579
Appendix M. FORTRAN Program SOUND.FOR Used to Calculate Sound Attenuation As a Function of Fire-Fighting Agent Concentration in Air .....	585

## 11.1 Introduction

An aspect of fire extinguishment which has not received a great deal of attention is the role that the dispersion and evaporation characteristics of the agent play in fire-fighting effectiveness. The reason for this lack of interest in the past was that these properties have been nearly optimized by the use of halon 1301 for total flooding applications and halon 1211 for spray applications. With regard to total flooding applications, which are of most interest for this study, the low boiling point of halon 1301 has ensured that, for the majority of applications, it can be dispersed and vaporized very rapidly into a space. The dispersal effectiveness of halon 1301 is a direct result of the rapid evaporation which occurs when the agent is released from a pressurized vessel. The rapid evaporation not only effectively converts liquid agent to the gaseous state, but also results in a strong "flashing" which aids greatly in the distribution of the agent within the volume. Due to the effectiveness of dispersal of halon 1301, designers of total flooding systems generally have focused on the use and placement of hardware designed to ensure all areas of an enclosure quickly receive concentrations of the agent sufficient to extinguish the fire.

The fire fighting applications which are the focus of the current investigation--nacelle and dry-bay fires on aircraft--have different requirements with respect to these agent characteristics. Due to the nature of dry-bay fires, detection and extinguishment is generally required within tens of milliseconds. On the other hand, nacelle fires tend to have burned for longer periods before extinguishment, and a premium is placed on the achievement of extinguishing concentrations which can be maintained for a period of time following extinguishment to prevent relight on heated surfaces. Effective dispersion throughout the volume is required, but the dispersion can take place over longer periods of time than for the dry-bay application.

Even though the physical mixing processes involved are not generally considered in designs of halon fire-fighting systems, they are crucial. The important processes can be characterized into three major categories--release rate, dispersion and mixing, and evaporation. The release rate determines the minimum time required to extinguish a fire. If the release is very slow, it is possible that the fire may never be extinguished.

In order to determine the characteristics of an agent's dispersion behavior which are most important in determining extinguishment efficiency, it is necessary to have the means to make accurate concentration measurements on the time scales of interest. As new agents are incorporated into fire-extinguishment systems, it will also be necessary to make quantitative measurements in order to certify that these new systems are meeting their design goals. Development of the capability for making the necessary concentration measurements for 1) the design of dispersion systems and 2) the certification of new systems is the focus of this effort.

At the present time, instruments sensitive to variations in viscosity which occur with changes in concentration are used to certify fire-extinguishing systems based on halon 1301, 1211, 1202 and CO<sub>2</sub>. Two similar devices of this type are known as the Statham analyzer and Halonyzer. See the discussion in Section 11.4 for further details. Response times for these instruments configured in the standard way have been listed as 0.25 s (New and Middlesworth, 1953; Pacific Scientific, 1988a). These times are clearly too long to allow their use for making measurements in dry-bay applications where the entire event is generally over in less than 0.1 s. Furthermore, the existing instruments have not been tested for their response to potential halon alternatives, and their sensitivity for certain chemicals may be poor.

Recognizing the need for improved instrumentation to make concentration measurements of halon 1301 and alternatives, the Air Force, Navy, Army, and Federal Aviation Administration jointly funded the project summarized in this section. The objective of this effort was "to evaluate possible methods



for real-time measurements of concentrations of alternative fire fighting agents for dry-bay and nacelle fire applications. If one or more feasible approaches are identified early in the investigation, a demonstration system will be developed for characterization under actual test situations." The major tasks were:

1. Review of the Concentration Measurement Literature
2. Evaluate and Test Instrumentation Developed with Air Force Funding
3. Evaluate and Test Hot-Film Probes
4. Development of Operating Procedures (Optional)

During the recent project on *Evaluation of Alternative In-Flight Fire Suppressants for Full-Scale Testing in Aircraft Engine Nacelles and Dry Bays* (Grosshandler *et al.*, 1994) an aspirated hot-film sensor was used to detect the presence of halon alternatives during releases of the pressurized agents (Pitts *et al.*, 1994). Commercial versions of these probes have been developed for concentration measurement (see the discussion in Section 11.2.1.2) which are capable of making measurements on a millisecond time scale. It was believed that these devices offered the best promise of commercially available measurement systems for making concentration measurements in full-scale dry-bay and nacelle test facilities. One component of the work described here was to test this hypothesis.

Wright-Patterson AFB staff members had anticipated the need for an instrument capable of detecting the presence of an alternative agent. A Small Business Innovation Research contract had been awarded to John Brown Associates to develop a device based on infrared absorption which would respond to transient concentrations of halons and alternative agents containing fluorine. The instrument could also be configured to respond to carbon dioxide. Several instruments, referred to as Fire Extinguishment Agent Sensors (FEAS), were delivered to the Air Force by John Brown Associates. At the request of the program sponsors, testing of these instruments for their potential to make quantitative concentration measurements was incorporated into the current research program.

In addition to testing of the two types of instrumentation, a literature review was to be carried out to identify additional techniques which might be employed for making the concentration measurements.

Very early in the investigation it was found that neither of the probes to be tested could be used to make the required measurements without substantial modification. With the agreement of the sponsors, the program was substantially extended to include the redesign and testing of modified approaches. Two instruments (a combined aspirated hot-film/cold-wire probe and an infrared absorption probe denoted as the Differential Infrared Rapid Agent Concentration Sensor (DIRRACS)) were developed and appeared promising enough that testing was carried out in the full-scale dry-bay test facility at Wright-Patterson AFB.

The following two sections describe the development and testing of the two instruments as well as providing the background necessary to understand their operation. Brief summaries and recommendations for additional research are included. These sections are followed by one describing the Statham analyzer and Halonyzer. The final section of this chapter contains a literature review assessing other potential techniques for making the required concentration measurements. A summary and recommendations for considering other possible techniques are included.

## 11.2 Development and Testing of a Combined Aspirated Hot-Film and Cold-Wire Probe

### 11.2.1 Background

**11.2.1.1 Hot-Film Anemometry.** Hot-wire and hot-film anemometers are devices which are normally used to measure velocity in flows of liquids or gases. Many books and monographs contain extensive discussions of their use and applications (*e.g.*, see Corrsin, 1963; Hinze, 1975; Bradshaw, 1971; Comte-Bellot, 1976; Fingerson and Freymuth, 1983; Perry, 1982). The principle of operation is fairly simple. An electric current passing through the conductive probe heats the sensor to a temperature higher than that of the ambient surroundings. Fluid flow over the sensor removes heat with the rate of heat transfer increasing with fluid-flow rate. Calibration of the amount of heat loss as a function of known flow velocity allows the velocity of an arbitrary flow of the fluid to be determined by measuring the heat loss of the sensor.

There are a number of different types, sizes, and shapes of probes which have been used. See the review articles listed above for details. In this paper we will only consider a hot-film anemometer operated in a constant-temperature mode. The hot-film detector is formed by depositing a thin film of platinum onto a 50  $\mu\text{m}$  diameter quartz rod. The active length of the probe is specified by depositing an approximately 6.4  $\mu\text{m}$  thick layer of gold at either end. The nominal active length is 1.0 mm. In order to limit oxidation, the entire probe is sealed with a thin layer of alumina.

During operation a current is passed through the probe sufficient to heat the sensor to a temperature well above the ambient. The resistance of the probe depends on temperature, generally increasing with temperature. Over the typical range of operating temperatures for hot films, the dependence of resistance on temperature is linear. The resistance of the probe can therefore be written as

$$R_{op} = \alpha_p(T_{op} - T_{ref}) + R_{ref}, \quad (1)$$

where  $R_{op}$  is the operating resistance of the probe,  $T_{op}$  is the nominal operating temperature,  $R_{ref}$  is the resistance of the probe at the reference temperature,  $T_{ref}$ , and  $\alpha_p$  is the thermal coefficient for the probe resistance. For a constant voltage across the probe, the current ( $i_p$ ) through the sensor varies with temperature.

As a fluid flow passes over the surface of the sensor, heat is convected away and the probe begins to cool. The amount of heat loss to the fluid per unit time ( $H$ ) can be written as

$$H = h\pi d_f l_f (T_{op} - T_\infty), \quad (2)$$

where  $h$  is the heat transfer coefficient,  $d_f$  is the sensor diameter,  $l_f$  is the active length of the sensor, and  $T_\infty$  is the ambient temperature of the fluid. In order to maintain the resistance of the probe (and hence the nominal temperature) constant it is necessary that heat be added to the sensor (*i.e.*, the amount of resistive heating must be adjusted by varying the flow of current to the sensor to balance the heat loss due to convection). A constant-temperature anemometer uses electronics to ensure that the resistance of the sensor remains constant at a preset value. The output signal of the electronics is a voltage which is proportional to the current flowing through the probe. Since values of  $h$  generally increase with velocity, the voltage output also increases with flow velocity.

Heat transfer correlations for heated cylinders are typically written in terms of the nondimensional Nusselt number ( $Nu$ ), defined as

$$Nu = \frac{hd_f}{k_o}, \quad (3)$$

and have the general form

$$Nu = \text{fun}(Re, Pr, Gr, \text{wire properties}), \quad (4)$$

where

$$Re = \frac{U_o d_f}{\nu_o}, \quad (5)$$

$$Pr = \frac{c_p \mu_o}{k_o}, \quad (6)$$

and

$$Gr = \frac{g \rho_o^2 d_f^3 \beta (T_{op} - T_\infty)}{\mu_o^2}. \quad (7)$$

Undefined variables are the thermal conductivity of the fluid,  $k_o$ , Reynolds number ( $Re$ ), flow velocity over the hot film,  $U_o$ , kinematic viscosity of the fluid,  $\nu_o$ , the Prandtl number,  $Pr$ , constant pressure heat capacity for the fluid,  $c_p$ , dynamic viscosity for the fluid,  $\mu_o$ , the Grashof number,  $Gr$ , gravitational constant,  $g$ , the fluid density,  $\rho_o$ , and the coefficient of thermal expansion of the gas,  $\beta$ .

The most commonly used heat-transfer law for cylindrical hot-film anemometers is known as King's (1914) Law,

$$Nu = C_1(Pr) + C_2(Pr)Re^n, \quad (8)$$

where  $C_1$  and  $C_2$  are constants which depend on  $Pr$ . King originally set the exponent  $n$  to  $1/2$ , but here it is treated as a parameter since experiments have demonstrated that it varies with flow conditions and gas.

The overheat ratio for a hot-film anemometer is defined as  $(T_{op} - T_\infty)/T_\infty$ . For normal operating overheats  $Gr$  effects can be neglected. Furthermore, the dependence of the heat transfer on  $Pr$  is generally weak. From the above equations it becomes clear that the heat loss from the cylinder should vary linearly with the overheat ratio and roughly as the square root of the velocity.

Recall that the heat loss from a hot-film sensor operated in the constant-temperature mode must be balanced by adding heat to the sensor by resistive heating. Since the amount of heat provided to

the cylinder is  $(i_f)^2 R_{op}$ , and the output voltage of the sensor is proportional to the hot-film current  $i_f$ , the output voltage for a constant overheat is expected to obey the following relation,

$$E^2 = A + BU_o^n, \quad (9)$$

where  $E$  is output voltage and  $A$  and  $B$  are constants. Equation (9) is known to be an approximation. Many other parameters can affect the output of a hot-film anemometer. A detailed discussion of such effects can be found in Pitts and McCaffrey (1986).

**11.2.1.2 Hot-Film Sensitivity to Composition.** Hot-film anemometers are most commonly used for velocity measurements in which the composition of the fluid does not change. The device response to changes in velocity is simply calibrated for the fluid of interest. It is well known that such calibrations are sensitive to the composition of the fluid which can be understood in the terms of the simplified description of hot-film response provided in the last section. Equations (3) - (7) contain molecular constants which vary with composition. In particular, the response of a hot film should depend strongly on the thermal conductivity and kinematic viscosity of the fluid surrounding the hot film.

The sensitivity of the hot-film anemometer to gas composition is a decided drawback when making velocity measurements. It is effectively impossible to make velocity measurements in a flow where the composition is varying with time using a single probe, since the response is a function of both velocity and an unknown composition. The same is true for flow fields in which temperature is fluctuating.

Several groups have developed probes which are capable of measuring concentration and velocity simultaneously by using two probes with very different responses (Way and Libby, 1970, 1971; McQuaid and Wright, 1973, 1974; Aihara *et al.*, 1974). Since two sets of measurements are available which have different dependencies on velocity and concentration, the signals can be deconvoluted to give velocity and concentration. These probes require extensive and tedious calibration in order to make quantitative measurements. They have only been used for constant-temperature flows. In order to operate them in situations where the temperature is also varying, it would be necessary to calibrate both sensors as functions of temperature and to provide an independent measurement of temperature at the sampling location during the measurement.

Other workers have attempted to use the sensitivity of hot wires and films to concentration to develop probes for measurements in binary mixtures based on single sensors. One of the earliest investigations is due to Adler (1972) who describes a system in which a hot wire is placed in a flow created by withdrawing gases from the sampling volume. The flow system incorporates a heater to ensure that the temperature of the gases is constant and a supersonic orifice is used to control the velocity. Since the flow velocity in the sampling volume is a function of the pressure in the volume and composition only, the hot-wire response is expected to be independent of gas temperature and velocity. Proper calibration allowed quantitative concentration measurements to be made. Adler does not report the time response of the instrument, but does indicate that "rapid response is ensured because of the high response of the hot wire." It is interesting that the design of this instrument is very similar to that for the Statham and Halonyzer instruments described in Section 11.4. The major difference is that the concentration response in the latter instruments is provided by measuring the pressure drop across a subsonic orifice. Of relevance to the later discussion, Adler pointed out the need to use this probe in a clean environment since probe contamination would change the probe

response. Response times for Statham and Halonyzer instruments have been characterized as being too long for the current application in Section 11.4.

Other researchers have developed probes based on hot-wires or hot-films in which single sensors are placed in choked flows of the gas to control the velocity, but for which the sensor and choke point are located very close to the probe sampling volume. These probes have the advantage of maximizing the time response since the flow only has to flow over a small distance before reaching the sensor.

The first report of such a sensor was by Blackshear and Fingerson (1962). This probe incorporated a unique cylindrical hot-film probe in which a small pyrex tube (0.15 mm outside diameter (o.d.), 0.10 mm inside diameter (i.d.)) was used as the cylindrical rod. The platinum film was deposited on the outside of the tube. Water was passed through the sensor to provide cooling. In this way it was possible to use the probe in highly heated flows. The probe was mounted at the entrance of a tube with a cap containing a sonic orifice. Dimensional details of the probe are not provided, but the overall o.d. of the probe was 8 mm.

The probe was found to respond to external velocity fluctuations even though ideally it should have been insensitive to such fluctuations. The sensitivity of the probe to velocity fluctuations was characterized by placing the probe on the centerline of an axisymmetric turbulent air jet fifteen diameters downstream of the exit and measuring the response of the probe to the external velocity fluctuations, which had a root-mean-square (rms) value equal to 0.17 of the average velocity. The fluctuations recorded by the probe increased with the ratio of the velocity in the probe and the average external air velocity. On the other hand, the velocity fluctuations were shown to be independent of the ratio of areas for the opening into the probe and the choked orifice. Blackshear and Fingerson reported that the velocity fluctuations at the probe were reduced by a factor of thirteen over those observed in the free stream.

Measurements using the probe were demonstrated for two very different systems. The first was as a temperature measurement device in flame globules created by discharging a voltage across a pair of electrodes located in a flowing combustible gas mixture. The measured rise time of the temperature using the aspirated probe was roughly 0.1 ms which was in good agreement with the expected temperature gradients for the flames. In the second experiment, the probe was used to measure either the concentration of helium or the temperature of heated air in axisymmetric turbulent jets. Radial profiles of the rms for the concentration and temperature fluctuations were reported. According to the authors, with the exception of measurements based on Mie scattering from seed particles, these results represented the first direct time-resolved measurements of concentration in turbulent flows.

The next reported use of an aspirated concentration probe was a study by Brown and Rebollo (1972). These researchers mounted a 12.7  $\mu\text{m}$  diameter hot wire across the 2 mm diameter of a tube which had been drawn down to a fine tip with an opening of 25  $\mu\text{m}$ . A vacuum was attached to the other end of the tube, and gases were withdrawn through the orifice. The vacuum was sufficient to ensure that the flow through the orifice was choked and therefore only depended on external pressure, temperature, and composition. Assuming constant temperature and pressure, the response of the hot-wire should only be a function of concentration.

Since the wire was located only 1.6 mm from the orifice and internal gas flow velocities were high, the probe was expected to have a rapid response time. It was experimentally demonstrated that actual response times were less than one ms. The authors also contended that the response of the probe was insensitive to the external flow velocity. The probe was calibrated for mixtures of helium, argon, and krypton in nitrogen. Measurements of helium concentration in a mixing layer formed between flows of helium and nitrogen were demonstrated.

Aihara *et al.* (1974) reported the use of a similar probe for helium concentration measurement. In their probe the velocity of the fluid at the sensor was reduced to a low level by passing the sampled

gases through a large area expansion. They reported that the output voltage of the hot wire was quite insensitive to velocity.

Perry (1977) performed an analysis of the flow over and through a Brown-Rebollo-type probe and estimated the frequency response as 10 kHz.

Ahmed and So (1986) developed a probe which was similar to that of Brown and Rebollo, but which incorporated a pumping port and BNC connector for the anemometer electronics. The glass tube was contained within a stainless steel tube. The hot wire used by Brown and Rebollo was replaced with a 50  $\mu\text{m}$  diameter hot film. The hot film was located 12.7 mm downstream of the 130  $\mu\text{m}$  diameter sonic orifice. Figure 1 is a schematic of the probe based on Figure 1 in their paper. These authors designed the probe for use in a swirled flow and were therefore concerned about the response of the probe to variations in upstream (*i.e.*, sampled gas) pressure with sampling position. By calibrating the response across the flow they showed that the probe was nearly insensitive to the stagnation pressure. This finding has important implications with regard to the findings of the current investigation.

The probe developed by Ahmed and So was used to measure helium concentrations in a variety of flows. These include a model cylindrical combustor (Ahmed and So, 1986) and a jet discharge into a swirled flow (So and Ahmed, 1987). Later the technique was combined with laser Doppler anemometry (LDV) to allow simultaneous measurements of concentration and velocity in a variety of helium/air flows (Zhu *et al.*, 1988, 1989; So *et al.* 1990, 1991). These later studies showed that the probe response was not sensitive to the presence of the roughly 1  $\mu\text{m}$  diameter 50 % water/50 % glycerine droplets used to seed the flow field for the LDV measurements.

A commercial aspirating hot-film probe, designated as Model 1440, was developed and marketed by Thermo-Systems Inc. (now known as TSI, Inc.) several years prior to 1979 (Jones and Wilson, 1979). A schematic of the Model 1440 is shown in Figure 2. Note that this design differs significantly from that reported by Brown and Rebollo (1972) in that the hot-film probe is mounted upstream of the sonic orifice, and the flow must pass down a tube before flowing through the sonic orifice.

Jones and Wilson (1979) have provided a detailed analysis of the flow through the device and the response of the hot-film to variations in gas composition. They pointed out that by holding the upstream dynamic pressure and temperature constant, the mass flow through the nozzle becomes only a function of the molecular weight of the gas. Using an expression similar to Equation (9) and standard expressions for electrical heating and heat loss, they derived the following expression for hot-film response,

$$\frac{E^2}{R_{op}} = \frac{\pi d_f k_o}{4} (T_{op} - T_\infty) \left[ A + \left( B \frac{d_f \beta (\rho V)^*}{\mu_o} \right)^n \right], \quad (10)$$

where  $\beta$  is the ratio of the nozzle area to the area of the tube containing the hot film and  $(\rho V)^*$  is the maximum mass-flow rate of fluid per unit area through the supersonic orifice which can be calculated using

$$(\rho V)^* = \sqrt{\frac{\gamma MW}{RT_o}} P_o \left[ \left( \frac{2}{\gamma + 1} \right)^{\frac{\gamma + 1}{2(\gamma - 1)}} \right]. \quad (11)$$

$P_o$  and  $T_o$  are the fluid pressure and temperature upstream of the nozzle,  $\gamma$  is the ratio of the constant pressure and volume specific heats,  $MW$  is the molecular weight of the gas, and  $R$  is the universal gas constant.

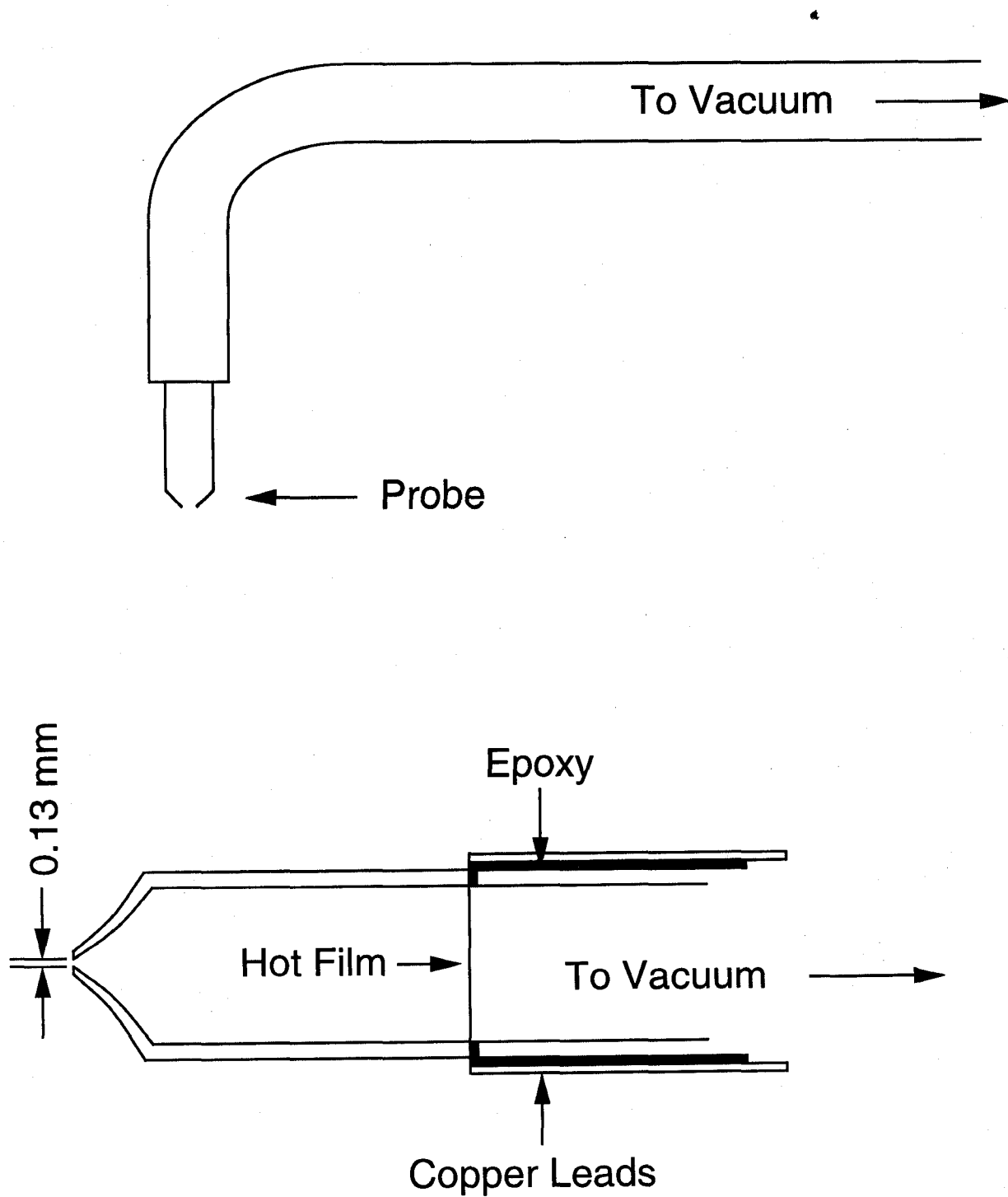


Figure 1. Schematic of the concentration probe developed by Ahmed and So (1986) based on Figure 1 of their paper.

# ASPIRATED HOT-FILM CONCENTRATION PROBE

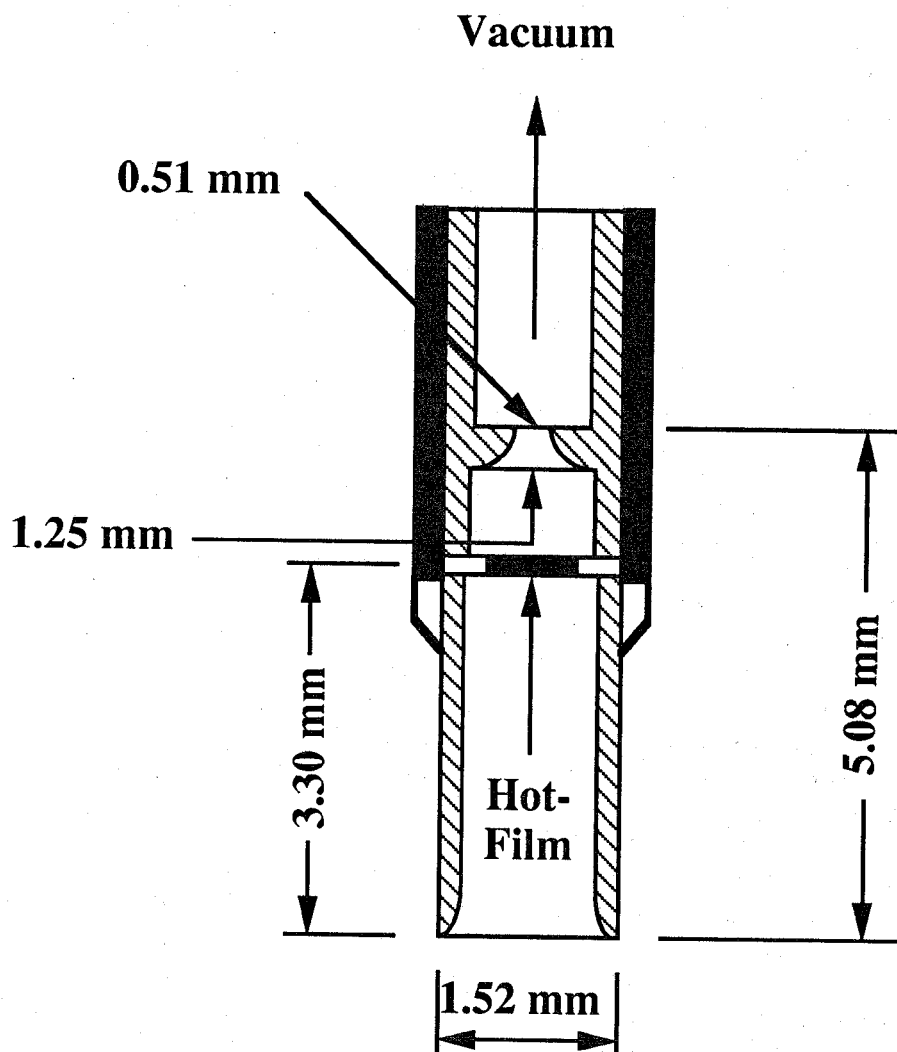


Figure 2. Schematic diagram of the TSI, Inc. Model 1440 aspirated hot-film probe.



The authors showed that Equation (10) provided a fairly good prediction of the observed variation in hot-film output for a range of helium-argon concentrations. They attributed much of the difference between the observed and calculated values of hot-film voltage to the neglect of end effects where the probe transfers heat to its supports. A detailed discussion of such effects can be found in Pitts and McCaffrey (1986).

Jones and Wilson were interested in making measurements in flow fields in which both the concentration and temperature were varying. As Equation (10) shows, the hot-film response varies with the ambient temperature,  $T_\infty$ . In order to correct for this temperature variation an independent temperature measurement is required. They obtained temperature measurements by installing a second 50  $\mu\text{m}$  diameter probe within the sampling tube 250  $\mu\text{m}$  upstream of the standard hot film. This second hot film was operated with a very low overheat such that its output was sensitive to temperature (LaRue *et al.*, 1975). In this way it was possible to record the temperature and correct the response of the primary hot film for temperature variations.

By recognizing that  $k_o$  and  $v_o$  are approximately proportional to the square root of temperature and that the mass flow is inversely proportional to temperature, Equation (10) can be used to show that

$$\left. \frac{E^2}{R_{op}} \right|_{T_1} = \left. \frac{E^2}{R_{op}} \right|_{T_2} \times \frac{T_{op} - T_1}{T_{op} - T_2}. \quad (12)$$

This equation allows the hot-film response to be predicted for a temperature  $T_1$  when it is known for a second temperature  $T_2$ . Experiments with variable temperature flows of argon, helium, and mixtures of these two gases indicated that Equation (12) predicts the observed changes in anemometer output voltage quite well. Jones and Wilson concluded that the aspirated hot-film could be used to make concentration measurements having an accuracy of 1 %.

Wilson and Netterville (1981) reported the development of an aspirated hot-film concentration probe based on a very different design. Figure 3 shows a schematic for their probe. In their system the gases to be sampled were drawn into a 1.7 mm diameter tube, which then expanded into a 2.4 mm diameter tube. The larger tube contained a short plug of cigarette-filter material. The filter was intended to dampen out turbulent stagnation pressure fluctuations by providing a pressure drop of nearly 50 kPa through what amounts to a bundle of parallel capillary tubes. After passing through the filter, the lower pressure flow continued down the tube where it ultimately reached a hot-film anemometer. After the hot film the flow entered a region containing a 600  $\mu\text{m}$  diameter sonic orifice. A pump lowered the pressure on the downstream side of the orifice to a sufficient level to ensure supersonic flow through the orifice. The authors pointed out the need to have the hot-film as close as possible to the sonic orifice in order to minimize the lag time between changes in sampling velocity at the orifice due to composition and heat transfer from the sensor. A novel configuration was used in which the flow from the hot film to the sonic orifice was through an angled channel. This modification from other probes of this type was designed to minimize velocity fluctuations within the device.

This new probe was calibrated for its response to helium and CFC-12 ( $\text{CF}_2\text{Cl}_2$ ) concentrations<sup>1</sup> in air. The calibrations covered the narrow concentration range of 0 % to 1 %. Differences in concentration smaller than 0.1 % were easily distinguishable for both gases, and both calibrations were

<sup>1</sup>For the purposes of this section concentration of agents will be expressed either as mole fractions or as percentages of agent (*i.e.*, mole fraction  $\times$  100)

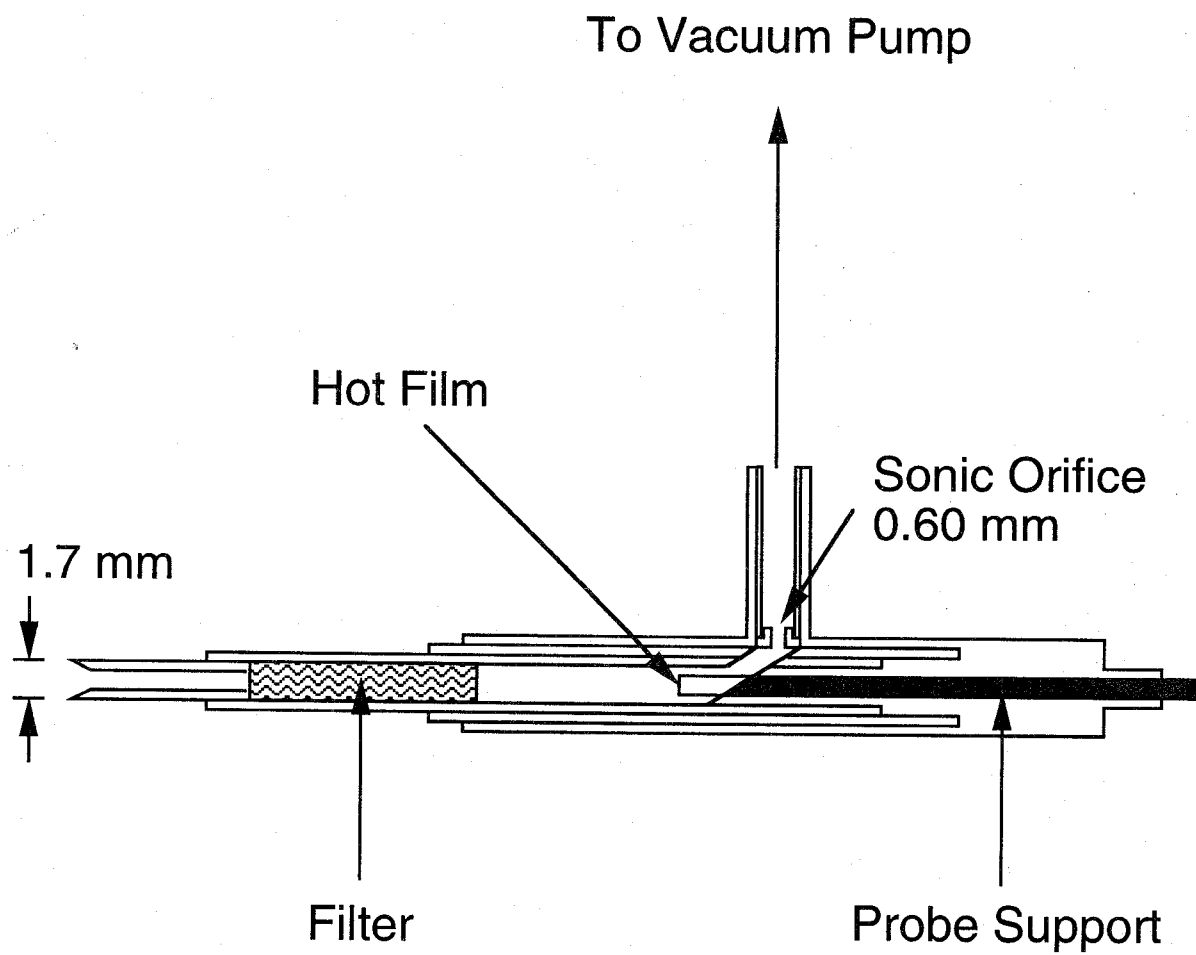


Figure 3. Schematic diagram of the aspirated hot-film probe developed by Wilson and Netterville (1981).

linear over this limited range. The lower detection limit for helium was reported to be 0.01 %. The slope of the calibration curve for helium was positive and had an absolute magnitude five times higher than the negative slope found for  $\text{CF}_2\text{Cl}_2$ .

The time response of the probe was investigated by placing the probe on the end of a pendulum and swinging it rapidly through a jet flow of 1 % helium in air and recording the transient response. The probe entered the flow sufficiently fast that the concentration change with time was effectively a step function. The response time was determined to be 500  $\mu\text{s}$  and was successfully modeled as consisting of a time constant associated with the flow through the filter and the response of the hot-film anemometer to changes in concentration and velocity. Wilson and Netterville used their probe to monitor concentration fluctuations in a turbulent boundary flow doped with helium. The probe response time was sufficient to fully resolve the concentration fluctuations.

Fedyayev *et al.* (1990) reported the fabrication of a probe similar in construction to that originally developed by Blackshear and Fingerson (1962). A three mm diameter steel tube was sealed at one end, and a 20  $\mu\text{m}$  diameter sonic orifice was machined into the end. Instead of placing the probe upstream of the orifice, as in the case of Blackshear and Fingerson, a 5  $\mu\text{m}$  diameter hot wire was mounted downstream of the orifice on the low-vacuum side of the probe. The hot wire was operated in the constant-temperature mode. The response of the probe to velocity fluctuations on the centerline of an axisymmetric jet of air was investigated. They found that the probe output was essentially independent of velocity and its fluctuations for velocities less than 20 m/s. At higher velocities a distinct response to velocity was observed, which increased with increasing velocity. The authors discussed how such noise levels can limit the resolution of an experimental measurement of concentration. The probe was used to measure helium concentration upon injection of helium into the turbulent boundary layer of a wind tunnel.

Ninnemann and Ng (1992) have reported still another design for an aspirated hot-wire probe for recording helium concentration in supersonic shear flows. The 51  $\mu\text{m}$  diameter hot film was placed downstream of a 28  $\mu\text{m}$  diameter opening into a tapered tube which opened to 1.2 mm. At a much larger downstream distance the flow in the tube passed through a 56  $\mu\text{m}$  diameter orifice which choked the flow. The probe was calibrated as functions of helium concentration, temperature, and pressure. The sensitivity of the constant-temperature anemometer output as a function of the angle of the probe to the flow direction of a supersonic air jet was shown to introduce errors in the concentration measurement of a few percent. In order to use the probe for quantitative concentration measurements, it was necessary to know the local stagnation pressure. For these experiments this was recorded using a low-frequency-response pressure probe. For this reason, only time-averaged helium concentration values were reported.

An earlier paper by Ng and Epstein (1983) discussed the development of a related probe designed to provide temperature and pressure measurements in unsteady high-speed flows. The design incorporated two hot wires into an aspirated probe having a 1.5 mm i.d. This paper is particularly relevant because it contains an excellent discussion of many of the design considerations which must be taken into account when designing aspirated hot-wire or hot-film probes.

All of the measurements discussed thus far have focused on the use of aspirated hot wires or films to record concentration in mixtures of helium with heavier gases. These are particularly advantageous cases since the thermal conductivity, and hence expected probe response, of helium is much larger than for heavier molecular weight gases. Birch *et al.* (1986) were the first to consider the response of an aspirated probe to mixtures of a wide range of gases (helium, natural gas, ethylene, argon, and Freon 12 ( $\text{CF}_2\text{Cl}_2$ )) with air. They used the TSI, Inc Model 1440 aspirating probe described above. Calibration curves for large numbers of mixtures are presented. Unlike the study of Wilson and Netterville (1981), calibration curves are provided for mole fractions of the gas of interest in air varying from 0 to 1.

The calibration curves for each gas were very well defined with little variation for a given concentration. The response of the probe varied widely with the gas mixed with air. Increasing concentrations of ethylene, natural gas, and helium led to increasing voltage outputs, while decreasing voltage outputs were observed for argon and Freon 12. As expected, the largest response was found for helium, while the remaining four gases had similar signal magnitudes. The output voltages for natural gas and argon varied linearly with concentration while the other three gases yielded curves with definite curvature.

The calibrated Model 1440 probe was used to make concentration measurements in an axisymmetric jet of natural gas flowing into air. The concentration behavior in this same jet had been reported earlier using Raman spectroscopy (Birch *et al.*, 1978). Time-averaged centerline concentrations measured with the aspirated probe were shown to be in excellent agreement with the earlier measurements. Root-mean-square (rms) values were also reported for the concentration fluctuations along the centerline of the jet. In the far field the agreement was excellent, while in the near field the rms values measured by the aspirated probe were somewhat lower. Birch *et al.* attributed the lower values to a high-frequency cutoff in the response of the aspirated probe which resulted in some averaging of the concentration fluctuations. Based on their results, they estimated the frequency response of the probe as 500 Hz.

Birch *et al.* also reported the development of a much simpler and ruggedized aspirating probe. The probe was based on a TSI, Inc. Model 1291 probe which consists of a hot-film sensor built into a Swagelok fitting. A tube having a 6.4 mm diameter tube with a length of 25 mm was inserted into one end of the swagelok. The end of the tube was closed by a disk having a centered orifice of 0.25 mm diameter which formed the sonic orifice and also served as the sampling port. The other end of the sensor was connected to a vacuum line. Note that this sensor was configured with the sensor downstream of the sonic orifice. Calibration curves for this sensor were very similar to those for the Model 1440. However, the response time was seriously degraded, being on the order of 10 Hz. A system for multi-point measurements of concentration consisting of 64 of these ruggedized probes was described.

An array of five of the ruggedized probes were subsequently used to record concentration fluctuations within a turbulent jet of natural gas entering an air cross flow. The noise level of these probes was reported as corresponding to a methane mole fraction of 0.0025.

**11.2.2 Design Considerations.** In developing a probe for measuring halon 1301 and alternative agents in real-scale facilities we relied heavily on observations of a series of tests carried out during the study on *Evaluation of Alternative In-Flight Fire Suppressants for Full-Scale Testing in Simulated Aircraft Engine Nacelles and Dry Bays* (Grosshandler *et al.*, 1994). As part of this investigation, many releases of nitrogen-pressurized (typically 4.1 MPa) vessels containing liquid agents were investigated (Pitts, 1994). A number of parameters were measured during the tests, but the two which are most relevant for the current study are aspirated hot-film response and dynamic pressure measurements within the flow generated by the release.

Flow visualization showed that the agents typically "flashed" on exiting the containment vessel and formed a rapidly expanding two-phase flow. The two-phase flow traveled over long distances. A piezoelectric pressure transducer located on the centerline of the flow 1.3 m from the vessel exit was used to record the dynamic pressures generated by the passage of the flow. Measured dynamic pressures varied with agent, but were generally on the order of several MPa. Pressures of this magnitude can only be due to the arrival of a high speed two-phase (high-density) flow. Such high pressures exert significant forces which have the potential to destroy sensors or other objects placed in the flow.

Flashing of an agent occurs when a pressurized agent is suddenly opened to atmospheric surroundings. Since the boiling points of the tested agents were generally below the ambient temperature, the release of the pressure generated a condition in which the liquid was superheated, *i.e.*, the liquid was at a temperature (ambient) which was significantly higher than its boiling point. The response of the liquid was to begin boiling very rapidly and, in the process, extract sufficient heat from the remaining liquid to lower the temperature to the boiling point. The mass fraction of the liquid which can be vaporized is determined by the amount of heat stored in the liquid and is characterized by the Jacob number,  $Ja$ , defined as

$$Ja = \frac{\Delta h}{\Delta H_{vap}}, \quad (13)$$

where  $\Delta H_{vap}$  is the heat of vaporization for the liquid and

$$\Delta h = \int_{T_{amb}}^{T_{sat}} c_{p,l}(T) dT. \quad (14)$$

$c_{p,l}$  is the constant pressure heat capacity for the liquid which varies slightly with temperature and  $T_{amb}$  and  $T_{sat}$  are the ambient temperature and liquid boiling point, respectively. Generally, the agents having smaller values of  $Ja$  resulted in higher overpressures.

An uncalibrated TSI Model 1440 aspirated hot-film probe was mounted at the same location as the pressure transducer, and its voltage output was recorded during the releases. Arrival of the agent at the measurement location resulted in large voltage changes for all agents. In many cases the response was much greater than expected for a change in concentration of a gas. It was concluded that the large response occurred when a two-phase flow was present. This suggested that the aspirated hot film could be used to detect the presence of two-phase flow.

As noted above, during the release of a superheated liquid, the fluid is expected to cool very rapidly to its boiling point. This suggests that there are likely to be large temperature excursions associated with measurements of agent concentration. Recall that this presents a difficulty in applying aspirated hot films for concentration measurements since they respond to temperature fluctuations as well as concentration changes.

In designing the system for agent concentration measurements major characteristics which had to be considered were:

1. The ability to record continuous records of time-resolved concentration with the desired response time of 1 ms,
2. The need to record measurements in flows subject to velocity and temperature fluctuations,
3. The need for the probe to be robust enough to survive high-velocity flows and significant overpressures in two-phase flows, and
4. The need to have an efficient and easily implemented calibration system.

The first decision was the type of aspirated probe to use for the system. Several different designs are discussed in the previous section. Given the short period of the project, it was concluded that insufficient time was available to design, fabricate, and test a probe based on one of the designs available in the literature, and that it was desirable to use a commercially available probe. The only

commercial aspirated probes that were identified were those produced by TSI<sup>2</sup>, Inc. For this reason, the decision was made to use Model 1440 aspirated hot-film probes manufactured from TSI, Inc. as the basis for the instrument. There were numerous descriptions of the use of these probes in the literature which provided confidence that they had sufficient time response and insensitivity to velocity fluctuations to be useful for our purpose. Since a probe of this type was used in the earlier investigation of two-phase flows (Pitts *et al.*, 1994), it was known that they were capable of surviving the environment generated by an agent release from a pressurized bottle.

In order to correct the response of the probe for temperature variations, it was necessary to record the fluid temperature at a location very near the hot-film sensor with a frequency response of at least 1 kHz. A number of approaches were considered including thermistors, thermocouples, and cold wires. Generally, the time responses for commercially available thermistors and thermocouples were too slow for this application. It was concluded that the use of a cold wire was the most viable approach for measuring temperature. Note that this approach had been adopted earlier by Jones and Wilson (1979). At the time this decision was made we were unaware of this previous work.

The operating principle of the cold wire is fairly simple. As shown by Equation (1), the resistance of a cold wire or film is a function of temperature. The resistance of the wire can be quantified by passing a small constant current through the wire sufficient to cause a measurable voltage drop, but too small to cause significant resistive heating of the sensor. The voltage output is therefore proportional to sensor resistance. Note that these measurements are done in the "constant-current" mode unlike the velocity and concentration measurements discussed earlier which generally employ the "constant-temperature" (*i.e.*, constant resistance) mode.

Due to the small heating of the wire, the sensor output voltage is nearly independent of the flow velocity across the sensor. However, the frequency response to temperature changes is a function of velocity. This is due to the need to transfer heat to or from the sensor when the temperature changes. As discussed in Section 11.2.1.2, the amount of heat transferred from a fluid is a function of the velocity as well as the fluid properties. Antonia *et al.* (1981) discuss the theory which can be used to estimate the frequency response and report measurements for cold wires of 0.63  $\mu\text{m}$ , 1.3  $\mu\text{m}$ , and 2.5  $\mu\text{m}$  diameter as a function of velocity of air. Response frequencies were found to vary nearly linearly with velocity. For the smallest wire, the frequency response was greater than 1 kHz.

Having decided which approach to use for the proposed measurements, the next step was to actually design and procure the required probes. The design work was done in collaboration with staff from TSI, Inc. Three members of the research team (W. Pitts, D. Hess, and B. Breuel) traveled to Minneapolis and met with Jagadish Buddhavarapu, Skip Kiland, and Steve Hoff of TSI for two days. A number of topics were discussed including the viability of the chosen approach, potential problems in the manufacture of the probes, and pricing. It was agreed that the best approach was to modify a standard Model 1440 aspirating hot-film probe by locating the cold wire just outside of the entrance to the probe.

The decision to locate the cold wire outside of the aspirating probe raised a potential problem. In order to have an adequate time response, the diameter of the cold wire was required to be on the order of a few microns. It was not at all clear whether or not such a small probe could survive the severe environment generated by the two-phase flow formed by the release of the fire-fighting agents. In order to determine whether or not such probes were robust enough, a test was run in which single cold

---

<sup>2</sup>Certain trade names and company products are mentioned in the text or identified in an illustration in order to specify adequately the experimental procedure and equipment used. In no case does such identification imply recommendation or endorsement by the National Institute of Standards and Technology, nor does it imply that the products are necessarily the best available for the purpose.

wires (Models 1210-T1.0 and 1210-T1.5, diameters of 2.5  $\mu\text{m}$  and 3.8  $\mu\text{m}$ , respectively) were placed in the flow generated by the release of FC-218 ( $\text{C}_3\text{F}_8$ ) from a vessel pressurized to 4.1 MPa. This test was run in the same facility used previously for investigating releases of fire-fighting agents (Pitts *et al.*, 1994). The probes were located 1.3 m from the vessel opening. Neither cold wire was operated during the test. Both were found to be operational after the superheated liquid was released.

Later releases were performed in which the Model 1210-T1.5 probe was operated with the cold-wire current set to 1 mA. Figure 4 shows an example of the signal recorded during one of these preliminary releases. The dynamic pressure measured during this test at the temperature measurement position reached approximately 9 MPa. The probe was not carefully calibrated, but a voltage change of 1 V corresponds roughly to a temperature change of 6  $^{\circ}\text{C}$ . The plot indicates that there was a rapid drop of approximately 55  $^{\circ}\text{C}$  when the discharge reached the cold wire. This is consistent with the boiling point of FC-218 (-37  $^{\circ}\text{C}$ ) for an initial starting temperature of 21  $^{\circ}\text{C}$ . After the passage of the two-phase flow, the temperature increased again, but still remained below the initial room temperature. This experiment demonstrates that the temperature does vary during releases of the agent, and that cold-wire probes can survive the harsh environment created by an agent released from a pressurized bottle striking the probe.

An experiment was run in which a cold wire was located at various distances from the entrance of an operating aspirated hot-film. The results indicated that the response of the cold wire was insensitive to the separation from the cold-wire to the aspirated probe. On the basis of these experiments, an order was placed with TSI, Inc. to design and construct a probe consisting of an aspirated hot film with a cold wire mounted just outside of the tube.

Figure 5 shows a schematic of the probe designed by TSI, Inc. It incorporates a standard hot film and a standard hot wire operated as a cold wire. The hot film sensor, designated as "-20", consists of a cylindrical quartz substrate having a diameter of 51  $\mu\text{m}$  with a thin layer of platinum deposited on the surface which conducts and serves as the heating element. The probe is overcoated with a thin protective layer of alumina. The hot-wire designation is "T1.5." It is made from tungsten wire having a 4.0  $\mu\text{m}$  diameter. A thin layer of platinum is overcoated on the wire to limit surface oxidation of the tungsten.

**11.2.3 Combined Aspirated Hot-Film/Cold-Wire Probe Electronics and Operation.** The combined aspirated hot-film/cold-wire probe requires two sets of control electronics in order to make measurements. The hot-film is operated by a constant-temperature anemometer and the cold wire by a constant-current anemometer. A TSI, Inc. IFA 100 modular system was used for both types of measurements. The overall system is contained within a system cabinet (Model 158) which includes a microprocessor that aids in setting up the instruments and provides slots and power for up to four constant-current and/or constant-temperature anemometers. A keypad on the cabinet allows all of the major function of the system to be accessed. Remote access by RS-232 signals is also possible, but was not utilized in the current study.

The constant-temperature anemometer was a Model 150. It was paired with a Model 157 signal conditioner which provided frequency filters, a high-gain amplifier, and DC offsets. As discussed above, this is a circuit designed to maintain the resistance of the probe at a preset constant level by varying the current flow through, and hence the heating within, the probe in response to variations in heat losses from the probe. This is generally done by placing the probe in one leg of a four-leg Wheatstone bridge as indicated in Figure 6. The particular circuit used for this study was a 5:1 bridge. The control resistance is set to a value five times greater than desired as the operation resistance for the probe. The control amplifier varies the current through the resistors in such a way that the bridge is balanced (*i.e.*, there is no flow of current into the amplifier). Thus the setting of the control resistance actually determines the operating resistance of the probe. A voltage output is available from

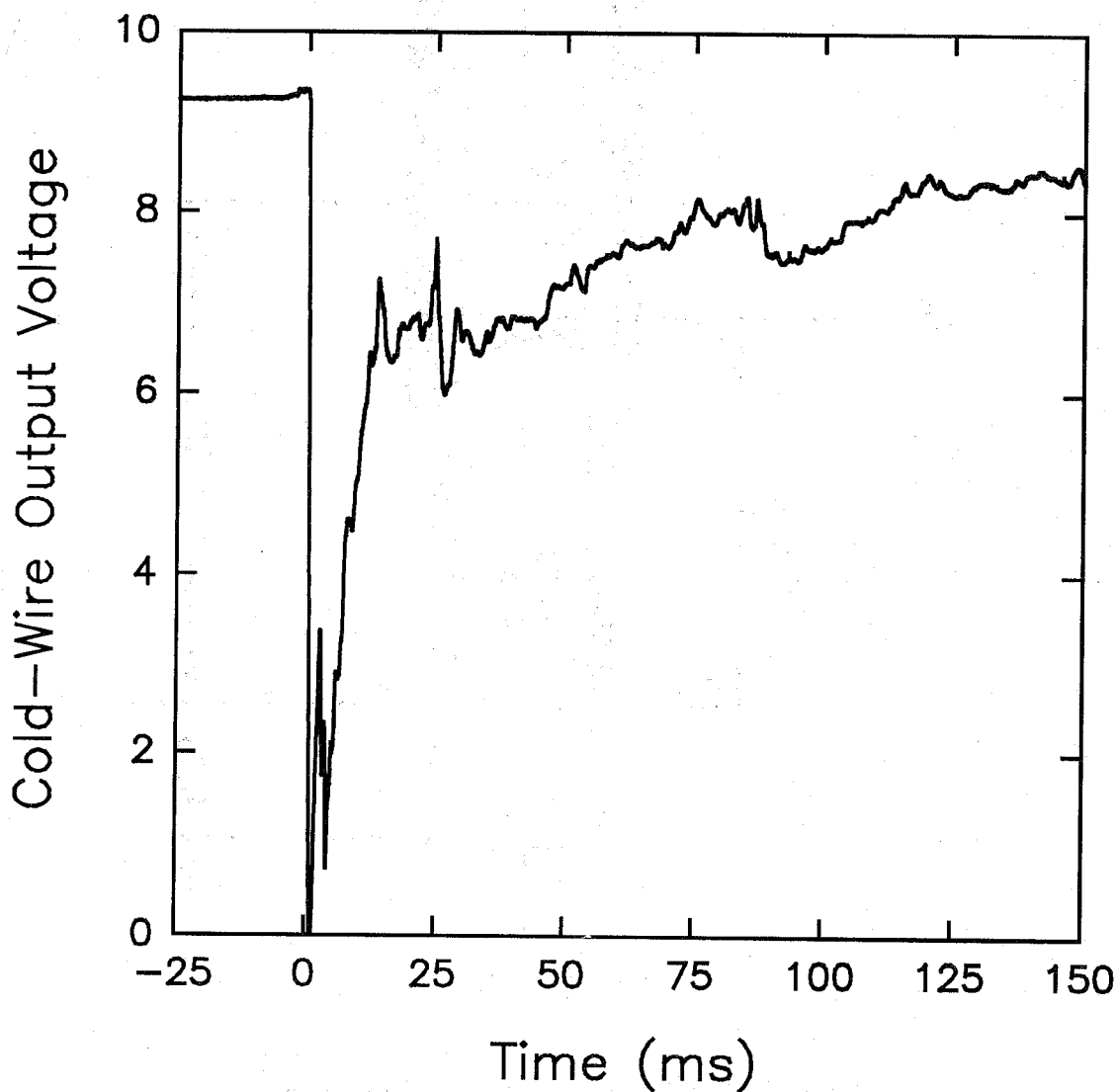
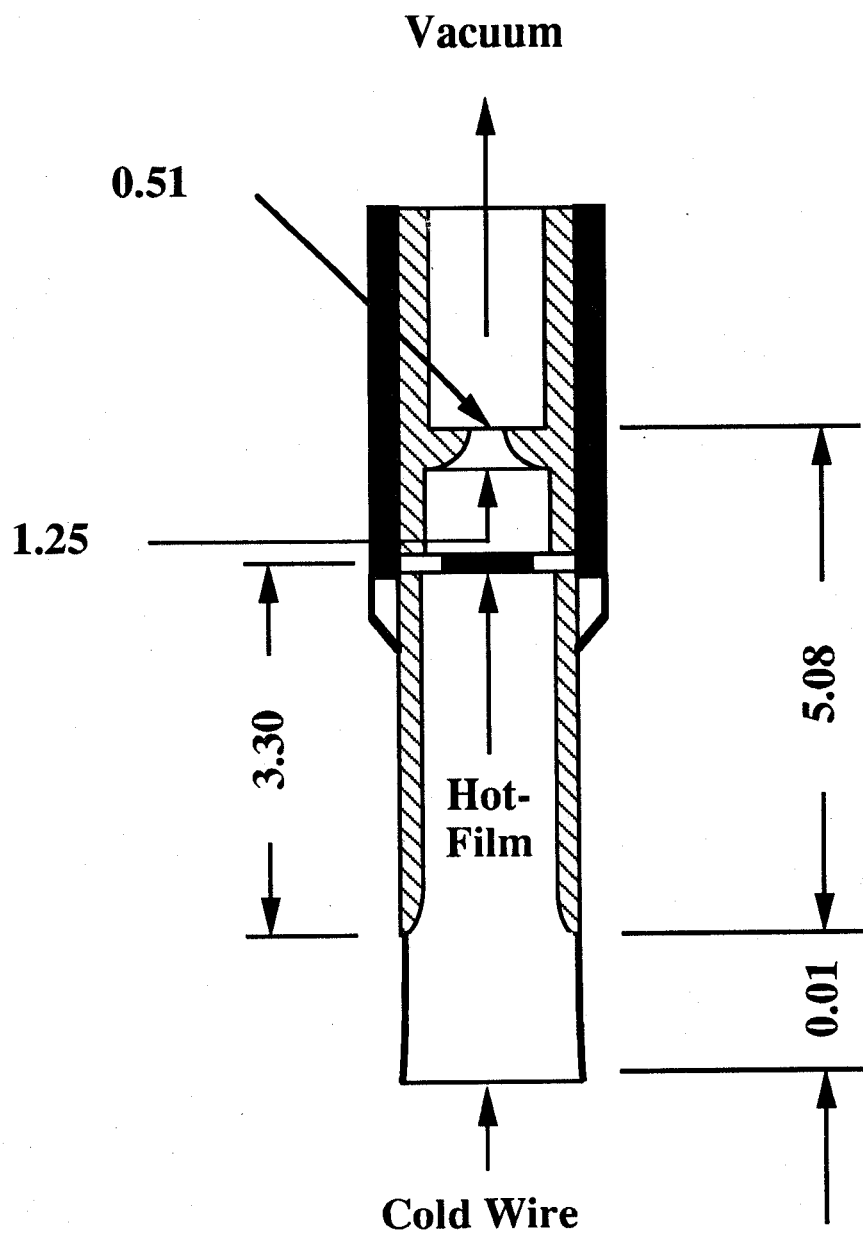


Figure 4. An example of the time-resolved voltage output from a cold wire recorded during a release of FC-218. A voltage change of 1 V corresponds roughly to 6 °C.





**\* All Measurements are in mm**

Figure 5. Schematic diagram of the TSI, Inc. combined aspirated hot-film/cold-wire probe which is designated by TSI, Inc. as a Model 1440S aspirated hot-film probe.

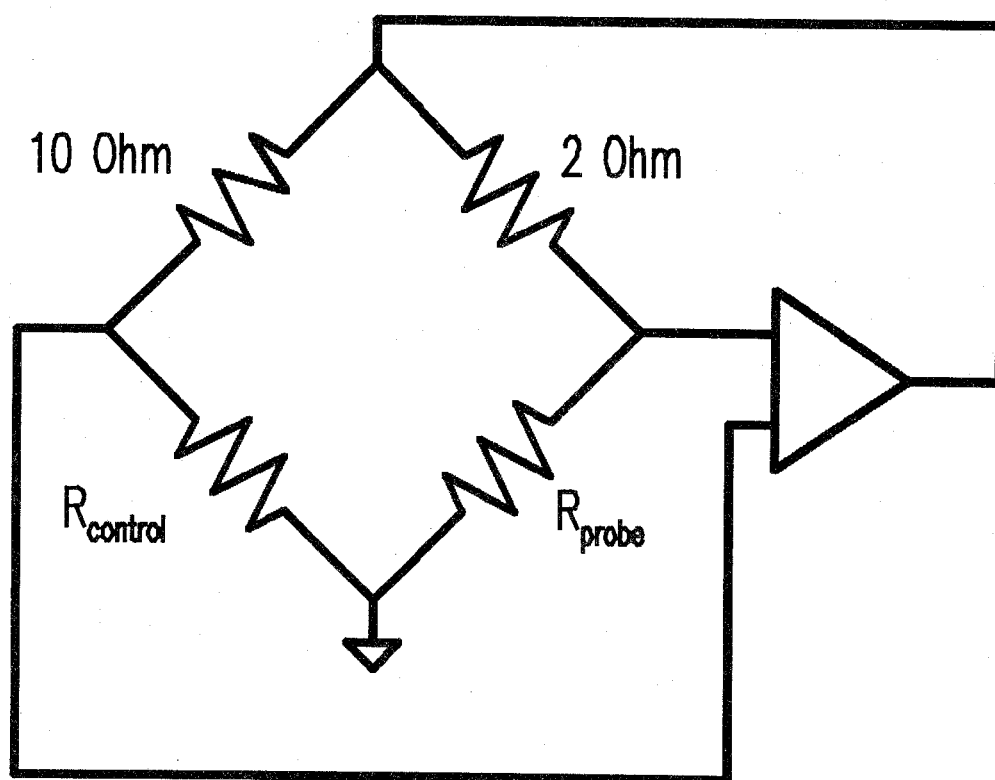


Figure 6. A schematic of the bridge circuit used for the constant-temperature anemometer is shown.

the Model 150 which is directly related to the heat loss of the sensor.

The aspirated hot film requires that the volume downstream of the supersonic nozzle be evacuated to a low enough pressure to ensure choked flow. For the ambient conditions of these experiments this required a pump capable of pumping 7 L/min at 33 kPa. A Thomas Industries, Inc. Model 905CA18 single cylinder, oil-less vacuum pump was used. The pump was connected to the aspirated probe through a stainless-steel tube attached to the 3.2 mm Swagelok vacuum connection of the probe.

The constant-current anemometer was a TSI Model 145 which was mounted in the Model 158 system cabinet. This module provides a preset constant current to the probe which is small enough to ensure that heating of the probe is minimal. It outputs a voltage which is proportional to the resulting voltage drop across the probe. The output signal is directly proportional to the resistance of the probe which, for small temperature changes, varies linearly with temperature. The Model 145 allows the voltage output to be adjusted such that a 0 V output corresponds to a reference temperature and the gain (50 to 1000) can be adjusted so that the  $\pm 5$  V output corresponds to the temperature range of interest.

**11.2.4 Calibration System.** Even though theories and models are available which have been used to predict the response of hot films and cold wires (see the discussion in Section 11.2.1.1), in practice, it is necessary to perform extensive calibrations of these devices, fit the calibrations, and then use the observed response of an instrument to an unknown condition along with the appropriate calibrations to deduce a value for the desired variable. The need for calibration presented a severe challenge for the proposed combined aspirated hot-film/cold-wire system since it had to be calibrated for variations in both agent concentration and temperature. Efficient algorithms were also required to convert the observed voltage outputs of the hot-film and cold-wire electronics to measurements of temperature and concentration using the calibration results.

In order to obtain meaningful calibrations, it was necessary to develop a system for generating known agent concentrations and temperatures over the full ranges of interest to this investigation. These ranges were chosen to be zero to one mole fraction of agent and  $-58$  °C (the boiling point of halon 1301 ( $\text{CF}_3\text{Br}$ )) to  $40$  °C (a relatively high ambient temperature) for temperature. The agents to be tested included the three alternative agents recommended for testing in full-scale systems (Grosshandler *et al.*, 1994), FC-218 ( $\text{C}_3\text{F}_8$ ), HFC-125 ( $\text{C}_2\text{HF}_5$ ), and HFC-227ea ( $\text{C}_3\text{HF}_7$ ), and halon 1301 for comparison purposes.

A unique computer-controlled calibration system was designed, constructed, and tested during the project. An overall schematic for the flow calibration system is shown in Figure 7. The major components are 1) sources for the air and agent, 2) mass-flow controllers for both the air and agent, 3) a mixing chamber to effectively mix the flows of agent and air, 4) a thermal bath capable of accurately controlling the temperature, 5) a heat exchanger to ensure the gas flow and bath temperature were equilibrated (not shown in Figure 7), 6) the test section where the probe was located, 7) a thermocouple to measure the temperature in the thermal bath, and 8) the computer control and measurement system. A personal computer interfaced to the calibration system was used to calculate the required flows of agent and air for a preset concentration, set the mass-flow controllers, open the appropriate solenoid valves, and record the voltage outputs of the aspirated hot film, cold wire, and thermocouple. The individual components of the calibration system are described in the following sections.

**11.2.4.1 Test Section.** The first step in the design process was to specify the calibration test section where the gas mixtures would be extracted by the aspirating probe. The mass-flow rate for gases extracted by the aspirated probe was first estimated for the agents and air using the equation for isentropic adiabatic flow of an ideal gas through a sonic orifice, Equation (11). Note that the mass-

## CALIBRATION FACILITY

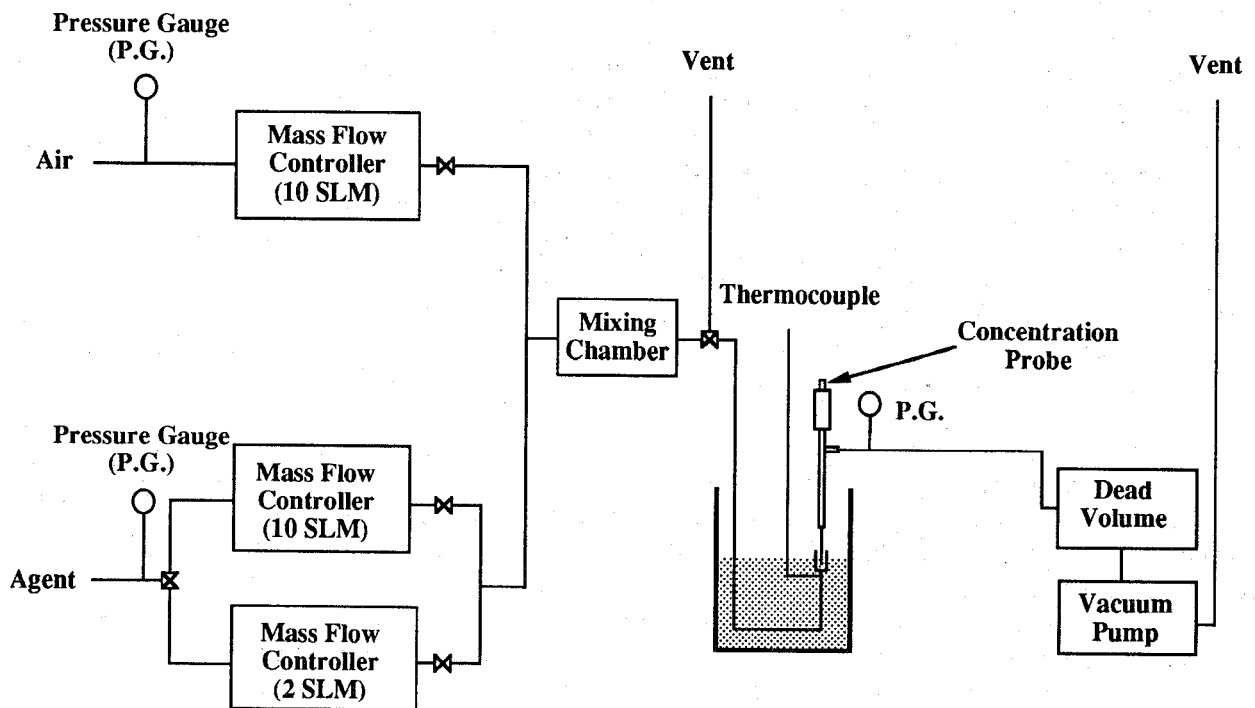


Figure 7. Overall schematic for the calibration facility used to generate flows of known agent concentration and temperature.

flow rate for the supersonic nozzle used in the aspirated probe is calculated by dividing  $(pV)^*$  by the area of the nozzle,  $0.02027 \text{ mm}^2$ . Gas temperatures were varied over the range from the boiling points of the individual agents ( $-60^\circ\text{C}$  for air) to  $40^\circ\text{C}$ . For comparison purposes, the mass-flow rates are expressed in comparable standard ( $0^\circ\text{C}$ ,  $101 \text{ kPa}$ ) liters per minute of nitrogen (slmn), the unit of measure for the mass-flow controllers used in the experiment. The gas correction factors required for the calculation (see ahead) were those recommended by the manufacturer. A FORTRAN program, included as Appendix A, was written to perform the calculations.

Table 1 lists the results. It can be seen that the values fall in a range of 2.25 slmn to 4.55 slmn. To ensure that the gas flow rate exceeds the withdrawal rate of the aspirated probe and to provide an excess flow to prevent backstreaming of gas from downstream of the probe, values of the actual flow rates must exceed the values listed in Table 1.

In order to accurately control the temperature of the gas at the probe entrance, it was necessary that the volume to be sampled be surrounded by the liquid of the temperature bath. This required the probe to be "plunged" into the flow since it was impractical to incorporate the probe into a closed flow system. In choosing an appropriate test section it was desirable to have a large cross section at the measurement location to limit flow velocities and to have a narrow exit from the test section to the atmosphere to create higher velocities and prevent backflow of air into the volume. A Whitey 304L-HDF4-50 sample cylinder was used to form the test section. This is a stainless-steel cylinder having a length of 95.2 mm with an i.d. of 34 mm. The inside dimensions are smoothly tapered at either end to 6.4 mm pipe-threaded exits. The cylinder was mounted vertically onto a pipe which was part of the mixing and flow system. The upper end of the test section was open to the air.

A lever designed for use with a drill press was placed near the test section. The probe to be tested was mounted on the lever. In this way it was possible to position the probe outside of and above the test section when the lever was in the "up" position, or manually lower the probe into the test section where it could be locked in place.

**11.2.4.2 Mixing Chamber.** Mixtures of agents in air were required having mole fractions ranging from zero to one. In order to ensure that the concentrations were constant, it was necessary to mix the gases uniformly before they were cooled and transported to the test section. A specially designed chamber was used for this purpose. Figure 8 shows a schematic of a horizontal cross-sectional cut through the gas mixer. It consists of a volume with baffles forming four sections that stir and mix the two gas stream flowing into the first section. The outside dimensions of the mixer are 51 mm (w)  $\times$  86 mm (l)  $\times$  51 mm (h). The outer walls are 6.4 mm thick and the baffle walls are 3.2 mm thick. Corners are curved on 6.4 mm radii. A single block of stainless steel was machined to form the inner volume of the mixer and a cover was then welded onto the block. Figure 9 is photograph of the machined mixer and its cover before final welding.

Four holes threaded for 6.4 mm pipe were drilled into the mixer. Three of these were centered in the three outer walls of the first section and the fourth in the opposite wall of the fourth section. 6.4 mm diameter stainless-steel pipe-to-BNC connectors were inserted in each of these positions. Figure 8 indicates the positions where air and agent flows enter the mixer. Note that the two gas streams enter perpendicular to each other which promotes efficient mixing. The third flow position in this section was capped. The mixed gases exit at the far end.

Subsequent experiments showed that this design was very effective in mixing the gas streams and that any fluctuations in concentration were too small to detect.

**11.2.4.3 Mass-Flow Controllers.** Three mass-flow controllers were used to provide the flows of air and agent required to prepare the gas mixtures. Note that mass-flow controllers are designed to deliver a known mass of gas, but that they are generally calibrated in terms of the volume flow rate

Table 1. Flow Volumes Required for Gases Listed in Mass-Flow Controller Units of Standard Liters Per Minute Nitrogen (slmn). Calculations for the Lower Temperatures Listed and 20 °C

Gas	Lower T	Lower T required flow	20 °C required flow
air	-60 °C	2.64 slmn	2.25 slmn
HFC-227ea	-16 °C	4.55 slmn	4.26 slmn
FC-218	-36 °C	4.89 slmn	4.40 slmn
HFC-125	-48 °C	4.12 slmn	3.61 slmn
halon 1301	-58 °C	2.78 slmn	2.38 slmn

( $Q_{slm}$ ) of gas delivered for standard conditions (0 °C, 101 kPa). Actual flow volumes delivered can be calculated by correcting the slm reading for the actual conditions using

$$Q_{actual} = Q_{slm} \times \frac{T_{actual}}{273.15 \text{ K}} \times \frac{101 \text{ kPa}}{P_{actual}}, \quad (15)$$

where  $Q_{actual}$ ,  $T_{actual}$ , and  $P_{actual}$  are the volume flow rate, temperature, and pressure for ambient conditions.

Figure 10 shows a schematic of the flow-control system. MKS Instruments, Inc. Type 1359C mass-flow controllers were chosen for the system because of their high accuracy ( $\pm 0.5$  % of full scale), resolution (0.1 % of full scale), and control range (1.0 % to 100 % of full scale). The flow system was designed to cover a concentration range from 0 to 1 mole fraction of air with a resolution of 0.01. The flow calculations described earlier indicated that a range of 10 slmn would be sufficient for the air mass-flow controller. Since the calibration curves for a flow meter using air or nitrogen are nearly identical, a single flow meter having a maximum flow rate of 10 slmn (Model 1359C-10000SN) was adequate for air. However, when using gases having properties which are different than those for nitrogen, the actual flow rate of the gas is equal to

$$Q_x = F \times Q_{full, N_2} \times GCF_x, \quad (16)$$

where  $Q_x$  is the volume flow rate for gas  $x$ ,  $F$  is the fraction of full-scale setting for the mass-flow controller,  $Q_{full, N_2}$  is the nominal full-scale range of the flow meter for nitrogen, and  $GCF_x$  is the gas correction factor for gas  $x$ . Table 2 shows the gas correction factors recommended by MKS Instruments for the gases of interest. From these values it is clear that a mass-flow controller having a range of 10 slmn cannot accurately provide the flow required to create a 1 % agent concentration (*i.e.*, the required setting for the mass-flow controller will be less than 1 %). For this reason, a second mass-flow controller was included in the agent stream so that lower flow rates of agent could be generated accurately. A meter having a full-scale range of 2 slmn (Model 1359C-02000SN) was chosen. The mass-flow controllers were connected to a MKS Type 247C 4-Channel Readout. The

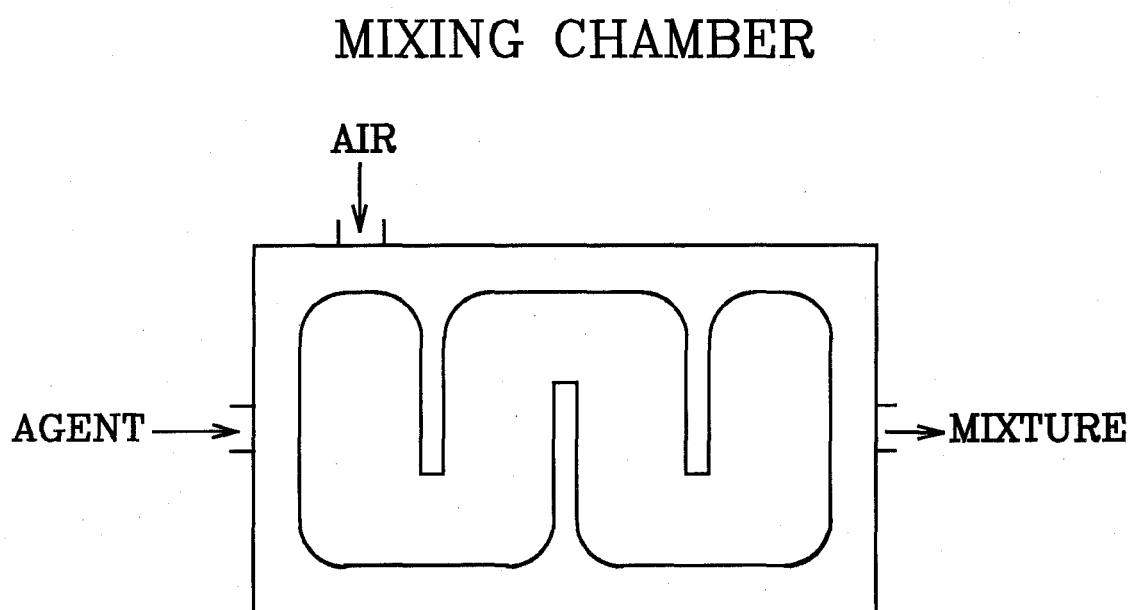


Figure 8. Cross-sectional view of the gas mixer for flows of an agent and air.

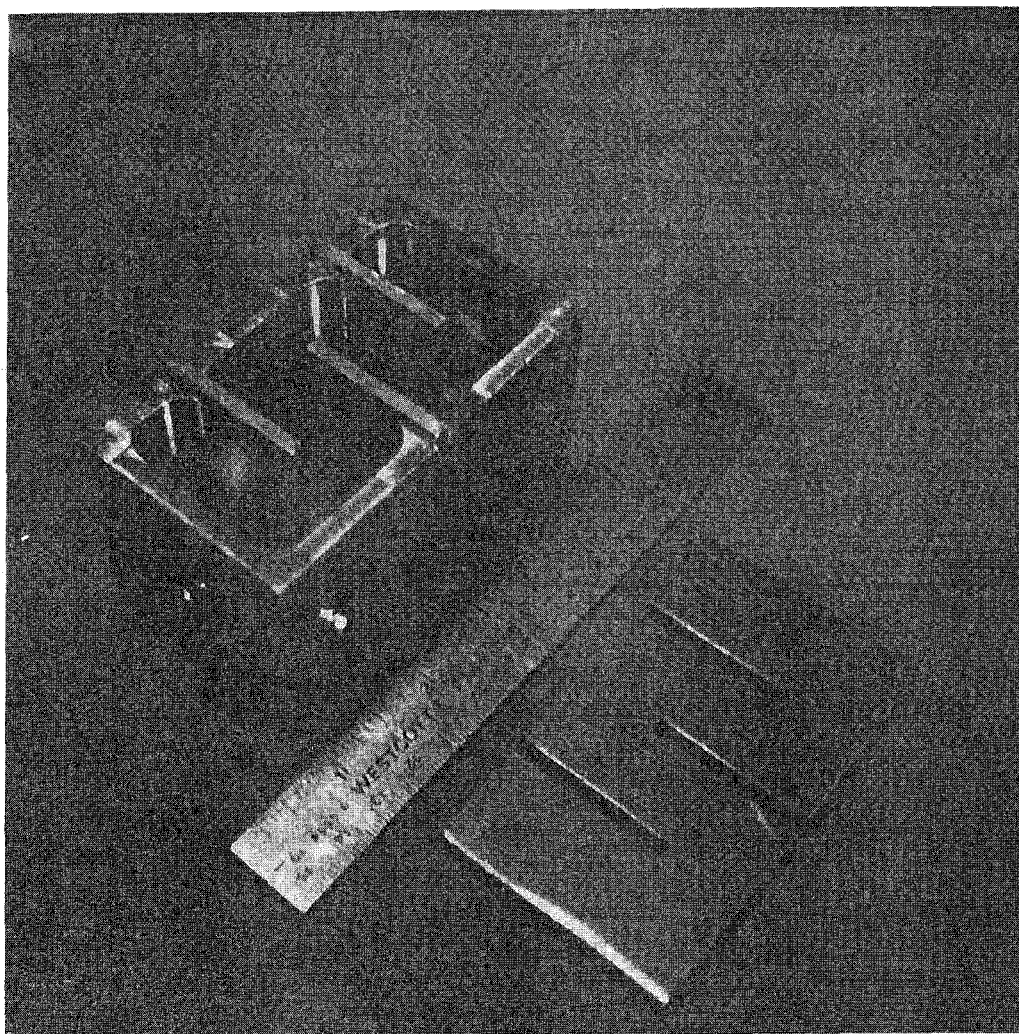


Figure 9. Photograph of the gas mixer showing the machined body and top before welding.



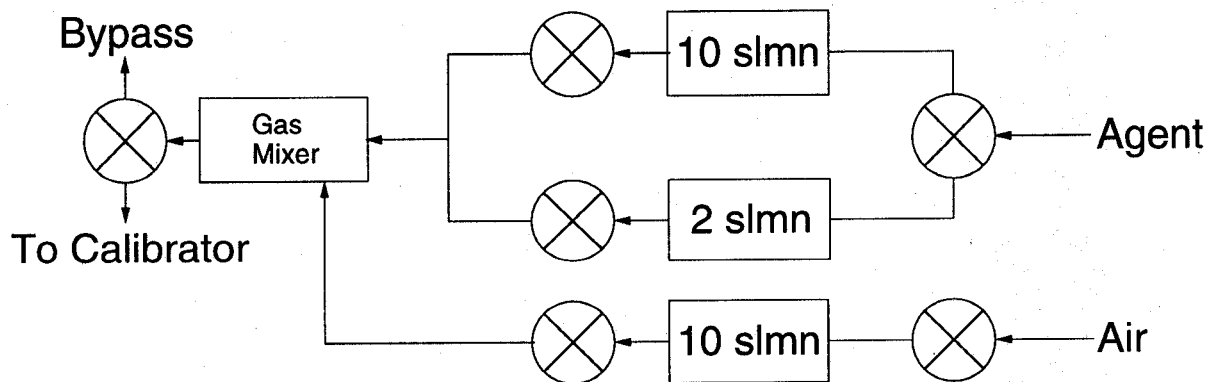


Figure 10. A schematic diagram of the flow meters and electro-pneumatic-actuated ball valves used to control agent and air flows for the variable-temperature concentration calibration system.

Table 2. Gas Correction Factors Recommended by the Mass-Flow Controller Manufacturer for the Gases Investigated

Gas	GCF
air	1.00
HFC-227ea	0.18
FC-218	0.17
HFC-125	0.30
halon 1301	0.37

readout system acted as the power supply, analog readout, and set point source for each of the three mass-flow controllers. In particular, the Type 247C accepts 0 V - 5 V analog inputs which act as set points for the selected mass-flow controllers. This allows the mass-flow controllers to be remotely set by computer.

Mass-flow controllers are sensitive to changes in temperature. In order to limit calibration changes due to temperature variations, the three mass-flow controllers were placed on a thermostated block of aluminum containing thermistors and two small heaters. The temperature of the block was set to be slightly higher (32 °C) than room temperature.

The mass-flow controllers were carefully calibrated for each of the gases to be used. Volume-flow rates of air and the agents were measured using a Humonics, Inc. Model 730 Digital Soapfilm Flowmeter. The accuracy of this device was checked by using a NIST standard piston prover. The accuracy was within 1 % over the entire range of the flowmeter. The gas to be calibrated was connected to the chosen mass-flow controller, a range of set point voltages were applied to the appropriate Type 247C 4-Channel Readout input, and the resulting volume-flow rate was recorded with the soap film flow meter. The temperature of the flow was recorded simultaneously.

In order to convert the volume-flow rate measured by the Humonics to standard L/min it was necessary to correct for pressure and temperature differences using Equation (15). Values for  $Q_{slm}$  are derived by substituting actual values of volume-flow rate, temperature, and pressure into this expression. The pressure correction was not made during the calibrations. Figure 11 shows an example of a calibration curve for the agent 10 slmn mass-flow controller using HFC-227ea as the test gas. For nitrogen at standard conditions, the full-scale voltage would be 5 V giving a slope of 2 slmn/V. The actual slope of 0.387 requires that the gas correction factor (GCF) be 0.194. GCFs were determined for the 2 slmn and 10 slmn agent mass-flow controllers in the same way. Table 3 lists the results for the four agents investigated. In most cases, the results are averages of two determinations. Comparison of Table 2 and Table 3 shows that the values of GCF determined experimentally agree well with those recommended by the mass-flow-controller manufacturer.

Since mass-flow controllers were utilized in the system, the flow system was designed to deliver a constant mass-flow rate. A value of 0.210 g/s was used because this corresponds to nearly the full-scale value of the air mass-flow controller (10 slmn) and provides sufficient volume flow rates for all mixtures to more than meet the extraction requirements of the aspirating probe.

A three-way (on-off, two flow directions) electro-pneumatic-actuated ball valve (Whitey Model SS-62XTS4-F4-N-51DD) was used to route the agent flow to the proper mass-flow controller. In

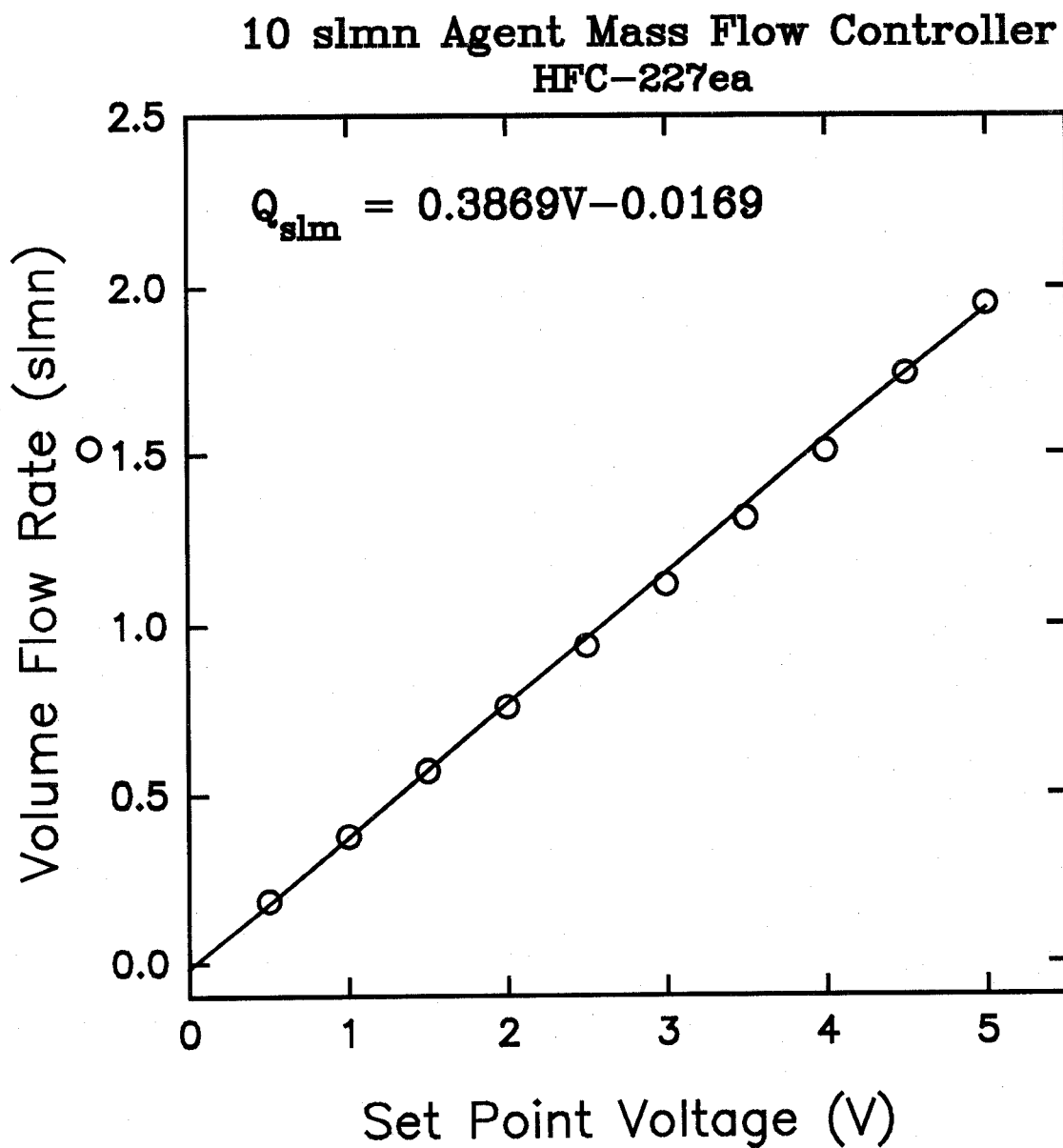


Figure 11. An example of the calibration results for HFC-227ea using the 10 slmn agent mass-flow controller.

Table 3. Experimental Gas Correction Factors for the Gases Investigated

Agent	2 slmn <i>GCF</i>	10 slmn <i>GCF</i>
HFC-227ea	0.190	0.192
FC-218	0.177	0.176
HFC-125	0.273	0.276
halon 1301	0.373	0.385

order to provide additional flow control and safety, a set of three two-position (on-off) electro-pneumatic actuated ball valves (Whitey Model SS-62TS4-N-31CD) were placed on the flow outlets of the mass-flow controllers. The ball valves were actuated by coupling 120 V ac to the proper connection of the actuator.

A second three-way valve was placed on the downstream side of the gas mixer. One of the outputs of the valve directed the gas flow to the test section. The second was connected to a line which simply dumped the flow into the hood where it was exhausted.

The valves were actuated by applying 120 V ac to the appropriate inputs. Small lamps connected to the valve power supplies were mounted on the top of each valve. When the valves were energized, the lamps would light and provide an indication that the valve had been opened or switched. A house 680 kPa air line was used to pressurize the electro-pneumatic actuated ball valves.

Pressurized bottles of air and the agent to be tested were coupled to the input solenoids. Regulated pressures were set to 137 kPa.

**11.2.4.4 Thermal Bath and Heat-Transfer Coil.** The temperature of the gas was controlled by passing the flow through a heat-transfer coil contained within a temperature-controlled bath of polydimethylsiloxane (Dow Corning Corporation Syltherm XLT Heat Transfer Fluid). The temperature bath was contained in a 7.75 L Agitainer-B vessel from Neslab Instruments, Inc. which provides a magnetic stirrer to mix the working fluid. In order to ensure that the fluid was well mixed and, therefore, at a uniform temperature, a second mechanical stirrer was added to the bath.

Temperature control was achieved by simultaneously heating and cooling the bath liquid. Cooling was provided by an immersion cooler (Neslab Instruments, Inc. CC-100II) equipped with a small diameter probe ("FV") for sensing temperature in the bath fluid. This cooler is capable of cooling to -90 °C with no thermal load. Over the temperature range of interest, it extracts more than 120 W of heat. The desired temperature for the bath was obtained by using a Neslab Exatrol Digital Temperature Controller in combination with a 250 W heater. The FV sensor measures the bath temperature, and the controller uses a feedback circuit to determine when it is necessary to add heat to the system and turns on the heater until the desired temperature is reached. A second 700 W heater was included in the system which was only used when it was required to rapidly raise the temperature from a lower value to a higher one. Once the desired temperature was reached, the second heater was turned off. Temperatures were adjusted simply by setting the desired temperature on the Exatrol controller.

A Type E thermocouple was placed in the bath fluid to provide an accurate measurement of the temperature. It was calibrated using ice- and boiling-water baths in conjunction with thermometers

calibrated by NIST. Temperatures were read using the computer system described below. It was determined that the bath temperature remained constant to within  $\pm 0.5$  °C.

The temperature of the gas to be calibrated must be brought to the bath temperature before entering the test section. In order to achieve this the gas must flow through a pipe for a sufficient period of time to ensure that the gas temperature reaches the same temperature as the pipe walls (*i.e.*, the bath temperature). Standard formulas are available (Pitts and Sissom, 1977) which allow the heat transfer to a gas flow within a pipe to be calculated assuming a constant wall temperature and either laminar or turbulent pipe flow. These formulas were used to solve for the pipe length required for the gas to come to the pipe wall temperature using a FORTRAN program named COIL.FOR, which is included as Appendix B. Table 4 lists the calculated lengths of a 6.35 mm diameter pipe required assuming either laminar or turbulent flow conditions along with minimum Reynolds numbers for the flows. Pipe flows are expected to be turbulent for Reynolds numbers greater than 2000. Therefore, it can be concluded that a pipe of 0.6 m length should be sufficient to cool these gases to the bath temperature.

A total pipe-flow length of 1 m was provided by coiling a 6.35 mm length of pipe and placing it at the bottom of the thermal bath. Swageloks on either end of this section were used to connect the coil to tubing joined to the gas mixing chamber and the measurement test section.

The temperature bath was placed on a x-y positioner controlled by manual micrometers. This positioner allowed the test section within the thermal bath to be accurately positioned relative to the lever arm used to lower the probe into the test section. In this way it was possible to lower the probe into the test section without risk of damage.

**11.2.4.5 Data Acquisition and Control.** All of the control and data acquisition functions required for the calibration of the combined aspirated hot-film/cold-wire probe, except for setting the temperature of the silicon oil bath, were automated. Central control was provided by a TCP 486-DX personal computer having a clock speed of 66 Mhz, 8 Mbytes of RAM, and a 250 Mbyte hard drive. Two plug-in modules--a Flash-12 Model 1 data-acquisition board and a ACAO-12-2 analog and digital output board--from Strawberry Tree were installed in computer bus slots and provided interfaces for the experiments. Workbench PC data acquisition software was used to provide overall control.

The Flash-12 Model 1 board has 16 single-ended or 8 differential analog inputs which can be digitized at a total rate up to 1 MHz. Eight TTL-compatible input/output lines are also available. The board is set up to provide thermocouple cold-junction compensation and linearization. An optional "daughter board" (Model DB03) was installed which provides on-board memory sufficient for recording one million samples. The daughter board allows large data sets to be recorded with the full temporal resolution of the digitizer. It also provides two 12-bit digital-to-analog converter outputs. Digital ribbon cable was used to connect the Flash-12 to a T21B terminal board which provided convenient electrical connections for the calibration system.

The ACAO-12-2 has two 12-bit digital-to-analog converters which have switch selectable ranges of 0 V - 10 V, 0 V - 5 V,  $\pm 5$  V, or 4 mA - 20 mA. Eight digital I/O lines which can be individually configured as either inputs or outputs are also available. This board was connected through digital cable to a T-31 general-purpose interface board.

A special interface box containing the T21B and T31 interface boards was constructed. Connections to the calibration system were made through these interface boards. Appendix C lists the various electrical connections to the output signals of the interface boards.

An icon-based work sheet named ACTRL3.WBB was assembled to control the calibration process. A copy of this work sheet is included as Appendix D. This work sheet provided all of the calculations and controls necessary to turn on and set the mass-flow controllers, open and close the proper valves, provide indicator lights on the calibration system, automatically step through a series of

Table 4. Calculated Lengths of 6.35 mm Diameter Pipe to Cool Air and Agent Flows to Temperature of Thermal Bath. Calculations Assume Laminar and Turbulent Pipe Flow. Reynolds Numbers are Calculated for the Lowest Flow Velocities.

Agent	Required pipe length (m) for laminar flow	Required pipe length (m) for turbulent flow	Reynolds number
air	1.41	0.51	2710
HFC-227ea	2.27	0.60	3850
FC-218	2.18	0.59	3710
HFC-125	2.15	0.58	3690
halon 1301	1.85	0.56	3200

concentrations, and record measurements of the bath temperature and the voltage outputs for the aspirated hot-film and cold-wire controllers. The entire process was controlled by "pushing" the appropriate buttons using a mouse on a computer-screen "control panel" created by the work sheet. An example of the control panel is shown in Appendix E.

The following events occurred when a calibration sequence was started. The data acquisition logs for the system were first enabled. Then commands were sent to open the electro-pneumatic valve on the air outlet and to switch the three-way solenoid valve to let gas pass through the test section. Simultaneously, a flag was set on the computer-screen control panel indicating that a test had started, and a logical pulse generator was triggered which generated a pulse every 42 s. The output of the pulser then traveled two paths. The first was to a counter which simply counted the number of pulses received. This number was multiplied by 0.1 to give the current air mass fraction for the calibration. When the air mass fraction became greater than one, a trigger was fired which halted further data collection. The second pathway from the pulse generator started a 20 s timer which then triggered a second one-shot pulse generator with a 20 s output. The end of the second 20 s period caused the current analog-to-digital values (see ahead) to be frozen in memory and triggered a 1 s one shot which requested the computer to record data. In this way a 40 s period was allowed for the flow to stabilize before the data was recorded. After the data was recorded, the pulse generator fired and the cycle repeated until the air mass fraction became greater than one. Note that the sequence of the test was through mass fractions of air of 0.0, 0.1, 0.2, . . . , 0.9, and 1.0.

The current mass-fraction setting for air ( $Y_{air}$ ) was used to set the air mass-flow controller. This value was displayed on the computer-screen control panel. The air mass-flow controller was set to  $Y_{air} \times 9.745$  slmn since 9.745 slmn is the air flow rate required for a mass-flow rate of 0.210 g/s. This value was also displayed on the control panel. Since the air mass-flow controller has a range of 0 slmn - 10 slmn and requires a set point of 0 V - 5 V, the number of slmn was divided by two to generate the number which was fed to the digital-to-analog converter connected to the voltage set point for the air mass-flow controller. This voltage was displayed on the control panel.

The next stage was to calculate the required agent flow rate, determine whether to use the 2 slmn or 10 slmn range agent mass-flow controller, and calculate the required voltage set point for the mass-flow controller. These calculations were implemented through a series of pathways which changed

depending on the agent being tested. Pathways exist for FC-218, HFC-125, HFC-227ea,  $\text{CF}_3\text{Br}$ , and  $\text{CF}_3\text{I}$ . The gas to be tested was chosen by modifying connections on page 1 (see Appendix D) of the icon worksheet.

The mass-flow rate of agent was determined by requiring that the total mass-flow rate of agent and air remain constant at 0.210 g/s. For an agent mass fraction of one, the mass-flow rate was therefore equal to 0.210 g/s. The required agent volume-flow rate ( $Q_{\text{agent}}$ ) for  $Y_{\text{agent}} = 1$  was therefore

$$(Q_{\text{agent}})_{Y_{\text{agent}}=1} = 9.745 \frac{\rho_{\text{air}}}{\rho_{\text{agent}}} . \quad (17)$$

where  $\rho_{\text{air}}$  and  $\rho_{\text{agent}}$  are the air and agent densities. The volume flow rate for the agent was obtained by multiplying this value by the mass fraction of the agent,

$$Q_{\text{agent}} = (1 - Y_{\text{air}})(Q_{\text{agent}})_{Y_{\text{agent}}=1} . \quad (18)$$

The result of this calculation was output on the computer-screen control panel.

The calculated agent volume-flow rate was in L/min. It had to be converted to slmn using the calibration curves previously determined, and these, in turn, had to be converted to set-point voltages for the agent mass-flow controllers. These steps were combined into overall equations which depended on both the chosen gas and flow meter. Table 5 lists the conversion formulas used for both flow meters with each of the agents. Whether the 2 slmn or 10 slmn meter was used depended on whether or not the calculated agent volume-flow rate fell above or below the full-scale range of the 2 slmn mass-flow controller. Values of standard L/min of agent corresponding to full-scale values for the 2 slmn meter are included in Table 5. The results of these calculations were a decision as to which agent mass-flow controller to use and the set-point voltage for that controller.

The calculated set point for the agent mass-flow controller was output to both the 2 slmn and 10 slmn controllers. However, when the 2 slmn controller was chosen the electro-pneumatic-actuated ball valve for this controller was opened and the lamp indicating the valve was open was turned on, while the valve for the 10 slmn remained closed, and the indicator light was off. The opposite occurred when the 10 slmn controller was required. The computer-screen control panel indicated which agent mass-flow controller had been turned on as well as the voltage set point being transmitted to the mass-flow controller.

An algorithm was included in the work sheet which converted the agent mass fraction into a mole fraction ( $X_{\text{agent}}$ ) which was ultimately saved with the other results of the measurements. The calculation implemented this equation:

$$X_{\text{agent}} = \frac{(1 - Y_{\text{air}})}{Y_{\text{air}} \left( \frac{\rho_{\text{agent}}}{\rho_{\text{air}}} - 1 \right)} . \quad (19)$$

The calculated agent mole fraction was displayed on the computer-screen control panel.

Data acquisition was initiated following the 40 s period allowed for the new mass-flow conditions to come into a steady state. Analog-to-digital converters continuously read the voltage outputs of the hot-film anemometer and cold-wire constant-current anemometer as well as the temperature measured

Table 5. Formulas Used to Convert slm for Given Mass Fraction of Agent ( $Q_{ag}$ ) to Set Point Voltages for Agent Mass-Flow Controllers. Formulas for the 2 slmn Controller Are Listed First

Agent	Maximum agent standard L/min for 2 slmn controller	Conversion formula
FC-218	0.348	$14.54Q_{ag}-0.074$ $-0.239Q_{ag}^3+0.553Q_{ag}^2+2.495Q_{ag}+0.0608$
halon 1301	0.745	$-3.670Q_{ag}^3+4.212Q_{ag}^2+5.518Q_{ag}+0.058$ $-0.018Q_{ag}^3+0.032Q_{ag}^2+1.378Q_{ag}-0.048$
HFC-125	0.540	$-0.055Q_{ag}^3+0.192Q_{ag}^2+1.650Q_{ag}+0.032$ $9.336Q_{ag}-0.049$
HFC-227ea	0.374	$-0.179Q_{ag}^3=0.424Q_{ag}^2+2.375Q_{ag}+0.028$ $13.551Q_{ag}-0.080$

by the coil thermocouple at data rates of 10 Hz. A running average of each of these outputs was calculated over 10 s periods (*i.e.*, 100 samples). Current values were updated on the computer-screen control panel. After a signal was received to sample-and-hold the averaged data, several different parameters were written into two hard-disk files. Values of the agent mole fraction, the voltage output of the hot-film anemometer, and the thermal bath temperature (*i.e.*, the gas temperature in the test section) were stored in the first file. The second file contained the thermal bath temperature and the voltage output of the constant-current anemometer. A flag on the computer-screen control panel was enabled during the period when data was recorded.

The mass-flow controllers generate voltages which are proportional to the actual flow rates through the instruments. Voltages generated by the 10 slmn air, 10 slmn agent, and 2 slmn mass-flow controllers were digitized and averaged over a running period of 1 s. The three voltages were then displayed on the computer-screen control panel. These outputs served to confirm the proper operation of the calibration system.

The work sheet incorporates three additional capabilities which could be implemented on the computer-screen control panel with push buttons. The first was "Air Enable" which turned on the air flow and allowed it to flow continuously through the test section. The remaining buttons were "Pause" and "Emerg. Stop" which could be activated during actual testing. The "Pause" temporarily halted testing until the button was pushed again, while the "Emerg. Stop" button aborted the test and turned off the gas flows when it was depressed. Status boxes were included on the computer-screen control panel which indicated the current state of a calibration.

**11.2.4.6 Calibration Procedures.** Calibration of the combined probe to variations in agent concentration and temperature were fairly simple with the calibration system. Appendix F contains the detailed procedure which was followed during a calibration. Briefly, a regulated pressure bottle of the



agent to be investigated was connected to the calibration system as was a tank of breathing-quality air. The instrumentation was turned on and allowed to warm up for half an hour. The temperature bath was set to the desired temperature and allowed to equilibrate. The calibration sequence was initiated by "pushing" the appropriate button on the computer-screen control panel. The calibration sequence acquiring probe-response data for a series of concentrations was then repeated for as many different temperature settings as desired. The system was then shut down.

### 11.2.5 Calibration Results and Probe Characterization

**11.2.5.1 Calibration Results.** The calibration system and the behavior of individual cold wires and aspirated hot films were characterized before the combined aspirated hot-film/cold-wire probe was delivered by TSI, Inc. Measurements were made separately for a TSI Model 1440R aspirated hot film and a Model 1210-T1.5 hot wire operated as a cold wire. The behaviors of these probes should be similar, but not identical, to those for the combined probe which are described below.

The cold-wire current was set to 1.00 mA. Figure 12 shows an example of the voltage output of the constant-current anemometer operated in the cold-wire mode. These measurements were recorded by placing the cold wire in a heated water bath while recording the temperature with a calibrated thermometer. As expected, the dependence on temperature is linear, and the sensitivity to temperature changes is quite good.

The resistance ( $R_{250} = 9.129 \Omega$ ) of the aspirated hot-film probe was set to a value corresponding to an operating temperature ( $T_{op}$ ) of 250 °C. Some difficulties were encountered when calibration of the aspirated hot film was initiated. Initially, the probe was held outside and only plunged into the test section when measurements were to be taken. The measurements were very irreproducible. This was ultimately traced to water condensation on the probe when it was removed from the cold test section. In order to overcome this problem, the probe was maintained in a flow of dry air or agent mixture at all times during a calibration sequence. Calibrations performed in this manner were reproducible. The first calibration measurements were done in a pipe instead of the vessel test section described above. A display of the constant-temperature anemometer voltage output showed that there was a very low noise level when no flow was present, but that the noise increased dramatically when the flow was started. This observation was very surprising because the literature indicated the output of an aspirated hot film should be insensitive to velocity fluctuations. By replacing the pipe with the vessel described above, it was possible to lower the flow velocity in the test section and decrease the measurement noise. The sensitivity of the probe to flow velocity remained a problem and is discussed in more detail shortly.

Once the above problems were solved, it was possible to record reproducible calibrations. Figure 13 to Figure 16 show calibration results for FC-218, HFC-125, HFC-227ea, and halon 1301 as a function of temperature and agent concentration. Several general points should be noted concerning the results. For a given temperature, the plots of hot-film voltage versus mole fraction of agent fall on well defined smooth curves. For a given concentration of agent, the voltage output of the anemometer increases as the temperature decreases. This is to be expected based on Equation (10) which predicts that the output voltage is proportional to the difference in the operating temperature of the probe and the ambient temperature. Since the operating temperature of the hot film is held constant during a calibration, the voltage increases as the ambient temperature is lowered. In general, the voltage changes with temperature depend somewhat on concentration, *e.g.*, the change in output voltage for a given change in temperature is found to be different for the pure agents as compared to those observed for air. The nonlinear dependence on temperature is most likely the result of the molecular properties (particularly thermal conductivity and kinematic viscosity) of air and the agents having different dependencies on temperature. These properties appear in Equation (10).

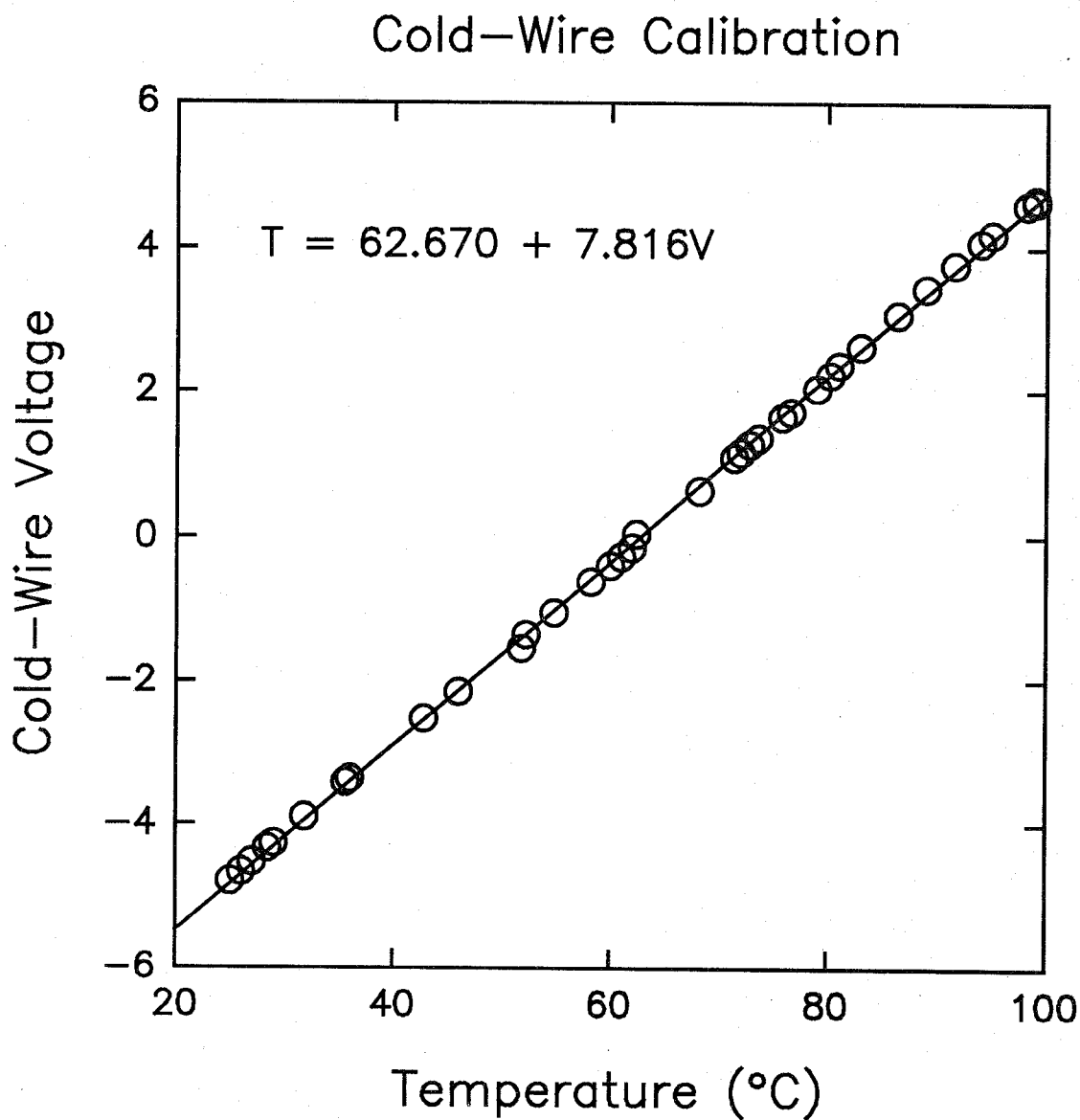


Figure 12. Voltage output as a function of temperature for a TSI Model 1210-T1.5 hot-wire probe operated as a cold wire with a 1.00 mA current. Measurements recorded in a heated water bath.

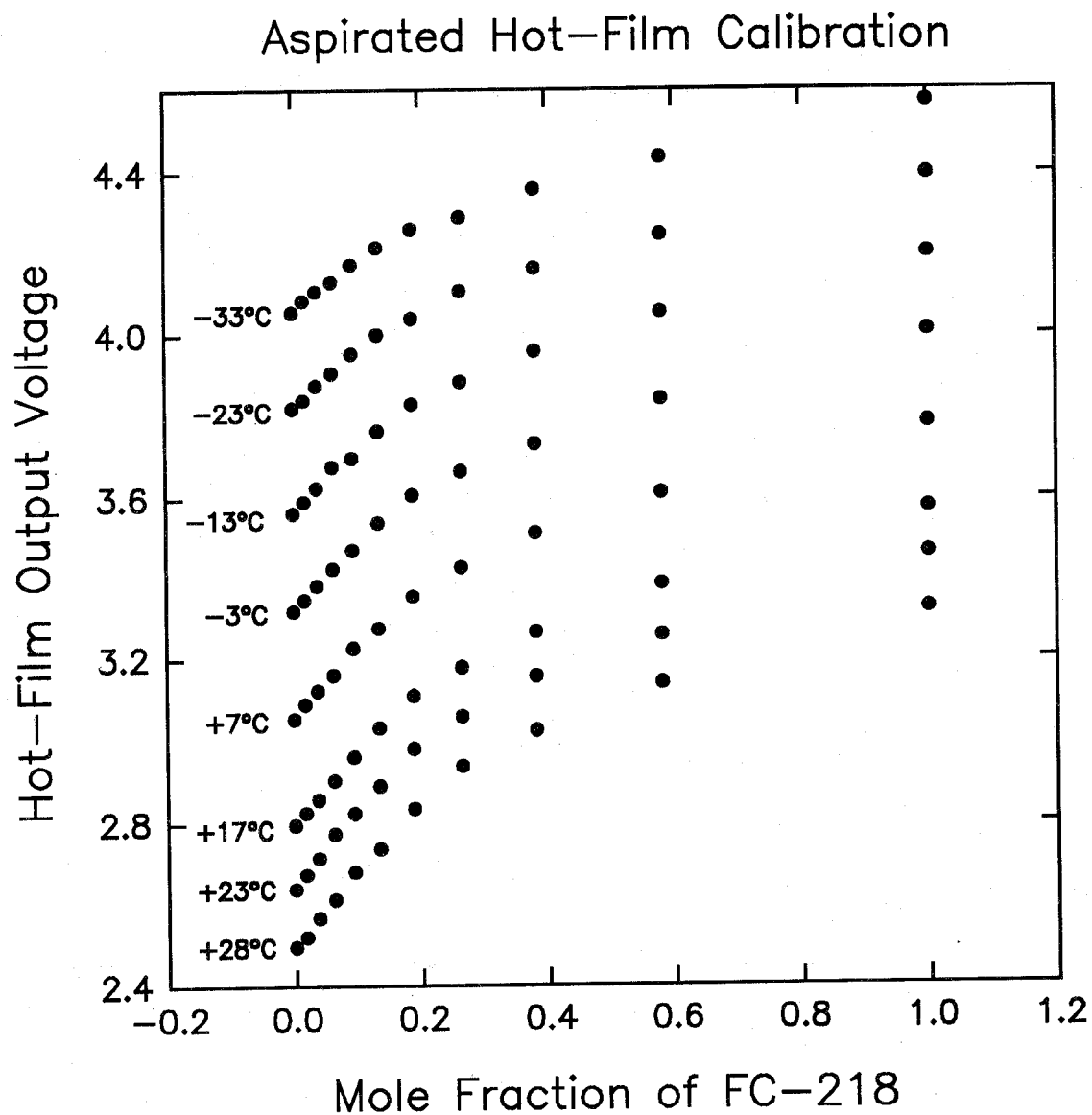


Figure 13. Voltage output of aspirated hot-film anemometer as a function of FC-218 concentration and temperature. The bridge voltage has been offset by 2 volts and a gain of 6 has been applied.

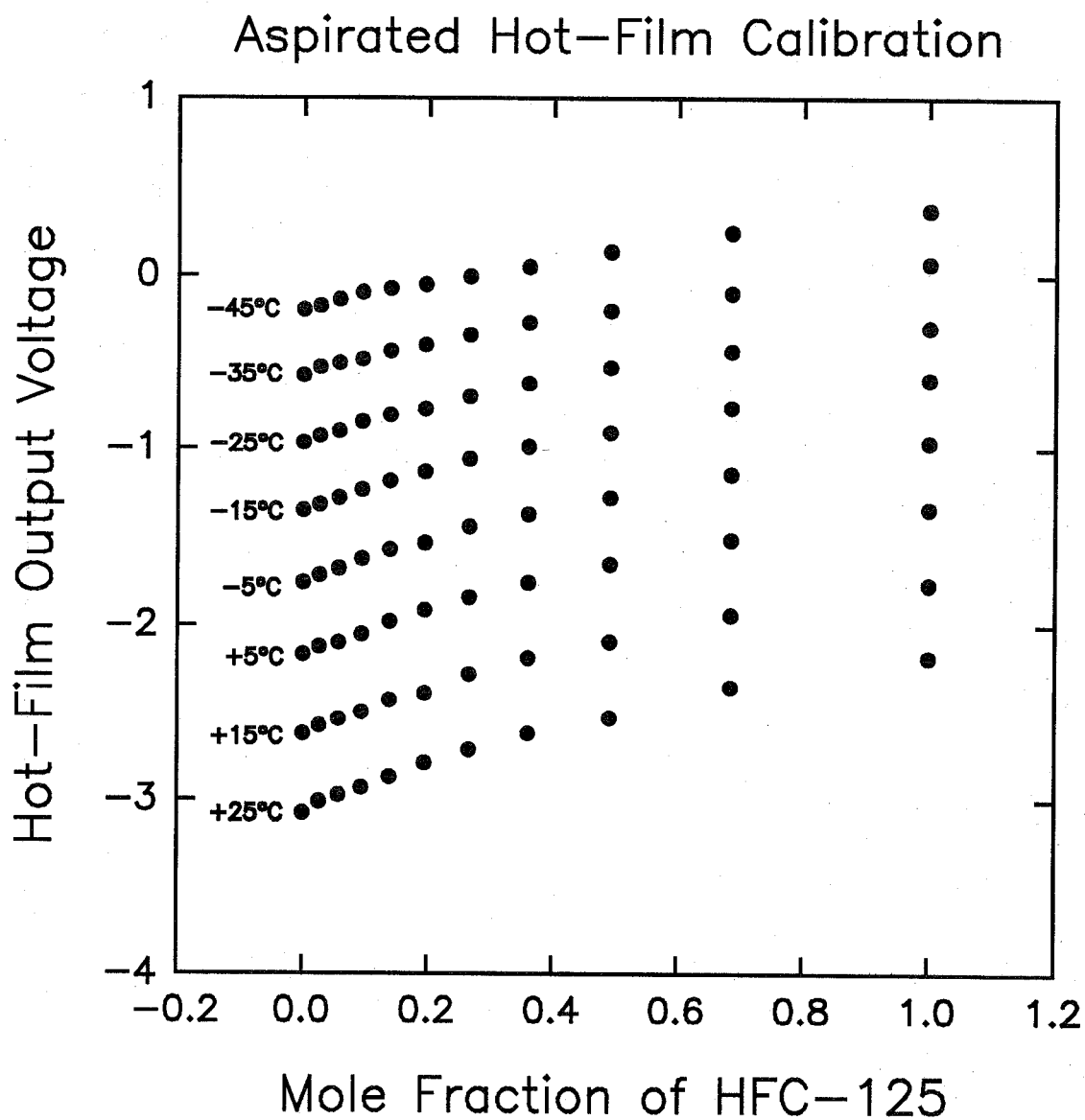


Figure 14. Voltage output of aspirated hot-film anemometer as a function of HFC-125 concentration and temperature. The bridge voltage has been offset by 3 volts and a gain of 10 has been applied.

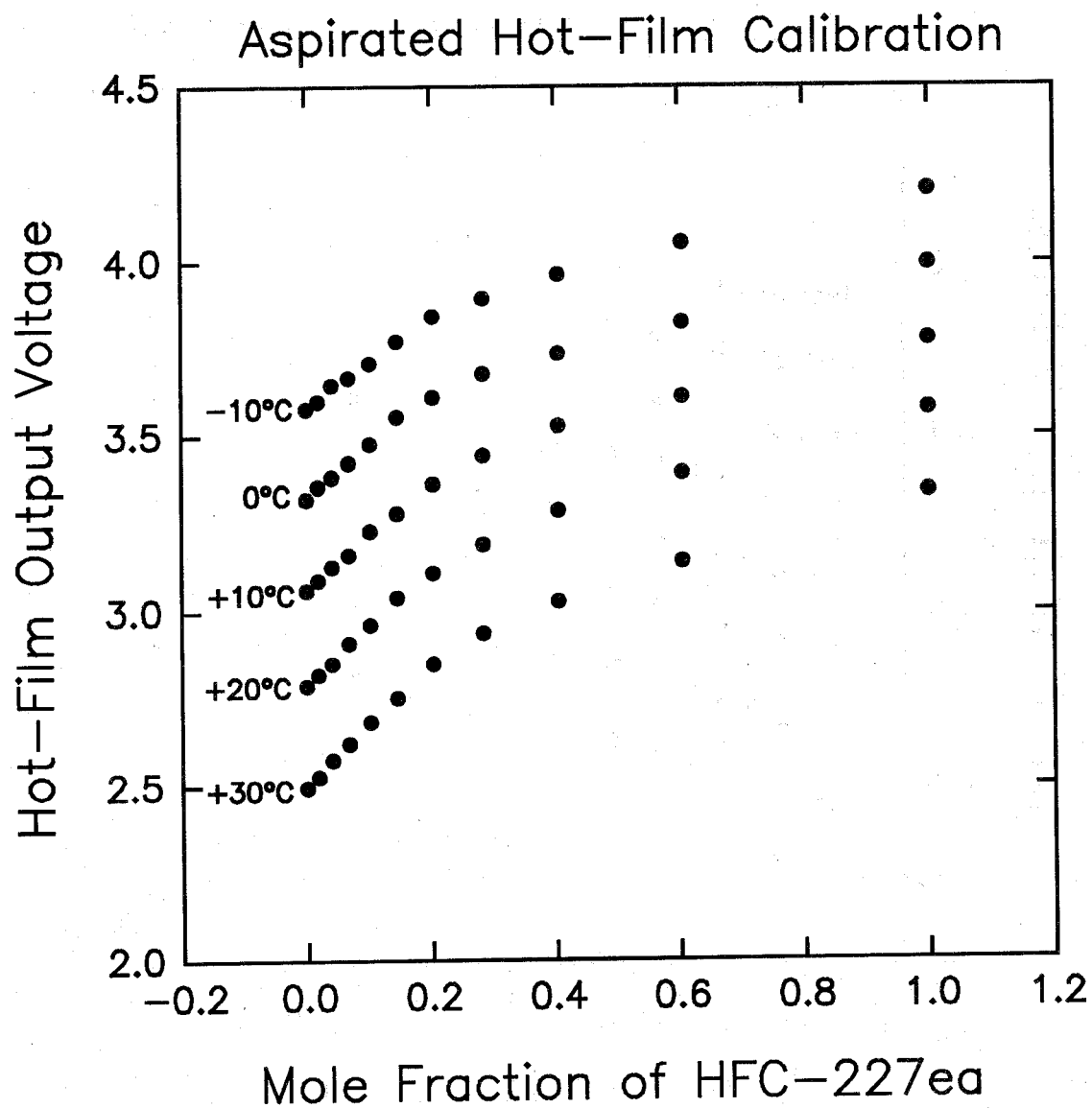


Figure 15. Voltage output of aspirated hot-film anemometer as a function of HFC-227ea concentration and temperature. The bridge voltage has been offset by 2 volts and a gain of 6 has been applied.

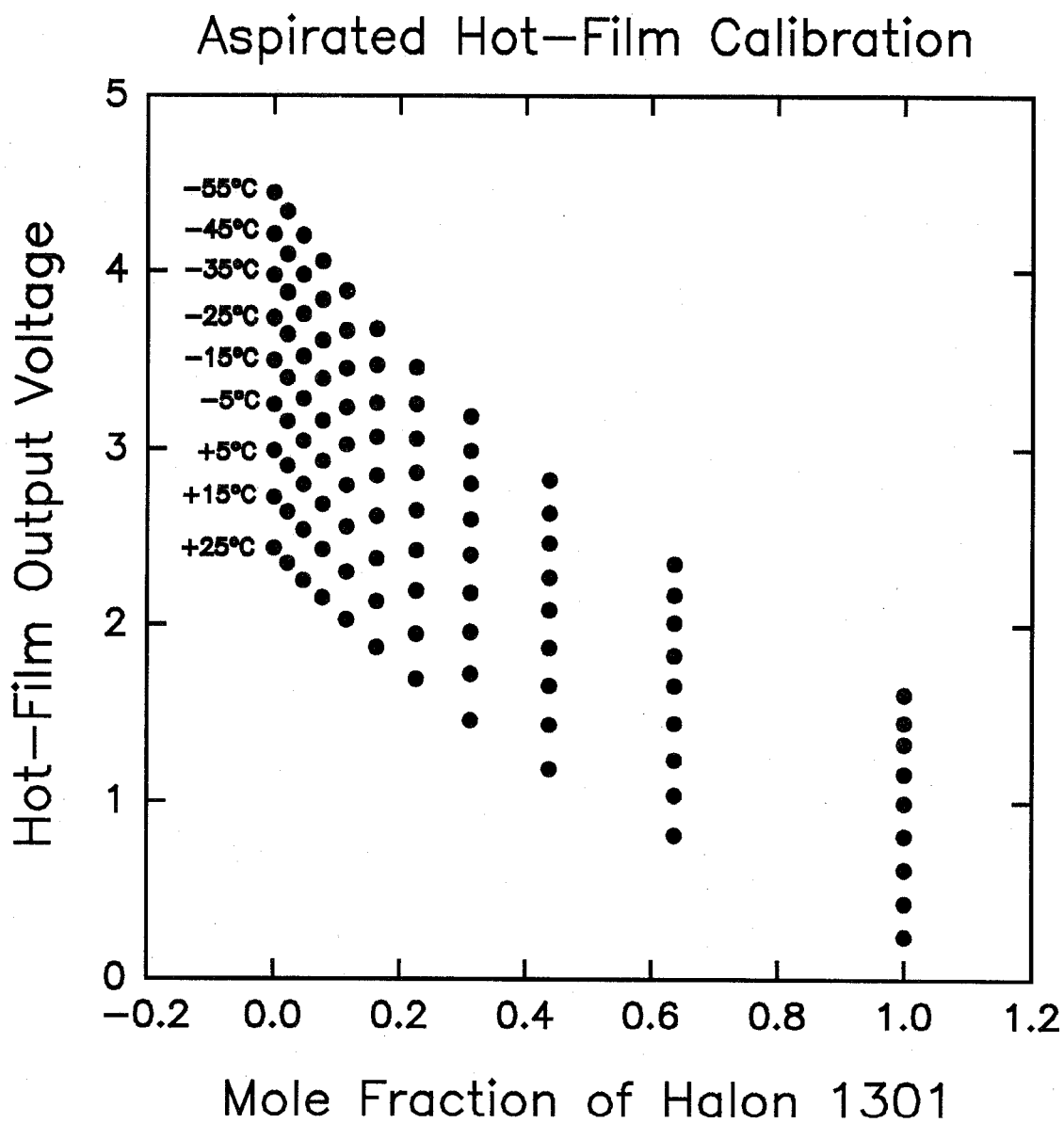


Figure 16. Voltage output of aspirated hot-film anemometer as a function of halon 1301 concentration and temperature. The bridge voltage has been offset by 2 volts and a gain of 6 has been applied.

Perhaps the most important characteristic of the calibration curves is the change in voltage as a function of agent concentration for a given temperature. Some immediate differences are apparent by comparing Figure 13 to Figure 16. The voltage is found to decrease with increasing halon 1301 concentration while it increases for FC-218, HFC-125, and HFC-227ea. The absolute magnitudes of changes in the voltage output on going from air to pure agent also depend on the agent. This is an important property because it ultimately determines the accuracy and precision which is possible using these probes for concentration measurements. Figure 17 shows the responses of the aspirated probe to concentration for the four agents at 24.5 °C. The voltage plots have been normalized such that the voltage is defined to be zero when the agent concentration is zero, and the voltage change has been divided by the gain used to record the signal. This transformation allows direct comparison of the probe responses for the four agents on the same scale. The largest response is for halon 1301. The responses for FC-218 and HFC-227ea are roughly equal, but more than a factor of two smaller than observed for halon 1301. The smallest response was observed for HFC-125, which was a factor of two smaller than those observed for FC-218 and HFC-227ea.

In principle it should be possible to predict the results shown in Figure 17 using Equations (10) and (11). In practice, quantitative predictions are difficult. By combining Equations (10) and (11) and assuming that the external temperature and pressure are constant, the dependence of the hot-film voltage on molecular properties can be written as

$$E^2 \sim k_o \left[ A + B \left( \frac{\sqrt{\gamma MW} \left( \frac{2}{\gamma + 1} \right)^{\frac{\gamma + 1}{2(\gamma - 1)}}}{\mu_o} \right)^n \right] \quad (20)$$

$A$  and  $B$  are often assumed to be constants. For finite probe lengths their values actually depend on molecular properties (Pitts and McCaffrey, 1986). For the purposes of this discussion they will be assumed to be constant. The relative slopes of  $E^2$  versus velocity ( $U$ ) for agent  $x$  normalized by the slope for air  $((\Delta E^2)_x / (\Delta E^2)_{air})$  can be calculated using Equation (20). Table 6 lists the results of these calculations for each of the four agents. Note that the exponent  $n$  in Equation (20) has been set to 0.40. This is based on findings for the response of a hot-film probe described in Pitts and McCaffrey (1986). These slopes are in qualitative agreement with the experimental observations if variations in the constant  $A$  are neglected. For instance, since the ratio is less than one for halon 1301, the voltage output for this agent should be lower than that measured for air. Similarly, voltage changes for the other three agents should be positive. The results of this simple calculation also predict the experimental observations that FC-218 and HFC-227ea have similar voltage behaviors which are somewhat higher than for HFC-125. However, close examination shows that even though the relative differences are captured, the approach fails to accurately predict the magnitudes of the effects. For instance, the calculations suggest that the absolute voltage change would be smallest on going from air to halon 1301, when it is in fact the largest. This suggests that additional factors not captured by this simple approach, such as varying  $A$  factors or probe end-loss effects, are also important. This conclusion is important because it implies that the relative responses can be modified somewhat by changing the probe design (e.g., by varying the probe diameter or the area ratio of the tube containing the probe and the sonic orifice). In this way it may be possible to design a probe in such a way as to maximize its response to changes in concentration of a particular gas pair.

**11.2.5.2 Characterization of Probe Response to Velocity Fluctuations.** During the calibrations discussed in the last section it was noted that the noise in the output voltage increased somewhat when

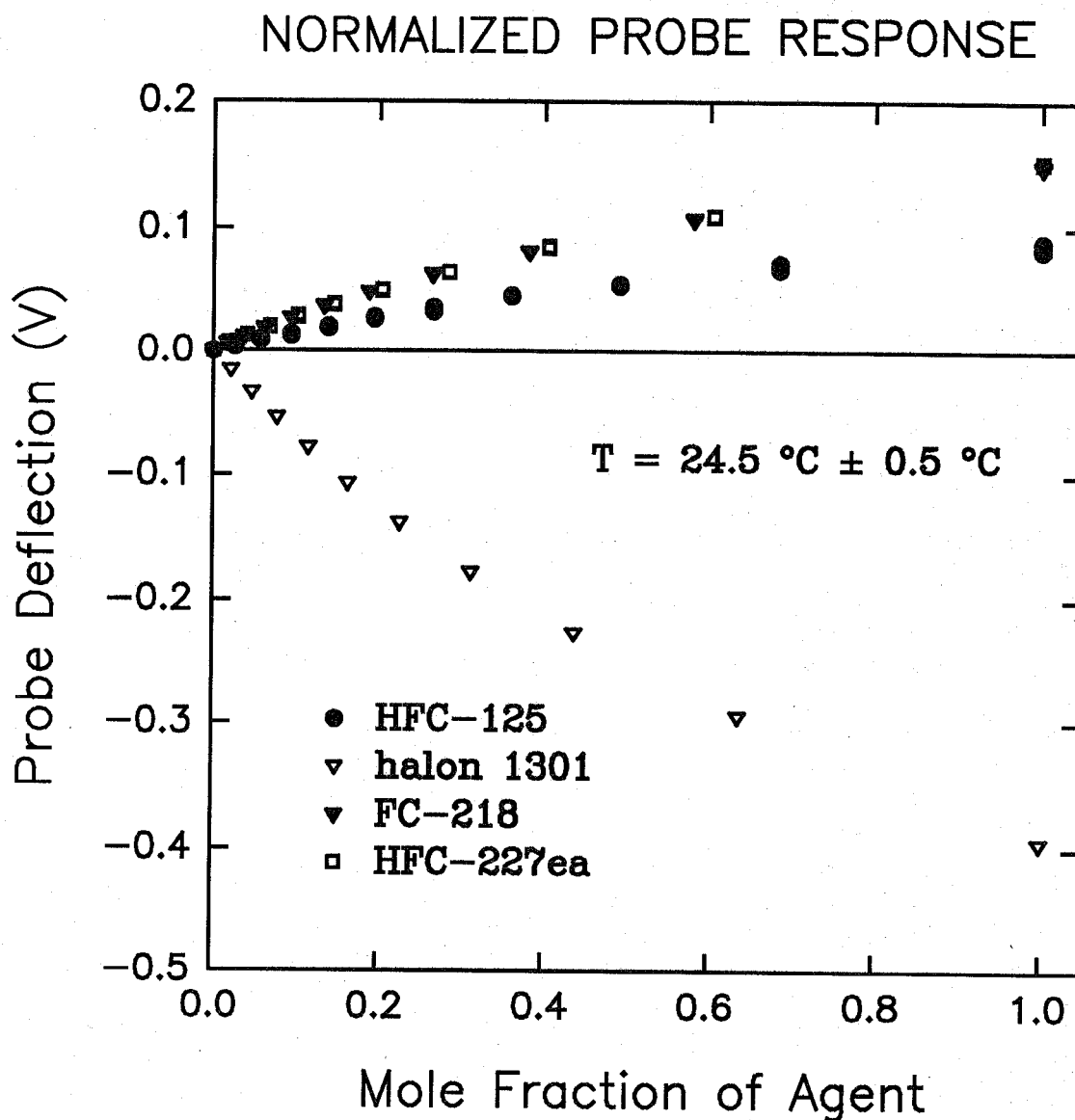


Figure 17. Voltage output of aspirated hot-film anemometer as a function of concentration for the four agents investigated. Normalized to be zero at zero agent concentration. Recorded voltages are divided by the applied gain.



Table 6. Predicted Values of Slopes of Plots of  $E^2$  Versus  $U^n$  for the Agents Normalized by the Value for Air.  $n$  Has Been Assumed To Equal 0.40

Agent	$((\Delta E^2)_x / (\Delta E^2)_{air})$
HFC-227ea	1.48
FC-218	1.48
HFC-125	1.44
halon 1301	0.94

the flow in the test section was initiated. When the probe was removed from the test section and placed in open air, it was found that there was a slight difference in the output voltage as compared to that predicted based on the air calibrations at room temperature. Both of these observations suggested that the probe was sensitive to velocity to some degree. This was unexpected since the literature indicated quite clearly that such sensitivity should be minimal.

In order to characterize the sensitivity of the hot-film response to velocity a series of tests in an air flow were run. Measurements were made in the flow generated by a TSI, Inc. Model 1125 Flow Calibrator. This system consists of a well contoured nozzle which generates a uniform flow at the exit. Measurement of the pressure drop across the orifice allows the exit velocity to be determined accurately. The aspirated hot-film probe was placed in the flow at positions near the nozzle where velocity fluctuations were very small, as well as at a larger distance (centerline, 51 mm downstream of the nozzle) where the flow had developed into a turbulent jet and therefore had considerable velocity fluctuations.

Figure 18 shows examples of the time records observed in the nonturbulent and turbulent regions of the flow field. The probe was oriented parallel to the flow direction. It is clear that the anemometer signal is much noisier in the presence of the turbulent flow. Figure 19 and Figure 20 show plots of average and rms voltage versus flow velocity at the two positions for the probe oriented parallel (vertical) and perpendicular (horizontal) to the flow. The time-averaged voltages indicate that the response of the hot-film anemometer is slightly dependent on flow velocity and more so on the probe orientation. Interestingly, the output voltage seems to decrease slightly as the velocity increases. If this velocity sensitivity were due to a dynamic pressure on the probe it would be expected to increase with velocity.

The aspirated hot-film response to turbulent velocity fluctuations is more complicated. As suggested by the results in Figure 18, the rms voltage is very low when the flow is laminar and the probe is oriented parallel to the flow. However, when the probe is oriented parallel to the flow, the rms voltage increases dramatically with velocity. We attribute this behavior to a resonant frequency as the air "whistles" by the opening of the aspirated probe. Also consistent with Figure 18, the rms for the probe located parallel to the flow increases significantly when the probe is moved into the turbulent region of the flow. Strangely, the rms seems to be independent of flow velocity. This is difficult to understand since the absolute magnitude of the turbulent velocity fluctuations must increase with flow velocity. However, the finding is encouraging because it suggests that a single rms value (0.04 V) can be used to characterize the noise which results from locating the probe perpendicular to a turbulent flow. On the other hand, the rms values measured at the downstream position with the probe oriented perpendicular to the flow again increase with velocity. This provides further confirmation

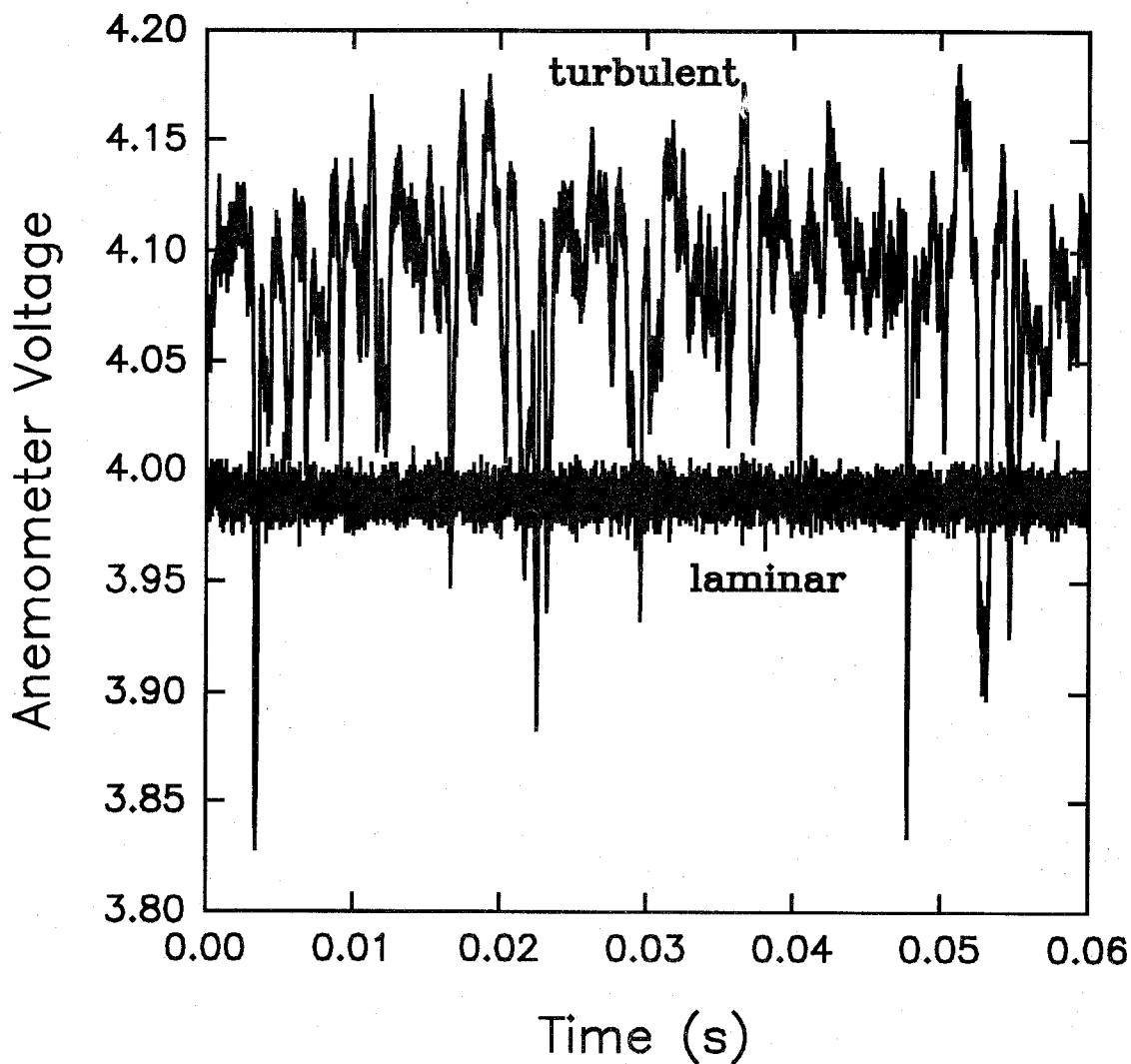


Figure 18. Time records of aspirated hot-film voltage for an air jet having a velocity of 15.0 m/s at the jet exit. Measurements were recorded at the jet exit (laminar) and 51 mm downstream (turbulent). A gain of 10 and offset of 2 V was used.

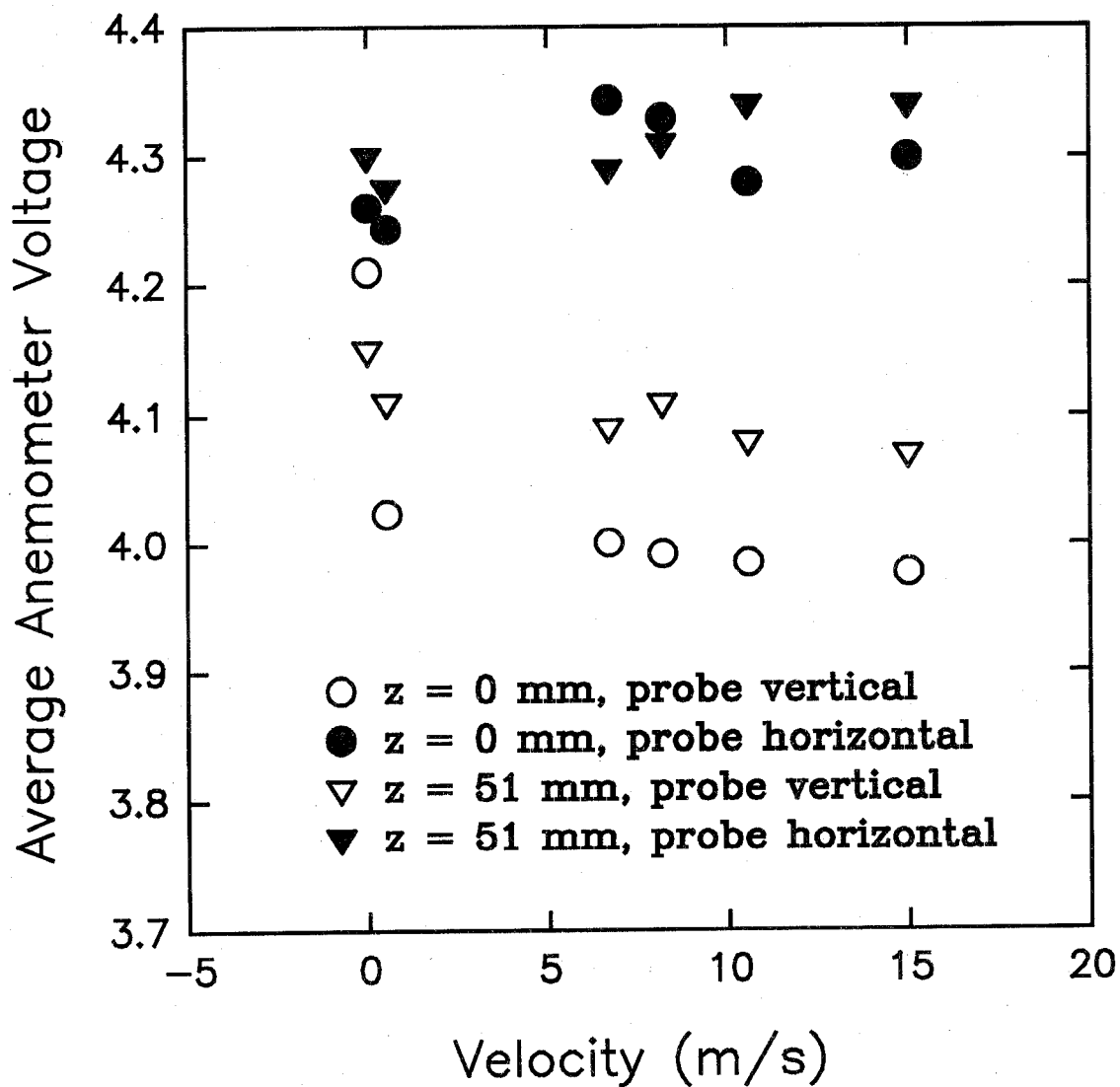


Figure 19. Time-averaged voltages for the aspirated hot-film probe oriented parallel and perpendicular to an air flow of 15.0 m/s at the calibration-jet exit. Measurements were recorded at the exit and 51 mm downstream. Gain of 10, offset of 2 V used.

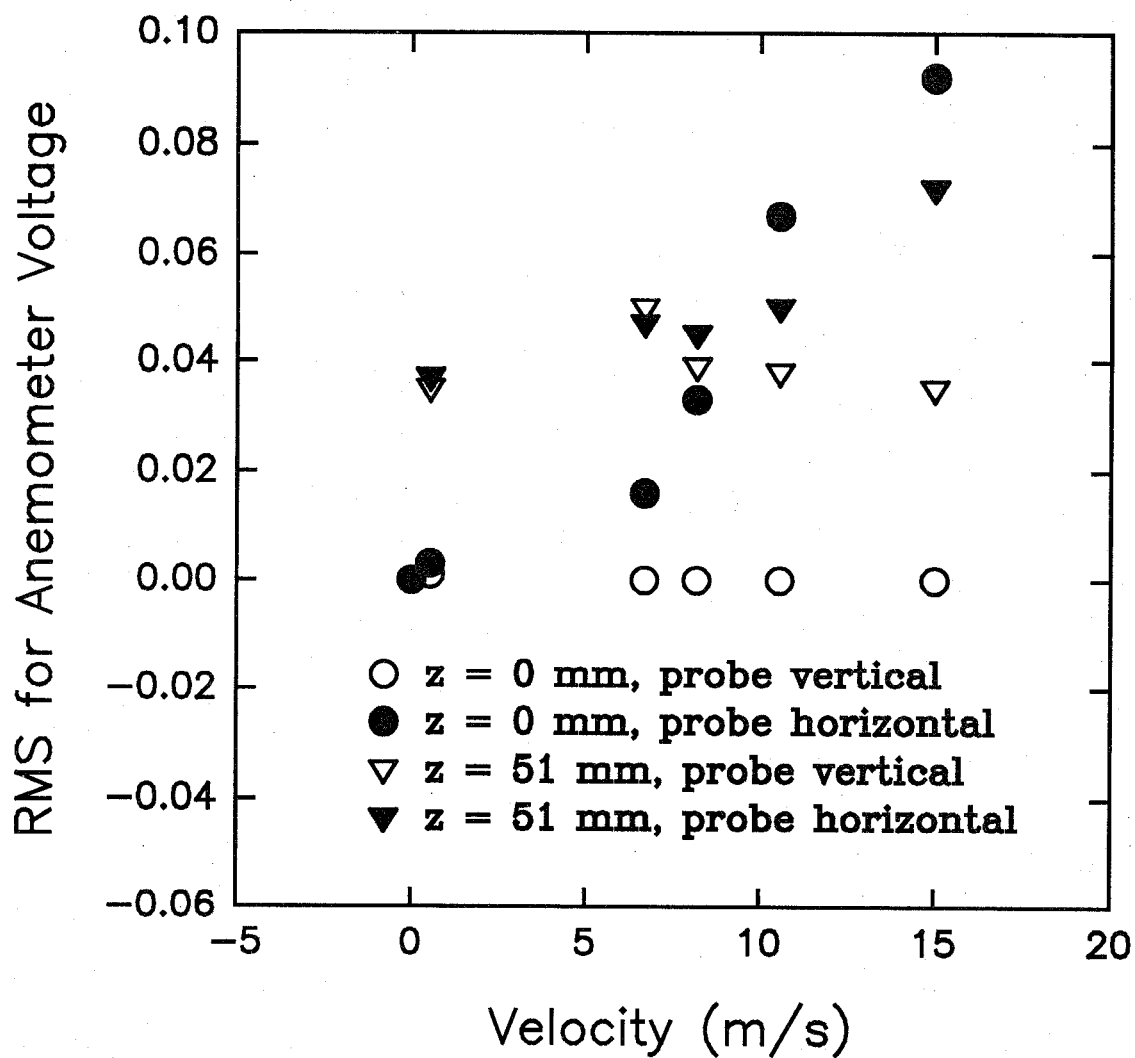


Figure 20. rms voltages for the aspirated hot-film probe oriented parallel and perpendicular to an air flow of 15.0 m/s at exit. Measurements were recorded at the jet exit and 51 mm downstream. Gain of 10, offset of 2 V used.

that the variations in response observed for the two probe orientations result from different flow effects.

These results were discussed with Professor Ronald So of Arizona State University and Anthony Birch of the British Gas Corporation. These researchers have used aspirated hot-film probes extensively for concentration measurements. Both expressed surprise at the sensitivity to velocity observed in the current work. At the present time it is impossible to determine whether this is a new observation characteristic of aspirated hot films in general, or an effect limited to the particular probe that was tested. The implications of the velocity sensitivity for the accuracy of real-time concentrations measurements is discussed in the following section.

Two additional tests were performed in an effort to understand the sensitivity of the probe to velocity fluctuations. A check was made to ensure that the flow at the sonic orifice of the aspirated probe was choked. The condition required for choked flow is

$$\frac{P}{P_o} \leq \left( \frac{2}{\gamma + 1} \right)^{\frac{\gamma}{\gamma - 1}}, \quad (21)$$

where  $P$  is the pressure on the downstream side of the sonic orifice. For air this requires  $P/P_o \leq 0.53$ . A valve and pressure gauge were installed in the pump line to allow control and measurement of the pressure downstream of the sonic orifice. The aspirated hot-film probe was placed 51 mm downstream of the flow calibrator and a flow of air with a velocity of 10.6 m/s at the nozzle exit was passed over the probe. The average and rms probe voltages were then recorded as a function of  $P/P_o$ . Figure 21 and Figure 22 show the results. It can be seen that both the average and rms voltages remain nearly constant for  $P/P_o \leq 0.45$ . The average voltage begins to drop and the rms voltage begins to rise at higher pressure ratios. These are the expected behaviors when the downstream pressure is insufficient to choke the orifice. The value of  $P/P_o$  where the flow is no longer choked is slightly lower than predicted by Equation (21), but the agreement must still be considered excellent. Since the probe is normally operated with no valve in the pump line, it is clear that the sonic orifice is choked during routine use.

Since the hot-film anemometer is sensitive to changes in temperature, it was possible that the apparent velocity sensitivity to turbulent fluctuations was, in fact, the result of temperature variations due to turbulence. In order to investigate this possibility, the calibrated constant-current anemometer operated as a cold wire was used to record temperatures in room air and at the nozzle of the flow calibrator for a range of air flow velocities. The average temperature of the ambient air was recorded as 24.4 °C while measurements of the temperature in the air flow were in the range 24.4 °C - 24.8 °C. This suggests that the maximum temperature fluctuations to be expected in the turbulent air flow (which is a mixture of jet and ambient air) are on the order of 0.5 °C with a somewhat smaller rms. Based on the calibrations shown in Figure 13 to Figure 16, the change in voltage output with temperature (assuming a gain of 10) is in the range of 30 mV/°C - 46 mV/°C. This suggests that the rms voltage change which can be associated with temperature fluctuations is less than 15 mV. The 40 mV rms observed in Figure 20 is much larger than this value, which indicates that the probe is indeed responding to velocity fluctuations.

**11.2.5.3 Estimation of Uncertainty in Concentration Measurements Introduced by Probe Sensitivity to Turbulent Fluctuations.** The response of the aspirated hot film to velocity fluctuations introduces a noise into the concentration measurements since they are interpreted as concentration fluctuations. Using the observed rms noise for a probe oriented parallel to a flow (0.04 mV with a

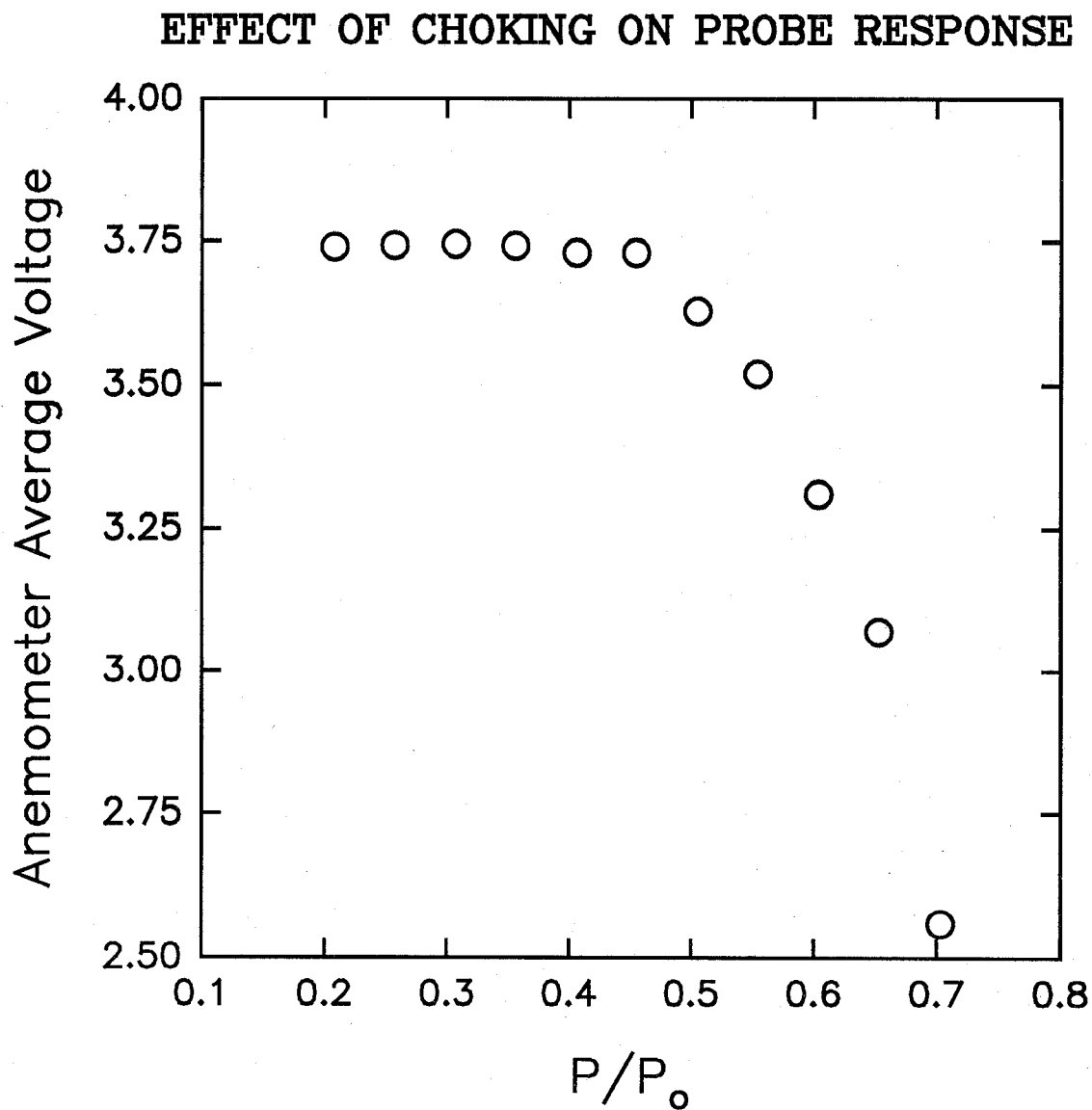


Figure 21. Average voltage output of hot-film anemometer as a function of the pressure ratio downstream of sonic orifice and ambient with probe located in a turbulent flow. A gain of 10 and offset of 2 V was used.

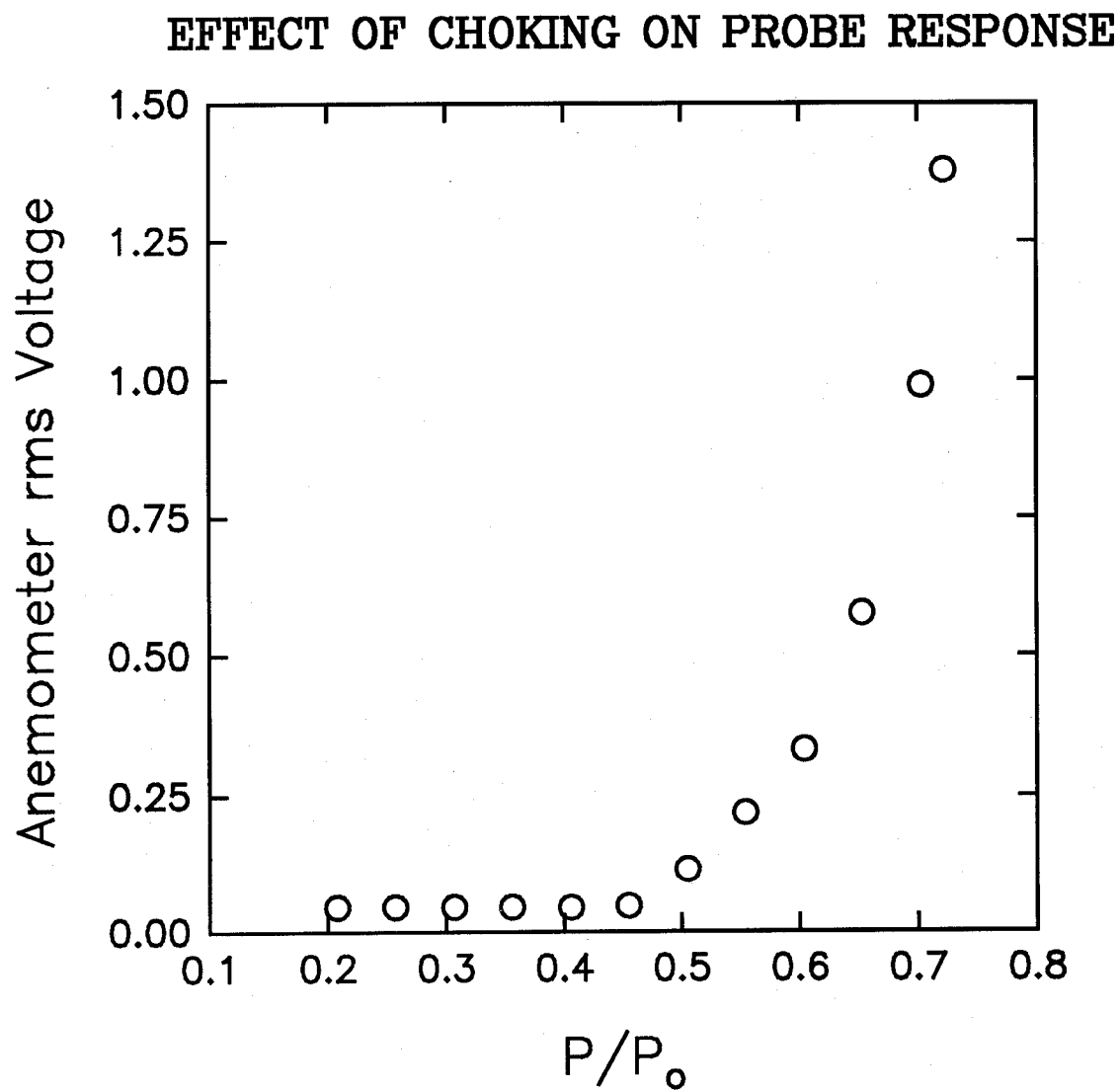


Figure 22. rms voltage output of aspirated hot-film anemometer as a function of the pressure ratio downstream of sonic orifice and ambient with probe located in a turbulent flow. A gain of 10 and offset of 2 V was used.

gain of 10) and the room-temperature calibration curves recorded for each agent, it is possible to estimate the uncertainty in individual time-resolved concentration measurements as the result of the velocity sensitivity. The results for agent mole fractions of 0.01, 0.05, and 0.10 are listed in Table 7. As expected, the predicted errors for a given mole fraction are largest for HFC-125, which has the smallest change of output voltage on going from air to pure agent. For a constant mole fraction of 0.01 the uncertainty in an individual measurement is  $\pm 0.03$ , a very inaccurate measurement. For a HFC-125 mole fraction of 0.1 the uncertainty in an individual measurement is approaching 30 %. On the other hand, the expected uncertainties for halon 1301 (for which the probe sensitivity is highest) are much smaller. For a 0.01 mole fraction the relative uncertainty in an individual measurement is 50 % and drops to 6 % for a 0.10 mole fraction. This is considered acceptable for the current purposes. The uncertainties for FC-218 and HFC-227ea are intermediate. It can be concluded that the aspirated hot-film probe should provide time-resolved concentration measurements for halon 1301 with good accuracy, for FC-218 and HFC-227ea with moderate accuracy, and for HFC-125 with poor accuracy.

Another way to characterize the sensitivity of the aspirated hot-film probe to velocity fluctuations is to calculate the minimum mole fraction of an agent required to give a signal-to-noise ratio of 1. Values have been calculated assuming a noise rms of 0.004 V (no gain) and using the experimental calibration curves shown in Figure 17. The results are tabulated in Table 8. The same conclusions concerning the relative accuracies of concentration measurements for the four agents are reached.

#### **11.2.6 Aspirated Hot-Film Concentration Measurements During Releases of Pressurized Agents.**

The next stage of testing was to calibrate the combined aspirated hot-film/cold-wire probe and attempt to use it for measurements in actual releases of agents. Measurements were carried out in three different experimental systems. This section summarizes the experimental methods used, the data analysis techniques, and the experimental findings.

**11.2.6.1 Experimental System and Data Analysis for Concentration Measurement.** The calibration system and its use has been described in previous sections. The result of these calibrations is an array of aspirated hot-film and cold-wire voltages versus agent concentration for a number of different temperatures. In order to record concentration in an actual release it is necessary to mount the probe at the desired measurement location, record the voltage outputs of the hot-film and cold-wire anemometers at a sufficient data rate during the period of interest, and convert these voltages to time records of temperature and concentration.

A special mount was fabricated to position and support the combined aspirated hot-film/cold-wire probe in the flow field. The mount consisted of a solid 25 mm aluminum rod which was cut in half and milled along the center such that the probe could be placed inside and held tightly. Set screws were used to join the two halves of the rod. The end of the rod was machined to a cone shape to minimize flow interferences. In general, the end of the probe would extend several tens of millimeters beyond the mounting rod. The holder could be bolted to a perpendicular plate for mounting in the experiment.

The same Flash-12 data acquisition system used for the calibrations was used to record the voltage outputs for the two anemometers. This system is described in detail in Section 11.2.4.5. The configuration of the data-acquisition system is somewhat simpler for experimental measurements than that required for the calibration system. All that is needed is the ability to "trigger" the system to start data acquisition and to record two voltage signals at the desired data rate for the desired period of time.

A second T21 terminal panel was used for experiments. It was mounted in an aluminum box equipped with eight BNC connectors. The BNCs were connected to the eight differential inputs of the



Table 7. Expected Uncertainties in Agent Mole Fraction for Three Average Values. rms Estimates Based on rms Voltage of 0.04 V from Figure 20 and Experimental Calibration Curves of Voltage Versus Mole Fraction

Agent	Assumed average mole fraction		
	0.01	0.05	0.10
HFC-227ea	0.0136	0.0145	0.0162
FC-218	0.0123	0.0138	0.0160
HFC-125	0.0285	0.0277	0.0283
halon 1301	0.0052	0.0058	0.0065

analog-to-digital converter. A digital ribbon cable was used to connect the interface box to the Flash-12. In order to switch from probe calibration to data acquisition, it was only necessary to disconnect the digital ribbon cable for the calibration interface box from the Flash-12 and replace it with that for the experimental measurement interface box.

An icon-based work sheet such as SHOT.WBB shown in Appendix G was used to control the experiment. The work sheet sets up the hardware to accept a trigger from the experiment on analog-to-digital input channel 1 which initiates data collection following a 0.8 s delay. The work sheet provides for recording three input voltages. Two of these are the outputs of the aspirated hot-film (channel 6) and cold-wire (channel 7) anemometers. The third channel was used for the Differential Infrared Rapid Agent Concentration Sensor (DIRRACS) described in Section 11.3. Three seconds following the trigger, data collection was halted and the data was written out to the hard disk. Note that the total data collection time using this work sheet was 2.2 s.

Since the physical processes of interest are quite fast, the data must be recorded at a high rate. Typically 20 kHz was used. With the current data-acquisition hardware, this requires that the data be recorded directly into memory located on the daughter board using the so-called "fast mode." Only after completion of acquisition is data transferred to the personal computer and stored to disk. The total number of data points which could be stored was limited by the daughter board memory to 1 000 000. For the 2.2 s sampling time, the total data sampling rate was 60 kHz and the total number of measurements recorded was 132 000, which was well within the limits of the device.

At the conclusion of an experiment the data was stored in a file containing two columns of readings corresponding to time records of the hot-film and cold-wire anemometer voltage outputs. It was necessary to convert these voltages to time records of temperature and concentration using the appropriate calibration curves. There are a number of ways in which this could have been done. Since the response of a cold wire has a linear dependence on temperature, the approach chosen was to directly calculate the temperature from the cold-wire voltages using an intercept and slope calculated by a least squares curve fit to the calibration data. Once the temperature was available, it was necessary to calculate the concentration knowing the output voltage of the aspirated hot film and the temperature. For this purpose a least squares fit of a concentration surface (either in mole fraction ( $X$ ) or mass fraction ( $Y$ ) terms) to the calibration values of temperature ( $T$ ) and aspirated hot-film output voltage ( $E_{hf}$ ) was used.

The general form of such a surface of order  $m$  can be written as

Table 8. Minimum Mole Fraction of an Agent Required To Give a Signal-To-Noise Ratio of 1. Voltage rms of 0.04 (No Gain) Has Been Assumed

Agent	Minimum mole fraction
HFC-227ea	0.015
FC-218	0.016
HFC-125	0.028
halon 1301	0.006

$$X = \sum_{i=0}^m \sum_{j=0}^m a_{i,j} T^j E_{hf}^i, \quad (22)$$

where the coefficients  $a_{i,j}$  are determined by a least squares fit to the calibration data. As examples, for  $m = 1$  Equation (22) would be written as

$$X = a_{0,0} + a_{0,1}T + a_{1,0}E_{hf} + a_{1,1}TE_{hf}, \quad (23)$$

while for  $m = 2$  the expression becomes

$$X = a_{0,0} + a_{0,1}T + a_{0,2}T^2 + a_{1,0}E_{hf} + a_{1,1}TE_{hf} + a_{1,2}T^2E_{hf} + a_{2,0}E_{hf}^2 + a_{2,1}TE_{hf}^2 + a_{2,2}T^2E_{hf}^2. \quad (24)$$

A Fortran code (SURFFIT.FOR, included as Appendix H) was written to determine the coefficients  $a_{i,j}$  for a file of input values of temperature, hot-film voltage, concentration, and a predetermined  $m$ . Once the values of  $a_{i,j}$  were available, Equation (22) could be used to calculate values of concentration from arbitrary pairs of temperatures and aspirated hot-film voltages. A Fortran program named CONCEN.FOR (included as Appendix I) read a file containing a time series of the voltage pairs and by using Equation (22), along with the input values of  $a_{i,j}$  from SURFFIT.FOR and the experimental dwell time at which the data was recorded, generated an output file containing listings of time, temperature, and concentration. Once the reduced data for temperature and concentration as a function of time were available, they could be plotted or analyzed further.

**11.2.6.2 Measurement of Halon 1301 Concentration Following Release From a Pressurized Vessel into an Open Room.** As an initial test of the experimental system and procedures, an attempt was made to measure the time behaviors of agent concentration and temperature during the release of halon 1301 from a pressurized vessel. The experimental system used to release the agent was that described in Section 8. The particular experimental configuration included the stainless-steel cylindrical vessel developed at NIST during our previous work on the selection of agents (Pitts *et al.*, 1994) with an attached Marotta solenoid valve. The vessel was oriented vertically, and, since the

valve turns the flow 90°, the fluid exited the vessel horizontally. The transmission behaviors of the photo-diode-detected laser beams described in Section 8 were recorded during the release. The extinction of the beam from laser No. 1, located at the vessel exit, was used to define a time of 0.000 s for the release.

The combined aspirated hot-film/cold-wire probe was mounted on the axis of the release valve 1.85 m from the valve exit. The DIRRACS infrared sensor described in Section 11.3 was also mounted at the same downstream distance and was operated during the test. A signal from the system used to initiate the release of the agent provided a trigger for the data acquisition system for the probe. The work sheet SHOT.WBB (Appendix 6) was used to control the data acquisition. Signals for both the aspirated hot-film/cold-wire probe as well as the DIRRACS were recorded simultaneously. Note that the data acquisition rate was 20 kHz per channel for 2.2 s following trigger detection.

A complete calibration of the combined aspirated hot-film/cold-wire probe was carried out for the first time the day before the agent was released. The results of the calibrations were used to generate the fits required in order to use CONCEN.FOR to calculate the temperature and concentration histories of the release at the measurement location. Figure 23 shows the results of the calibration for the cold wire. The least-squares fit of the experimental data to a line is included on the graph. The coefficients of the line were used as inputs for CONCEN.FOR. Figure 24 shows the corresponding data for the calibration of the aspirated hot-film probe. SURFFIT.FOR was used to calculate least-squares surface fits of halon 1301 mole fraction to the aspirated hot-film voltage and temperature for a range of surface orders,  $m$ . The case with  $m = 3$  was determined to be the most appropriate for fitting the data. Figure 25 shows the calculated mole fraction surface as a function of temperature and observed aspirated hot-film anemometer voltage. Note that nonphysical values (*e.g.*, mole fractions  $> 1$  or  $< 0$ ) are shown, but, voltages corresponding to these values should not be observed experimentally. The coefficients used to generate the surface of Figure 25 were input to CONCEN.FOR.

For the release, the vessel was filled two-thirds full (0.605 kg) with liquid halon 1301. The liquid agent was saturated with nitrogen with the nitrogen pressure above the liquid increased to 4.1 MPa. Measurements of the pressure behavior within the vessel indicated that the total release time for the liquid was on the order of 45 ms.

Figure 26 and Figure 27 show the voltage outputs of the constant-current (cold-wire) and constant-temperature (aspirated hot-film) anemometers for 200 ms following the release of the halon 1301. Both signals show strong responses at around 30 ms following the start of the release. This corresponds to the time required for the agent to travel from the vessel to the location of the probe (*i.e.*, a distance of 1.85 m). Very strong oscillations in the voltage outputs are observed during the period from 30 to 80 ms following release. After this time the voltages are still significantly different than those observed before the agent reached the measurement location, but the magnitudes and intensities due to the presence of the agent are much smaller than recorded earlier. It is significant that the largest voltages and fluctuations occur over a period which is roughly the same as that required to expel the liquid agent from the vessel. It seems certain that the strong signals and fluctuations are associated with the forced flow of agent driven from the pressurized vessel.

The voltage signals displayed in Figure 26 and Figure 27 along with the coefficients derived from fits to calibrations of the probe response as a function of concentration and temperature were used to calculate the temperature and concentration of halon 1301 as a function of time. Figure 28 and Figure 29 show the measured temperatures and mole fractions of halon 1301 following release of the agent from the pressurized bottle at 0 s. Some very interesting behaviors are observed in the data.

The temperature data look very reasonable. Before the agent reaches the probe at roughly 34 ms following the release, the recorded temperature is on the order of 23 °C which is reasonable for the experimental room. Careful scrutiny of Figure 28 shows that there appears to be a very small increase in temperature with a maximum at 29.4 ms just before the temperature begins to drop rapidly. At

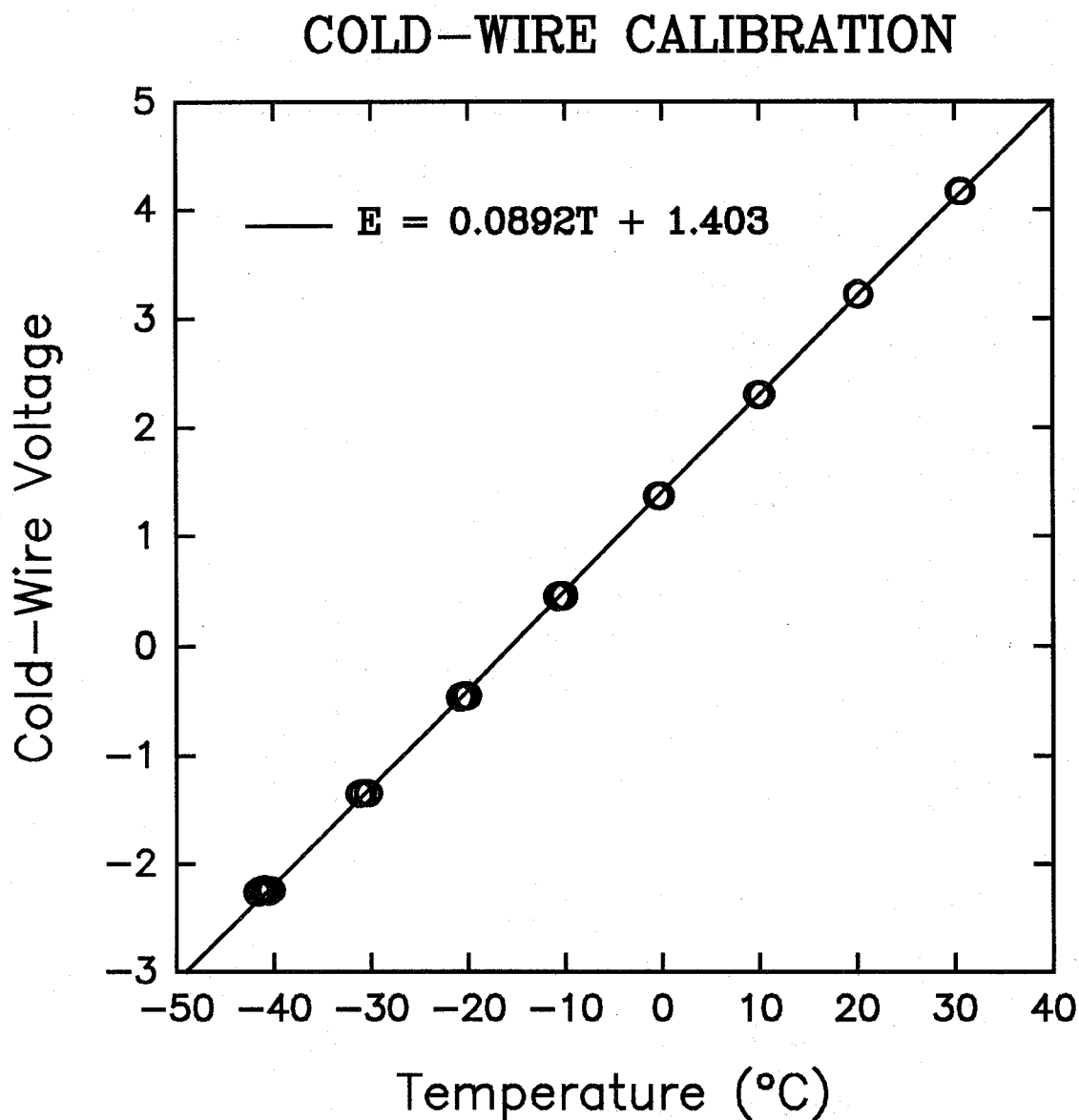


Figure 23. Values of constant-current anemometer voltage are plotted as a function of temperature. Note that eleven measurements were made for each nominal temperature. The line is a linear-least-squares curve fit of the experimental data.

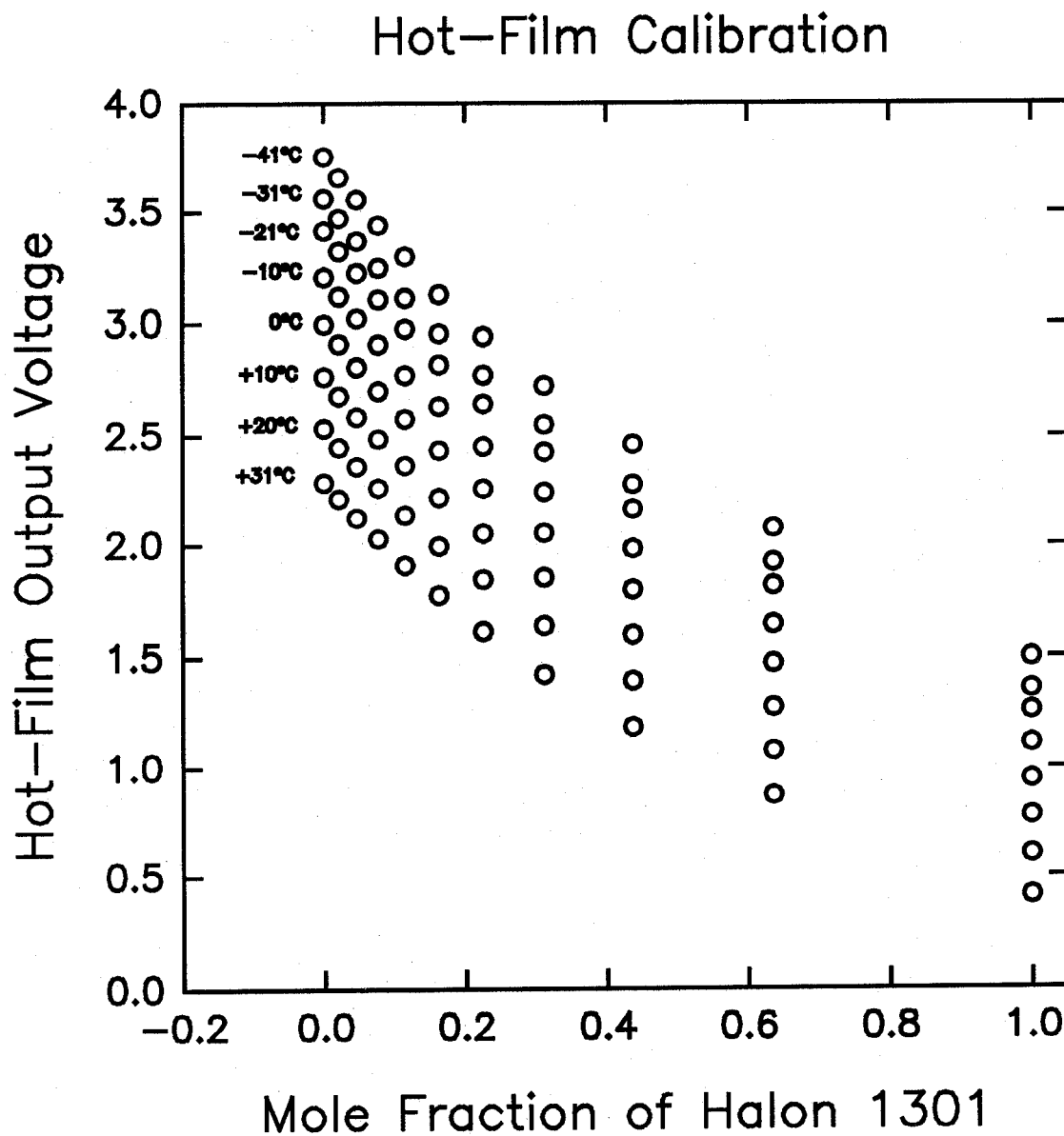


Figure 24. Values of aspirated hot-film anemometer voltage are plotted as a function of halon 1301 mole fraction for a range of temperatures.

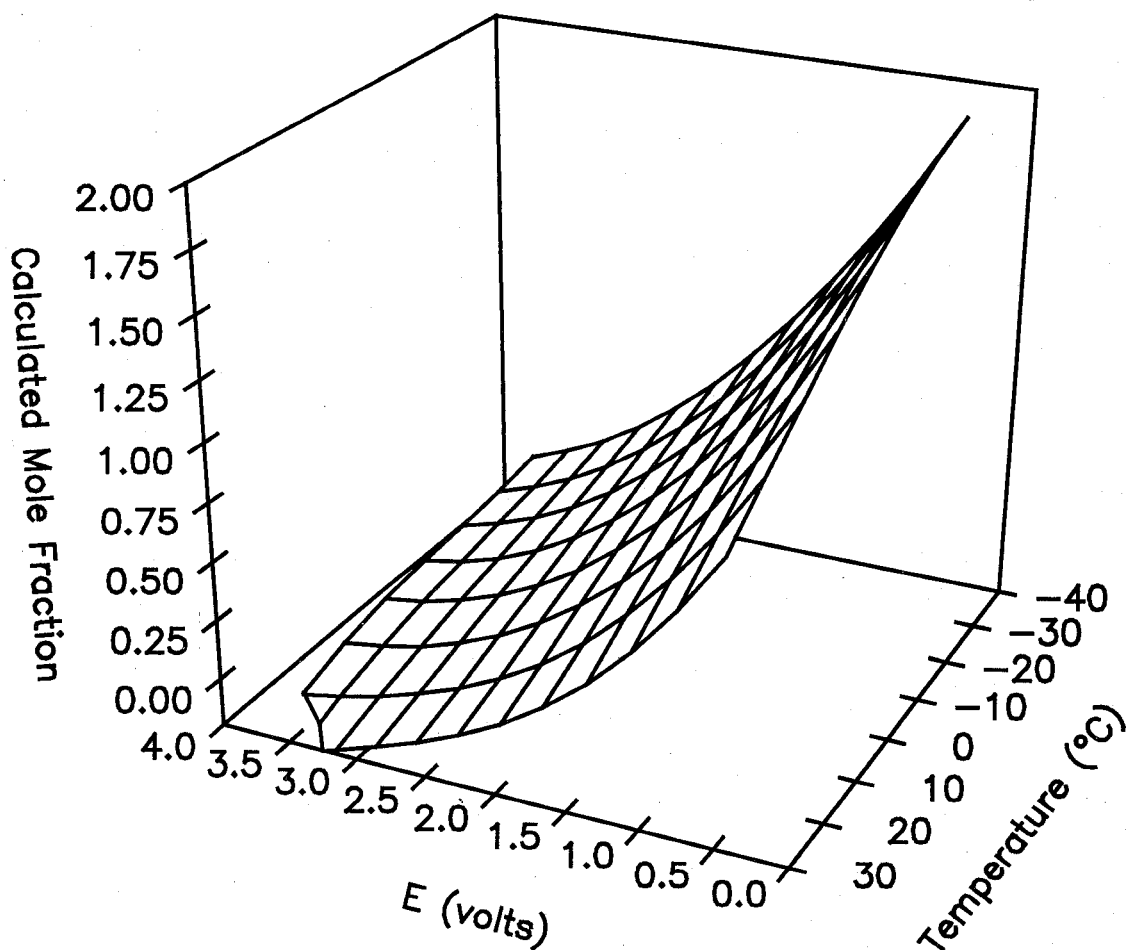


Figure 25. Plot of the mole fraction of halon 1301 surface calculated as a function of temperature and aspirated hot-film voltage based on a fit of a third-order surface to the data shown in Figure 24.

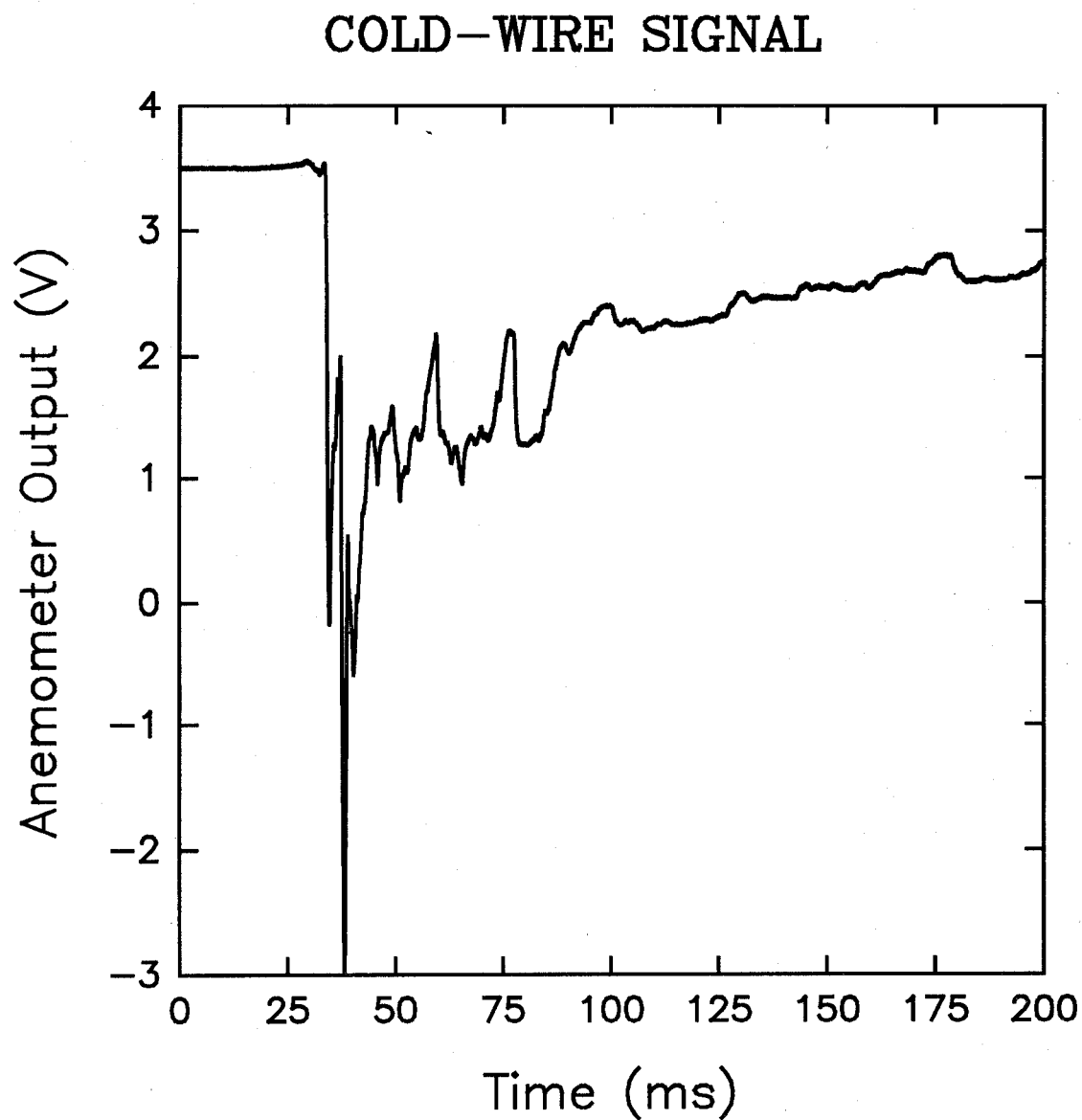


Figure 26. The output voltage of the constant-current anemometer is shown as a function of time following the release of halon-1301 from a pressurized vessel.

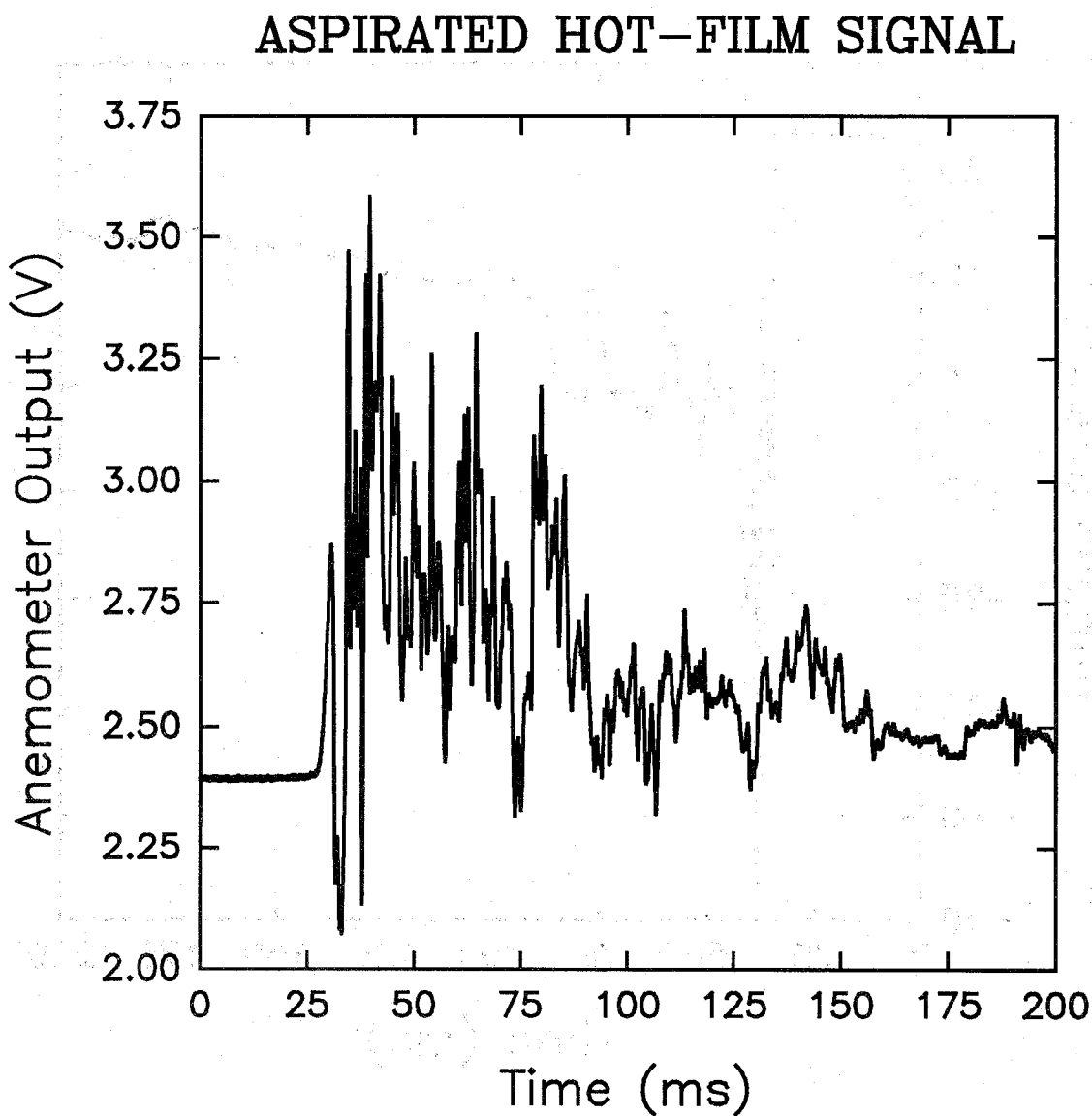


Figure 27. The output voltage of the constant-temperature anemometer is shown as a function of time following the release of halon 1301 from a pressurized vessel.



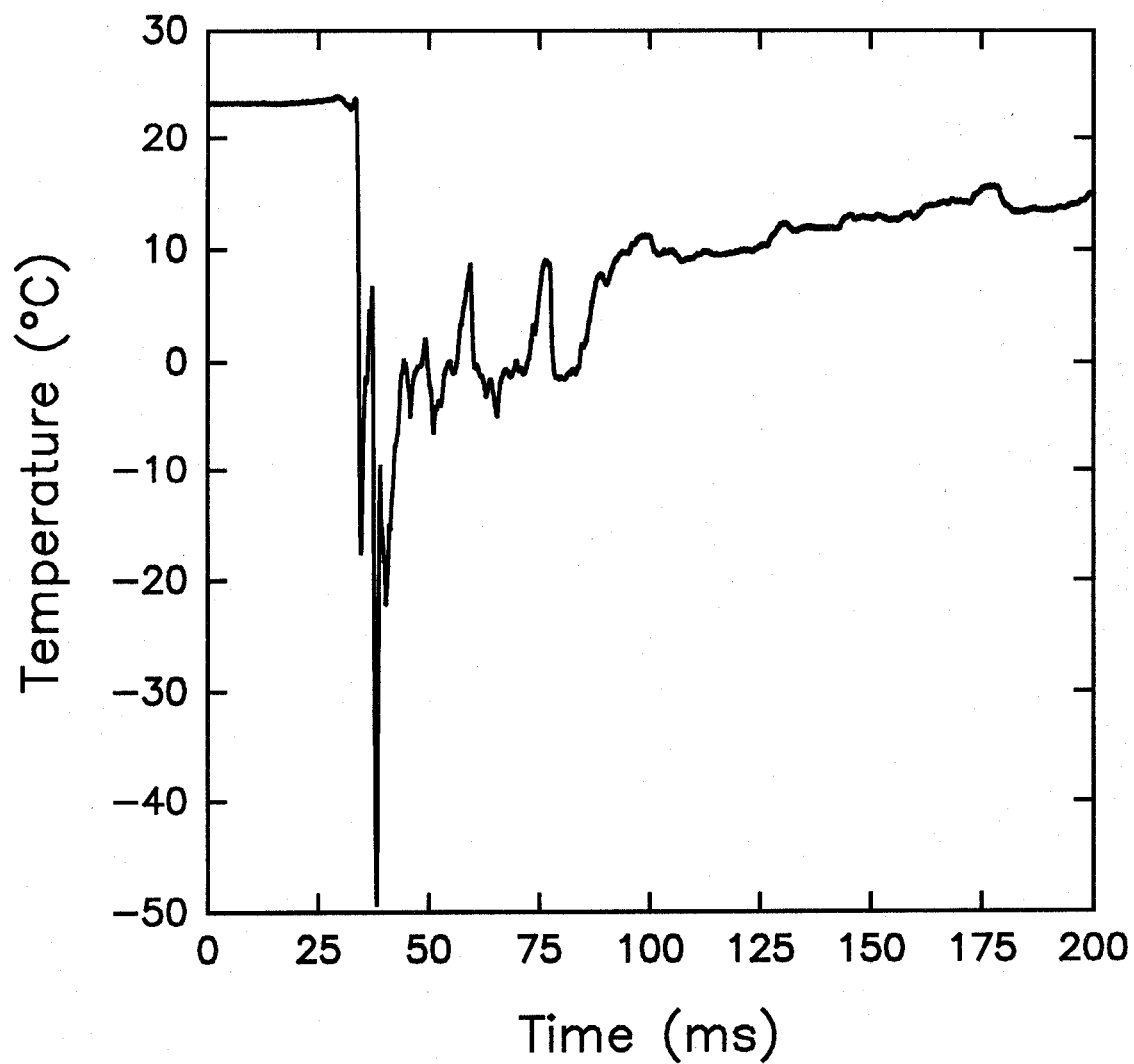


Figure 28. Measured temperature is shown as a function of time following the release of halon 1301 from a pressurized vessel. The probe was located 1.85 m from the vessel exit.

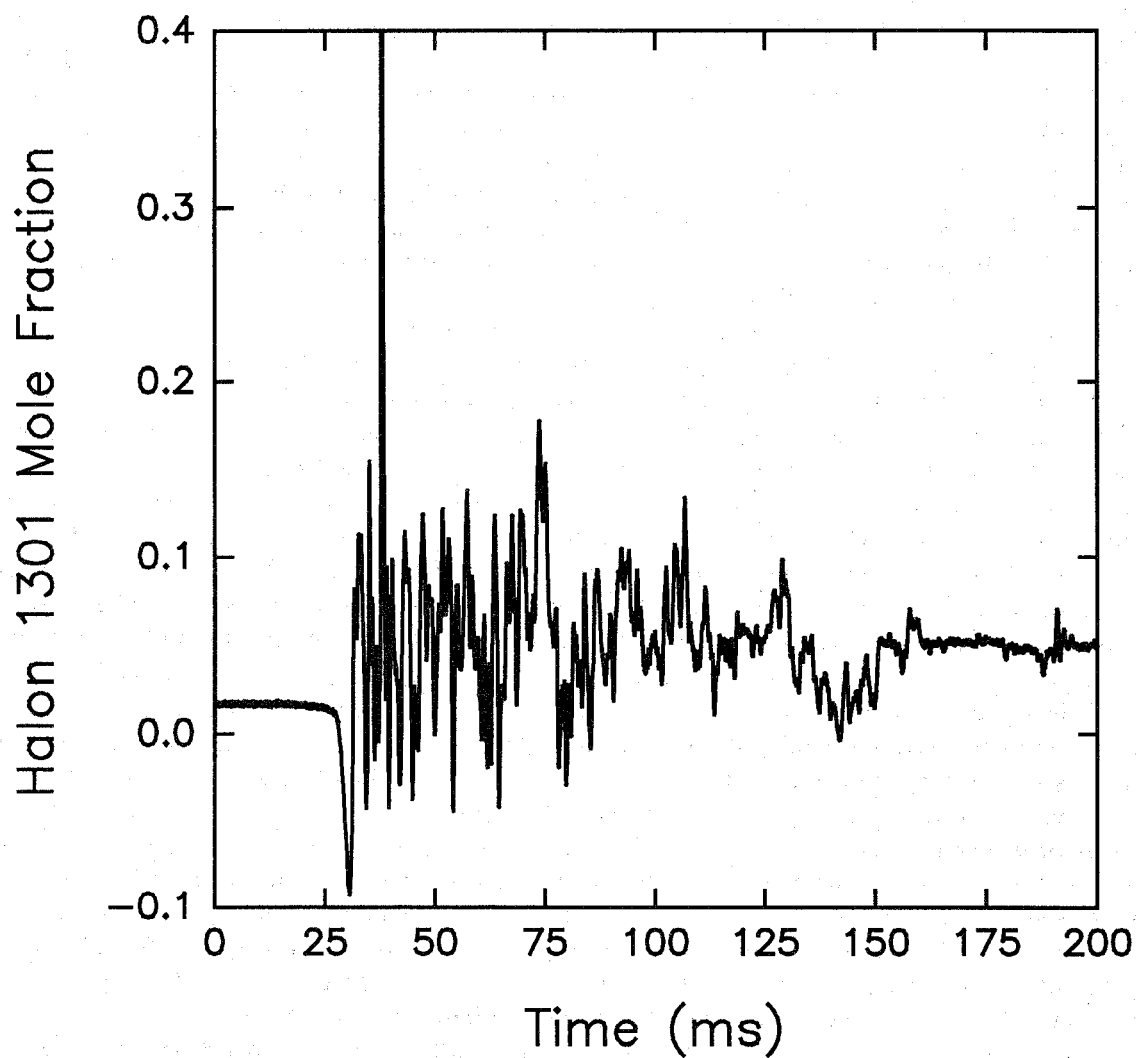


Figure 29. Measured halon 1301 mole fraction is shown as a function of time following release of the agent from a pressurized vessel. The probe was located 1.85 m from the vessel exit.

33.6 ms following release the temperature shows a sharp drop falling to  $-17.5\text{ }^{\circ}\text{C}$  at 34.7 ms. There is a small increase in temperature before the temperature drops rapidly to  $-49.3\text{ }^{\circ}\text{C}$  at 38.2 ms. This temperature is very nearly as low as the halon 1301 boiling point of  $-57.8\text{ }^{\circ}\text{C}$ . The temperature remains at these very cold levels only briefly before rising to values on the order of  $0\text{ }^{\circ}\text{C}$ . Following the passage of the released agent, the temperature begins rising slowly, reaching  $11\text{ }^{\circ}\text{C}$  at 100 ms,  $15\text{ }^{\circ}\text{C}$  at 200 ms, and  $21.8\text{ }^{\circ}\text{C}$  recorded at the end of experiment, 2 s following the release (not shown).

In considering the concentration data in Figure 29 a problem is immediately evident. In the period before the agent release reaches the probe, concentrations on the order of 0.016 are calculated, even though there is no agent present. This demonstrates there is some uncertainty in the calibrations. The source of this uncertainty is difficult to identify. It could be due to small changes in probe response due to flow effects as described above. The probe is calibrated in flows of agent/air mixtures, while the probe was located in ambient air when these measurements were recorded. Another possible source of error is the quality of the fit concentration surface to the experimental calibration data. Whatever the source, the results suggests that there will be an offset in the results corresponding to a mole fraction of 0.016.

An even more troubling aspect of the concentration data is the observation of physically unrealistic negative values at times earlier than the temperature measurement indicates the agent reached the probe. The negative concentration results reach a minimum at 30.5 ms following release. Based on the calibration results in Figure 24, such negative concentrations must correspond to voltages which are higher than those for air alone. Interestingly, the period of negative concentrations corresponds closely to the time when a very small temperature rise was observed. The actual cause of these observations is uncertain, but a reasonable hypothesis can be proposed. When the agent is released from the vessel it accelerates rapidly in the direction of the probe. As it does so it "pushes" air in front of it. If the flow velocities are high enough, the pressure of the air will increase, and it will be heated. When the compressed air reaches the probe it will be detected as a higher temperature by the cold wire, and the aspirated hot film will lose heat more rapidly due to the increased pressure, which will increase the voltage output and appear to correspond to a negative concentration.

During the period from roughly 34 ms to 75 ms, corresponding to the release period of the agent from the vessel offset by the passage time from the vessel to the probe, the mole-fraction data are very noisy and even occasionally display negative values. In a previous investigation (Pitts *et al.*, 1994) such behavior was attributed to the presence of two-phase flow at the measurement point. The same explanation is likely for the current data. Once this period is over, the data has a smoother appearance and looks more reasonable. At 100 ms the measured mole fractions are on the order of 0.11 (0.09 assuming an offset of 0.02) and by 200 ms have dropped to 0.05 (0.03 assuming an offset of 0.02). By the end of the period during which data was recorded (2 s), the concentration had dropped back nearly to the ambient levels recorded before the agent/air mixture reached the probe.

This series of tests was repeated at a later time. The results were somewhat different, but in general the overall behaviors were consistent with those described above.

It is impossible to say whether the measured concentration time history accurately reflects the true concentration behavior without an independent measurement of the concentration. Such a measurement was not possible for these experiments. However, the observed concentration behavior is consistent with the observed temperature changes which were recorded independently. Both indicate that significant concentrations of cooled agent are present during the passage of the flow generated by the release of the agent. Following this passage, the concentration rapidly drops, and additional mixing of the gas left behind by the agent release occurs with the surrounding air.

Although the quantitative findings of this test must be considered suspect due to the offset in concentration observed for ambient air, overall the results demonstrate that the combined aspirated hot-

film/cold-wire probe has the required time response and sensitivity to temperature and concentration of halon 1301 to allow accurate quantitative measurements at high data rates.

**11.2.6.3 Attempt to Measure Halon 1301 Concentration Following Release From Pressurized Vessels into a Simulated Dry Bay.** As noted in Section 11.1, a decision was made mutually with the program sponsors to test the combined aspirated hot-film/cold-wire probe during releases of agent into the dry-bay test facility at Wright-Patterson AFB, Dayton, OH. During the week of July 18, 1994, members of the BFRL research staff traveled to Dayton, OH and performed the tests which are summarized here. The goal of these tests was to assess the performance of the new probe for agent concentration measurement under "real-world" conditions (*i.e.*, in an environment where actual measurements are required).

All of the equipment required to perform the tests, including the calibration system, was transported from NIST and reassembled at Wright-Patterson AFB. The TSI, Inc. Model 1440S (SN 943064) combined aspirated hot-film/cold-wire probe was used. Figure 30 and Figure 31 show calibration curves for the cold-wire and aspirated hot-film probes recorded prior to testing in the simulated dry-bay facility. Also included in the figures are calibration results recorded immediately following the tests. Reasons for the differences in the two sets of curves are discussed below.

Following calibration, the combined aspirated hot-film/cold-wire probe was mounted in the dry-bay simulation facility. The tests were carried out in the large dry bay which is 6.1 m (long)  $\times$  1.5 m (high)  $\times$  0.30 m (deep). Figure 75 in Section 11.3.9.1 shows a schematic drawing of the facility. Small fans were located on the right edge of the dry bay which blew a constant volume of air into the facility. Three vents were located on the lower left edge. During the tests an additional opening of 0.30 m  $\times$  0.30 m, which was intended to represent an opening due to battle damage, was placed near the base in the center of the dry-bay front wall. The facility was equipped with a "high-clutter environment" which significantly blocked free flow within the dry bay. The agent to be released was stored in two vessels, which were placed on either side of the centerline, mounted at the top of the dry bay. The agent was released by firing "squib" charges which were exploded electronically under computer control.

Normally the dry-bay facility is used to perform fire tests under simulated battle and flight conditions. During these tests aviation fuel is located in a tank on the back side of the dry bay. An external high-speed air flow is passed along the front side of the dry bay. A fire is initiated by firing a high-explosive incendiary (HEI) antiaircraft round through a plate on the front. This round pierces the fuel tank and generally starts a fire. The result of the test is whether or not the agent extinguishes the fire upon release. During the current tests the dispersion of the agent was monitored under ambient conditions. The only air flow was the internal ventilation flow. There was no fuel, fire, or HEI rounds used.

The probe was mated to the facility using the mounting system described in Section 11.2.6.1. A hole of sufficient diameter to pass the probe and its mount was cut in the aluminum back panel of the dry bay along with holes for securing the plate which holds the mount. The probe was inserted to the center of the dry bay (*i.e.*, 0.15 m from the back wall). By creating a number of such mounting positions, it was possible to make measurements at different locations within the dry bay.

The outputs of the cold-wire and aspirated hot-film anemometers were recorded using the data-acquisition system described above. A trigger for the data-acquisition system was provided by the computer used to control the release of the agent into the dry bay. This trigger arrived approximately 0.2 s before the squib charges were fired. The Workbench PC work sheet for the experiment was set up to record voltages from both the cold wire and hot film. Additionally, voltage outputs were recorded for the two DIRRACS probes described in Section 11.3. Data were taken at 20 kHz/channel with a total data-acquisition time of 10.2 s. Note that this required that 816 000 measurements be

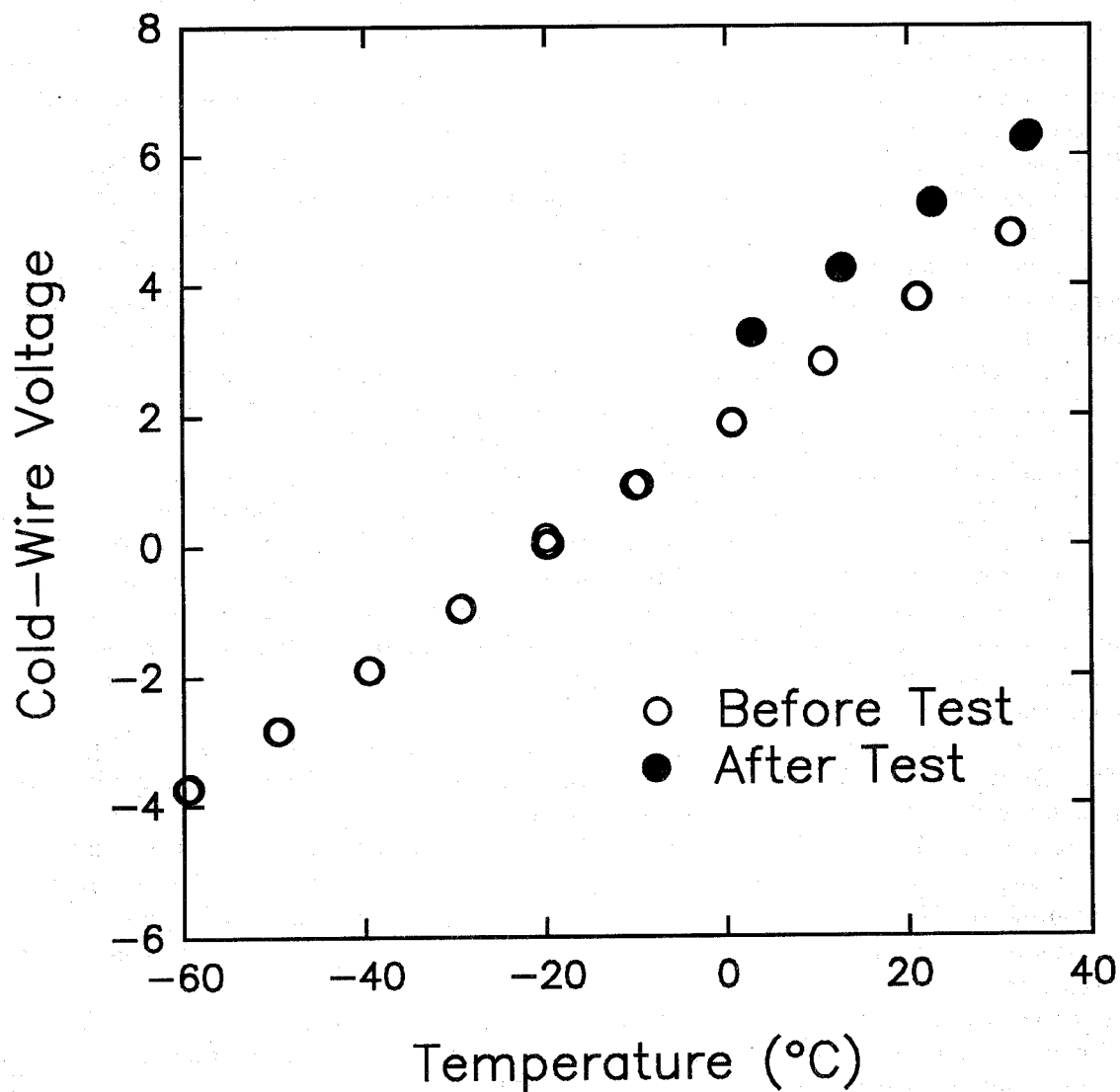


Figure 30. Calibrations of the cold wire before and after a series of measurements in the simulated dry-bay facility. See text for a discussion of reasons for the change in response.

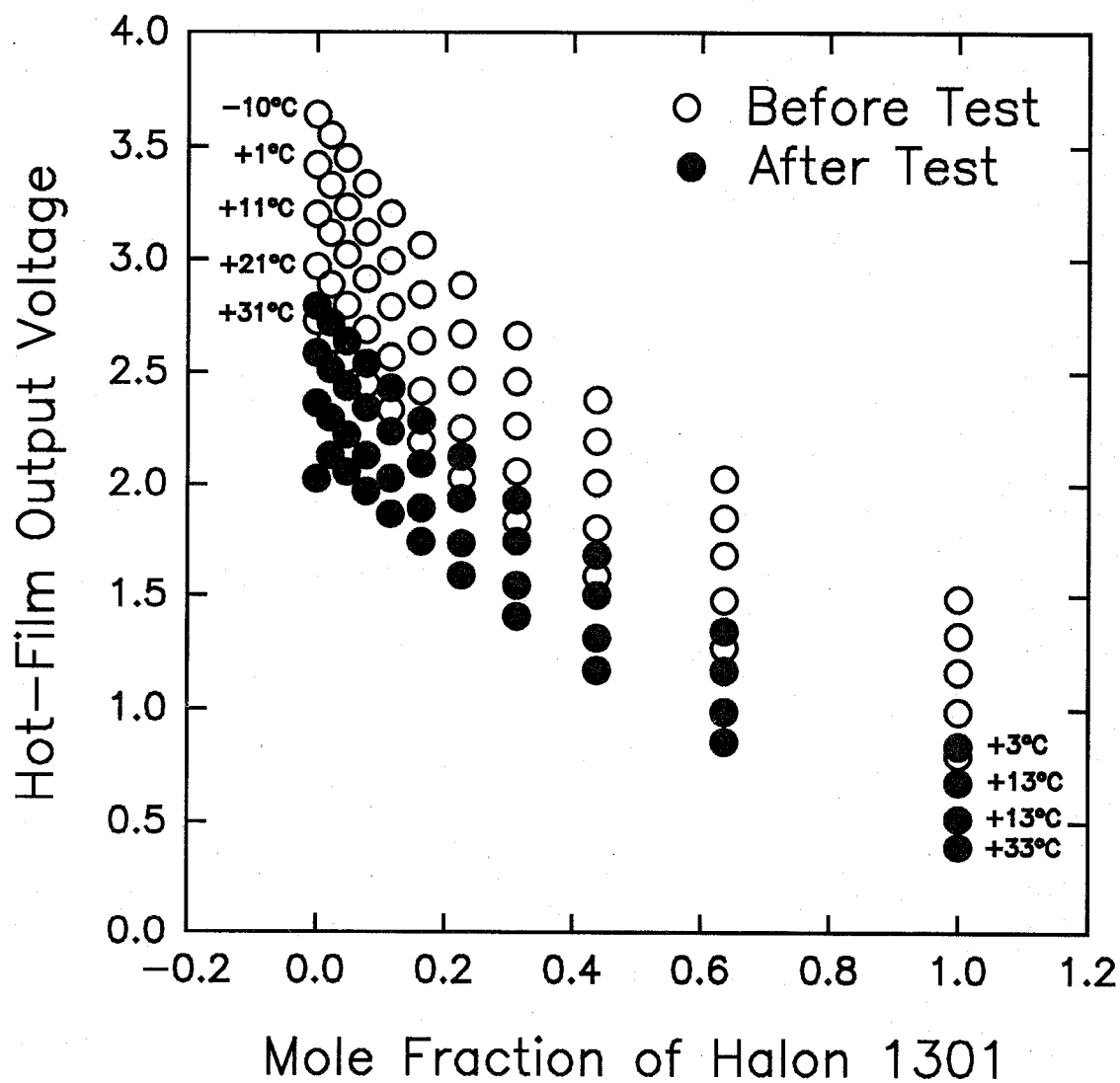


Figure 31. Calibrations of the aspirated hot-film before and after a series of measurements in the simulated dry-bay facility. See text for a discussion of reasons for the change in response.

made during a single experiment.

A total of six releases of halon 1301 were carried out. For one set of data the trigger was missed so only five sets were saved. During releases the probe location and amounts of agent were varied as indicated in Table 9. For reasons which will become obvious, only the results of the first release are summarized here. Figure 32 and Figure 33 show the cold-wire and aspirated hot-film voltages observed following initiation of halon 1301 release No. 1. Close inspection of Figure 32 shows a sharp voltage spike at 0.21 s after data collection was initiated. This is a noise signal associated with the firing of the squib charges and provides an accurate indication of the release time for the agent. No changes in the cold-wire output are observed until roughly 1.8 s following the release of the agent. At this time the voltage begins to rise slowly (indicating a temperature rise), reaching a maximum roughly 3.5 s following the release. The overall voltage increase is small indicating a small temperature change.

The voltage output for the aspirated hot film has a very different behavior. It remains nearly constant for the first 2 s following initiation of the experiment, but then begins to drop. The drop in voltage continues at a relatively constant rate for the remaining 8 s that data was recorded. The decrease in hot-film voltage is relatively large.

The raw voltage signals were converted to measured values of temperature and concentration using the CONCEN.FOR program described earlier. A third-order surface fit was used to fit the concentration data. The results are shown in Figure 34 and Figure 35. The initial temperature of roughly 36.6 °C seems somewhat high since the air temperature outside of the dry bay was recorded as 28 °C. It seems likely, however, that temperatures in the dry bay were somewhat higher since the clear-walled facility was located in the open on a bright sunny day. Even though the release of halon 1301 occurred at 0.21 s, no changes in temperature were detected until nearly 1.8 s following the discharge. The earlier tests had shown that the release of pressurized agents leads to a strong cooling since the superheated liquids cool to their boiling points (-57.8 °C for halon 1301). Despite this expected cooling, only a small temperature increase of roughly 0.7 °C was detected 4 s following release. After the maximum, the temperature began to decay back toward the original ambient levels. As discussed below, the measured temperature rise may be associated with a change in cold-wire calibration and may not be real. However, it does seem clear that there is no large temperature drop at the measurement position associated with the halon 1301 release. This observation requires either that the agent did not reach the detector, or that a large amount of heat transfer to the dry-bay walls and baffles occurred before it did.

The recorded time behavior of halon 1301 mole fraction shown in Figure 35 is nonphysical. Initially negative mole fractions on the order of -0.05 were recorded. Recall that negative values were also observed during the earlier tests of agent release at NIST. This is possibly due to the sensitivity of the aspirated hot-film calibrations to velocity. At roughly 1.8 s following release, the calculated agent concentration began a relatively constant rise, and by 10 s following the release, the measured mole fraction was slightly higher than 0.10. Including the negative offset, this indicates the halon 1301 concentration rose by 0.15 during the test. If the initial mass of halon 1301 were distributed evenly throughout the dry bay, the average concentration would be 0.014. The measured increase therefore seems very unreasonable.

The unusual behavior of the aspirated hot-film response continued after the conclusion of release No. 1. Data recorded prior to later releases (*i.e.*, in air) yielded calculated mole fractions of halon 1301 which were on the order of 0.10. As the later tests progressed, the voltage output for the cold-wire anemometer in air continued to increase while that for the aspirated hot-film anemometer continued to decrease. The voltage variations were so large that the operators suspected that the calibration curves for the probe were undergoing large changes. Following release No. 6 the probe was inspected. It seemed to be coated with black particles. It was believed that the residue was black

Table 9. Locations of the Combined Aspirated Hot-Film/Cold-Wire Probe and Masses of Released Halon-1301 for Dry-Bay Tests

Test #	Location (m) <sup>1</sup>	Total mass halon 1301 (kg)
1	0.20 × 0.58	0.23
2	0.20 × 0.58	0.91
3	3.05 × 0.36	0.23
4	3.05 × 0.36	0.91
5	5.89 × 0.51	0.91

<sup>1</sup>Measured from lower left-hand corner of the dry-bay test facility

powder which was released during the firing of the squib charges used to release the agent.

Immediately following the dry-bay tests the probe was returned to the calibration facility, and the calibration runs were repeated. The results are included in Figure 30 and Figure 31 where they are represented by the filled symbols. It is clear that the temperature calibration has been shifted upwards by over a volt. Note that this means the resistance of the wire has increased between the two sets of calibrations. At the same time the slope of the plot has changed less than 10 %. For a given voltage, the change in calibration represents a temperature difference of nearly 15 °C. Clearly this is unacceptable.

The changes in the response of the aspirated hot film were equally dramatic. For a given temperature, the output voltage for the constant-current anemometer was 0.6 V lower than prior to the test. In fact, the change in calibration corresponded to roughly 1/3 of the entire voltage difference observed between air and halon 1301 at a given temperature. Again, it is clear that such dramatic changes in probe response make accurate measurements of concentration impossible.

The modifications in response observed during the dry-bay tests were a complete surprise. Even though minor changes in calibration curves are often observed experimentally, they tend to be small. Test experiments at NIST had indicated that such changes were small, despite severe experimental conditions. Based on the use of squibs to release the agent and the observation of a black residue on the probe, it is most likely that contamination by black powder is the cause of the shifts in calibration curves for the two sensors. Deposition of a conducting solid on the cold wire would be expected to increase its resistance. This is consistent with the increased voltage output of the constant-current anemometer observed for a given temperature. Deposition of a solid on the sonic orifice of the aspirated probe would reduce the diameter and, therefore, the mass flow through the orifice. Since the mass flow is reduced, the flow velocity over the hot-film sensor would also be decreased. This would result in a smaller heat loss and a decrease in the output voltage as observed experimentally. Based on the observations, it seems certain that the deposition of a black residue as the result of squibs firing was the source of the shifts in calibration curves for the combined aspirated hot-film/cold-wire probe.

Following this short series of tests it was necessary to return the probe to TSI and have it repaired.

Since these tests indicated that it would be impossible to use the aspirated hot-film/cold-wire probe for measurements in the dry-bay configuration, the decision was made to abandon further



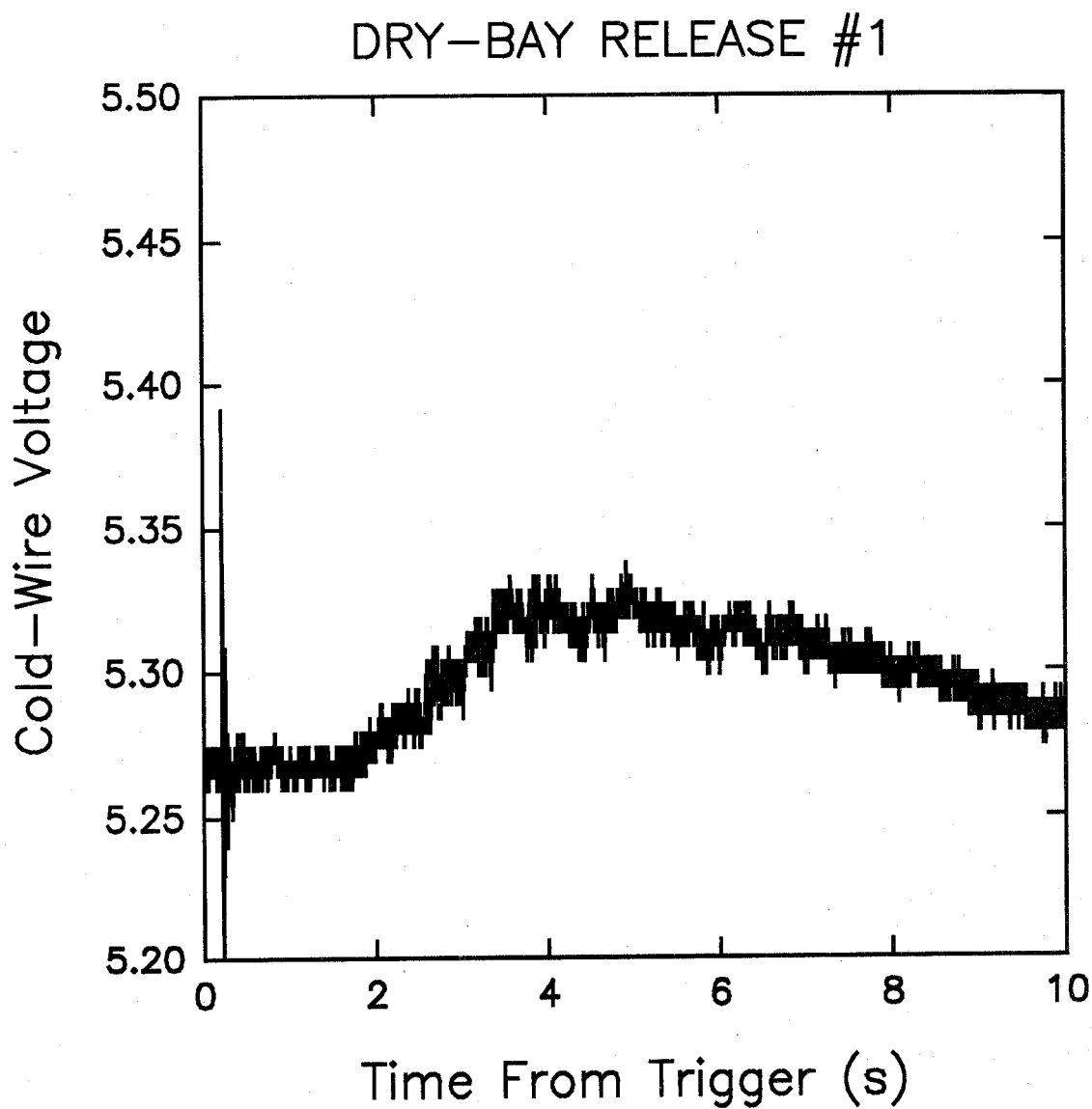


Figure 32. The voltage output of the cold-wire anemometer is plotted as a function of time following release No. 1 of halon 1301 into the dry bay. Data are plotted at 1 ms intervals.

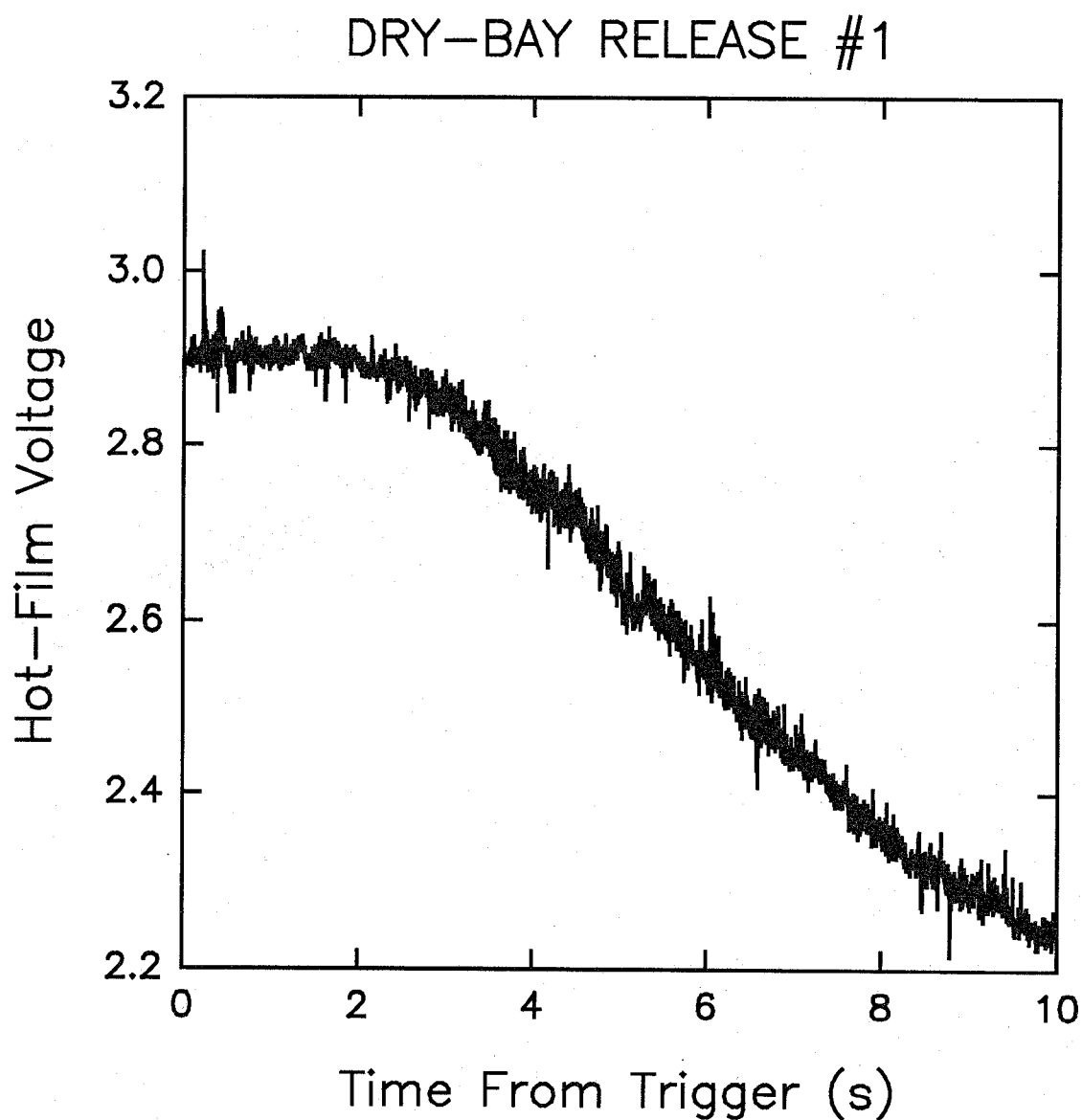


Figure 33. The voltage output of the aspirated hot-film anemometer is plotted as a function of time following release No. 1 of halon 1301 into the dry bay. Data are plotted at 1 ms intervals.

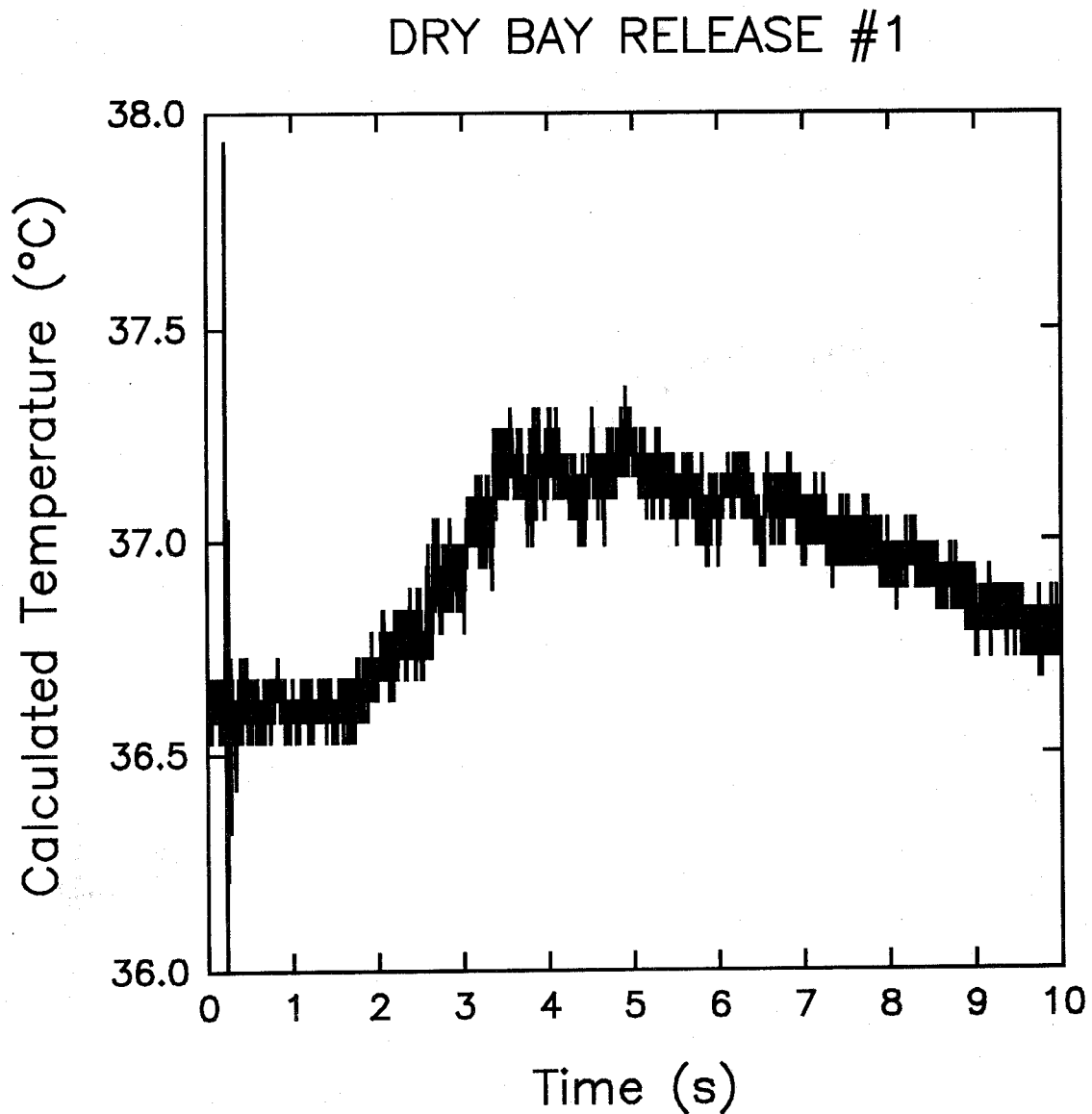


Figure 34. Calculated temperature is shown as a function of time following release of the agent into the dry bay at 0.21 s. The probe was located in the lower left-hand corner of the facility. Data are shown for 1 ms intervals.

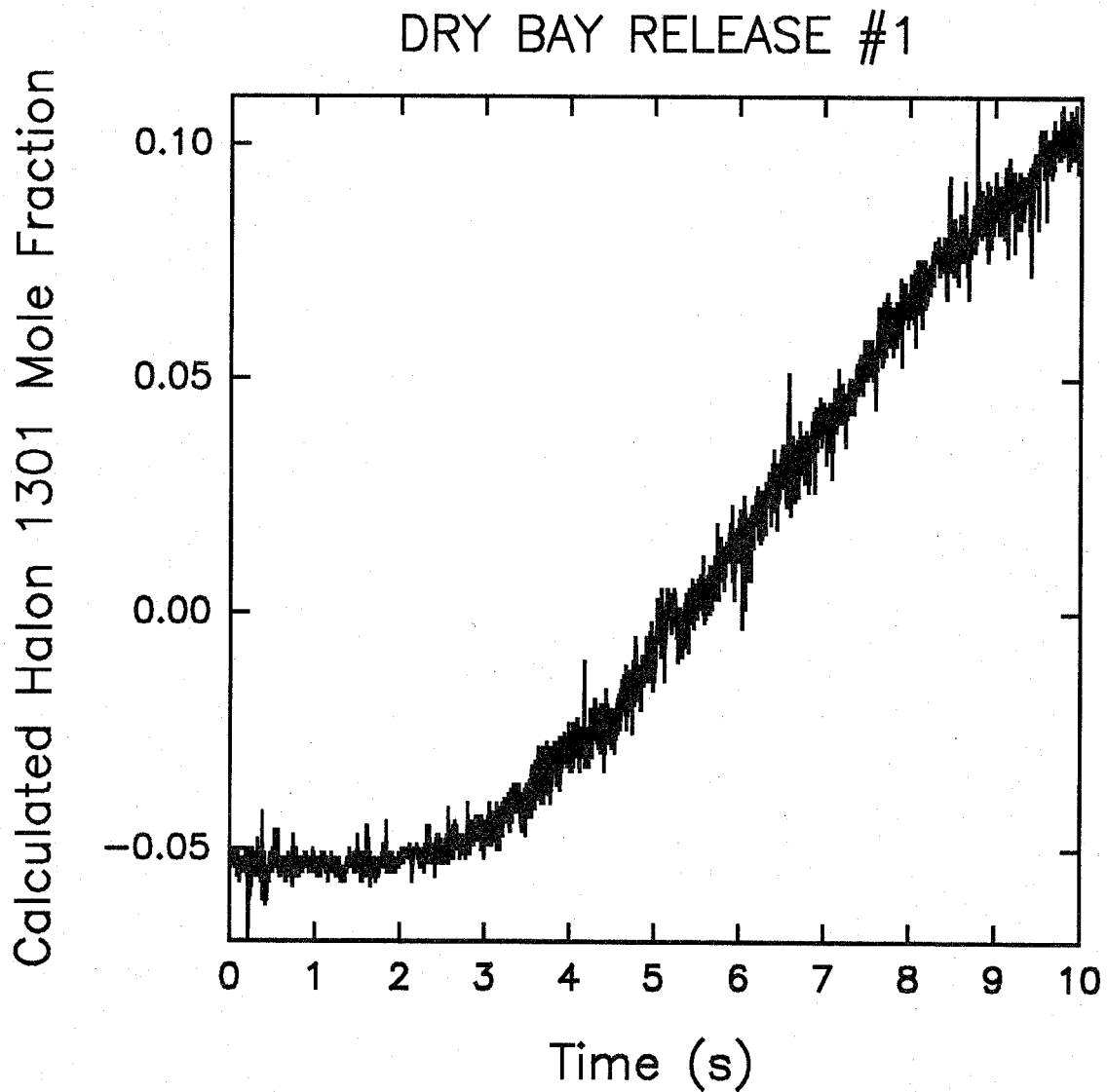


Figure 35. Calculated halon 1301 mole fraction is shown as a function of time following release of the agent into the dry bay at 0.21 s. The probe was located in the lower left-hand corner of the facility. Data are shown for 1 ms intervals.

development of these probes and focus our efforts on completing development of the DIRRACS discussed in Section 11.3.

**11.2.6.4 Measurement of Halon 1301 Concentration Following Release Into a Turbulent Spray-Flame Burner.** The turbulent spray-flame burner is a facility which has been utilized to investigate the extinction of bluff-body-stabilized turbulent flames by halon 1301 and various replacement agents (Hamins *et al.*, 1994). The system is discussed in detail elsewhere in this report (see Section 9), and only a brief description is provided here. Figure 36 is a schematic diagram of the turbulent spray-flame burner facility. It consists of a 0.5 m long, 73 mm diameter stainless-steel tube containing an air flow for which the velocity and temperature can be varied. A 6 mm diameter fuel tube capped by a liquid pressure-jet spray nozzle is centered in the air pipe with the nozzle outlet located at the open end of the outer pipe. A 35 mm diameter steel disk located just downstream of the nozzle serves to stabilize the flame. The gaseous agents to be added to the air flow were injected impulsively 0.5 m upstream of the nozzle through two 6 mm diameter tubes. Screens were placed downstream of the injection port to aid mixing. By recording the dynamic pressure drop inside the vessel used to hold the agents, it was possible to estimate the average mass-flow rate of the agent into the air flow as a function of time.

Even though this burner and an earlier version (Hamins *et al.*, 1994) had been used extensively for testing fire-fighting agents, the time behavior and spatial distribution of agent in the air flow had not been experimentally characterized. As a test of the aspirated hot film for concentration measurements and to characterize the temporal and spatial concentration of the agent near the pipe exit, a series of measurements of halon 1301 mole fraction were carried out. These measurements were made at room temperature in the absence of a fuel flow or combustion. The air flow velocity was varied over a range of 2.5 m/s - 10.0 m/s. Due to the presence of the stabilization disk and the relatively large diameter of the air-flow tube, the flow at the stabilization point is expected to be turbulent. Measurements downstream of the stabilization disk were found to be very noisy due to high turbulence and recirculating flow. For this reason measurements were made 25 cm upstream of the disk.

Since the temperature was not expected to change during these experiments, a single aspirating probe without the cold wire was used. The probe was designated as a TSI, Inc. Model 1440R-20 (Serial #941102). Halon 1301 was the agent added to the air flow. Measurements were made at various locations in the air flow by moving the probe horizontally across the pipe. Table 10 summarizes the radial locations where data were recorded. The output of the aspirated hot film was digitized and stored using Workbench PC and the Flash-12 analog-to-digital converter described in Section 11.2.4.5. Data were recorded at 1 kHz.

The response of the aspirated hot film was calibrated by measuring the anemometer output voltage as a function of halon 1301 mole fraction. The calibration temperature was chosen to closely match that in the laboratory where the turbulent flame burner was located. Figure 37 shows the calibration results plotted as mole fraction versus the constant-temperature anemometer voltage. The data were fit to a third-order polynomial for which the result is included and compared with the data in Figure 37. The calibration curve reproduces the experimental data quite well. During the actual measurements in the turbulent spray-flame burner, small variations in the voltage recorded when only air was present were noted. During data analysis these were corrected by adding or subtracting a small voltage such that the average halon 1301 mole fraction in the presence of air was 0.00. Over 30 measurements were made for various conditions in the burner. Only a few are summarized here in order to provide an indication of the quality of the measurements using the aspirated hot-film probe.

Figure 38 shows an example of the time behavior of halon 1301 concentration following release into the air coflow of the burner. It can be seen that the noise level for the concentration measurement is quite good. No halon 1301 is detected until 0.8 s after the start of the release. This corresponds to

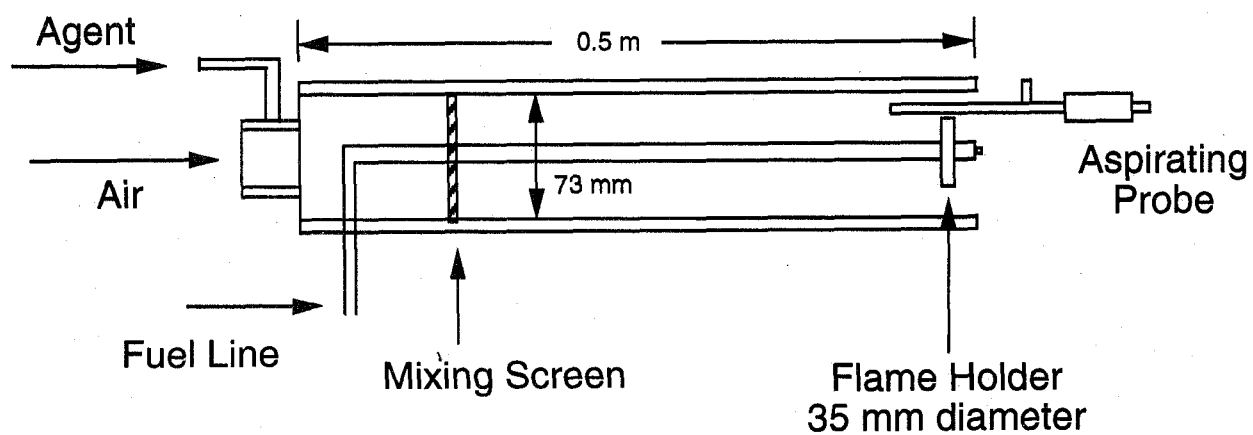


Figure 36. Schematic diagram of the turbulent spray-flame burner. The aspirated hot-film probe was used to monitor halon 1301 concentration at various positions in the air coflow.

Table 10. Positions of the Aspirated Hot-Film Probe for Agent Concentration Measurements in the Turbulent Spray-Flame Burner. Positions Relative to the Left-Hand Edge of the Coflow Air Tube

Position #	Radial Location (mm)
1	0.5
2	4.6
3	15.9
4	17.3
5	53.3
6	61.1
7	67.4
8	70.1

the period required for the agent to flow from the release point to the probe. The data show that a finite period of roughly 50 ms is required for the concentration of the agent to increase to a relatively constant level, where it remains for a period close to the nominal time during which the valve is open. When the valve is closed, there is a tailing of the agent mole fraction which suggests that the closing time for the solenoid valve used to release the agent is somewhat longer than the period required to open. The measured mole fraction is in good agreement with the mole fraction calculated assuming that the agent is released as a square-wave pulse.

The measured concentrations for a series of tests in which the nominal concentration of the release was varied by changing the pressure in the agent containment vessel are shown in Figure 39. All of these experiments had release times on the order of 230 ms. It can be seen that the measured concentrations increase with the nominal concentrations. A detailed comparison of the measured and nominal concentrations is provided below.

Figure 40 shows the time behaviors recorded for releases of halon 1301 in which the release times were varied. It is clear that for the shortest time release the concentration does not reach a clear plateau, but instead appears as a spike. For intermediate release times the halon 1301 mole fractions do attain relatively constant values. However, as the release times are lengthened further, the concentration shows a distinct drop with time. The concentration fall off is the result of the pressure drop which occurs in the halon 1301 holding tank during a release. As the pressure falls off the release rate decreases and the concentration falls. In order to hold the concentration at a given level for a longer period it would be necessary to increase the size of the holding tank.

Average concentrations for the releases were calculated by averaging the measured concentrations over periods of time after a nearly constant concentration was achieved. A series of these measurements were made across the turbulent burner at the positions which were accessible on either side of the stabilization disk. Figure 41 shows the results. Even though there appears to be slight asymmetry in the distribution with higher concentrations on the right, it does appear that the agent is distributed relatively uniformly across the entire flow.

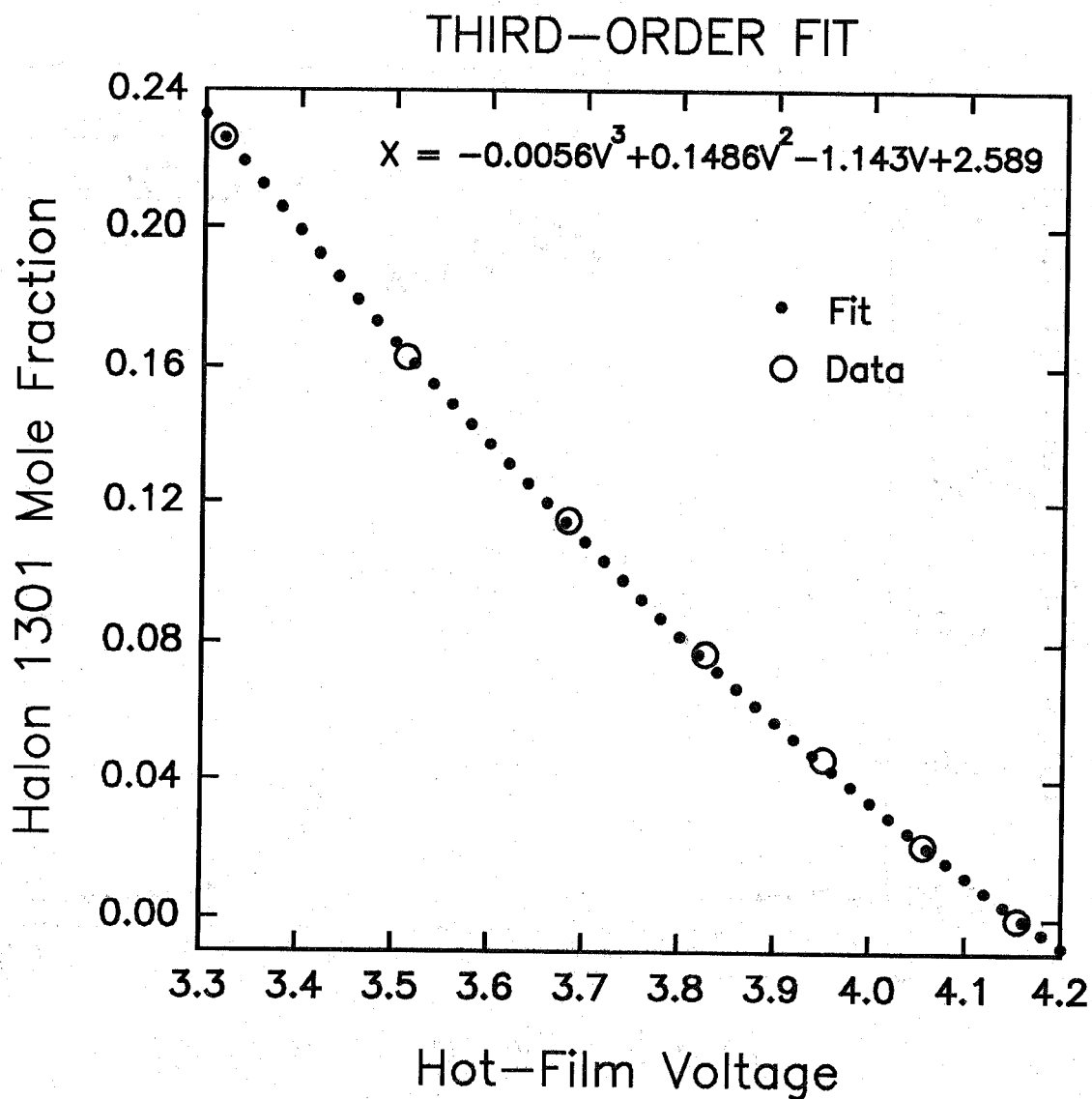


Figure 37. Halon 1301 mole fraction is plotted as a function of the output voltage of the constant-temperature anemometer. These values are compared with a least squares fit of a third-order polynomial to the data.



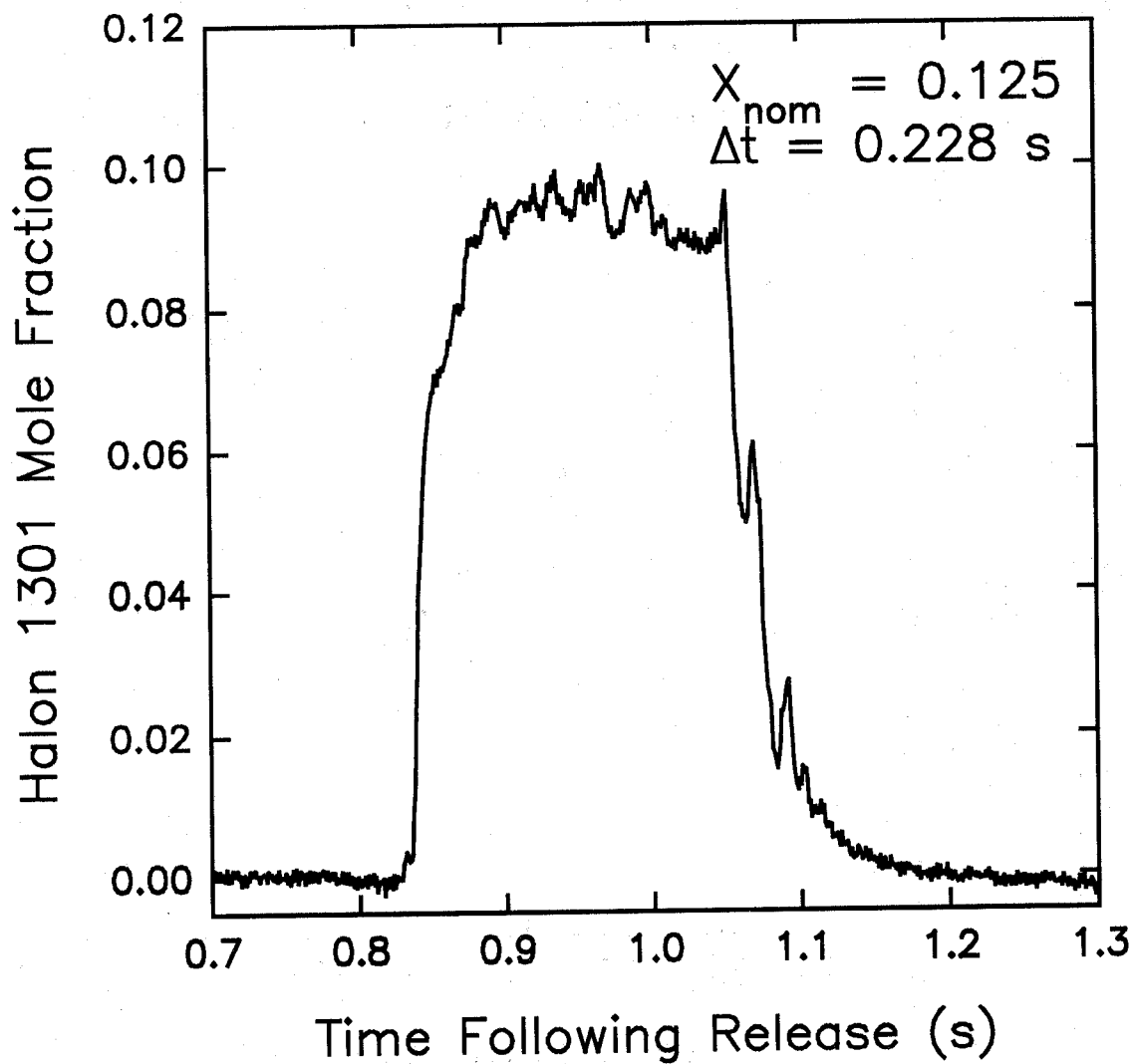


Figure 38. Halon 1301 concentration as a function of time following release of the agent into the air coflow of the turbulent spray-flame burner. The nominal mole fraction and period of the release were 0.125 and 0.228 s, respectively.

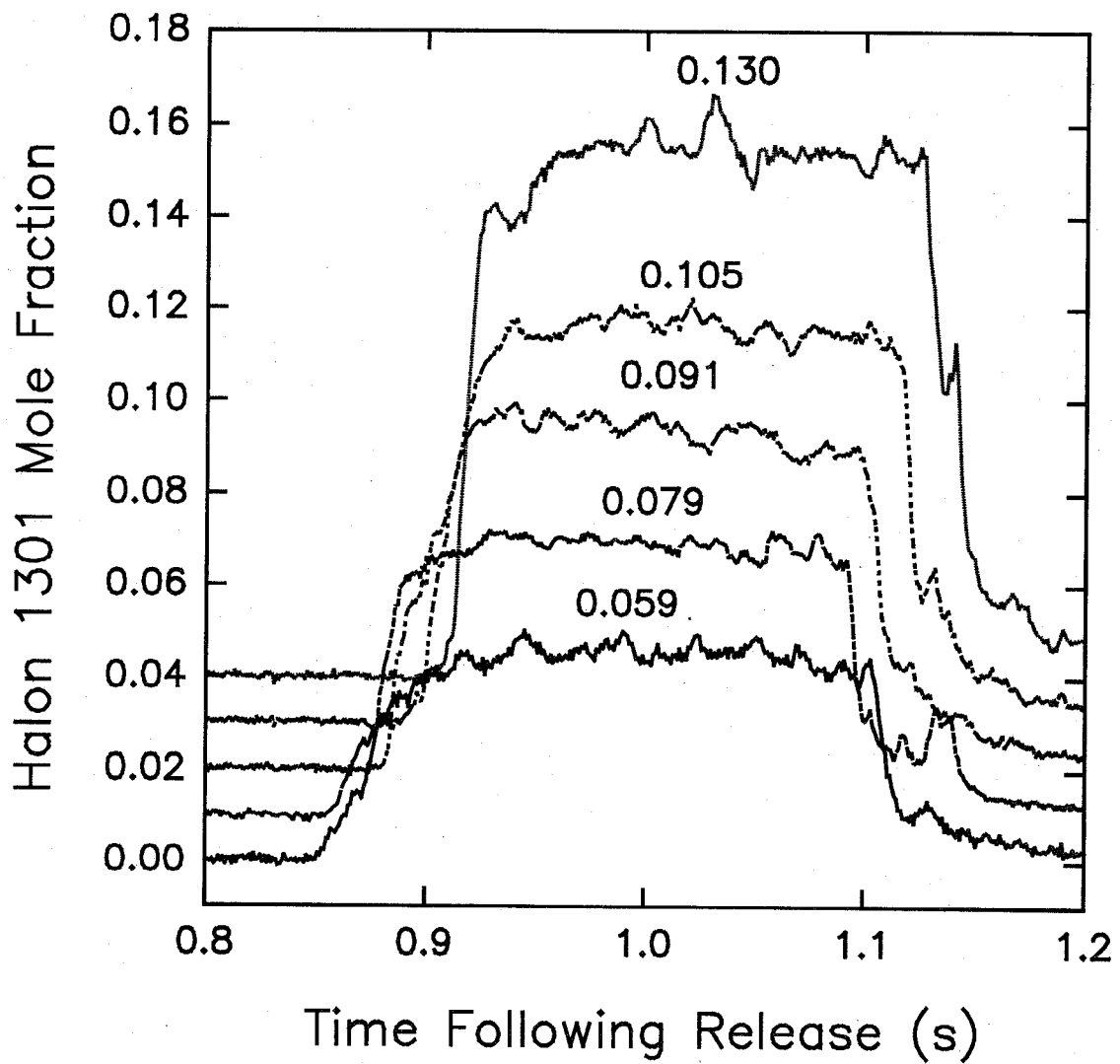


Figure 39. Halon 1301 mole fraction as function of time following release of varying mole fractions (indicated by numbers on the plot) into the air coflow of the turbulent spray-flame burner. Nominal release periods of 0.230 s. Plots offset by 0.01.

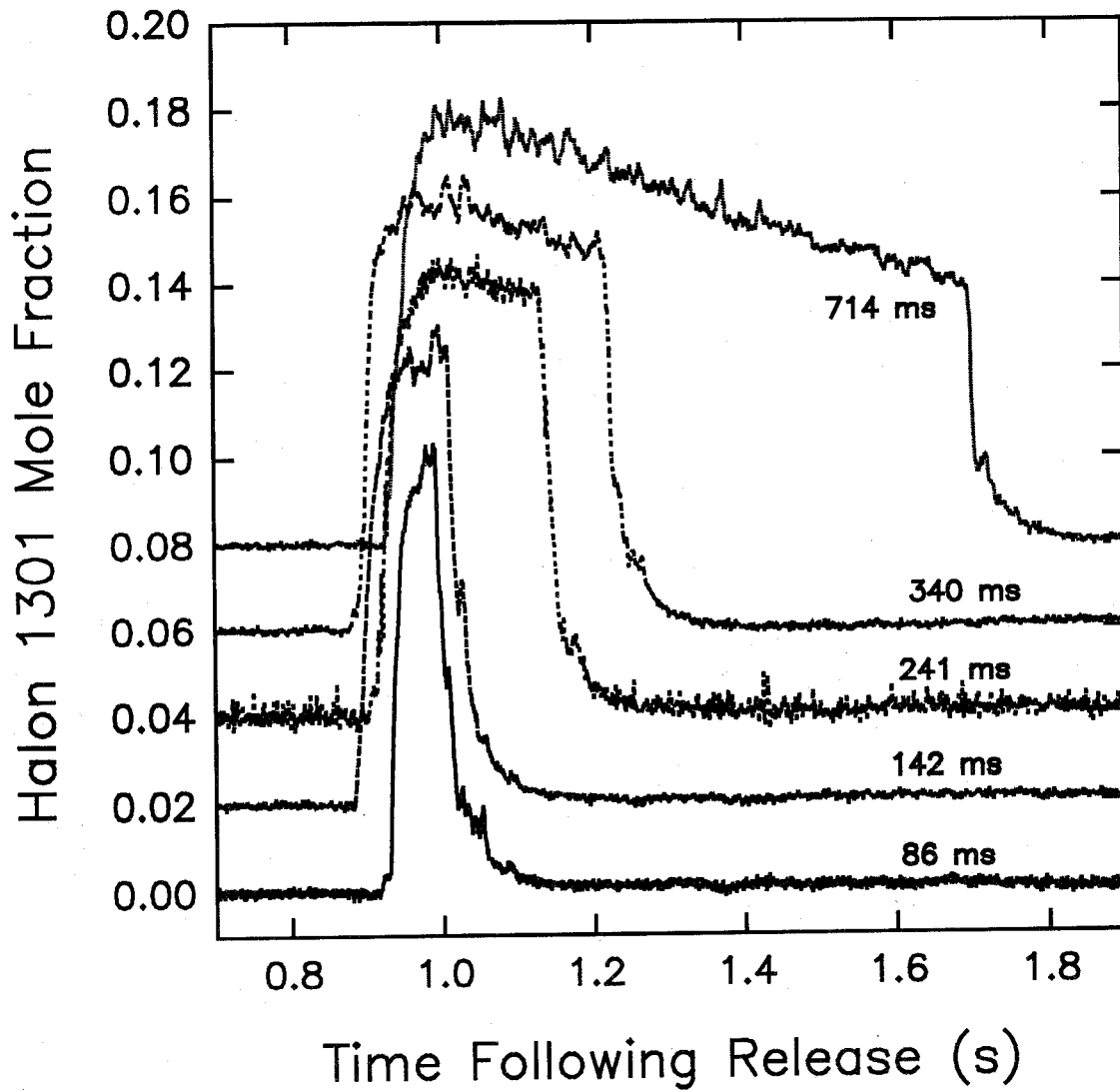


Figure 40. Halon 1301 mole fraction as function of time following release with varying release periods (indicated on the plot) into the air coflow of the turbulent spray-flame burner. Nominal mole fractions were 0.10. Plots offset by 0.02.

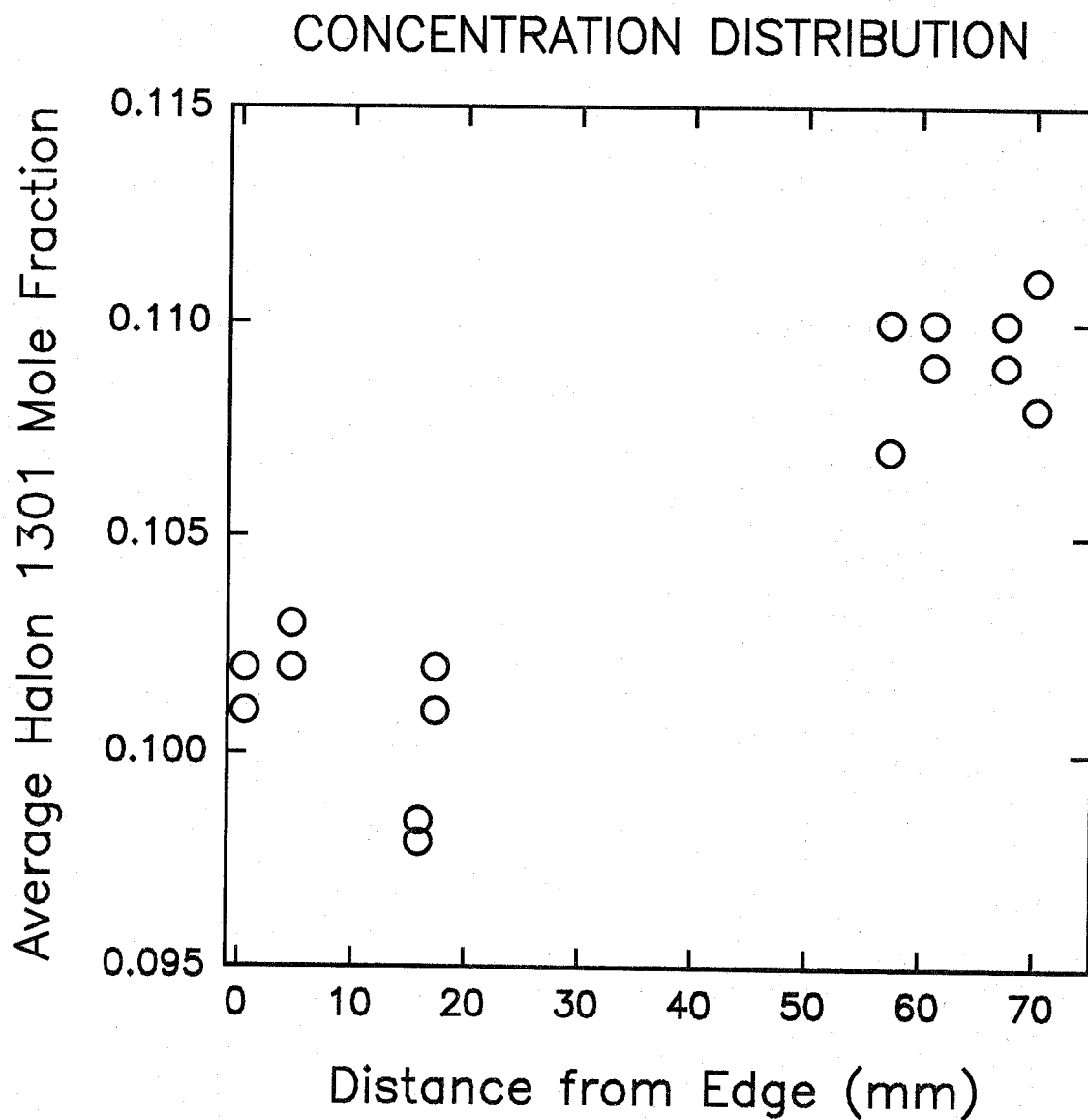


Figure 41. Average halon 1301 concentration is plotted as a function of location across the turbulent spray-flame burner as measured from left to right. Nominal halon 1301 mole fractions based on pressure measurement were 0.104.

Comparison of the measured concentrations with nominal concentrations based on pressure drops in the agent vessel provides an opportunity to assess the accuracy of the measurement technique. Figure 42 shows a comparison of the measured average mole fractions of halon 1301 with those estimated using the pressure drop within the containment vessel. Even though the general agreement is good, some scatter is obvious. In particular, some of the measured mole fractions seem to be systematically offset to lower values from the estimated values. These measurements were the first recorded during the experiment, but we have been unable to provide an explanation as to why they should be different than later results. On the basis of this plot, we conclude that the aspirated hot film does respond well to changes in halon 1301 concentration and that measured values are accurate to within 20 %. More definite statements concerning accuracy will require more careful experiments.

This brief series of experiments has demonstrated that the aspirated hot film is capable of recording accurate agent concentrations with high temporal resolution. At the same time, it has provided a useful characterization of the efficiency of mixing of an agent into the air flow of the turbulent spray-flame burner.

**11.2.7 Summary and Recommendations.** During the work described in this section it was demonstrated that a combined aspirated hot-film/cold-wire probe can be utilized to record simultaneous temperature and agent concentration measurements with high temporal ( $\approx 1$  ms) and spatial resolution ( $\approx 1$  mm<sup>3</sup>). A unique facility was developed which allowed the probe to be calibrated over a wide range of temperature (-65 °C to 40 °C) and a full range of concentration for five fire suppressants. At the same time, an unexpected sensitivity of the aspirated hot film to velocity fluctuations was identified and characterized. This sensitivity to velocity limited the accuracy of concentration measurements to such a degree that the current approach does not seem feasible for FC-125, and the accuracy for the other agents was compromised. Measurements of halon 1301 concentration in the turbulent flame burner demonstrated that aspirated hot films are capable of accurate quantitative concentration measurements with good temporal resolution.

When the probe was tested in the dry-bay test facility at Wright-Patterson AFB, it was found that a black residue generated by the facility clogged the probe and prevented accurate measurements. For this reason, further development of the probe was halted, and our further efforts were focused on the development of the DIRRACS system.

There are several modifications which could be made to the aspirated hot-film/cold-wire probe which would be likely to improve its performance. It is possible that the velocity sensitivity observed during the current effort was due to the design of the system which placed the hot-film probe within a narrow tube at a significant distance from the tube entrance and the downstream sonic orifice. Alternative probe designs discussed in Section 11.2.1.2 might well have much lower sensitivity to velocity. It is also possible that experimental conditions could be identified which would improve the response of the hot film to changes in concentration of the fire-fighting agents and therefore improve the accuracy of the measurements.

The contamination of the probe in the dry-bay test facility was ultimately the factor which led us to halt further work on the development of this measurement approach. Wilson and Netterville (1981) have described an aspirated hot-film probe containing a filter, but which still provides good time response. The use of a filter might be expected to dampen velocity fluctuation sensitivity. It is also possible that the filter could remove the contaminant present in the dry-bay experiment and allow the concentration measurements to be made in this environment.

The success of any or all of the above changes in the probe design could lead to the development of more effective combined aspirated hot-film/cold-wire probes for the measurement of concentration. Unfortunately, the additional design and experimental studies required were beyond the fiscal and time constraints of the current effort. While we feel that there is a reasonable probability that such

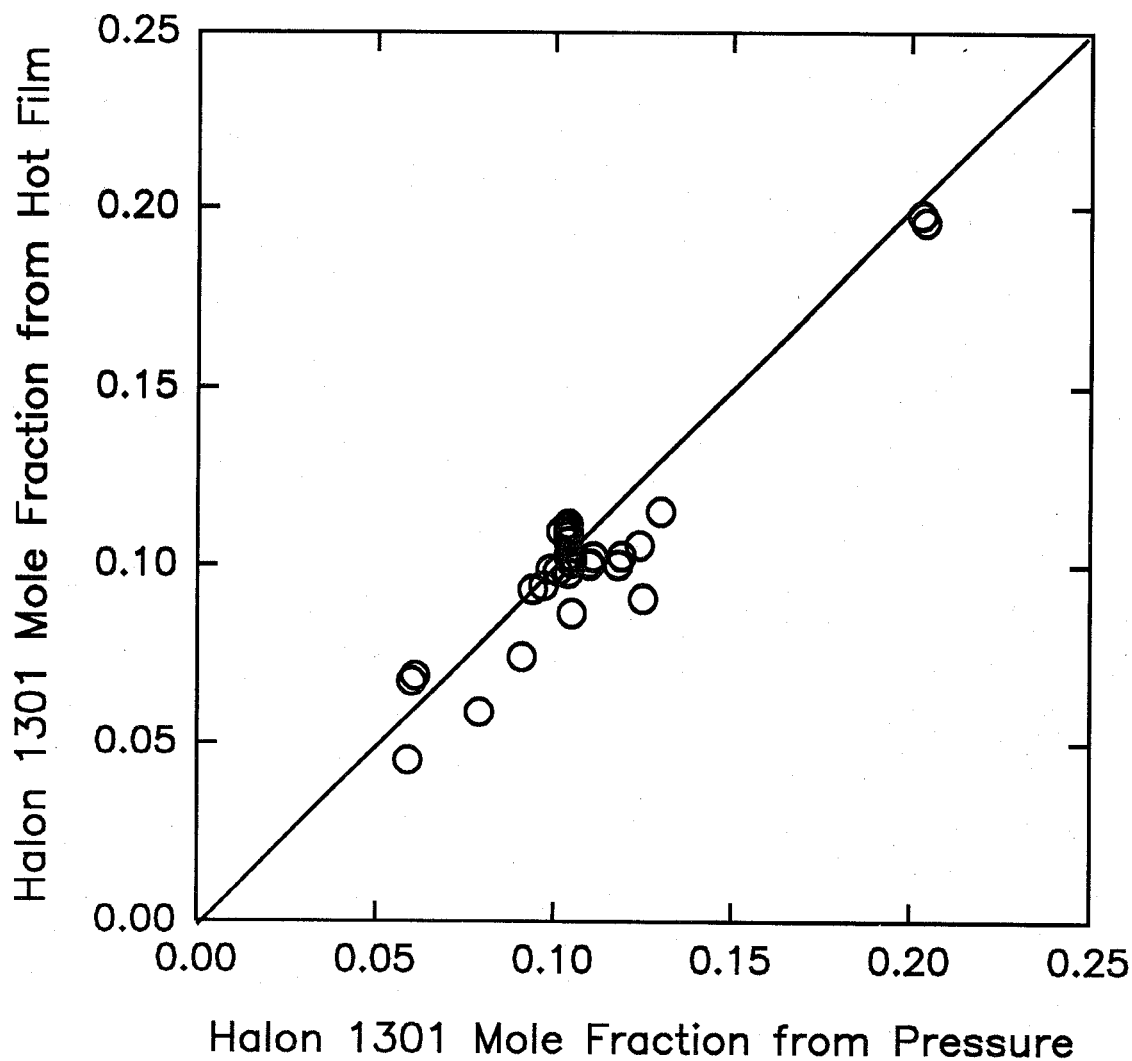


Figure 42. Average measured halon 1301 mole fraction is plotted as a function of nominal halon 1301 mole fraction estimated using the measured pressure drop. The solid line represents perfect agreement.

modifications would lead to the desired measurement capability, it would be impossible to guarantee success. Any future decision to continue further development of this type of probe must keep this in mind.

### 11.3 Evaluation of Infrared Sensing For Rapid Measurement of Halon Replacement Chemicals

**11.3.1 Background.** As discussed in Section 11.1, there is a need for monitoring the concentration of potential halon replacement chemicals with millisecond response time. One scenario of great concern to the sponsors is the penetration of an enemy shell into the fuel tank of an aircraft. To prevent structural damage to the aircraft wing or fuselage to the point where the plane would crash, the sponsors and NIST consider it crucial that the fire extinguishing agent be distributed throughout the interior region surrounding the fuel tank, the so-called dry-bay, in less than 30 ms. The existing instrumentation for monitoring the concentration of halon 1301, including the Statham analyzer and the Halonyzer (Yanikoski, 1952), have response times on the order of 200 ms or longer. Clearly they are not capable of monitoring the spread of the agent in a dry-bay type environment. So there is the need for a much faster time response instrument for monitoring potential halon replacement chemicals. The design goal is an instrument with a response time of 1 ms that could be used with a variety of fire suppression agents over a concentration range from 1 % - 20 % with an accuracy of  $\pm 10$  % of the nominal value. The Fire Extinguishing Agent Sensor (FEAS) was developed by John Brown Associates (Brown and DeStefano, 1992) to provide a fast time response instrument capable of detecting the presence of an agent. The original intention of the current study was to test the FEAS and determine its suitability for field measurement of agent concentration. The scope of the project was broadened with the sponsors' agreement to include redesign and testing of a modified instrument. The report includes calibration results of the improved device and field testing of the unit at Wright-Patterson AFB.

**11.3.2 Description of FEAS.** The FEAS sensing head illustrated in Figure 43 contains an incandescent wire as the infrared (IR) source behind a germanium window, a sensing gap of about 3 cm, a narrow bandpass IR filter, a pyroelectric detector, and an operational amplifier to couple the detector signal to a data collection console. Six detector heads can be run from a single power supply unit which provides  $\pm 15$  V dc for the detector and amplifier and a separate AC power supply for the incandescent wires. The narrow-pass IR filter has a peak transmission of 73 % at a wavelength of 8.2  $\mu\text{m}$ ; the transmission drops to 50 % of the peak value at wavelengths of 8.116  $\mu\text{m}$  and 8.231  $\mu\text{m}$ . This wavelength range corresponds to strong absorption bands of fire-extinguishing agents containing carbon-fluorine bonds.

The basic idea of an IR absorption measurement is that the flux of IR radiation is reduced as the agent concentration is increased. Standard IR detectors yield a signal directly related to the IR flux. So a high flux would give a high signal and a lower flux resulting from increased IR absorption from the agent would produce a lower signal. A key concept behind the FEAS is the use of a pyroelectric detector. Such a detector produces no signal for a steady source intensity independent of whether the IR flux is strong or weak. Instead the detector responds to changes in the IR radiation reaching the detector. Potential advantages of this type of detector are immunity to ambient light levels or slow drifts, and a chopper with associated electronics is not required. Below we present a more detailed description of the phenomenology of the pyroelectric detector and the mathematical relationship between the detector output and the IR intensity. The reader interested in the calibration results only may skip to Section 11.3.2.5.

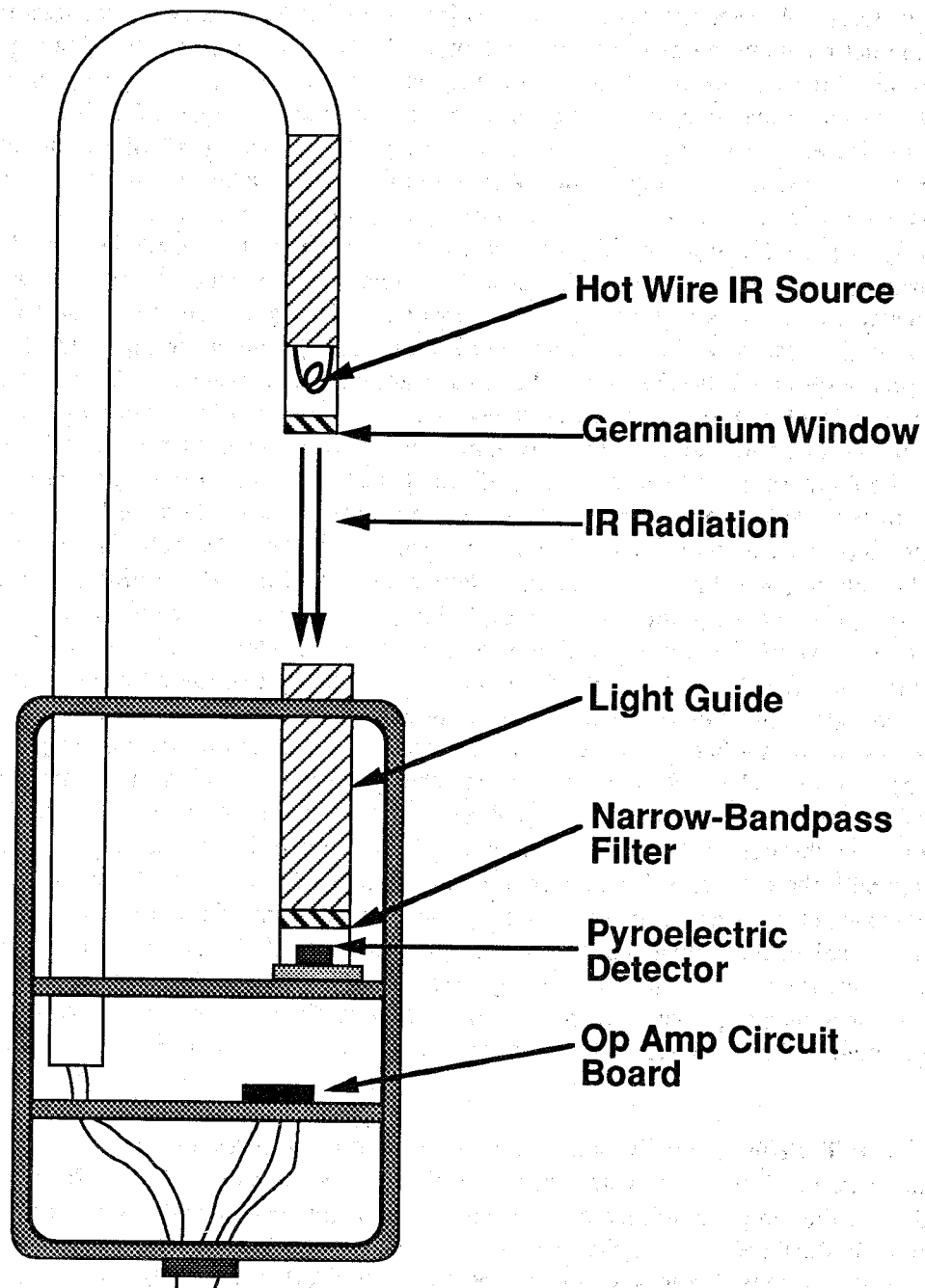


Figure 43. Schematic of the sensing head of the Fire Extinguishing Agent Sensor (FEAS).



**11.3.2.1 Phenomenology of a Pyroelectric Sensor.** A pyroelectric material is an electric analog to a magnetic material. A magnetic material such as iron or nickel has a large magnetization, which is a measure of the net magnetic moment per unit volume. The "atomic magnets" (originating from the unpaired electrons of the iron or nickel atoms) are aligned in one direction leading to a strong magnetic field. As the temperature of the magnetic material increases, the field from the magnet and its magnetization decrease due to thermal motion breaking up the alignment of the magnetic domains until it reaches zero at the Currie temperature. Above the Currie temperature, the magnetization is zero. For a pyroelectric material, the center of positive and negative charges in each unit cell of the crystal is slightly displaced leading to a dipole moment. In analogy to the magnetic case, the polarization, which is the electric dipole field per unit volume, is temperature dependent. As the temperature changes, there are slight changes in the positions of the atoms in the crystal lattice resulting in a change in the polarization (Putley, 1970; Lang, 1974). However, an external electric field is not normally observed, because stray charges are attracted and trapped on the surface until the surface charge associated with the polarization is neutralized. The charge distribution produced in this way near the surface of an insulator is relatively stable, unable to respond quickly to sudden changes of the internal dipole moment. When there is a sudden change in temperature of the material resulting from a change in the intensity of radiant energy absorbed by the material, there will be a variation in the polarization, and this will result in an observable electric field at the detector surface. So even though the polarization is not directly observed, its temperature coefficient,  $p = dP/dT$ , is observable. The material used in the FEAS pyroelectric sensor,  $\text{LiTaO}_3$ , has a pyroelectric coefficient at 25 °C of  $6 \times 10^{-9} \text{ C cm}^{-2} \text{ K}^{-1}$ , where C refers to Coulombs. For a 5 mm diameter detector, a  $1 \mu^\circ\text{C}$  temperature generates a charge of  $1.2 \times 10^{-15} \text{ C}$ , which can be measured with state-of-the-art electrometers.

Figure 44 provides a schematic representation of how a pyroelectric detector functions. The IR radiation impinges on the surface of the pyroelectric where it is absorbed by the thin (typically on the order of 20  $\mu\text{m}$ ) detector. The heating of the detector changes the polarization of the material leading to an excess of positive charge on one surface and negative charge on the other. To neutralize the charge, current flows through an RC circuit, where the resistance and capacitance represent the combined values for both the device itself and a preamplifier. The values of  $R$  and  $C$  determine the electronic time constant,  $\tau_e = RC$ , which is generally much smaller than the thermal time constant for the device. If the radiant flux remains constant, the temperature reaches a steady-state value and the current decreases toward zero. This is why the pyroelectric device will not respond to a steady source. It is only useful for a changing source intensity. To show how the instrument output can be related to the radiant flux incident on the device, the appropriate heat-transport modelling is discussed in the next section.

**11.3.2.2 Heat Transfer for a Pyroelectric Sensor.** The pyroelectric device is a thin plate of material on the order of 20  $\mu\text{m}$  thick with a heat capacity  $H$ . As the radiant flux is absorbed by the pyroelectric device, the temperature increase is determined by the heat capacity of the plate together with the thermal conductance  $G$ . The thermal conductance includes both conductive losses through leads to a heat sink and radiative losses. From a heat balance (Putley, 1970) the following equation is obtained for a time-dependent radiant source  $\phi(t)$ :

$$\phi(t) = H \frac{d\Delta T}{dt} + G \Delta T \quad , \quad (25)$$

where  $\Delta T$  is the plate temperature minus the temperature of the heat sink. One can see from Equation (25) that if the rate of temperature change is fast enough, and the magnitude of the change is small,

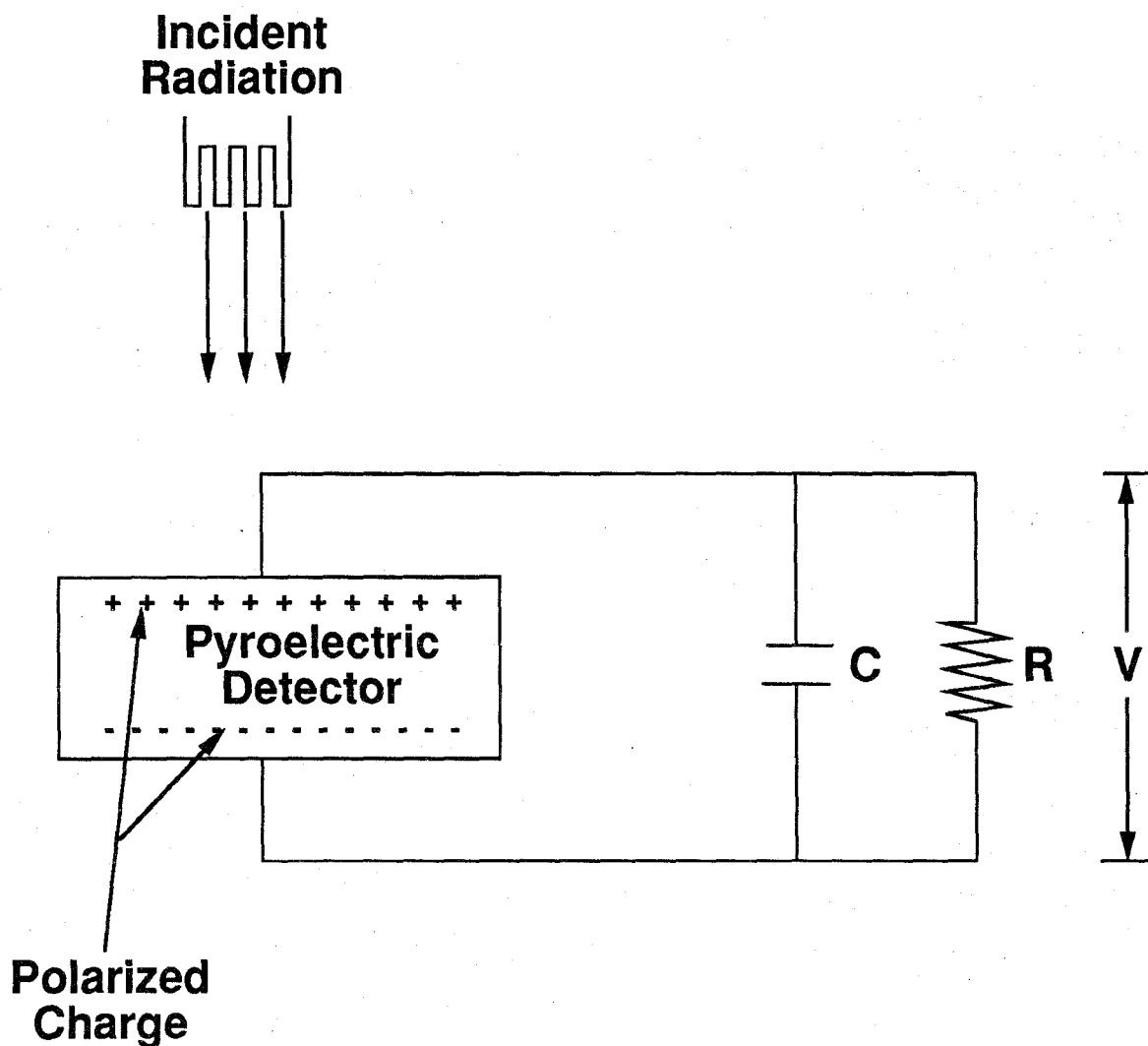


Figure 44. Illustration of the operating principle for a pyroelectric sensor. The changing incident radiation heats the sensor leading to a polarization of the charge on the device. The output signal is taken from the voltage drop across a resistor.

the heat-conductance term can be ignored relative to the heat-capacity term. Under these conditions the rate of change of the temperature is directly proportional to the source intensity,  $\phi(t)$ . Furthermore, the rate of change of the temperature difference is directly related to the pyroelectric current  $i$ ,  $dq/dt$ , via the following equation involving the pyroelectric temperature coefficient:

$$i = pA d\Delta T/dt \quad (26)$$

$A$  is the surface area of the sensor. In this limit of negligible heat conductance, the pyroelectric current provides a direct measure of the time-dependent source intensity. A limitation of the pyroelectric device is also evident from Equations (25) and (26). For a steady source intensity  $\phi$ ,  $\Delta T$  is constant and the current vanishes. So, as pointed out above, the pyroelectric device by itself is not useful for monitoring the radiant output of a constant source.

Below the heat transfer equation is solved for two assumed source-intensity time behaviors. The first is for a Gaussian pulse in order to assess the range of conditions for which the second term on the right-hand side of Equation (25) can be ignored. The second is a harmonic time-dependent source, which is important in the design of the new IR absorption-type instrument to be described subsequently.

**11.3.2.3 Response to a Gaussian Thermal Pulse.** To make the previous discussion quantitative, we consider the specific case of a Gaussian source intensity  $\phi(t)$  with half width  $\tau_s$  and peak intensity  $\phi_0$ ,

$$\phi(t) = \phi_0 \exp[-(t/\tau_s)^2] \quad (27)$$

Solving the linear differential equation given by Equation (25) for the source intensity given by Equation (27), we obtain:

$$\Delta T(t) = \frac{\phi_0}{H} \tau_s \exp[1/4(\tau_s G/H)^2 - Gt/H] \int_{-\infty}^{\beta} \exp(-w^2) dw \quad (28)$$

where the integration limit  $\beta$  is given by:

$$\beta = \frac{t}{\tau_s} - \frac{\tau_s G}{2H} \quad (29)$$

Computing the differential  $d\Delta T/dt$  we obtain:

$$\frac{d\Delta T}{dt} = \frac{\phi_0}{H} \exp[-(t/\tau_s)^2] - \frac{\phi_0 \tau_s}{H \tau_T} \exp[1/4(\tau_s/\tau_T)^2 - t/\tau_T] \int_{-\infty}^{\beta} \exp(-w^2) dw \quad (30)$$

where the thermal time constant  $\tau_T$  is equal to  $H/G$ .

It can be seen from Equation (30) that for a pulse width much smaller than the thermal relaxation time, the first term in the equation will be larger than the second for small values of reduced time. This is true since the exponential terms and the Gaussian integral will be of order unity for these conditions. This result confirms the intuitive explanation given above for why the rate of temperature change is proportional to the radiant source for a fast enough rate of temperature change. A

quantitative comparison of the rate of change of the temperature and the source function for a wide range of conditions is shown in Figure 45. The results are presented for a thermal time constant of 500 ms and for  $\tau_s$  values of 10 ms, 30 ms, 100 ms, and 250 ms. The plots are expressed in terms of a reduced rate of temperature change,  $(d\Delta T/dt)_r$ , and reduced time,  $t_r$ , defined as:

$$(d\Delta T/dt)_r = \frac{H}{\phi_0} \frac{d\Delta T}{dt} \quad (31)$$

and

$$t_r = t/\tau_s \quad (32)$$

This choice of variables allows direct comparison of time dependencies of the source intensity and the rate of change of temperature. The agreement is good for pulse half widths of 30 ms or less, and the difference becomes greater for the longer times. At 100 ms, the difference in the peak heights is 17 %. So the proportionality between source intensity and rate-of-temperature change is quantitative only in the limit of small pulse widths.

The analysis presented above is really only half the story. The other half concerns the electronics used to characterize the response of the detector. An important question is: How fast can the electronics respond to a temperature change? A measure of the electronic time response of the sensor is the effective  $RC$  time constant (see Figure 44). The approximate values of the capacitance and resistance of the pyroelectric device used in the FEAS were 75 pF and  $1 \times 10^8 \Omega$ , respectively, leading to a time constant of 7.5 ms. The useful operation range therefore corresponds to times less than 100 ms set by the thermal response and times longer than 20 ms set by the electronic cutoff. This is a rather narrow window of operation.

**11.3.2.4 A Periodic Source Intensity.** It is of interest to consider the response of the pyroelectric device to a periodic signal for two reasons. First it is convenient to test the FEAS performance by using a chopper. Secondly, a chopper is used in a new IR absorption type instrument developed in this study. The analysis given below is similar to Putley's study (1970).

Equation (25) is solved for the following harmonic source:

$$\phi(t) = \phi_0 e^{j\omega t} \quad (33)$$

where  $j$  equals  $(-1)^{1/2}$ . After solving Equation (25) by standard linear differential equation analysis, we take the time derivative and obtain the following expression for long enough time that transients have died out:

$$\frac{d\Delta T}{dt} = \frac{j\omega \phi_0 e^{j\omega t + j\theta}}{G(1 + \omega^2 H^2/G^2)^{1/2}} \quad (34)$$

where  $\theta$  is the phase angle between the harmonic source and the resulting rate of temperature change wave form, which is expressed as

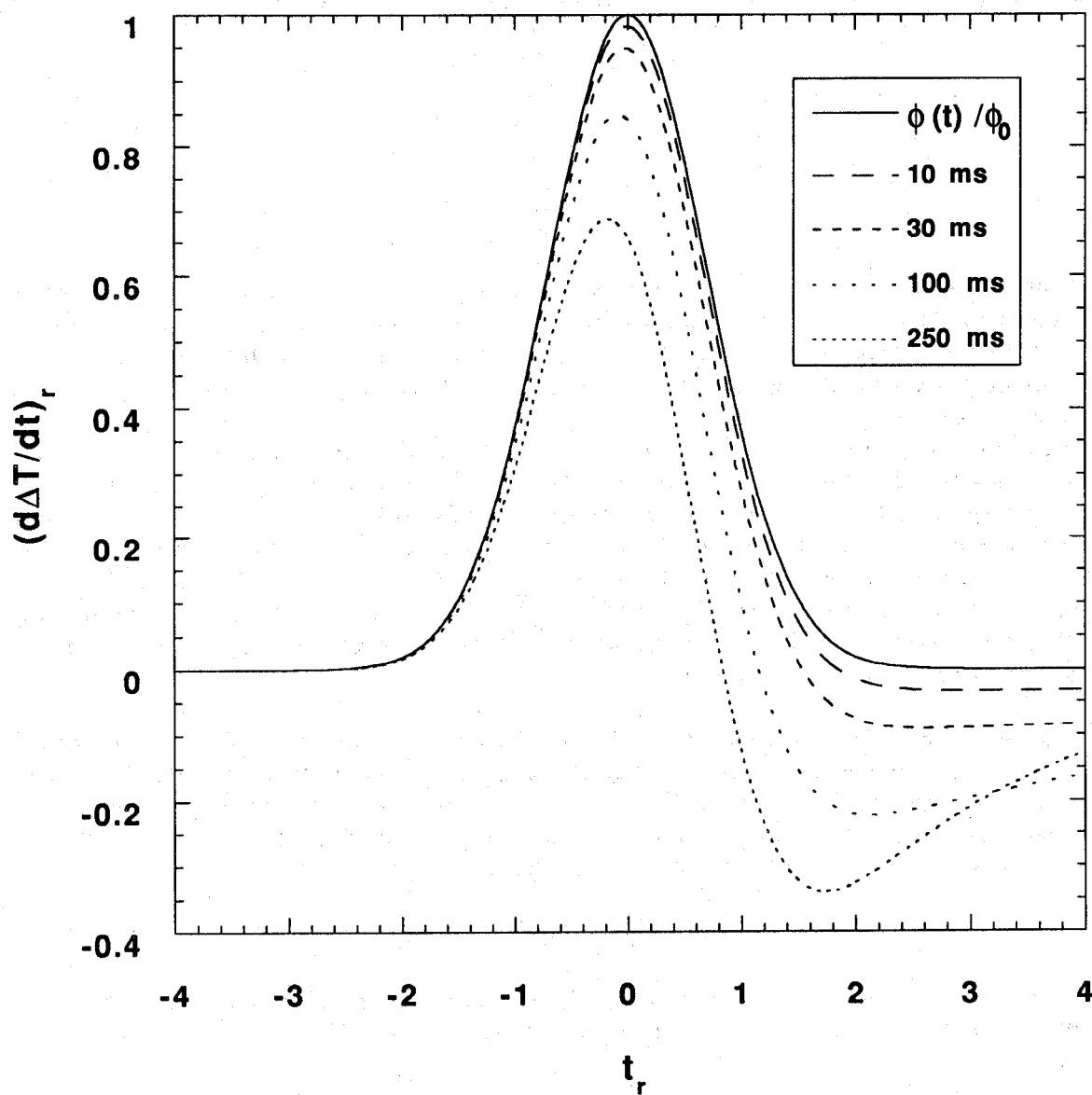


Figure 45. Reduced rate of temperature rise is plotted versus reduced time,  $t/\tau$ , for a thermal relaxation time of 500 ms for various pulse widths. The solid line is the source function.

$$\tan^{-1}\theta = \omega H/G \quad (35)$$

This time-varying temperature produces a time-varying current obtained from Equations (24) and (34) as:

$$i = \frac{j\omega p A \phi_0 e^{j\omega t + j\theta}}{G(1 + \omega^2 H^2/G^2)^{1/2}} = i_0 e^{j\omega t} \quad (36)$$

where  $i_0$  is the combination of terms multiplying the exponential time dependent term.

What is ultimately measured is the voltage, which can be deduced from the circuit illustrated in Figure 44 which has a capacitance and resistor in parallel. Using Kirchhoff law, the current from the pyroelectric element is equal to the sum of the currents through the capacitor and resistor:

$$C \frac{dV}{dt} + \frac{V}{R} = i_0 e^{j\omega t} \quad (37)$$

This differential equation is of the same form as the thermal equation given by Equation (25). Solving by the same method we obtain the following expression for the voltage:

$$V = \frac{i_0 R e^{j\omega t + j\theta_1}}{(1 + \omega^2 R^2 C^2)^{1/2}} \quad (38)$$

where

$$\tan^{-1}\theta_1 = \omega RC \quad (39)$$

The performance of the pyroelectric device is often expressed in terms of its responsivity,  $R_v$ , which is the amplitude of the signal divided by the source intensity flux  $\phi_0$ . From Equations (36) and (38), we obtain:

$$R_v = \frac{\omega p A R}{K(1 + \omega^2 H^2/K^2)^{1/2} (1 + \omega^2 R^2 C^2)^{1/2}} \quad (40)$$

In Figure 46, the reduced responsivity,  $R'_v = R_v/pAR$ , is plotted versus  $\omega$  for a thermal time constant equal 0.5 s and  $RC$  time constant equal 10 ms. We see that for small  $\omega$ ,  $R'_v$  increases with  $\omega$ , becomes flat around 5 Hz due to the 0.5 s thermal relaxation time constant, remains flat to about 50 Hz, above which the 10 ms time constant for the electronic circuit leads to a  $1/\omega$  dependence. Of course, the ideal system would have a flat frequency response to more than 1000 Hz. In the next section we present the measured frequency response of the FEAS Instrument.

**11.3.2.5 Characterization of FEAS Performance.** First a qualitative test was carried out to determine whether the FEAS would respond to an agent release. Using the same facility as was previously used for measuring agent dispersion (Pitts *et al.*, Section 3.5, 1994), 189 g of  $C_3HF_7$  (HFC-227ea) were released towards a pressure transducer and 3 FEASs located near the floor, 1.3 m from the release point. The pressure transducer was directly below the discharge point while the

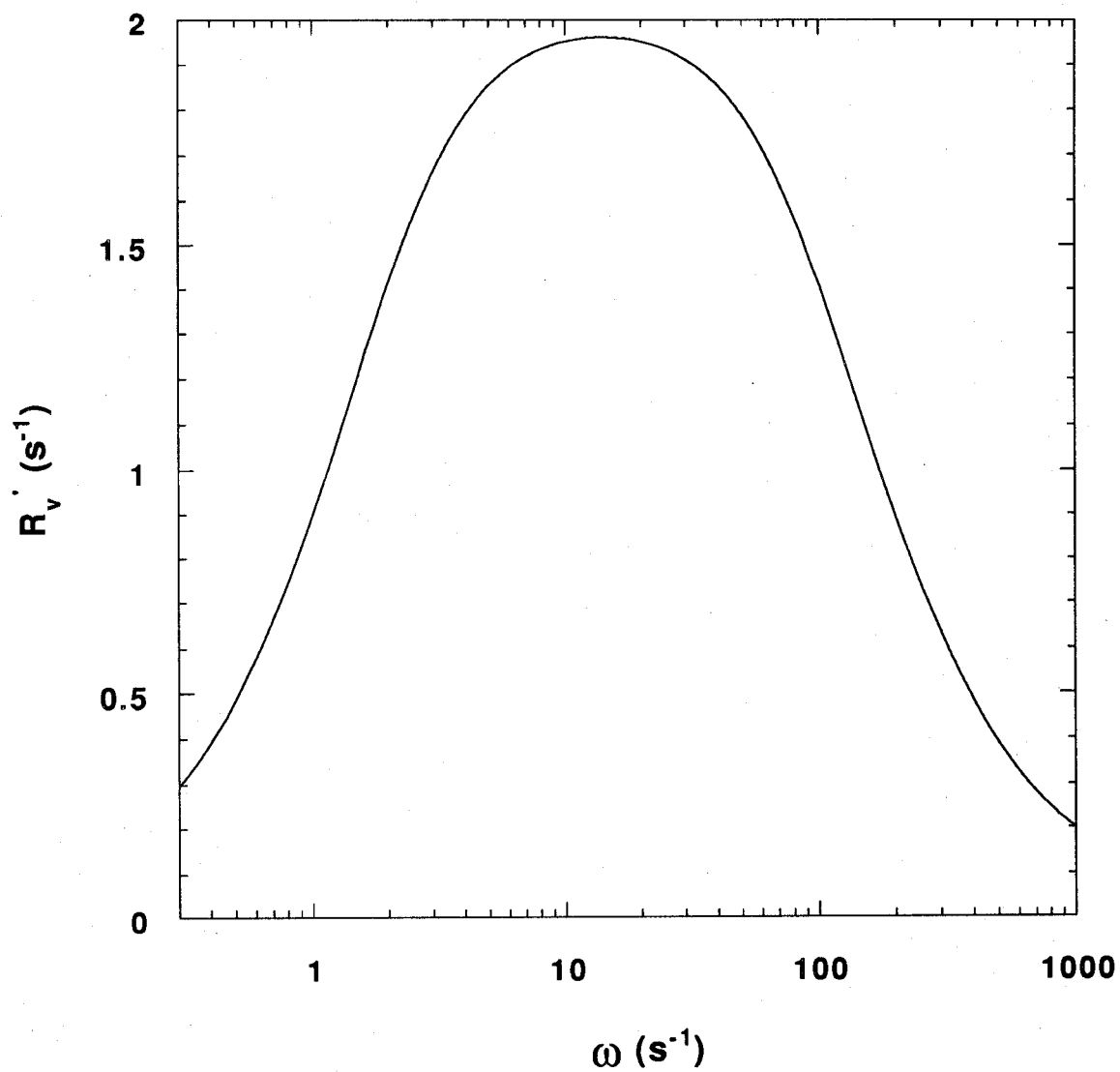


Figure 46. Plot of the frequency response of the reduced responsivity function,  $R'_v$  for a thermal time constant = 0.5 s and  $RC$  time constant = 10 ms.

FEASs were about 60 cm off the centerline. The response of one of the three units is shown in Figure 47. Two spikes are observed in the voltage output shortly following the agent release at 0 s. The first spike reaches 10 V at about 20 ms. This can be compared to a time of about 30 ms for which the pressure transducer output peaks. The time interval between the narrowly spaced saturation readings of the FEAS is approximately 20 ms compared to a 30 ms release time obtained from a pressure transducer reading in the release vessel. Two characteristics of the FEAS signal are the large noise, on the order of 2 V, and the saturation of the output. It is not known whether the peaks around 200 ms are artifacts or not.

The performance of the FEAS was evaluated by measuring the instrument response as a function of frequency. A chopper was positioned between the source and the detector. It was necessary to replace the  $10\,000\times$  amplifier in the FEAS with a  $100\times$  amplifier to avoid saturation of the output signal. The output from the amplifier was read with an oscilloscope triggered on the chopper. A typical plot of peak-to-valley voltage versus frequency is shown in Figure 48. There is a peak in the frequency response at about 10 Hz and then a decrease with increasing frequency with a five-fold reduction in signal at 75 Hz. However, based on the analysis in the previous section, a flat frequency response over the frequency range of interest is required to relate the instrument output to the change in radiant flux.

To obtain a flatter frequency response, an  $18\text{ M}\Omega$  resistor was added in parallel with the  $100\text{ M}\Omega$  load resistor of the pyroelectric sensor in order to reduce the overall resistance to  $15.3\text{ M}\Omega$ . Equation (40) predicts that a decrease in the output resistance will flatten the detector's frequency response. The frequency responses with and without the added resistor are plotted in Figure 49. With the added resistor the frequency response is relatively flat out to a frequency of 450 Hz, with about a factor of two decrease in signal over this frequency range. Without the added resistor, there is about a 15-fold reduction in signal as the frequency is increased from 10 Hz to 450 Hz. There is a penalty to pay in using a lower resistance. The output signal is lower. According to Equation (40), the responsivity is proportional to the resistance. So the output signal with the reduced resistance is flatter but it is also smaller, especially at the lower frequencies.

We summarize the FEAS performance and its potential for improvement. The modelling indicates that semi-quantitative results can be obtained for time scales fast compared to the thermal time constant,  $H/G$ , and slow compared to the electronic time constant,  $RC$ . Operationally it is possible to improve the time response by decreasing the load resistance. Still the response is not perfectly flat. Even a slight deviation can be significant, because, as we show below, the relation between voltage and concentration is non-linear so that even a few percent change in signal could correspond to a change in concentration from 10 % to 20 %. Another problem is the calibration of the device, which would require changing both the concentration and the rate at which the concentration is changed. The great advantage of the device is its simplicity. It could be useful for qualitative applications, but it does not meet the requirements of accuracy and time response needed for a satisfactory instrument for monitoring the agent concentration in a dry bay. Below an alternative design is presented which is more quantitative, responds faster, and is easier to calibrate.

### 11.3.3 Description of An Improved Differential Infrared Rapid Agent Concentration Sensor (DIRRACS)

**11.3.3.1 Design Improvements.** The existing FEAS, even with a modified amplifier and added resistor, was shown to be unsatisfactory for making quantitative concentration measurements with a time response of a few milliseconds. The basic idea motivating the new design was to add an optical chopper, which was operated at high enough frequency to obtain the desired time response. This method of collecting data at a fixed frequency has the following major advantages:



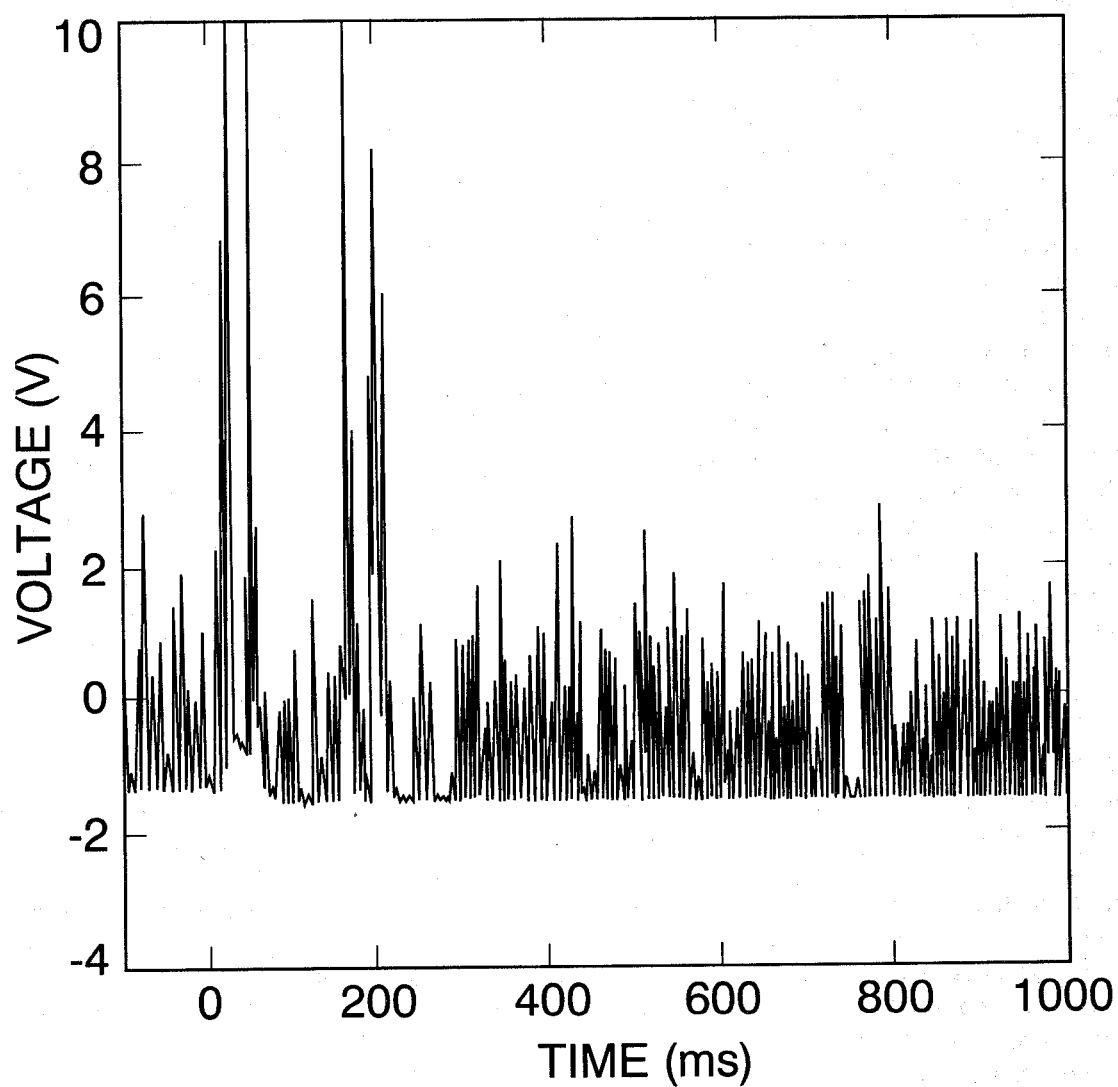


Figure 47. The response of a FEAS to a release of 190 g of HFC-227ea. The FEAS was located 1.3 m below the release point and about 0.6 m off the centerline.

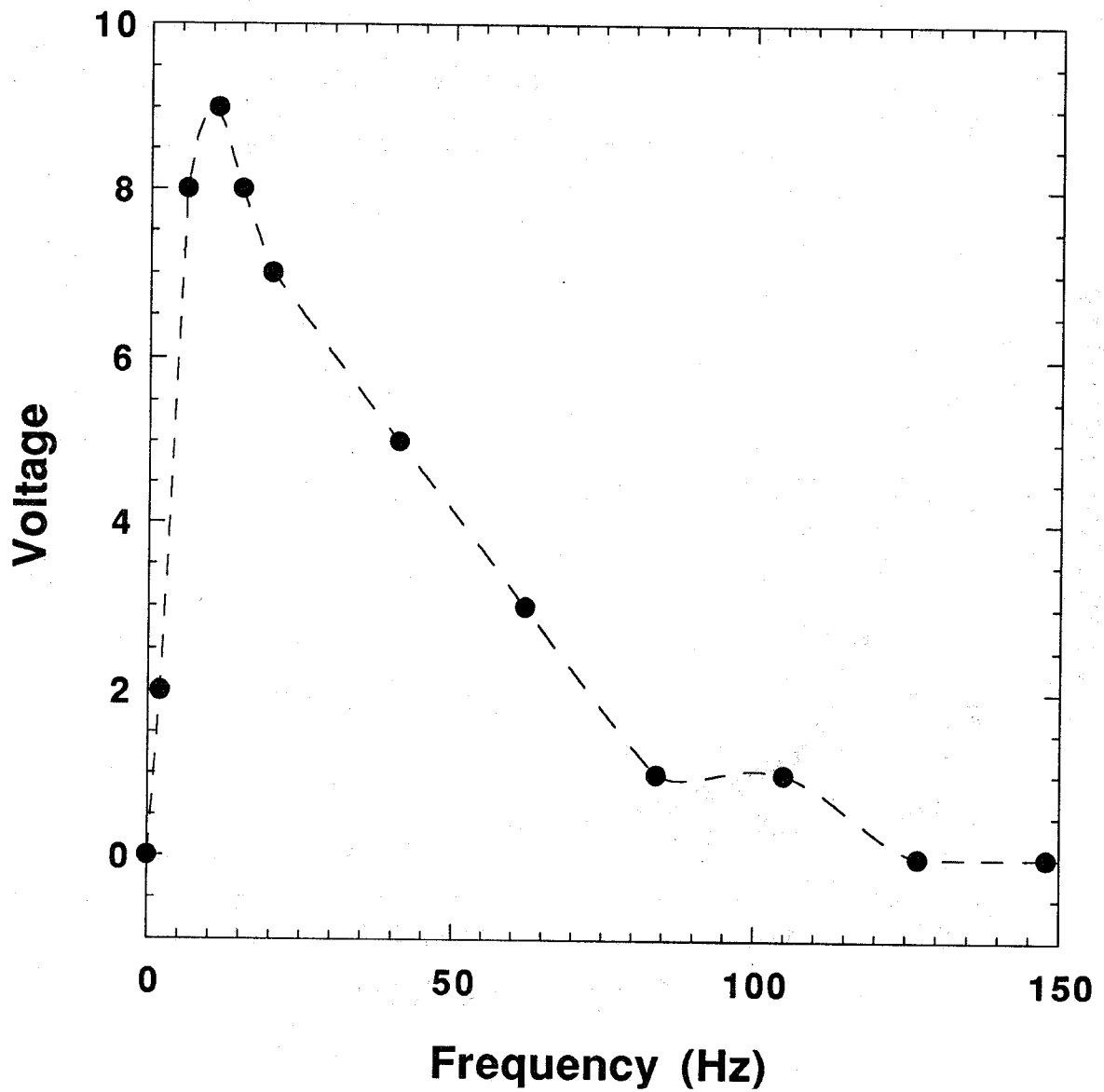


Figure 48. Frequency response of the FEAS measured in air using an optical chopper.

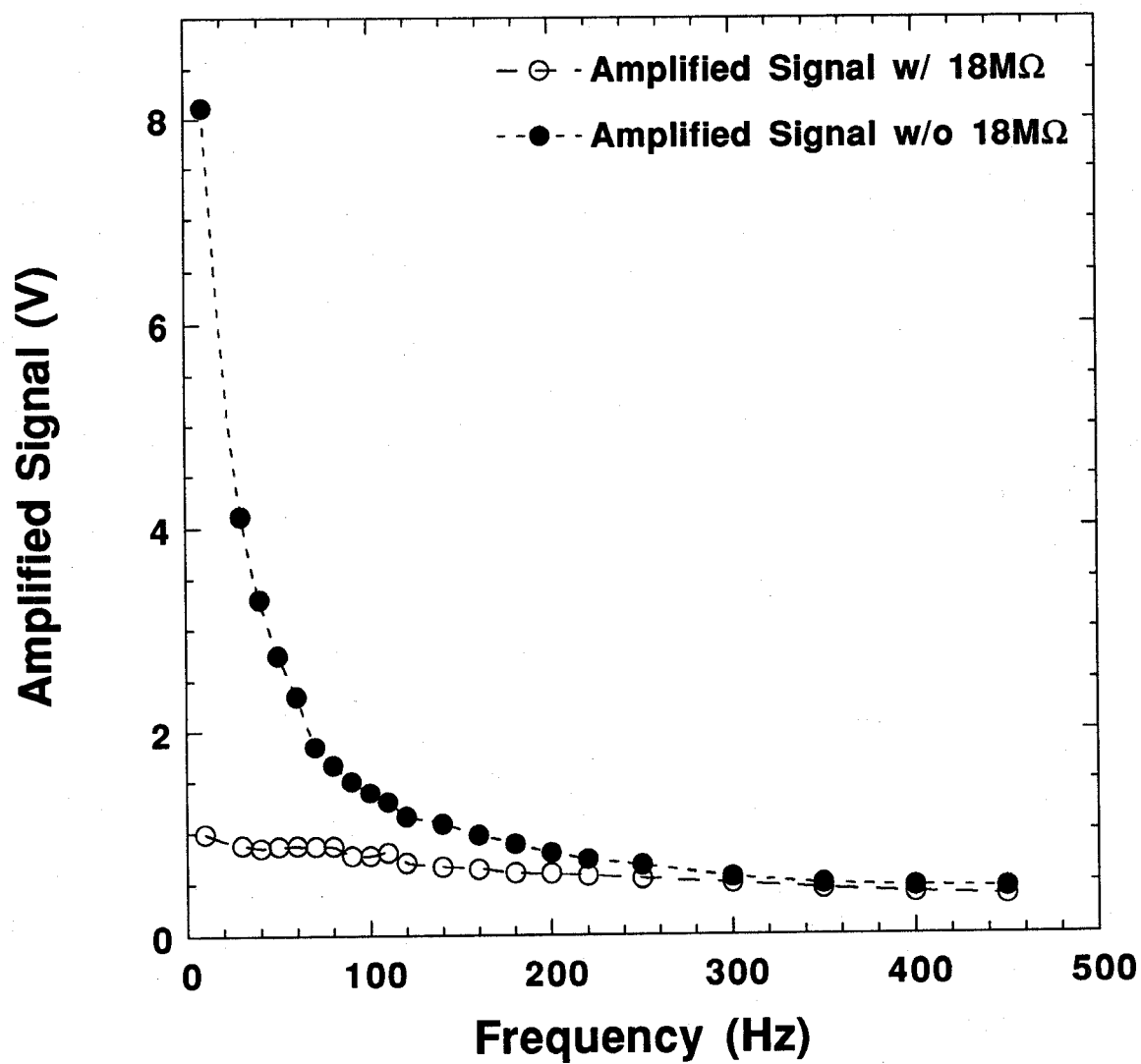


Figure 49. Frequency response of the FEAS for two overall output resistances differing by a factor of 6.5. An 18 MW external resistor is used to lower the overall output resistance.

1. Calibration data need only be collected for one frequency.
2. The signal-to-noise ratio can be increased by use of a single frequency.
3. There is no need for the pyroelectric detector to have a flat frequency response.

In order to obtain a good signal-to-noise ratio at 1000 Hz it was necessary to increase the radiant flux reaching the detector beyond that available in the FEAS. This was accomplished by increasing the size of the source, increasing the width of the IR band pass filter, and increasing the detector size. Below we provide a detailed description of the instrument design.

**11.3.3.2 Instrument Design.** An overall schematic of the Differential Infrared Rapid Agent Concentration Sensor (DIRRACS) is shown in Figure 50. All of the components of the device are listed in Appendix J. The instrument is designed so that the tube assembly can extend about 15 cm inside an engine nacelle or dry bay with the agent flowing through the 2.8 cm long test section located next to the IR source. For rigidity of design and alignment, the IR source chamber, sample volume, and IR transmission tube are assembled from a single 3.18 cm OD brass tube with a length of about 20 cm. A major design challenge was to assemble a system that could fit through a 1 1/4 inch NPT fitting into an engine nacelle simulator and allow monitoring of the agent near the nacelle wall.

The IR source was a 120 V cable heater. The 1.57 mm diameter element was coiled in a cylindrical shape to fit within the 3.2 cm long section of the 3.02 cm ID brass tube. An elliptical cross section was used to contain the 61 cm cable without allowing it to touch the brass housing. A 2.8 cm diameter ZnSe window was attached to the source housing with high temperature RTV. It was found during testing that the seal leaked and agent entered the source housing. To prevent this leakage of agent into the housing a small flow of nitrogen, on the order of 0.3 cm<sup>3</sup>/s, was fed into the housing. Flexible stainless steel tubing (1.6 mm diameter) such as is commonly used with gas chromatographs was silver soldered to the housing wall and was routed with the heater cables along the tube assembly and through the 1 1/4 inch NPT fitting. The nitrogen exited the source chamber through a 1 mm diameter hole in the end of the housing.

Next to the source was a 2.8 cm length of the brass tubing which had been milled out leaving four 6 mm wide segments to connect with the source housing. The agent flowed through this region during a test. The IR radiation passed through the sample region, through a 1 mm thick ZnS window, and then through an IR version of a light transmission tube with the light reflecting off the walls of the brass tube. The interior of the tube was cleaned with solvent and tissue to improve its reflectivity. The ZnS window was sealed with RTV to a retaining ring that had been soldered into the tube. In a later version of the DIRRACS, a wide-bandpass IR filter was added at the end of the IR transmission tube just before the chopper to remove IR radiation over the 10  $\mu$ m - 14  $\mu$ m range. A standard 1 1/4 inch pipe fitting was soldered to the brass tube for mounting purposes. Three small holes were drilled through the fitting for the nitrogen purge line and the heater cables.

The IR radiation then passed through the frequency-controlled optical chopper operating at 500 Hz. The IR radiation was filtered with a narrow band-pass filter, which passed radiation from 8.396  $\mu$ m to 8.913  $\mu$ m. This narrow wavelength range of radiation entered a conical collector, which focused the IR radiation onto the LiTaO<sub>3</sub> pyroelectric sensor with a 5 mm active diameter. The design of the collector is illustrated in Figure 51.

The electronics board with detector was attached directly to the collector. The pyroelectric detector has an FET built into the device. Additional amplification was provided by a 100  $\times$  low-noise amplifier designed for use in the DIRRACS. The circuit for the amplifier is shown in Figure 52. To further reduce noise, the voltage signal was passed through a low-frequency filter with 24 dB per octave filter set at about 300 Hz.

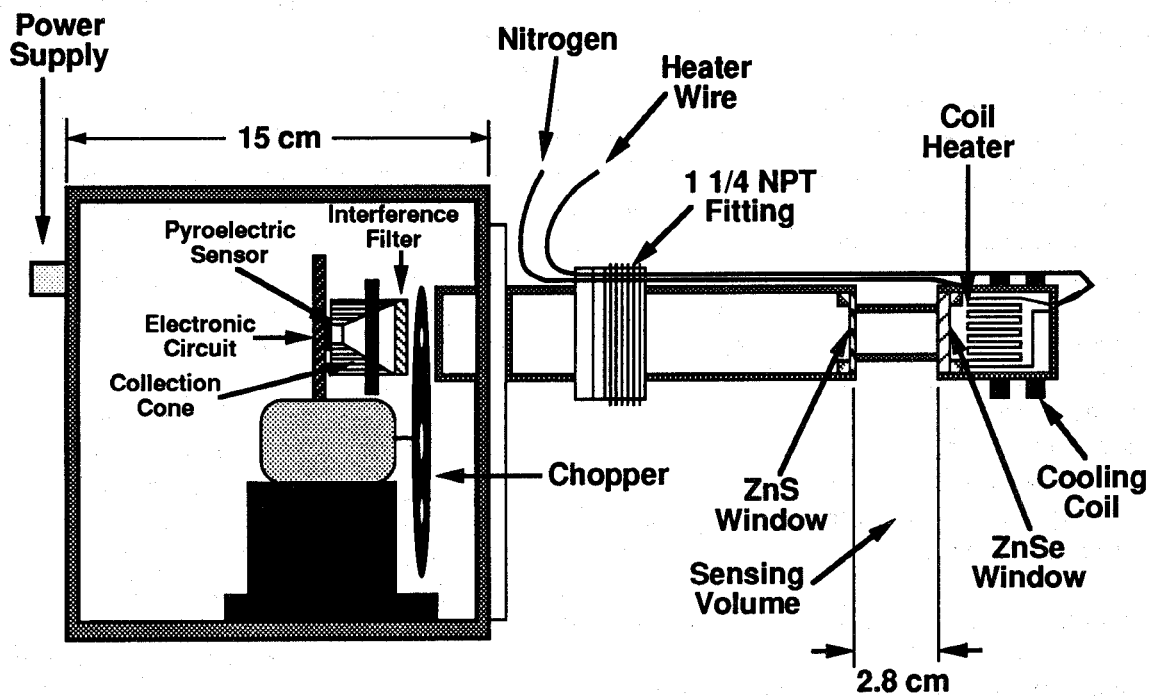


Figure 50. Overall schematic of the Differential IR Rapid Agent Concentration Sensor (DIRRACS).

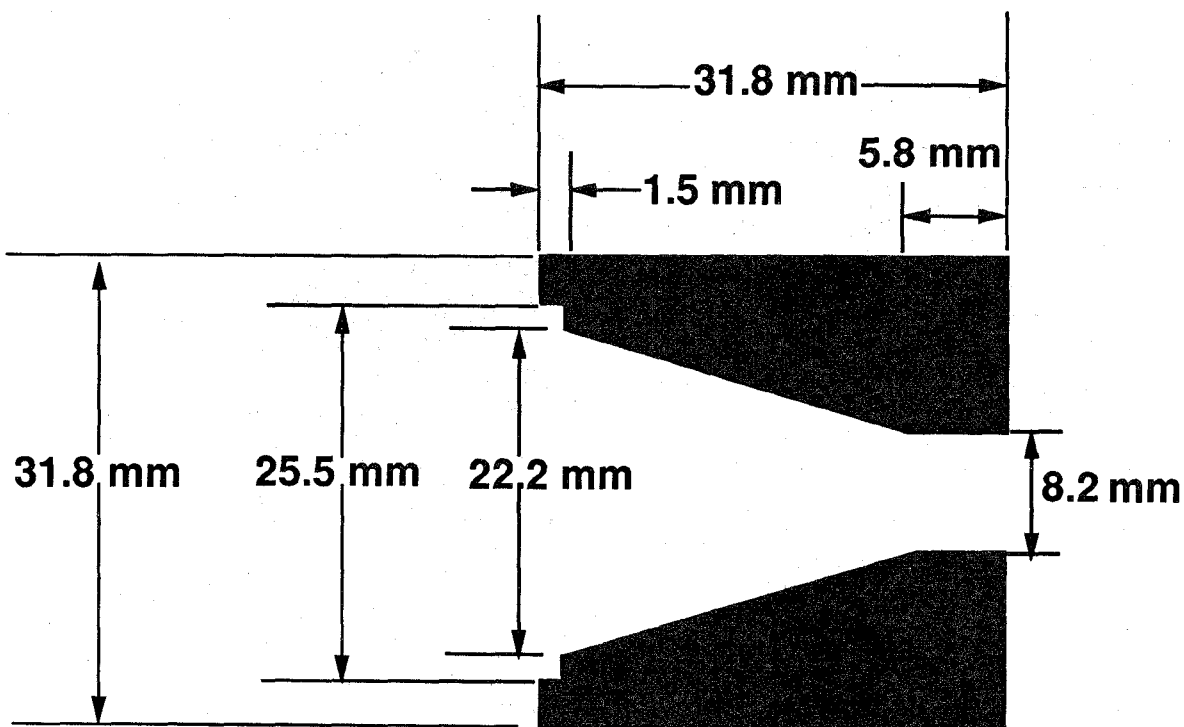


Figure 51. Design of collection cone for focussing the IR radiation from a diameter of 15 mm to about 8 mm. The cone was machined from brass with the narrow-bandpass filter attached at left and the detector inserted at the right.

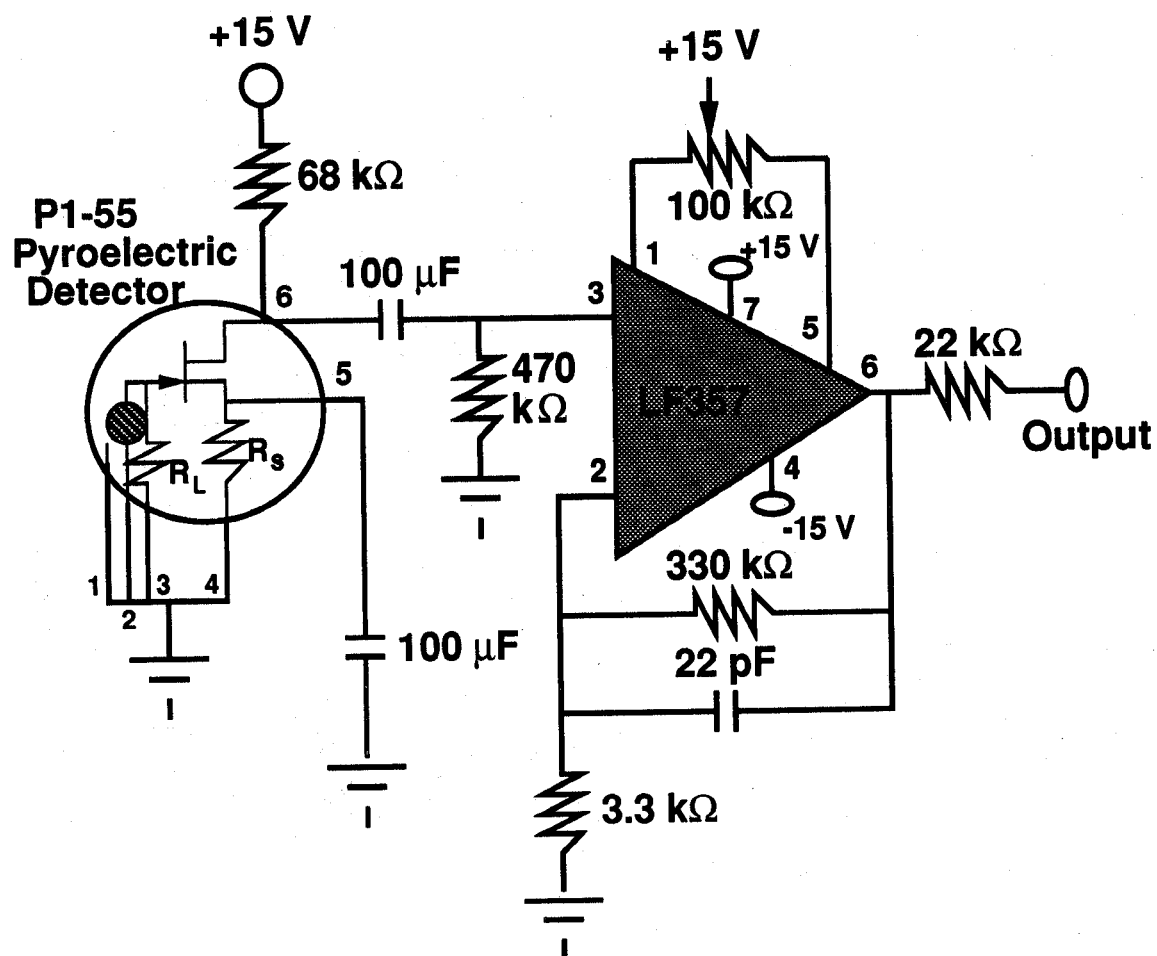


Figure 52. Design of the  $100\times$  low-noise amplifier used with the DIRRACS.

Two DIRRACS with nominally identical designs were fabricated and are referred to in the text as the "blue" and the "black" units for the color of the boxes housing the electronics and chopper.

**11.3.4 Theory of Operation.** A schematic of the optical system for the DIRRACS is shown in Figure 53. The radiation from the heated wire is emitted in all directions striking the ZnSe window with about 20 % reflection loss. Some fraction of the IR radiation is absorbed by the agent depending on the concentration and pathlength and is then transmitted through the ZnS window with reflection loss before passing through the transmission tube. The remaining optical components through which the IR radiation passes before reaching the detector are the wide-band-pass filter, chopper blade with a limiting slot size, narrow-band-pass filter, and conical collector. Each one of these optical components has losses that reduces the IR radiation reaching the detector.

The choice of optics was in large part an effort to increase the signal detected relative to the original FEAS device. The signal of the FEAS with the improved amplifier was measured at a chopper frequency of 500 Hz and was found to have a value of about 100 mV with a noise of roughly 20 mV. We increased the signal by about a factor of 20 to improve the signal-to-noise ratio. This increase was obtained by increasing the source size from 6 mm to 18 mm, increasing the width of the narrow-band-pass filter by a factor of 5, and increasing the diameter of the detector from 1 mm to 5 mm. The factor of 3 longer pathlength in the DIRRACS compared to the FEAS, the addition of a conical collector to focus the IR radiation on the detector, and the addition of a wide-band-pass filter were competing factors that reduced the IR flux in the DIRRACS relative to the FEAS. It was found empirically that these changes increased the signal to a value of about 1 V for one device and about 2 V for the second. By using a 300 Hz low-pass filter, the noise was 10 mV to 20 mV so that signal-to-noise ratios were typically about 100.

As the agent enters the sensing volume, the IR radiation is absorbed by the agent reducing the flux of radiation reaching the detector. The higher the concentration, the lower the flux reaching the detector. The IR spectrum of HFC-125 ( $\text{C}_2\text{HF}_5$ ) is plotted in Figure 54 for a concentration of  $6.3 \times 10^{-3}$  moles/ $\text{m}^3$  with a 10 m pathlength along with the spectrum of the narrow-band-pass filter. The HFC-125 spectrum was taken in a 10 m multipass cell at a partial pressure of about 16 Pa. It is seen that the region where the filter passes IR radiation is also a region of strong IR absorption by HFC-125. There is also strong IR absorption, resulting from C-F stretch vibrational modes, in the same spectral region for other agents with C-F bonds including HFC-227ea ( $\text{C}_3\text{HF}_7$ ), FC-218 ( $\text{C}_3\text{F}_8$ ), halon 1301 ( $\text{CF}_3\text{Br}$ ), and  $\text{CF}_3\text{I}$ . The spectra plotted in Figure 55 illustrate that both HFC-125 and halon 1301 have strong absorption features over the 8.4  $\mu\text{m}$  to 8.9  $\mu\text{m}$  wavelength region of the narrow-band-pass filter. The strong absorption peak in halon 1301 at 9.2  $\mu\text{m}$  corresponds to a symmetric stretch of the  $\text{CF}_3$  (symmetry type  $A_1$ , frequency assignment  $\nu_1$ ) (McGee *et al.*, 1952). While the absorption peak for halon 1301 is slightly outside of the wavelength range for the narrow-band-pass filter, the peak for HFC-125 is within the range of the filter. As discussed below, this leads to a greater sensitivity of the DIRRACS to HFC-125 relative to halon 1301. These are the two agents tested in this study.

The starting point for modelling the IR transmission through the agent is Bouguer's law, which relates the intensity of incident monochromatic light of wavelength  $\lambda$ ,  $I_\lambda^0$ , and the intensity of the radiation  $I_\lambda$  transmitted through a pathlength  $L$  of the agent,



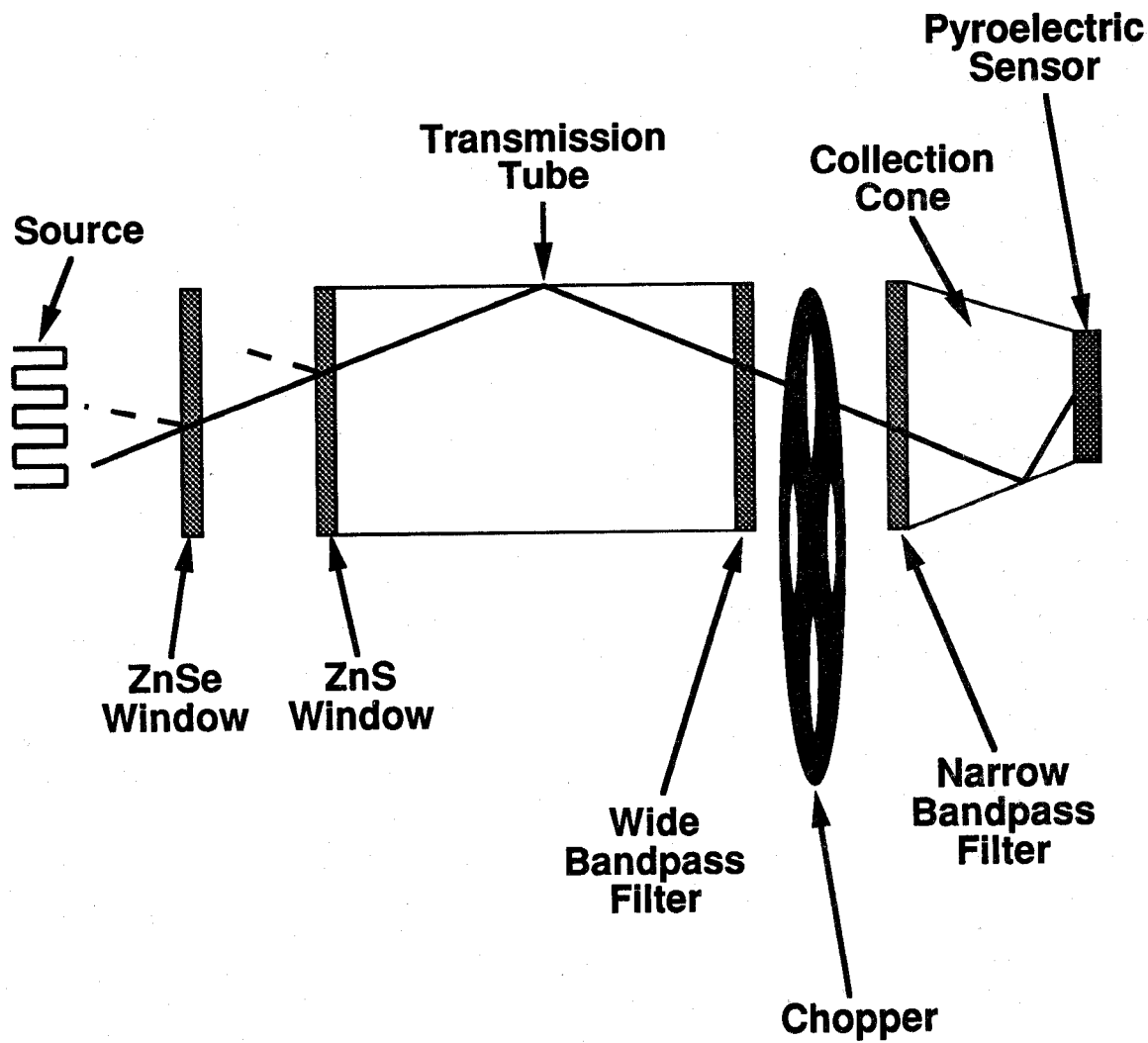


Figure 53. Schematic (not to scale) of the optical system of the DIRRACS. The dashed lines represent reflected IR radiation.

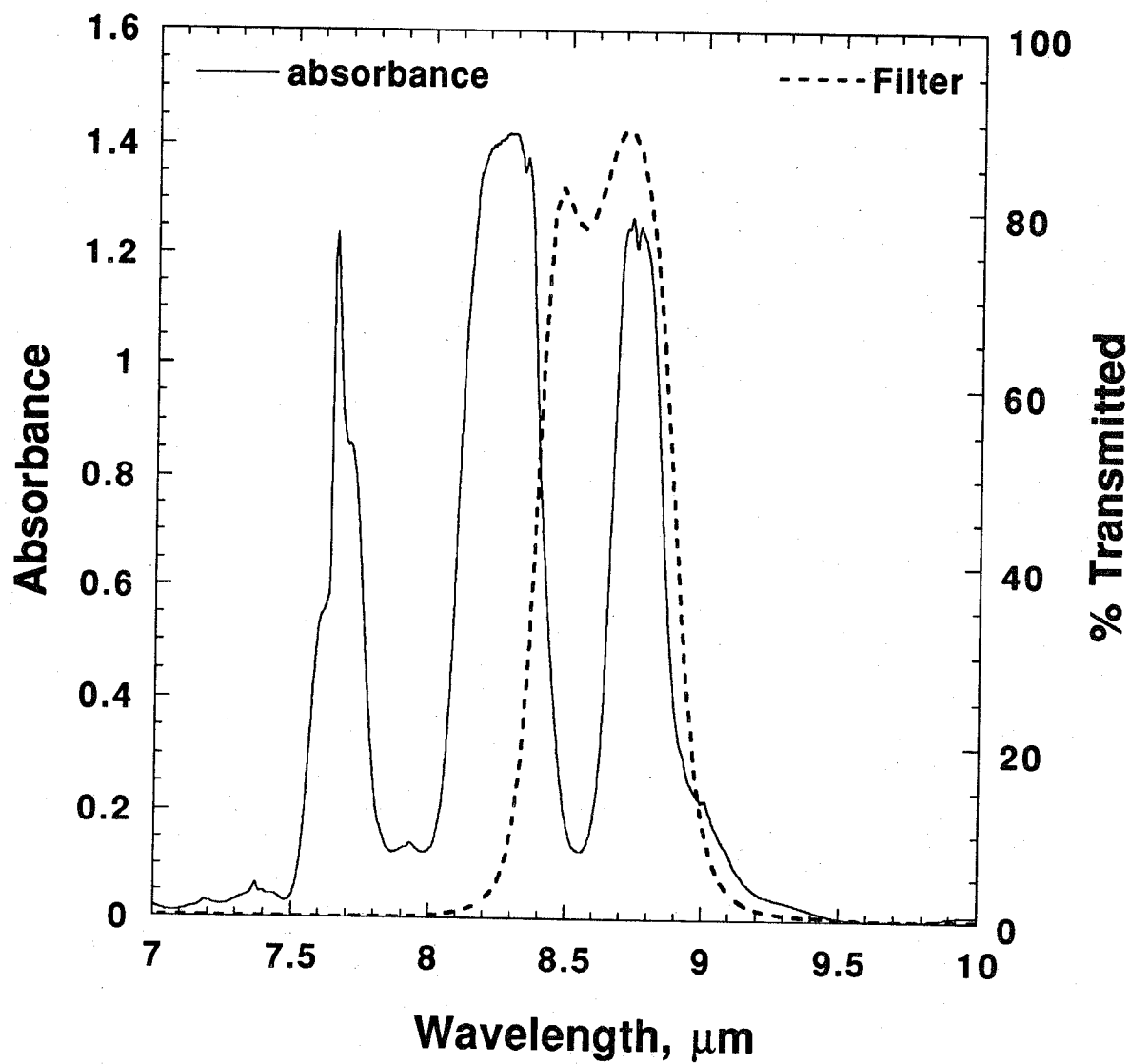


Figure 54. IR absorbance spectra of HFC-125 and of the narrow-band-pass filter.

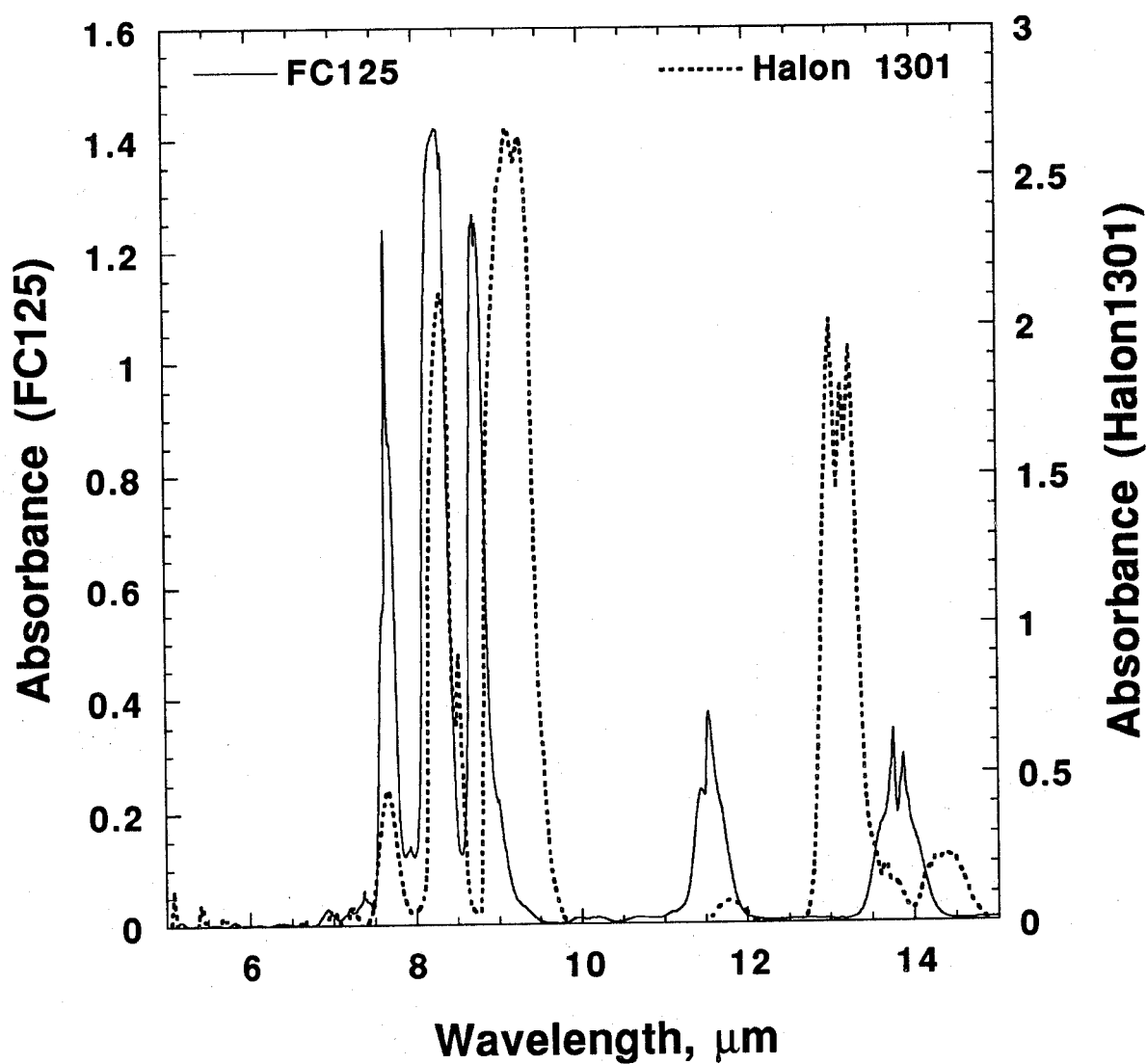


Figure 55. Absorption spectra are plotted for HFC-125 and halon 1301. Both agents have absorption features over the wavelength region of the narrow-band-pass filter (8.4  $\mu\text{m}$  - 8.9  $\mu\text{m}$ ).

$$I_{\lambda}/I_{\lambda}^0 = e^{-K(\lambda)CL} \quad (41)$$

where  $C$  is the molar concentration of the agent. The quantity  $K(\lambda)$  is the wavelength dependent absorption coefficient of the agent. The absorbance,  $A(\lambda)$ , is simply related to the transmittance,  $I_{\lambda}/I_{\lambda}^0$ :

$$A(\lambda) = -\log_{10}(I_{\lambda}/I_{\lambda}^0) \quad (42)$$

From Equations (41) and (42), we obtain the following relation between  $K(\lambda)$  and  $A(\lambda)$ :

$$K(\lambda) = \frac{2.3A(\lambda)}{CL} \quad (43)$$

We make use of this relation in deriving  $K(\lambda)$  from the absorbance measurements made for HFC-125 ( $C_2HF_5$ ).

The cable-heater IR source is approximated as a so called "blackbody" radiation source. The blackbody spectral radiance  $L_{\lambda}$ , which has the units of Watts per steradian, per cubic meter, is given by the following equation (Dereniak and Crowe, 1984):

$$L_{\lambda} = \frac{2hc^2}{\lambda^5(e^{\frac{hc}{\lambda kT}} - 1)} \quad (44)$$

In this expression  $h$  is Planck's constant ( $6.63 \times 10^{-34}$  W s<sup>2</sup>),  $c$  is the speed of light ( $3.00 \times 10^8$  m s<sup>-1</sup>),  $k$  is Boltzmann's constant ( $1.38 \times 10^{-23}$  W s K<sup>-1</sup>), and  $\lambda$  is the wavelength of light (m). In Figure 56 the spectral distributions are plotted for three temperatures including the estimated source temperature, 800 K, and the IR source housing temperature, 330 K. We see that while the higher temperature source has a greater radiance at all  $\lambda$ , the fractional increase is smaller as the wavelength increases.

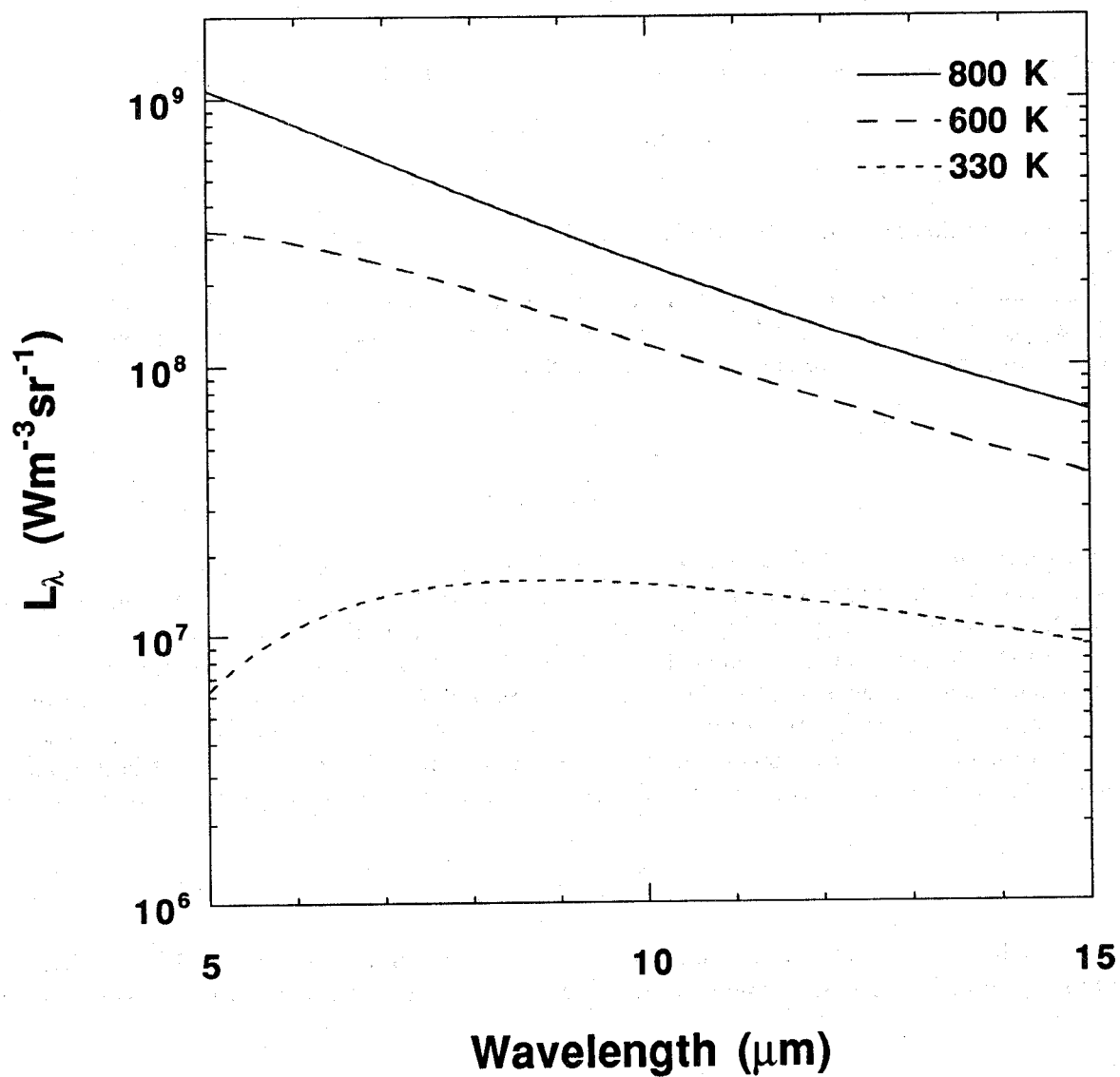
We are interested in estimating the effect of agent concentration on the radiant heat flux reaching the IR transmission tube. If the source diameter and the transmission-tube diameter are both small relative to the separation distance, the radiant flux incident on the window of the transmission tube is given by:

$$\Phi = L_{\lambda} A_s \Omega_d \quad (45)$$

where  $A_s$  is the cross-sectional area of the source and  $\Omega_d$  is the solid angle subtended by the transmission tube. The radiant intensity without agent present  $I_{\lambda}^0$ , defined as the flux per solid angle, is given by:

$$I_{\lambda}^0 = L_{\lambda} A_s \quad (46)$$

In our case, diameters of both the source and the transmission tube are comparable to the pathlength so that Equations (45) and (46) are not exact. A full treatment of this optical arrangement would involve integrating over both the source area and the cross section of the transmission tube. However, Equation (46) is a useful approximation for studying the effects of wavelength and temperature on the radiant intensity reaching the detector. Besides the source, the optical components most sensitive to the wavelength are the narrow and wide-band-pass filters. We use the quantity  $F(\lambda)$  to represent the

Figure 56. Effect of temperature on blackbody radiance  $L_\lambda$ .

combined wavelength dependent filter function for both filters. The windows, transmission tube, conical collector, and chopper affect the amount of radiation passing through the device, but are not very sensitive to wavelength.

Now it is possible to compute the total radiant intensity  $I_t$  reaching the transmission tube as a function of agent concentration. This involves integrating the expression for the transmitted intensity over wavelength. The following expression is obtained for the ratio of the total transmitted radiant intensity  $I_t$  with agent present to the intensity  $I_t^0$  in the absence of agent:

$$\frac{I_t}{I_t^0} = \frac{\int_{\lambda_1}^{\lambda_2} e^{-K(\lambda)CL} I_\lambda^0 F(\lambda) d\lambda}{\int_{\lambda_1}^{\lambda_2} I_\lambda^0 F(\lambda) d\lambda} \quad (47)$$

A FORTRAN program, which is listed in Appendix K, was developed to compute  $I_t/I_t^0$  based on Equation (47). The program returns the theoretical output of the device for a given concentration of agent. The program first reads in the filename for the blackbody absorbance of the agent, the agent concentration, the temperature, and the path length. Next, the program reads the filter transmittance and the absorbance as a function of wavelength. A conversion is made of the absorbance function from a basis of inverse centimeters to meters.

An integration loop with a step size of 0.01  $\mu\text{m}$  is started wherein three terms are calculated and combined to generate the light intensities transmitted through the agent and through air. The terms are an exponential term based on the agent concentration, an intensity term based on the wavelength, and a filter transmittance term also based on the wavelength. The wavelength is incremented each time through the loop. The filter function is indexed when its next wavelength-transmittance pair is applicable. Each term is calculated using the trapezoidal rule. The light intensity through the agent is calculated by multiplying the exponential, intensity, and filter terms by the wavelength step size and adding this to the previous sum. The light intensity through air is calculated by multiplying the intensity and filter terms by the wavelength step size and adding to the previous sum. When the integration loop is complete, the two intensity terms are summed and then divided to generate the fraction of light transmitted through the agent mixture relative to that which would have passed through air. The ratio is written to the screen as well as intermediate sums of the two intensities.

The integration was performed over the wavelength range from 5  $\mu\text{m}$  to 10  $\mu\text{m}$  for a pathlength of 2.8 cm. The calculated intensity ratio is plotted in Figure 57 as a function of HFC-125 mole fraction for three source temperatures. It is seen that the source temperature has very little effect on the intensity ratio. In Figure 58 the intensity ratio is plotted for a hypothetical narrow-band-pass filter that only allows passage of the radiation at the peak in the absorbance of 1.2 for  $\lambda$  equal 8.75  $\mu\text{m}$ . In this case of a single wavelength, Equation (47) reduces to Equation (41) (Bouger's Law). The exponential decrease in the intensity ratio with respect to concentration limits the concentration range that could be measured relative to using the wider band-pass filter. Another advantage of a wider band-pass is the ability to use one instrument for several agents.

In the above analysis it is assumed that there is no long wavelength radiation with  $\lambda > 10 \mu\text{m}$  reaching the detector. The spectra of the narrow-band-pass filter and of the ZnS window are shown in Figure 59 for  $\lambda$  up to 25  $\mu\text{m}$ . It is seen that both optical elements transmit a significant fraction of light over the wavelength range from 12  $\mu\text{m}$  to 15  $\mu\text{m}$ . The product of these two transmission curves is computed to obtain the combined filter function,  $F'(\lambda)$ . This function is substituted into Equation (47) and the integration is performed from 5  $\mu\text{m}$  to 15  $\mu\text{m}$ . No molecular absorption for  $\lambda$  greater than 10  $\mu\text{m}$  is assumed in this simplified example, though a more detailed analysis would account for the two absorption features above 10  $\mu\text{m}$  for HFC-125. The intensity ratio versus mole fraction for source

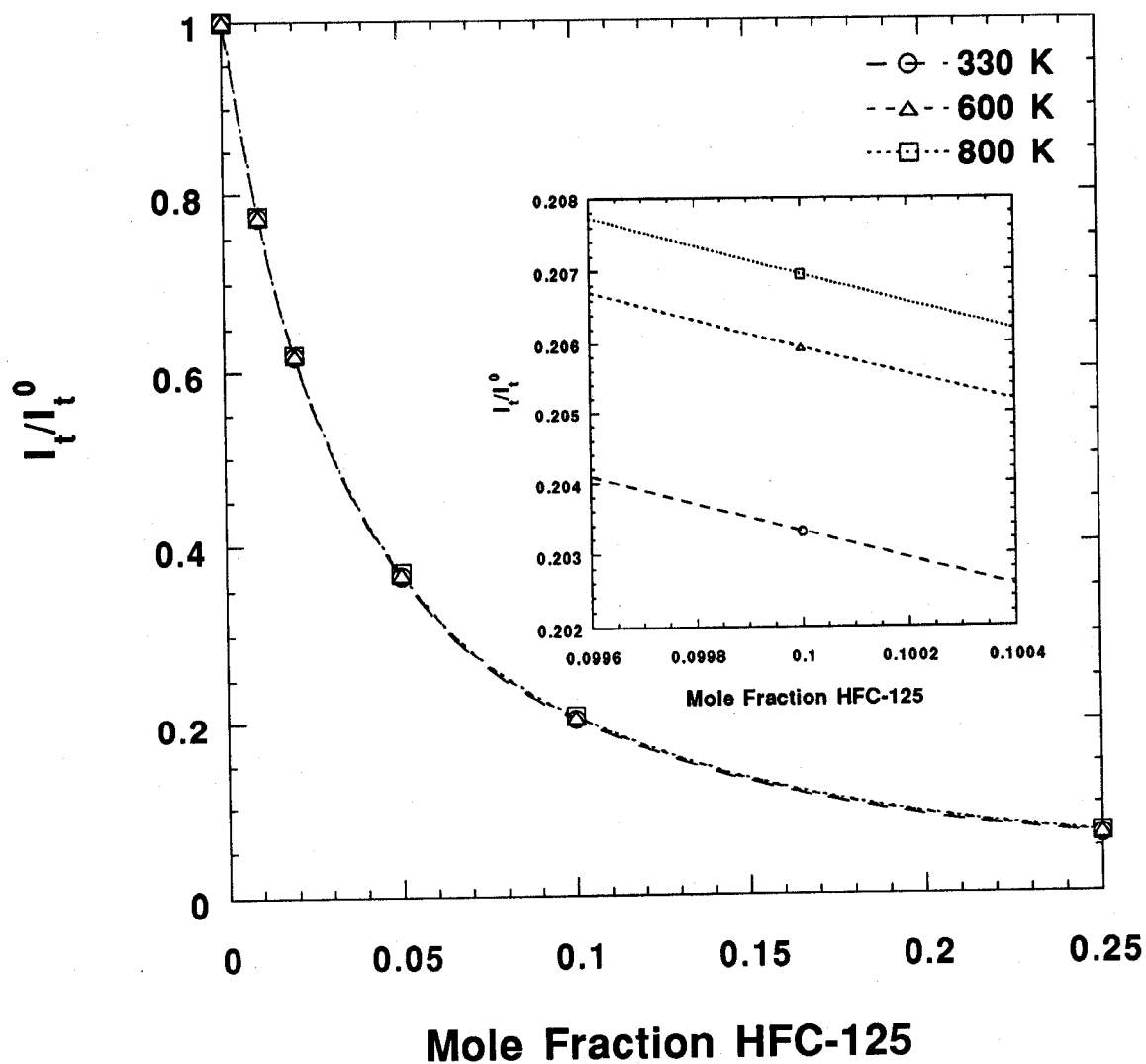


Figure 57. Predicted ratio of the wavelength integrated intensity of the transmitted IR radiation and the incident IR radiation versus mole fraction of HFC-125 for three IR source temperatures.

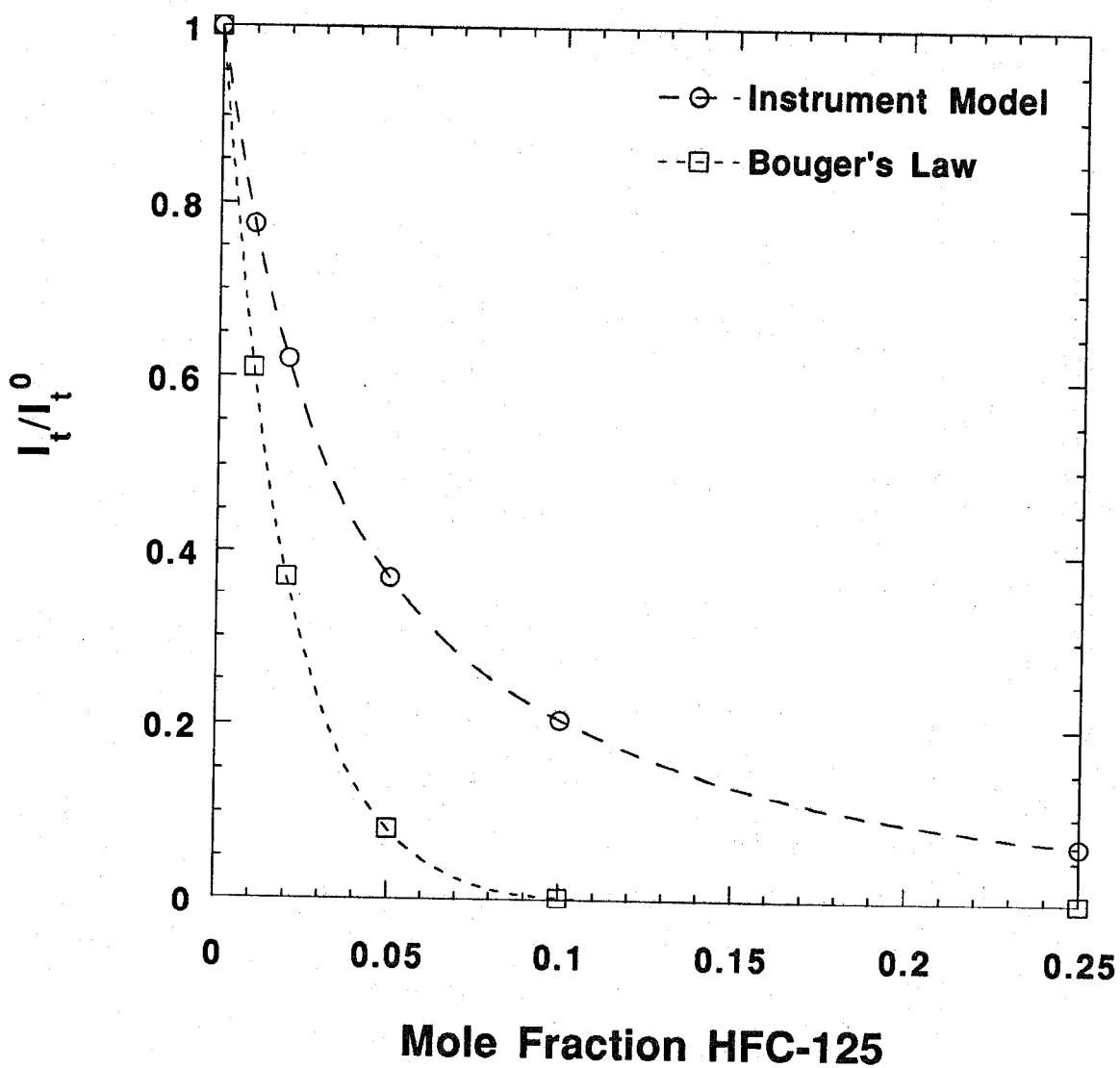


Figure 58. Comparison of the intensity ratio for the instrument (DIRRACS) model and Bouger's law.



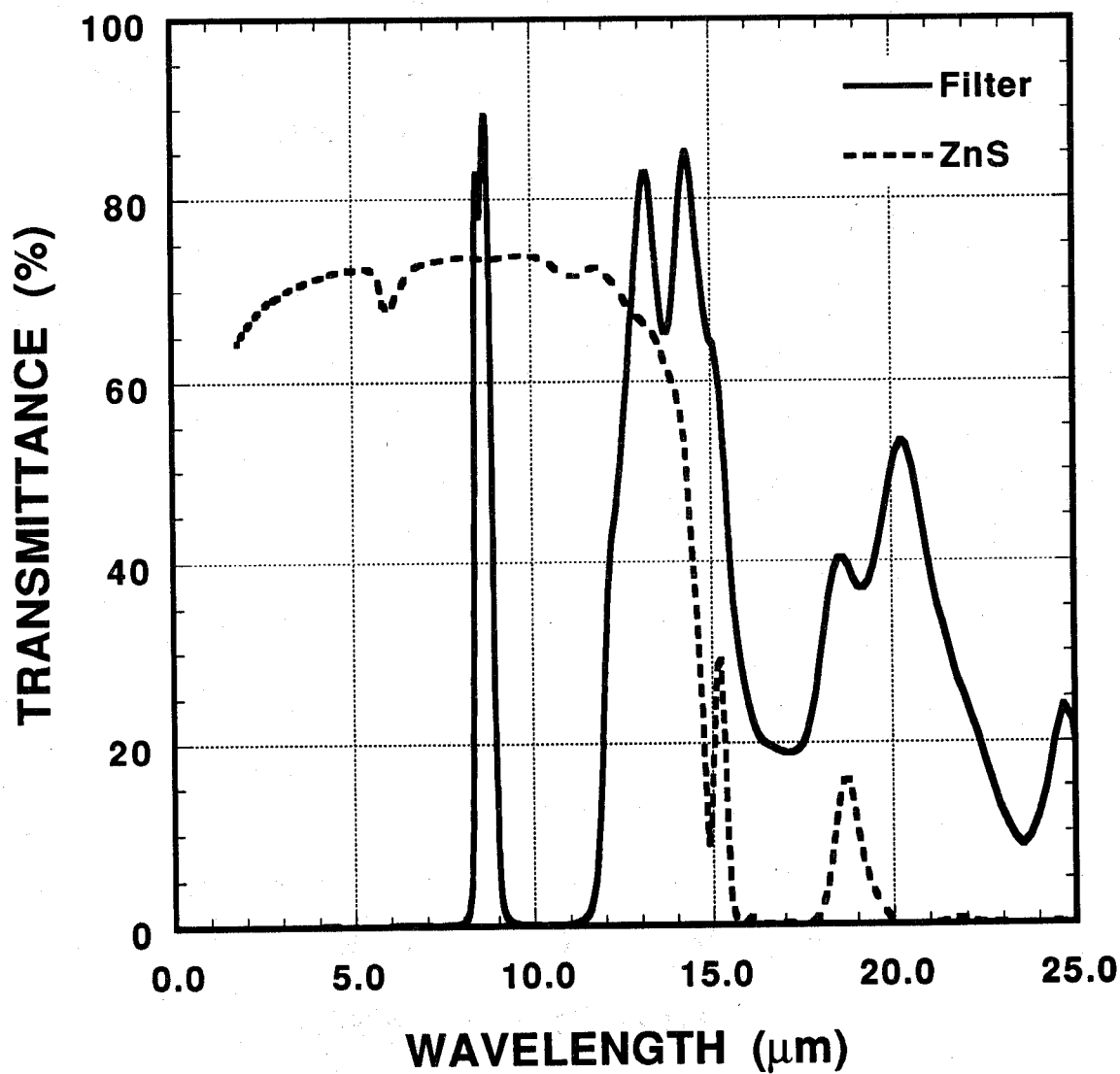


Figure 59. Transmittance versus wavelength for the narrow-band-pass filter and for the ZnS window.

temperature of 800 K are compared with the results with the reduced integration region in Figure 60. It is seen that the unfiltered light penetrating the filter results in a higher value of the transmitted ratio for all concentrations.

There are a number of secondary factors not included in the analysis that may be important to the instrument's performance. As the source heated up to about 500 °C, the temperature of the housing was found to increase to a temperature of about 70 °C over a 30 min period, and even the temperature of the conical collection tube was heated from 25 °C to about 30 °C. The significance of this heating on the performance of the instrument will be discussed in the calibration section. Other factors important for quantitative modeling of the system include the spatial distribution of the source radiance, the transmission characteristics of the ZnSe and ZnS windows, and the transmission characteristics of the IR transmission tube and conical collector.

**11.3.5 Data Acquisition.** Two methods of data acquisition were used. As illustrated in Figure 61, the output signal from the 100 × amplifier was filtered with a low-band-pass filter and analyzed with a digital oscilloscope with 8 bit resolution. The scope was triggered by the controller for the chopper. The DIRRACS voltage output has a cosine shape as can be seen in Figure 62. The scope provided peak-to-valley (Pk-Vy) voltages of the oscillatory signal. Typically 100 sweeps with a single peak and valley per sweep were taken and the average and standard deviation,  $\sigma$ , were computed from these values. This was the primary method for data acquisition during the calibration of instrument response versus agent mole fraction.

A TCP 486DX personal computer having a clock speed of 66 MHz, 8 Mbytes of RAM, and a 250 Mbyte hard drive was used for data acquisition. The same data acquisition and control system as described in detail in Section 11.2.4.5 was used. Two of the channels were used for acquiring data from the two DIRRACS. As described above, the system included two plug-in modules--a Flash 12 Model 1 data-acquisition board and a ACAO-12-2 analog and digital output board--from Strawberry Tree which were installed in computer-bus slots and provided interfaces for the experiments. The standard configuration involved operating at a data-acquisition rate of 20 000 Hz for 1 s to 10 s after a trigger signal.

The data acquisition/analysis involved several steps. First the output voltage versus time data was acquired. Then the data were transferred from a multi-channel output to a single file for subsequent analysis. An algorithm was developed for determining the peaks and valleys in the voltage for each cycle. The infrared detector output data was reduced with a FORTRAN program listed in Appendix L that returns normalized voltages and concentrations for a given set of raw voltages. The program begins by reading the input and output filenames and the operating parameters of chopping frequency, sampling frequency, zero-concentration peak-to-peak voltage, and whether the blue or black DIRRACS is the source of the data. The number of data points is determined from the data file. The number of points per cycle and total number of cycles are then calculated. A loop is started to read the voltages and store the minimum and maximum values and their times for each cycle in an array.

The program next calculates agent concentrations based on a concentration versus Pk-Vy equation fit to the data for either the blue or black detector. The calibration methodology is described in the Instrument Calibration Section. Pk-Vy voltage differences are calculated and normalized by the appropriate zero-concentration value. The appropriate calibration function is applied to each normalized voltage. If a normalized voltage is below the 100 % agent value, 100 % is assigned to that cycle. If a normalized voltage is greater than one, 0 % is assigned to that cycle. The time of the cycle, maximum and minimum voltages, peak-to-valley voltage, normalized peak-to-valley, and concentration are written to a file for each cycle.

The shape of the normalized voltage plot in Figure 62 is close to a cosine function. This is more apparent from the expanded plot in Figure 63 where the reduced voltage output of the DIRRACS is

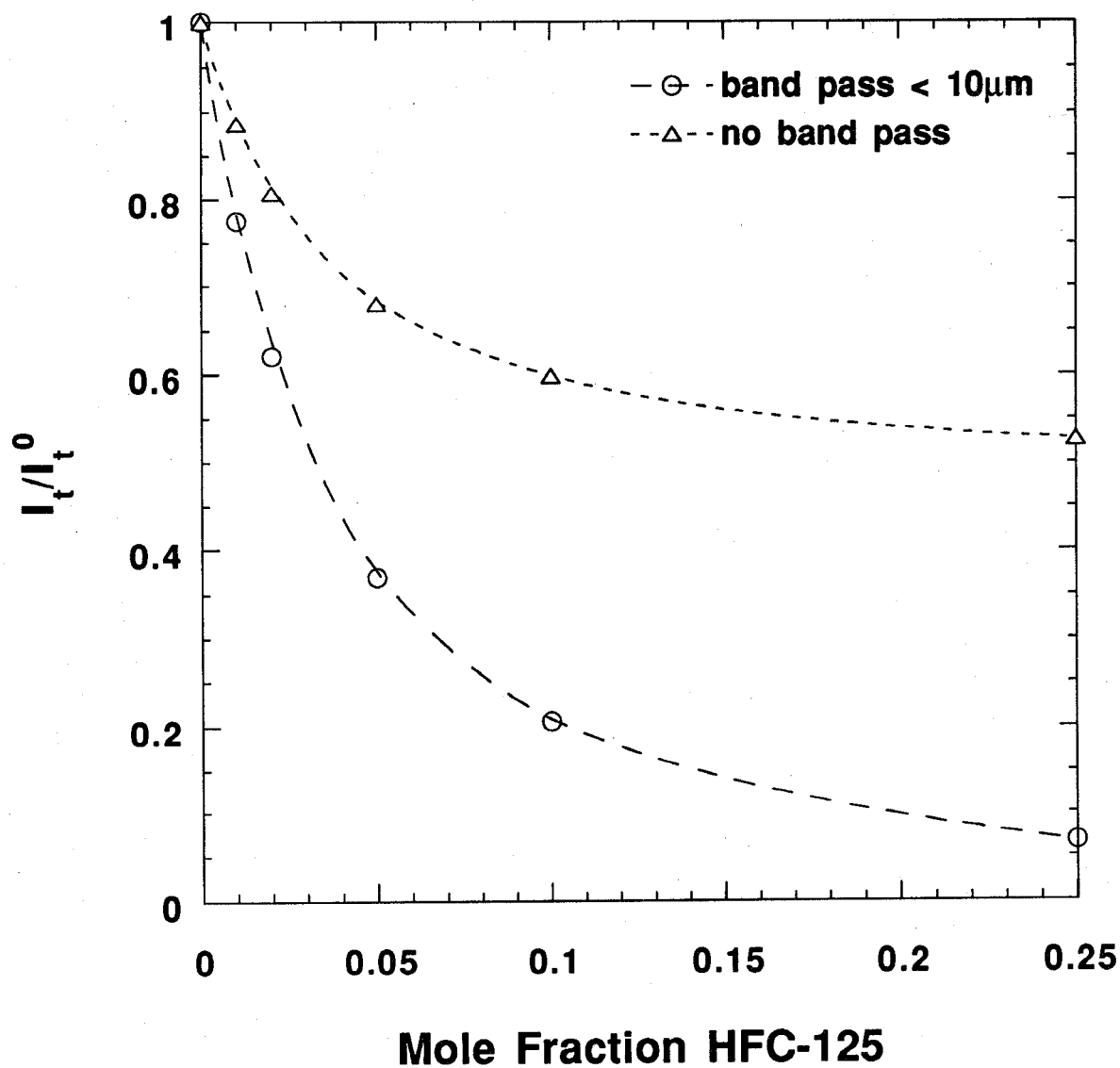


Figure 60. Effect of the integration range of  $\lambda$  on the predicted intensity ratio (5  $\mu\text{m}$  - 10  $\mu\text{m}$ , added band pass, 5  $\mu\text{m}$  - 15  $\mu\text{m}$ , no band pass).

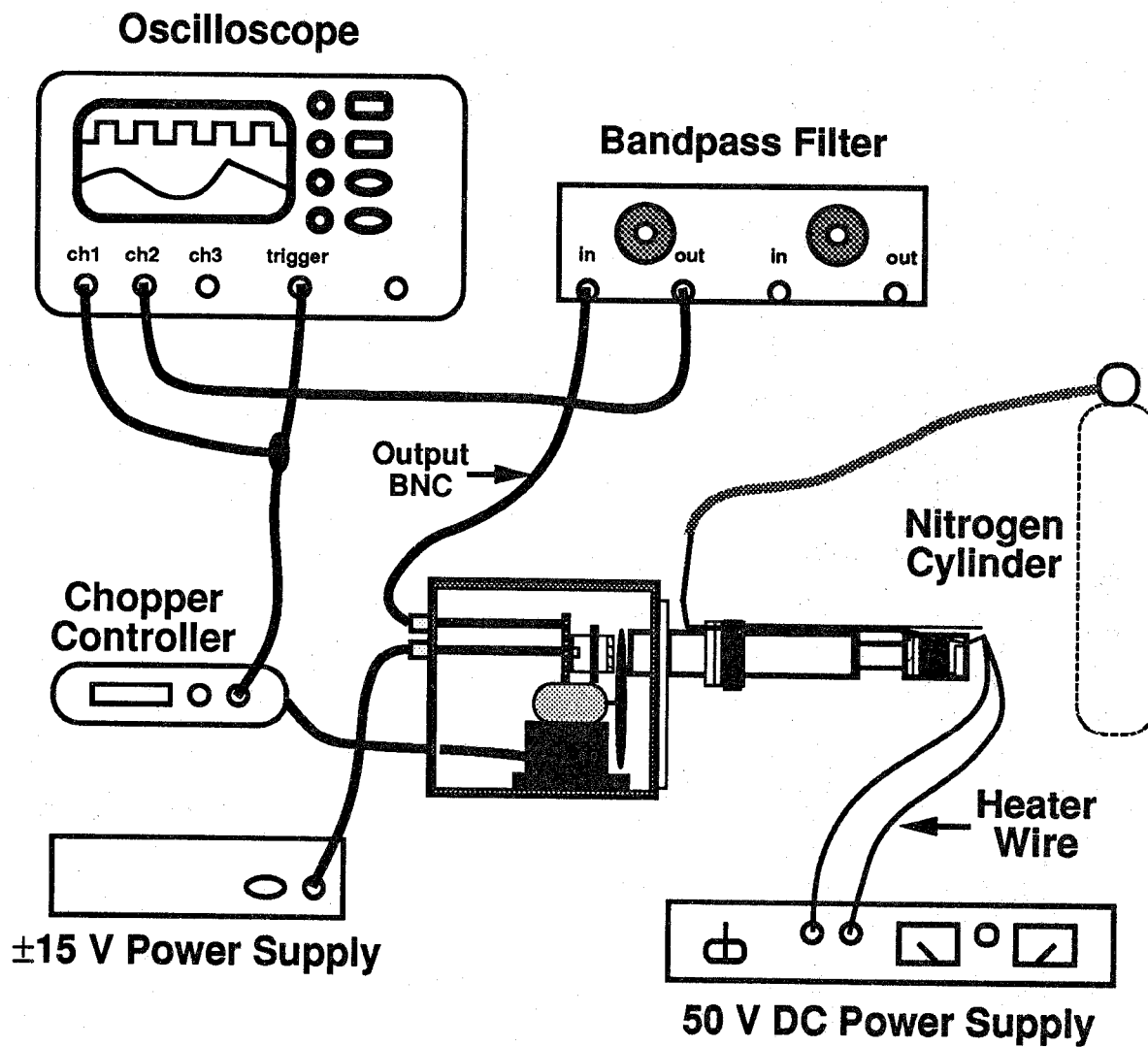


Figure 61. Schematic of experimental setup including data acquisition.

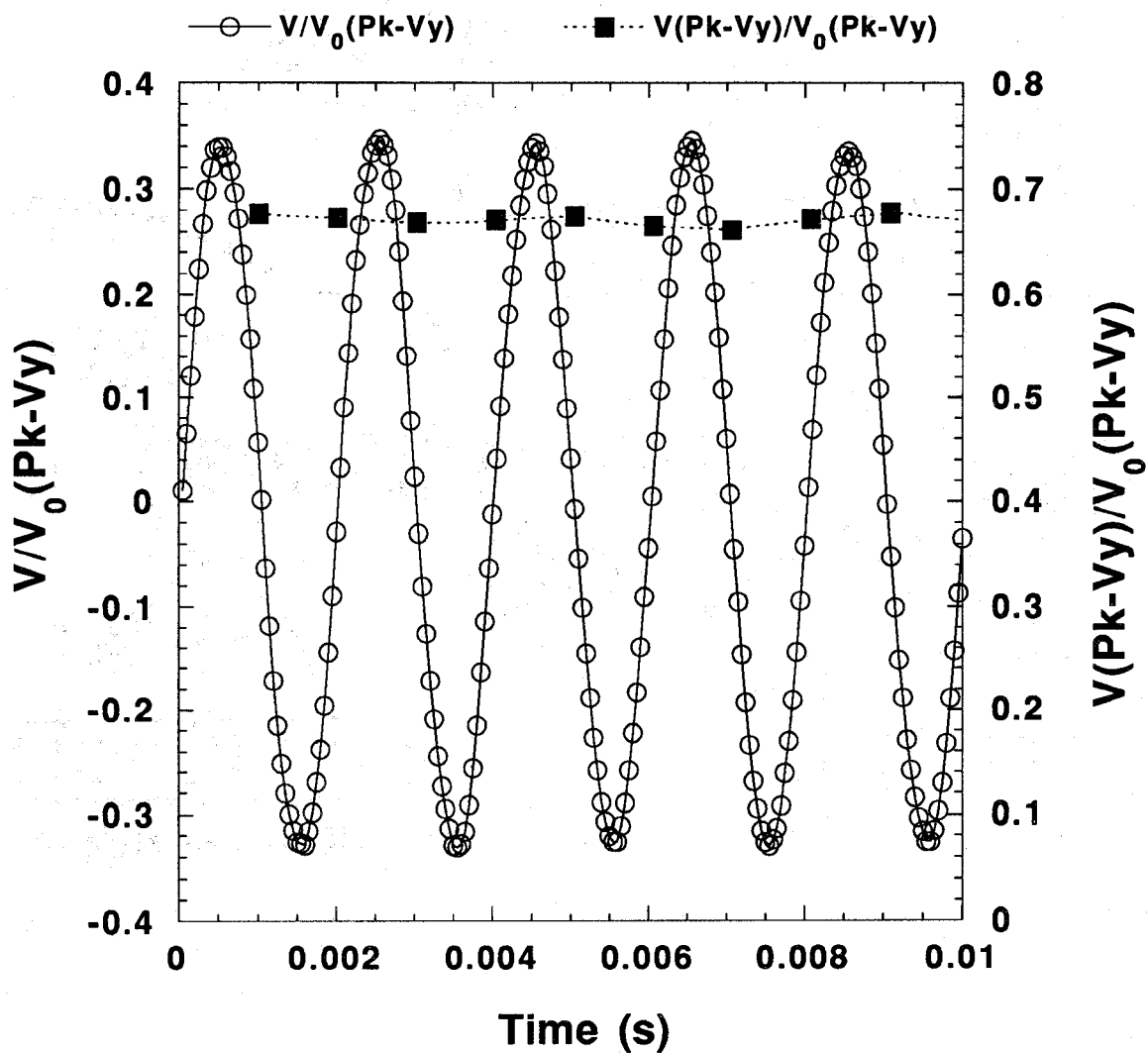


Figure 62. Plots of DIRRACS output voltage normalized by the Pk-Vy signal in air and the normalized Pk-Vy voltages versus time for 0.10 mole fraction HFC-125.

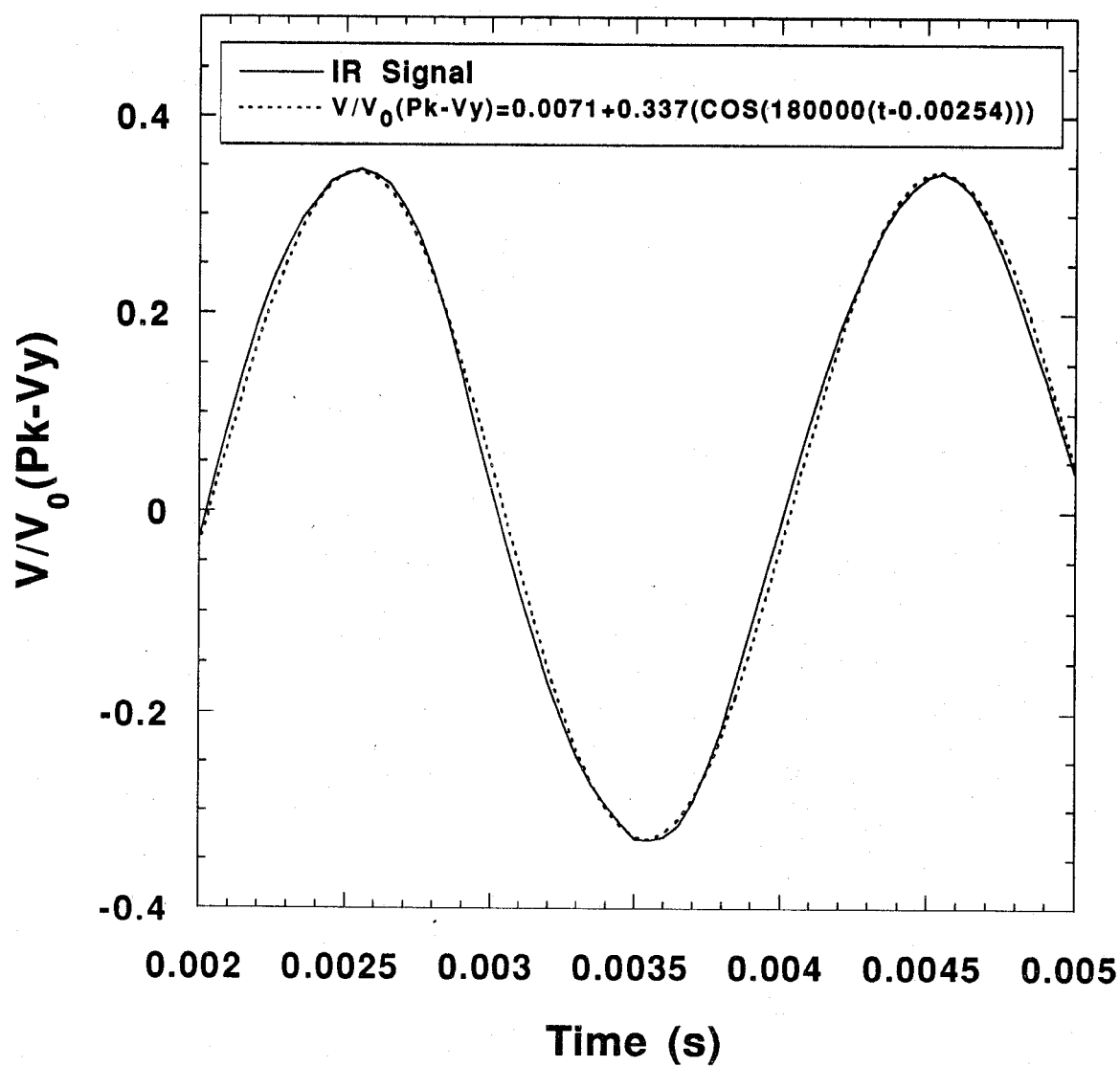


Figure 63. The reduced voltage signal from the DIRRACS is compared with a cosine function on an expanded time scale.

compared with the following expression:

$$V/V_0(Pk - Vy) = 0.0071 + 0.337 \cos[180000(t - 0.00254)]. \quad (48)$$

The cosine behavior arises from the IR beam leaving the wide-band-pass filter being approximately the same size as the opening on the chopper blade. As a result, as the blade rotates, first an increasing fraction and then a decreasing fraction of the IR radiation passes through the opening. This pattern differs from the case of a beam narrow relative to the chopper opening where the voltage increases linearly with time while the beam passes through the opening in the chopper and then decreases linearly while the beam is blocked (Molelectron, 1994). We show that this linear time dependence can be derived from the equations given above for the pyroelectric detector operation. In the limit of time short compared to the thermal time constant, one finds from Equations (25) and (26) that the pyroelectric current is constant for a step increase in the radiant flux. The voltage output of the pyroelectric detector is obtained from Equation (37) with the right hand side replaced with a constant current as indicated below:

$$C \frac{dV}{dt} + \frac{V}{R} = i = \frac{V_0}{R} \quad (49)$$

Solving for  $V$ , we obtain

$$V = V_0(1 - e^{-t/(RC)}) \quad (50)$$

For the small time limit of Equation (50), the voltage increases linearly with time. When the beam is blocked a similar analysis yields a linearly decreasing signal.

The DIRRACS response to HFC-125 at a mole fraction of 0.1 is plotted in Figure 62. The output signal is normalized by the  $Pk - Vy$  voltage in the absence of the agent. The voltage difference between peak to valley is computed and then valley to peak etc. as shown in Figure 62. Using this procedure we obtain 1000 values per second even though we are operating the chopper at 500 Hz. Finally, these results are expressed in terms of mole fraction versus time by use of a concentration calibration curve.

**11.3.6 Temporal and Spatial Resolution.** The unique feature of the DIRRACS is its high speed of data acquisition. One data point is obtained every millisecond based on the peak-to-valley analysis method. The instrument is therefore capable of measuring the average concentration within the observation volume at 1 kHz. However, the effective temporal resolution can be degraded significantly by the relatively large sampling volume of the current instrument.

The volume sampled by the DIRRACS is a cylinder having a length of 2.8 cm and a diameter of 3 cm. The probe is designed such that the sampled gas must flow through the partially blocked sampling volume. In order to understand how sampling volume can limit temporal resolution, consider an idealized two-dimensional flow of gas perpendicular to the probe consisting of air which instantaneously increases to pure agent (*i.e.*, a step increase). Assuming no flow blockage, a period,  $\tau_p$ , equal to

$$\tau_p = \frac{d_p}{U}, \quad (51)$$

where  $d_p$  is the probe diameter and  $U$  is the flow velocity, is required for the step increase to cross from one side of the sampling volume to the other. A flow velocity of 30 m/s yields  $\tau_p = 1$  ms. If

the velocity is less than 30 m/s, the concentration will be averaged and the step increase will not be completely temporally resolved. For example, if the flow velocity is 1 m/s, a period of 30 ms will be required for the measured agent concentration to monotonically increase from 0 % to 100 %. In this case, the effective temporal resolution is on the order of 30 ms. Note that the direction of the flow is important. A similar concentration gradient oriented parallel to the flow direction would result in a constant concentration measurement which would depend on the location of the step increase within the observation volume. Partial blockage of the flow will tend to degrade the effective temporal resolution still further. A determination of the effective temporal resolution in a given experimental configuration requires a detailed understanding of the flow velocity. Such spatial averaging effects will tend to average (*i.e.*, smooth) agent concentration fluctuations except in the case of high-speed flows.

**11.3.7 Signal-to-Noise Behavior.** It is the standard deviation,  $\sigma$ , associated with the peak height that is the relevant measure of noise for the highest speed operation, since this is the quantity measured at 1000 Hz. We expected that a signal-to-noise ratio of at least 100 would be required to obtain adequate instrument performance when expressed in terms of agent concentration. The Pk-Vy voltages for the blue DIRRACS were about 2.0 V and about 1 V for the black DIRRACS with no agent present when operating the IR source at 50 V, which corresponded to about 60 W. When using a low-band-pass filter with 24 db per octave set at 300 Hz to remove low frequency noise, the signal-to-noise was found to be in the range 100-140. A possible negative feature of the low-band-pass filter is to distort the instrument response for a slowly changing concentration. Results presented below in Section 11.3.9.2 suggest that the low-band-pass filter does not substantially effect the response of the DIRRACS for a release lasting about 240 ms.

The manufacturer's specification for the noise of the pyroelectric detector is 1.1  $\mu\text{V}$  at a frequency of 15 Hz. The unamplified signal corresponding to a 1 V output of the DIRRACS is 10 mV. Assuming a noise equal to 0.7 % of the signal corresponds to 70  $\mu\text{V}$ . So the apparent noise is a factor of 70 greater than the manufacturer's specification. The difference in frequency between the manufacturer's specification and our measurement is not the source of the difference, since the dominant detector related noise sources, the Johnson noise of the detector itself and the noise associated with the preamplifier (Putley, 1970), should decrease with increasing frequency. Other contributions to the noise could be mechanical vibration from the chopper and lack of temperature control of the detector housing. The amplified signal at 500 Hz with the IR source off is about 40 mV with a dc offset from zero of about 50 mV compared to a signal of 1 V to 2 V with the source on.

The responsivity of the detector is approximately 1 V/W at 500 Hz. The nominal 10 mV to 20 mV unamplified detector output corresponds to a radiant flux of 10 mW. The maximum power rating for the detector is about 50 mW, so it is operated well below this limit. For an 800 K blackbody source, the total flux emitted from a unit surface area integrated over all wavelengths is obtained from the Stefan-Boltzmann law:

$$\Phi(T) = \sigma_e T^4, \quad (52)$$

where  $\sigma_e$  is the Stefan-Boltzmann constant ( $5.67 \times 10^{-8} \text{ WK}^4/\text{m}^2$ ). This corresponds to 2.32 W/cm<sup>2</sup> or a total of about 8.4 W for the total source area of 3.6 cm<sup>2</sup>. The total heat produced by the heater is estimated as 60 W when operated at 50 V dc. To estimate the radiant flux emitted and transmitted by the narrow-band-pass filter, we assume a flat source area  $A_s$  of 3.6 cm<sup>2</sup>, that the source is 3.0 cm from the collection tube with a 2.86 cm diameter, and that the source is Lambertian. Every point on the source is treated as if it has the same collection angle as the center of the disk,



$$\Phi(\Delta\lambda) = 0.19\pi L_{\lambda} A_s \Delta\lambda \quad . \quad (53)$$

The simplified wavelength dependence results from the small variation in  $L_{\lambda}$  with a nominal value of  $1.8 \times 10^8 \text{ W sr}^{-1} \text{ m}^{-3}$  for the small change in  $\lambda$ ,  $\Delta\lambda = 0.517 \text{ }\mu\text{m}$ . The resulting value is 20 mW, which is twice the 10 mW flux actually detected. Additional loss terms not accounted for include reflection losses by the windows, losses in the transfer tube, losses at the chopper, losses in the collector, and reflection of some radiation from the detector.

**11.3.8 Instrument Calibration.** The calibration of the DIRRACS was a major component of this study. The approach was to flow a known concentration of agent through the sample volume and to measure the Pk-Vy signal. A unique computer-controlled calibration system described in Section 11.2.4 was used to generate flows of agent having a specified concentration. In operating the system one would simply enter the desired concentration and the software/interface would change the air and agent mass-flow controller settings to give the desired concentration within a few seconds. The ability to rapidly change the concentration was an important feature because of the possibility of drift in the source or detector over a long period of time. The system was designed to provide a constant mass-flow rate. The volumetric flow rates varied from about  $167 \text{ cm}^3/\text{s}$  (10 L/min) for pure air to about  $67 \text{ cm}^3/\text{s}$  (4 L/min) for pure agent.

After leaving the mixing chamber, the agent/air mixture entered the cell surrounding the sensing volume of the DIRRACS. Three different cells were fabricated for containing the agent/air mixture as it flowed through the DIRRACS. The first device consisted of a rectangular plastic chamber having dimensions of  $20 \text{ cm} \times 20 \text{ cm} \times 40 \text{ cm}$ . In the development phase, all of the components of the DIRRACS were located in the cell. There was a small fan to provide mixing within the chamber. Later this facility was modified so that only the tube assembly was in the cell. Because of the long time required to reach a constant concentration, on the order of 10 min with a nominal flow of  $167 \text{ cm}^3/\text{s}$  (10 L/min), a smaller chamber was designed as illustrated in the top portion of Figure 64. The total volume was reduced to  $320 \text{ cm}^3$ . In this case 5 s were required for displacing the cell volume (the total volume of the flow to equal the chamber volume) at the minimum flow of  $67 \text{ cm}^3/\text{s}$  (4 L/min). However, experimentally, we observed that the time required to reach steady-state behavior was up to 100 s. It was thought that the long time resulted from poor mixing in the measurement volume. A third cell was fabricated allowing direct flow of the agent through the cell. It consisted of a cylindrical tube with a diameter slightly larger than the pathlength of the DIRRACS. Oversized openings were machined to allow clearance for the heater wires and purge tube, and the cell was sealed to the DIRRACS using fiberglass tape. A subsequent addition of a cooling coil to the IR sensor housing required that the cell be split in half along the axis of flow to allow mounting to the DIRRACS, since it could no longer slip on over the housing. Screens were placed near the inlet and outlet of the cell to ensure uniform flow. With a cell volume of  $90 \text{ cm}^3$ , only 1.3 s was required for displacing the cell volume. Empirically it was found that 10 s was sufficient time to reach a steady state. Some fraction of the 10 s is the settling time of the flow controllers to a new voltage setting.

The standard calibration procedure was to allow 10 min after energization for the IR source to reach a steady temperature. Figure 65 includes data on temperature versus time for a similar IR source to the one located in the DIRRACS. The ZnSe window was removed to provide access. The thermocouple was attached to the heating coil with high-temperature cement. The temperature typically varied by less than  $\pm 2 \text{ }^{\circ}\text{C}$  over a period of 5 min, which is longer than the period required for a typical calibration. We verified that the system was in steady state by requiring that two Pk-Vy readings taken 1 min apart with air flowing through the cell agreed within 0.5 %. Following achievement of a steady state, the Pk-Vy output was measured for increasing agent concentrations, allowing

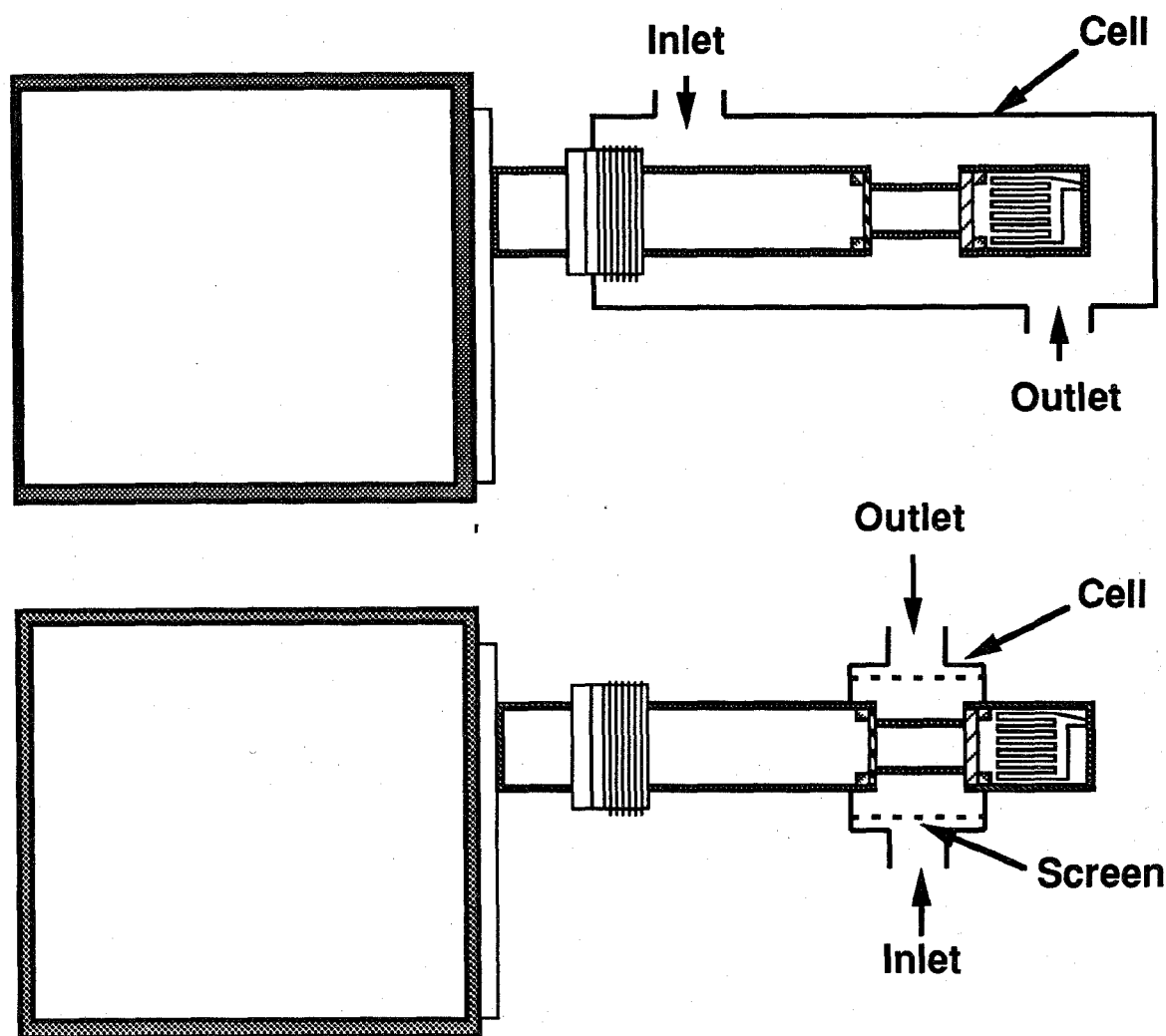


Figure 64. Illustrations of two of the cells used for calibrating the DIRRACS.

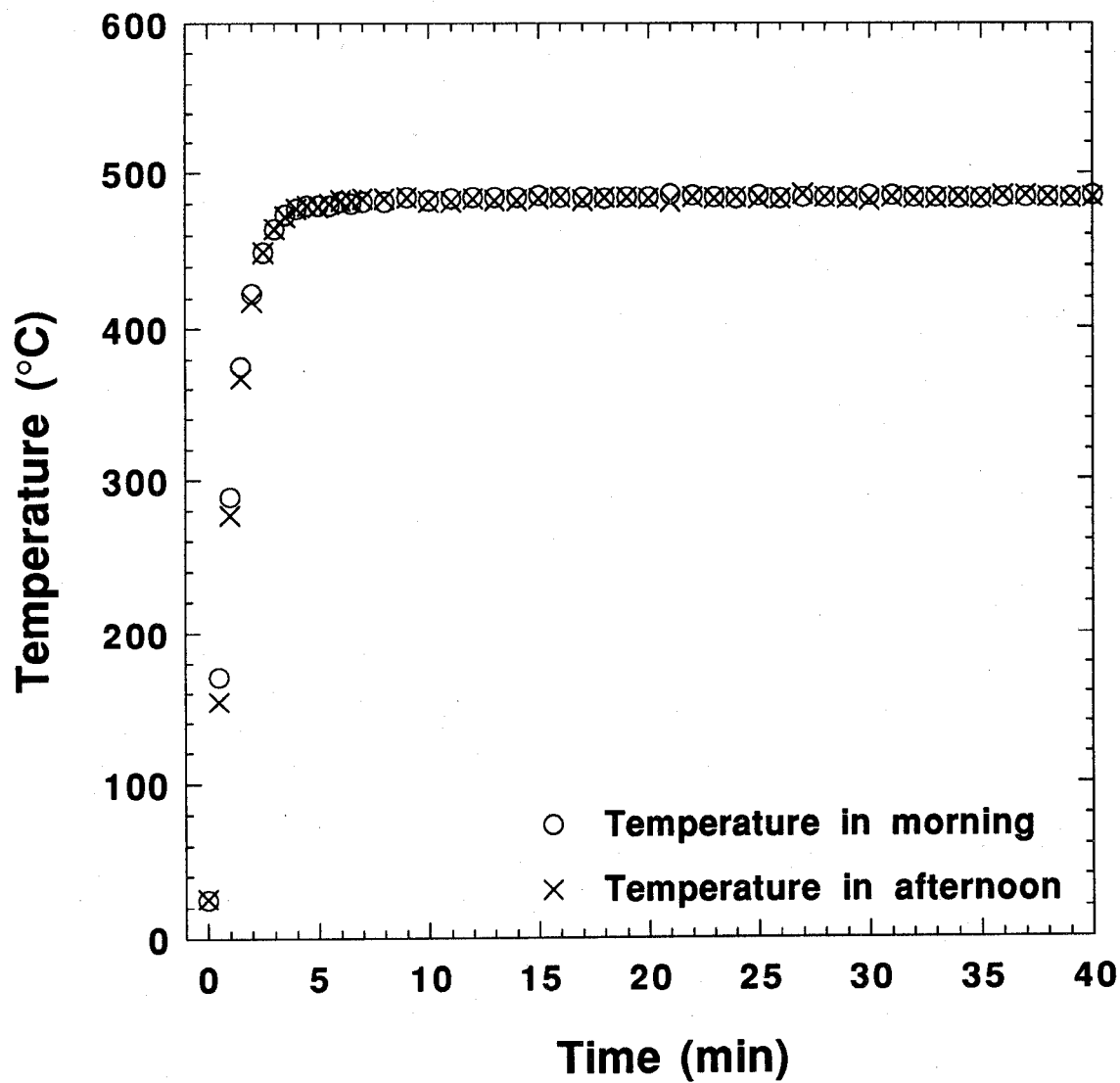


Figure 65. Temperature versus time for IR source with window removed.

about 30 s per concentration; after measuring the highest concentration, a final measurement was made for air to verify the output for air was unchanged. Five to seven concentrations could be measured in 3 min to 5 min. Typical mole fractions were 0.01, 0.02, 0.05, 0.10, 0.25, 0.50, and 1.00. This entire procedure was repeated three times to determine variations in the calibration curve. Typical data are shown for four repeats for HFC-125 in Figure 66 for mole fractions up to 0.25. These results show that the instrument sensitivity is much higher at low concentrations. Calibration data for halon 1301 is plotted in Figure 67. By comparing the two calibration curves, it is seen that the DIRRACS is slightly more sensitive to HFC-125 than halon 1301. This is consistent with the much stronger absorption features for HFC-125 compared to halon 1301 over the wavelength range of the narrow-pass filter (see Figure 54 and Figure 55)

An important quantity for characterizing the performance of the DIRRACS is the uncertainty in the concentration for a given concentration,  $\Delta C$ , divided by the concentration. The standard deviation based on three repeat calibrations is used as  $\Delta C$ . Figure 68 shows results based on two repeat series of calibrations for both DIRRACS. We see in all cases that the value of  $\Delta C/C$  is less than 0.1. One expects high  $\Delta C/C$  for both small  $C$  because of the small denominator and for large  $C$  because of the flatness of the calibration curve, and one expects the lowest  $\Delta C/C$  over the middle range. The decrease in  $\Delta C/C$  for a mole fraction of 0.25 for the one test is the opposite of our expectation. Below we provide estimates of  $\Delta C/C$  for a rapid release.

During our testing it was noticed that changing the air flow across the detector housing affected the DIRRACS response. A flow effect is of concern since high flows are produced as an agent is released in a dry bay and engine nacelle. A series of measurements were performed to quantify this effect. A small fan with a 10 cm diameter blade was positioned about 5 cm from the IR source housing resulting in an estimated velocity of 5 m/s. Figure 69 illustrates the effect of this flow on the calibration curve. The effect is especially pronounced for high concentrations. For example, for a 0.20 mole fraction, using the calibration curve for the case of no external air flow would lead to a measured mole fraction of 0.35.

A number of measurements were performed to try to determine the cause of the shift in the calibration curve. One conjecture was that the increased air flow cooled the IR source housing and reduced the source temperature. Calibration measurements were carried with filament voltages of 45 V and 50 V corresponding to IR source temperatures of about 450 °C and 500 °C. As shown in Figure 70, there was essentially no detectable change in the calibration curves. This result of no temperature effect is also consistent with the model calculation presented in Figure 57.

A second conjecture for the cause of the discrepancy was based on the difference between the predicted and measured voltage ratios at large concentration. As indicated in Figure 57, the predicted voltage ratio for a mole fraction of 0.25 is less than 0.1, while the measured value is greater than 0.5. It was suspected that the narrow-band-pass filter was allowing longer wavelength radiation to pass to the detector. In our initial spectral measurements, we were limited to wavelengths less than about 15  $\mu\text{m}$  by the optics of the Fourier transform infrared instrument which was used. Later spectra taken with an infrared absorption spectrometer allowed measurements from 2  $\mu\text{m}$  to 25  $\mu\text{m}$ . The results are included in Figure 59. It is clearly seen that there is radiation in the range 11  $\mu\text{m}$  - 15  $\mu\text{m}$  that is transmitted though both the narrow-band-pass filter and the ZnS window. To block the 11  $\mu\text{m}$  to 15  $\mu\text{m}$  radiation, a wide-band-pass filter which transmits radiation in the 8  $\mu\text{m}$  - 10  $\mu\text{m}$  range but blocks at least 99 % of the radiation in the 11  $\mu\text{m}$  - 15  $\mu\text{m}$  range was installed at the end of the IR transmission tube near the chopper. Figure 71 shows a comparison of the original results and the results with the additional band-pass filter installed. We see that there is almost a factor of two decrease in the signal for an agent mole fraction equal 1. This indicates that previously half the radiation was transmitted through this long wavelength region. The spectrum for HFC-125 from 7  $\mu\text{m}$  to 15  $\mu\text{m}$  shown in Figure 55 indicates that the agent absorbs over a portion of the 11  $\mu\text{m}$  to 15  $\mu\text{m}$

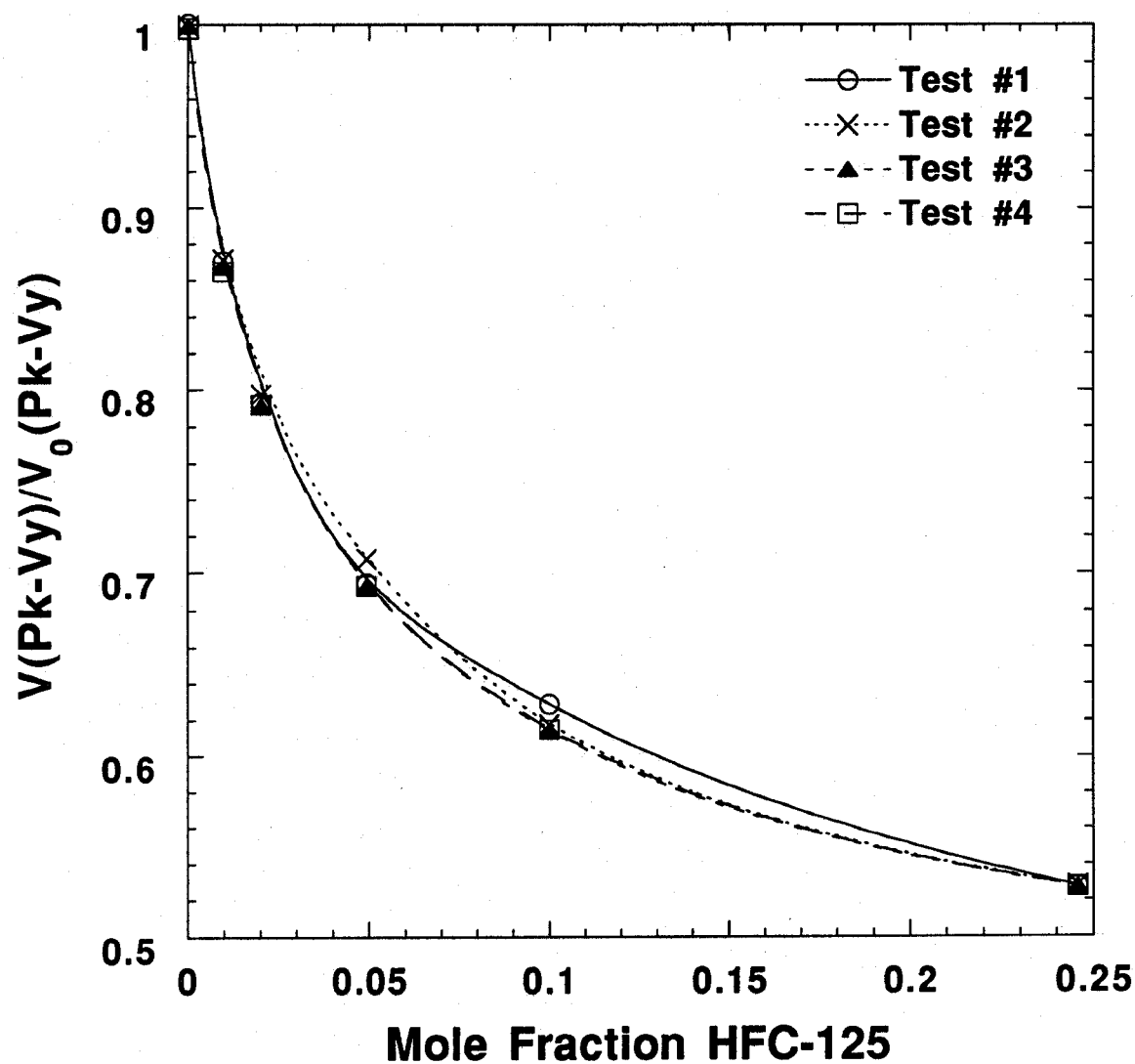


Figure 66. The ratio of the Pk-Vy voltage with various agent/air mixtures versus the mole fraction of HFC-125. Results are presented for four repeat tests.

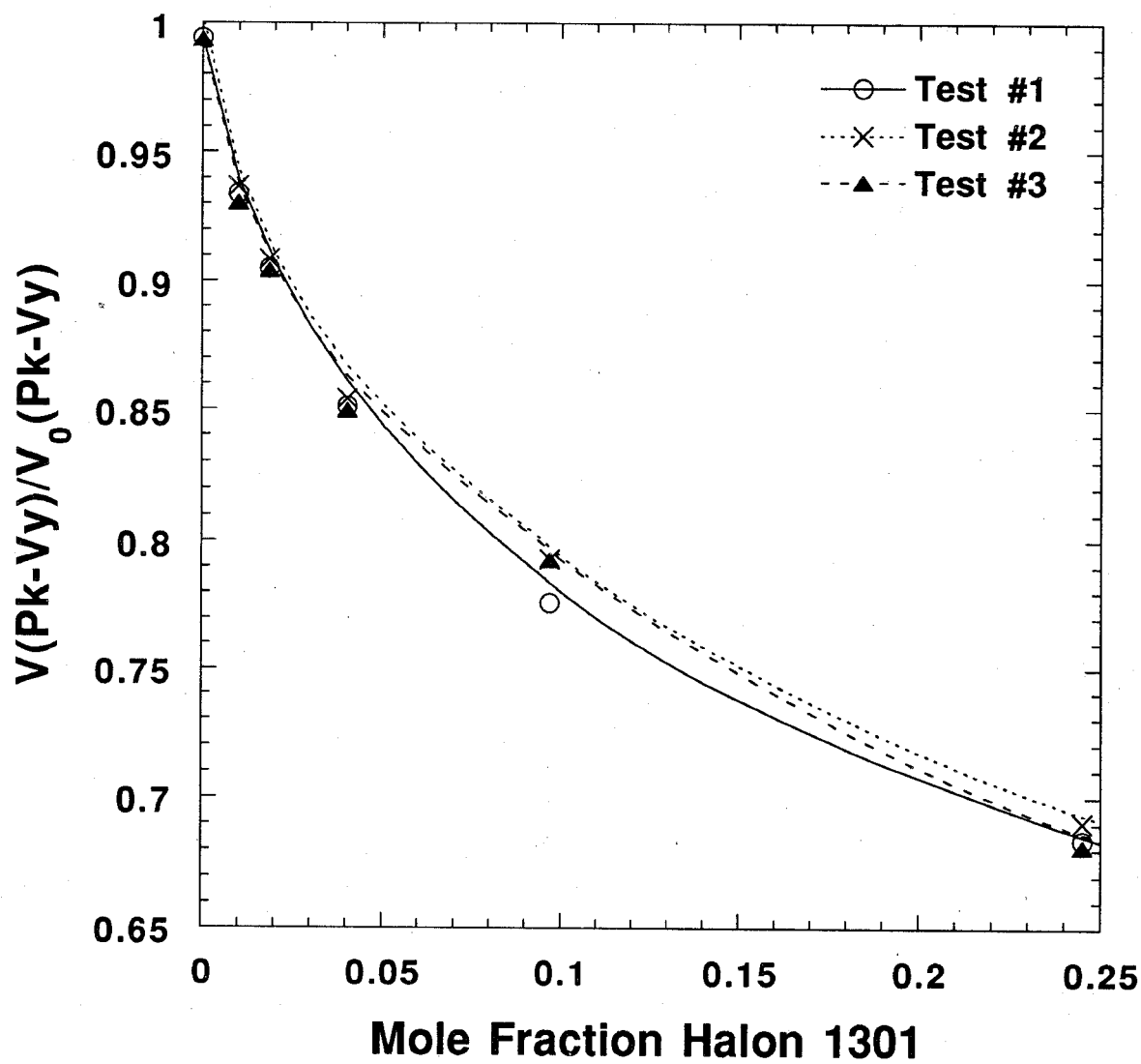


Figure 67. Calibration curves for halon 1301 based on three repeat tests.

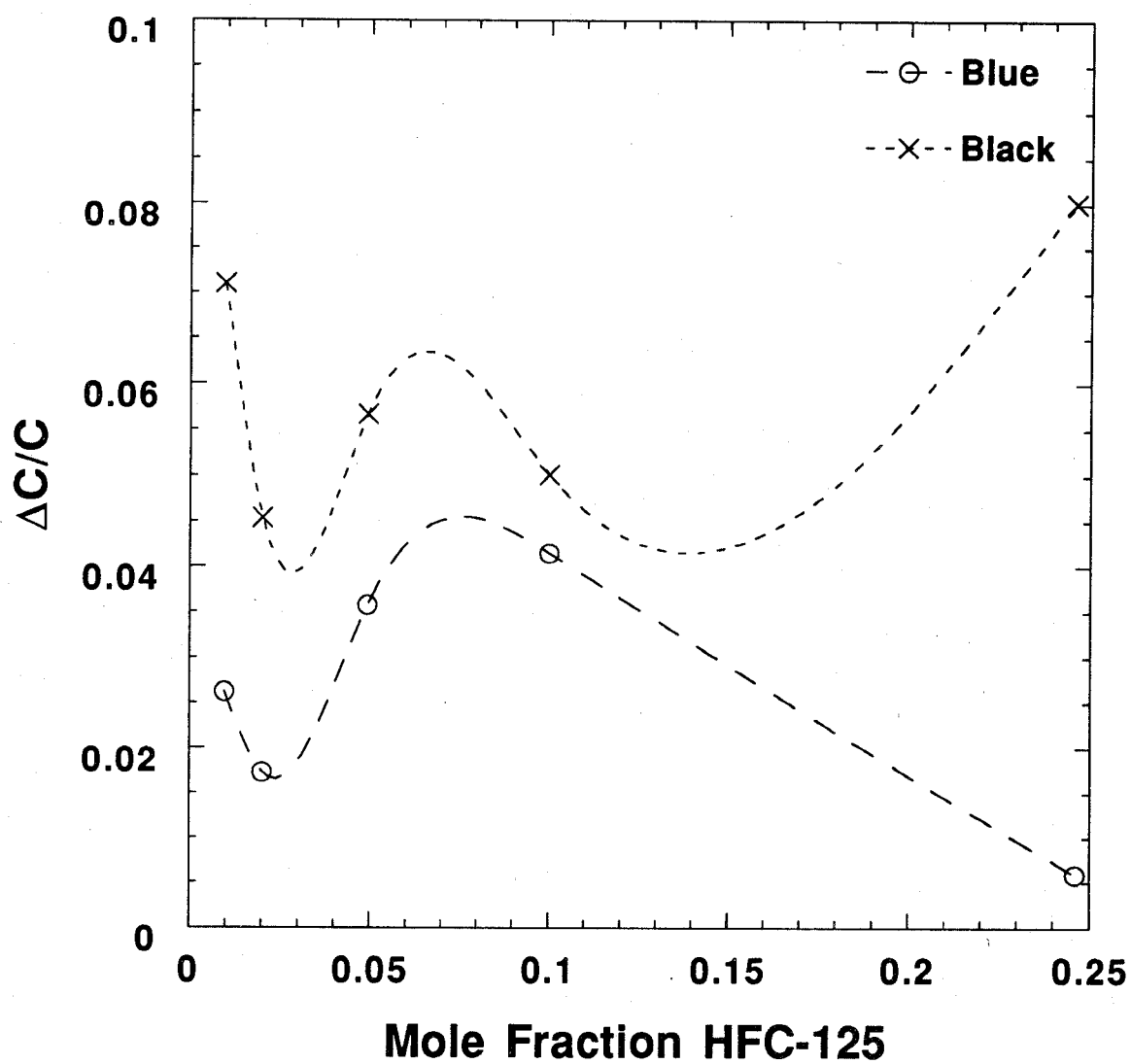


Figure 68.  $\Delta C/C$  versus  $C$  based on three repeat calibrations for both the "black" and the "blue" DIRRACS with HFC-125.

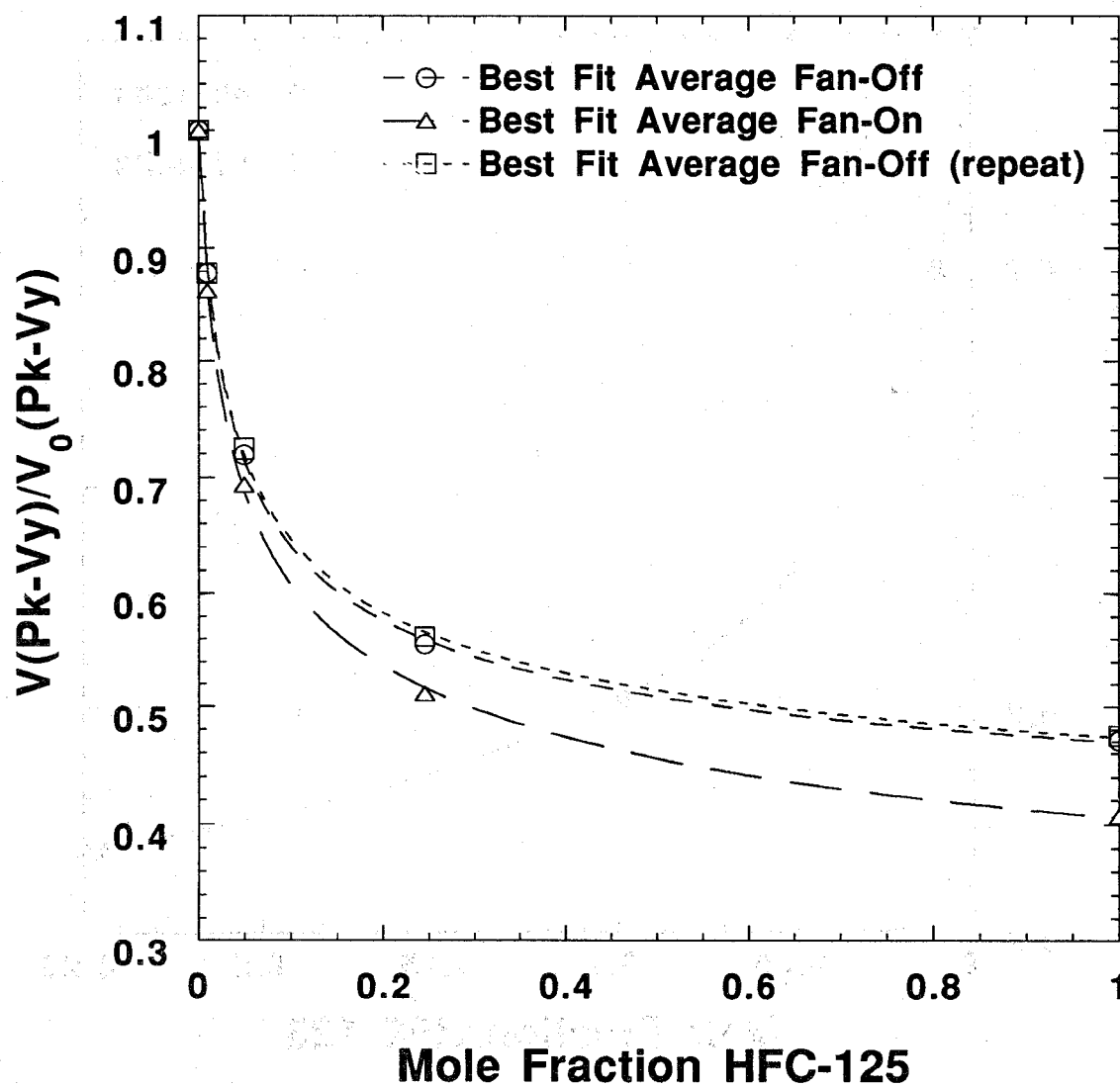


Figure 69. The effect of air flow on the DIRRACS calibration.



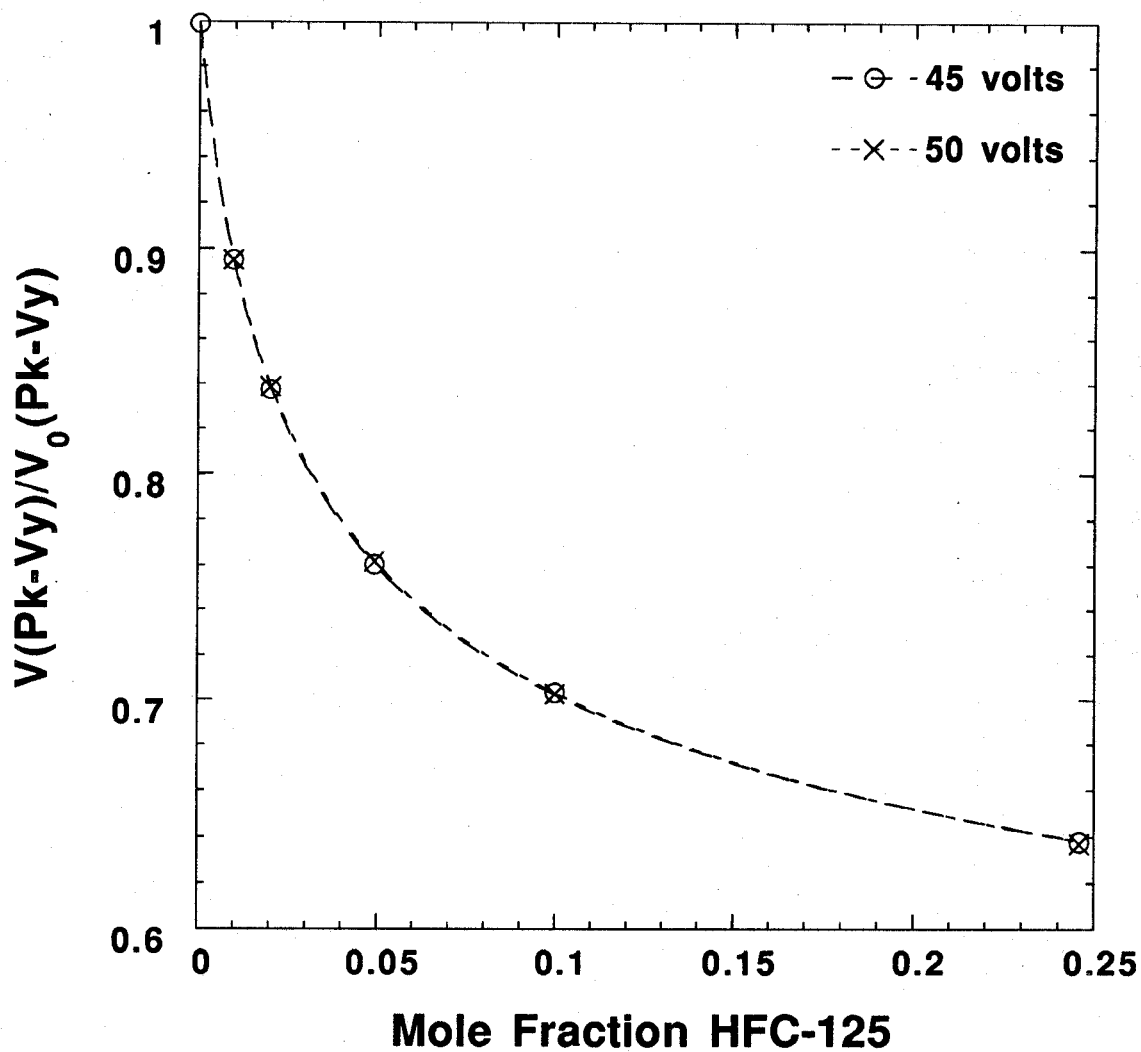


Figure 70. The effect of the source temperature on the calibration curve. Voltage settings of the IR source of 45 V and 50 V correspond to source temperatures of approximately 450 °C and 500 °C.

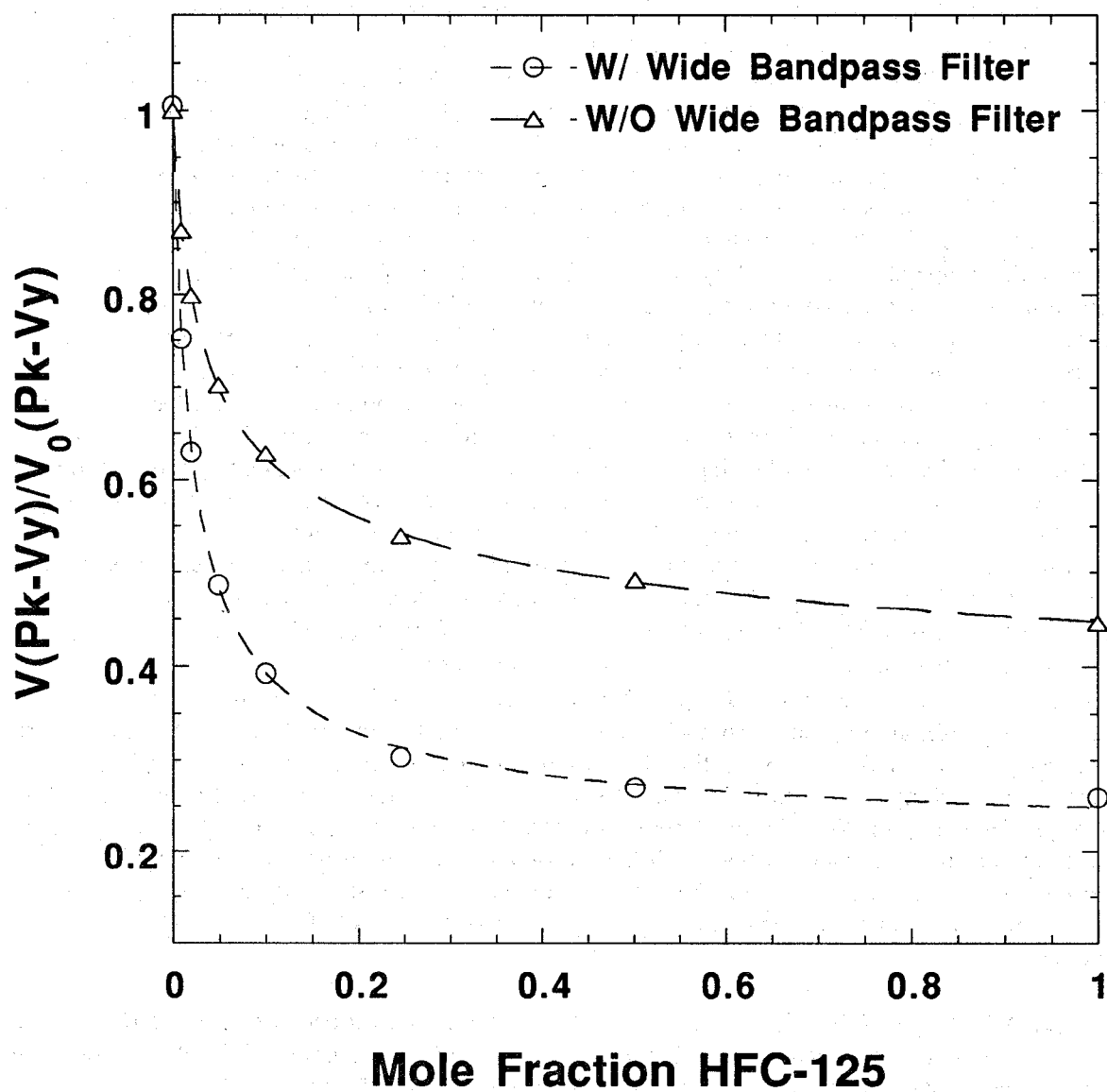


Figure 71. Comparison of the calibration curves with and without the addition of the wide-band-pass filter.

region. The addition of the filter decreased the output signal by about a factor of 3 and also appeared to decrease the signal-to-noise ratio. We also point out that the measured value of about 0.3 at a mole fraction of 0.25 is still larger than the predicted value of 0.07. Possible causes for the remaining discrepancy include the DC offset of the detector and uncertainty in the spectral data of HFC-125.

In Figure 72 it is shown that even with the addition of a band-pass filter there is still a flow effect of about the same order of magnitude as before. Additional temperature measurements were made of the source housing and of the metal collection cone holding the detector. It was observed that the temperature of the housing increased to about 80 °C without the flow and to only about 50 °C with the flow. The resulting temperature change of the agent/air passing through the sensing volume is at most 10 °C. The study of Edgell and May (1953) indicate that an increase in temperature from 30 °C to 160 °C changes the percent transmission at 13.5  $\mu\text{m}$  from about 40 % to 50 %. A gas temperature change of 10 °C is estimated to change the percentage of transmission by approximately 1 % and thus can not account for the observed change in calibration curve with an external flow.

The cone temperature increased by about 5 °C over a 30 min period as a result of heat transmitted down the brass tube through the box and then convectively heating the interior components. Since the pyroelectric coefficient and the band-pass filter transmission curves are temperature dependent, this could lead to a change in response. Figure 73 shows calibration curves for two different temperatures of the conical collector obtained by placing the DIRRACS chassis without lid in the large calibration cell and heating the air in the chamber with a heat gun. This is not an ideal test since there is also flow, however, it does show that heating of the pyroelectric sensor and optical components could be an issue. There was also concern that there could be a gradual heating of the detector from the incident IR radiation. To assess the significance of this effect, the output was monitored, then the beam was blocked for 1 min - 5 min and the output again monitored. It was found that the detector signal changed by no more than 0.5 %. The manufacturers' reported detector drift is 0.2 %/1 °C and interference filter drift is also 0.2 %/1 °C. So the expected effect of a 5 °C temperature drift is at most 2 % which does not account for the measured 6 % change.

Since it could not be determined which thermal effect was responsible for the change in the instrument response, an empirical approach was taken of trying to limit heat transfer from the source to other parts of the DIRRACS by cooling the area around the IR source. Three turns of 3.2 mm diameter copper tubing were soldered to the IR source housing. The water flow through the coil was set at approximately 5  $\text{cm}^3/\text{s}$ . Figure 74 shows the effect of cooling the housing. It is seen that in this case the same results are obtained both with the fan on and off! Unfortunately, the modified system in its present form is not consistent with the use in an engine nacelle test facility because of the addition of the cooling coil. Below we present field testing results of the units before the inclusion of the cooling coil.

**11.3.9 Field Testing of DIRRACS.** Two types of testing were performed with the DIRRACS. The first was carried out at the simulated dry-bay test facility at Wright-Patterson AFB. The second was testing with controlled agent releases at NIST in the turbulent spray flame facility.

**11.3.9.1 Dry-Bay Testing at Wright Patterson AFB.** During the week of July 19-22, 1994, two DIRRACS were tested at Wright-Patterson with releases of halon 1301 in the simulated dry-bay facility. The dry-bay configuration shown in Figure 75 had dimensions of 6.0 m  $\times$  1.5 m  $\times$  0.3 m (20 ft  $\times$  5 ft  $\times$  1 ft). One of the DIRRACS was positioned close to the extinguisher on the left side and the second monitor was positioned near the exhaust close to the lower left hand corner. The probe assemblies were mounted to aluminum plates, and the plates were attached to the metal plate on the back of the simulated dry bay. A total of 10 locations were prepared for positioning the DIRRACS. A second opening was cut in the plate for use of a combined aspirated hot-film/cold-wire

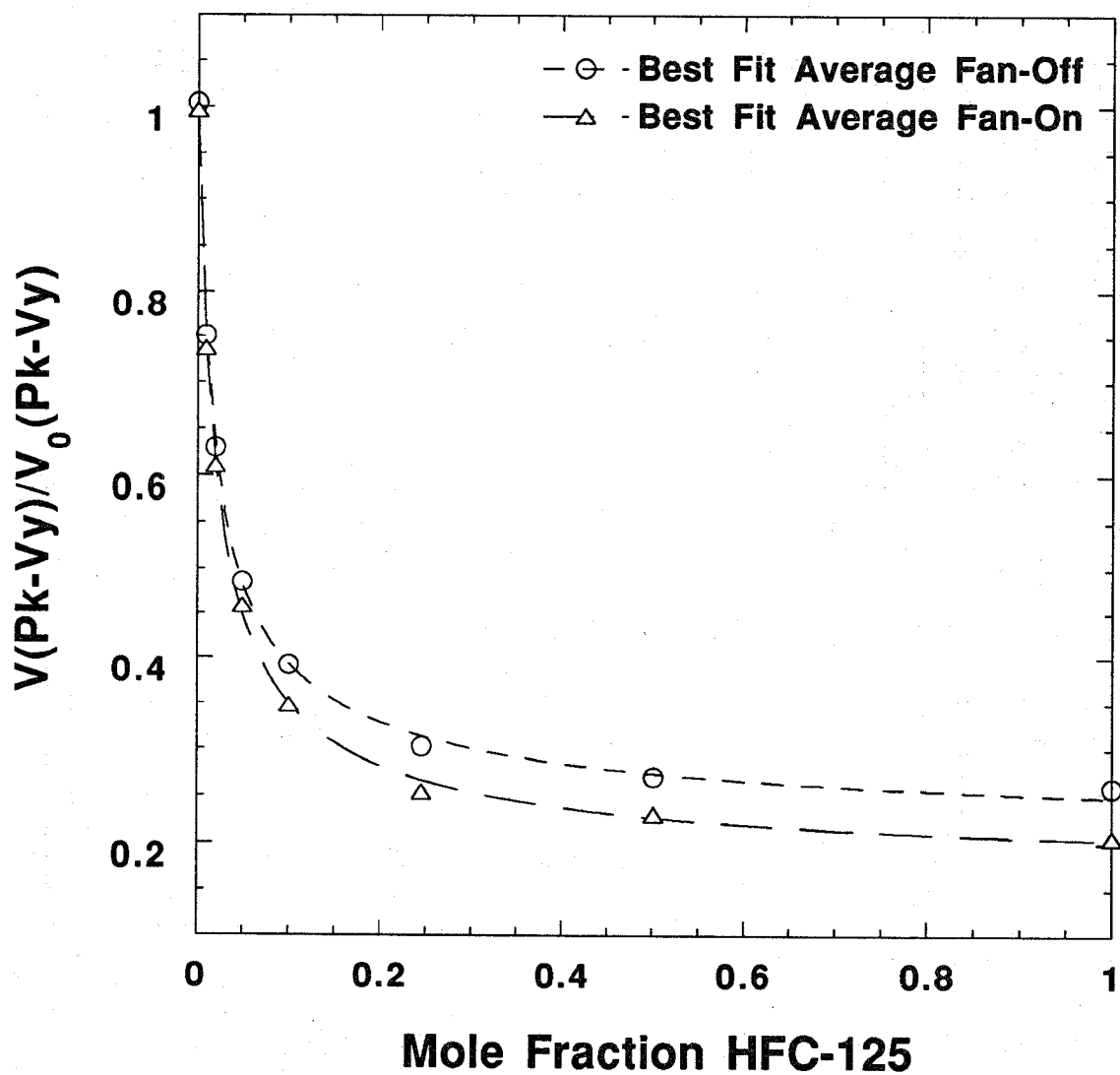


Figure 72. The effect of air flow on the calibration curve of the DIRRACS modified with a wide band-pass filter.

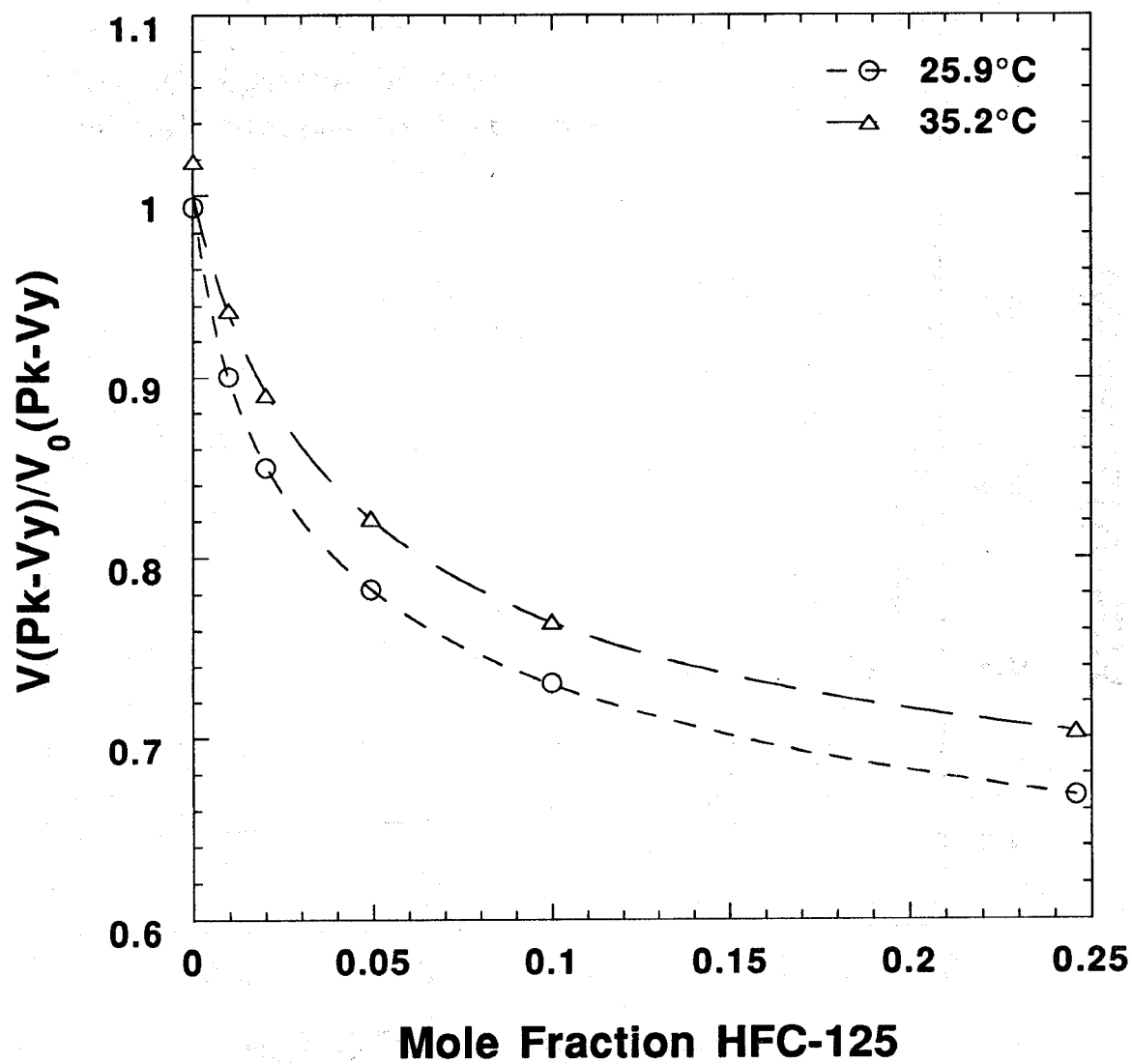


Figure 73. Effect of temperature within the "box" chamber on the DIRRACS calibration.

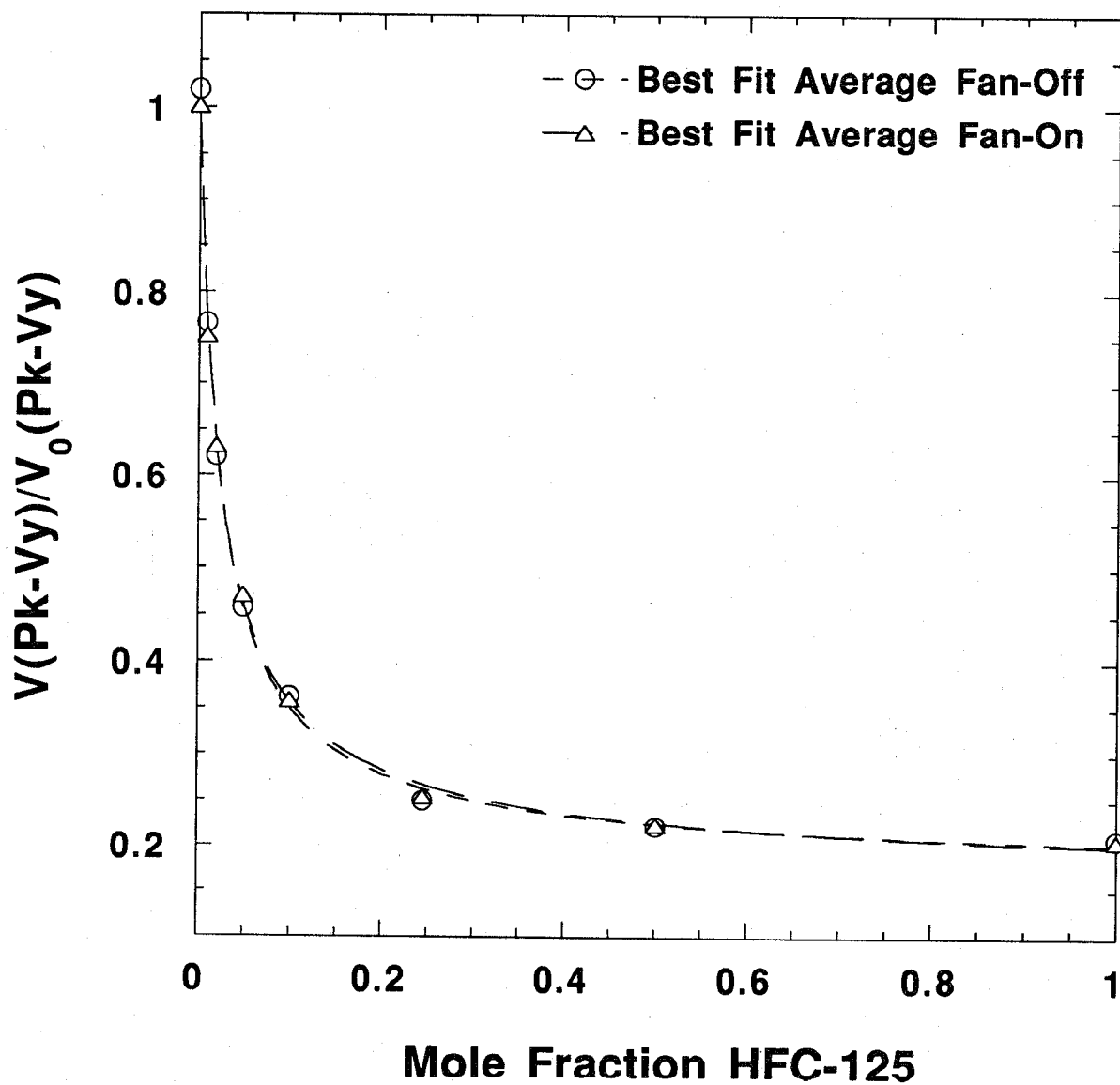


Figure 74. Effect of air flow with water-cooled IR source housing on the DIRRACS calibration.

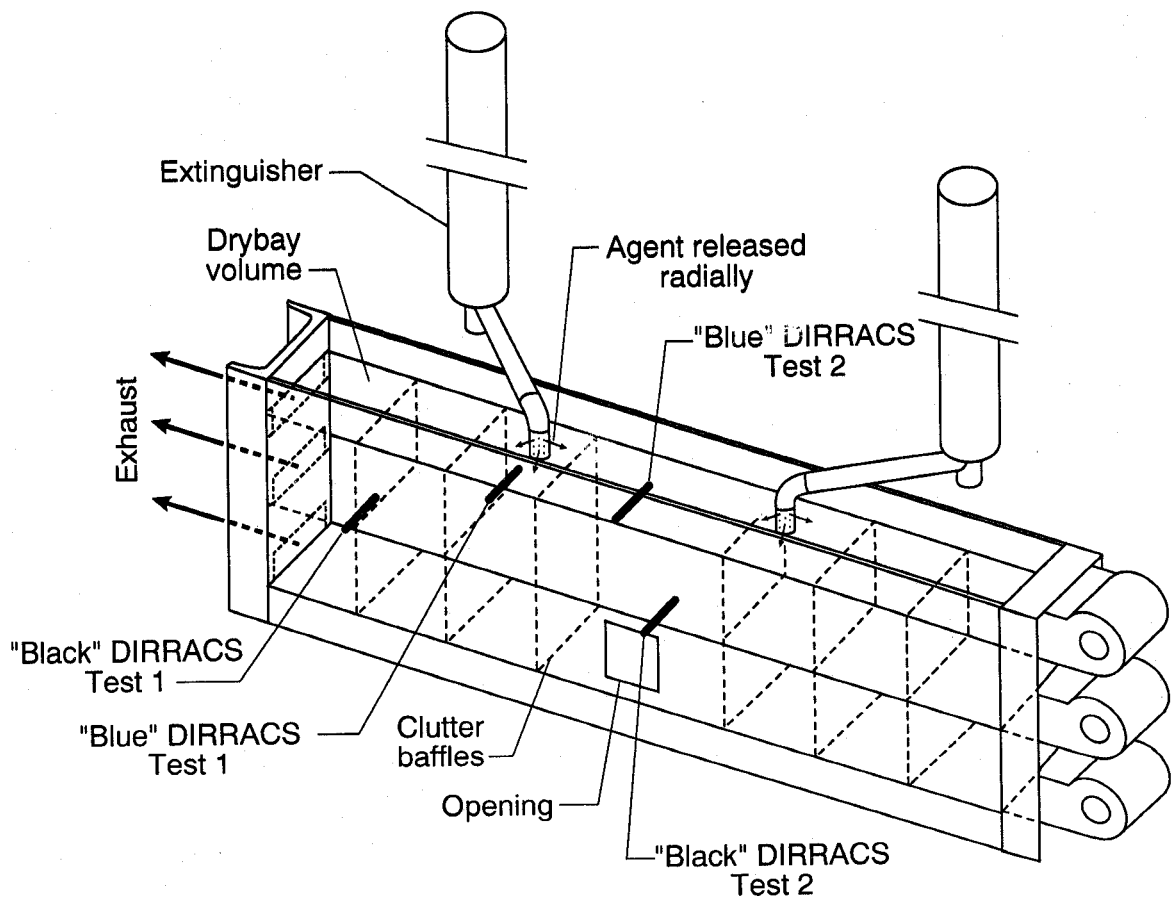


Figure 75. Illustration of simulated dry bay at Wright-Patterson, AFB.

agent concentration probe, which was tested at the same time (See Section 11.2.6).

Figure 76 shows smoothed concentration data versus time as 0.23 kg (0.5 lb) of the agent were released. The agent was released simultaneously from two extinguishers by the firing of squibs, one each, positioned below metal diaphragms. An electrical discharge fired the squibs, which perforated the diaphragms allowing the agent to be discharged. If the agent had been uniformly distributed throughout the volume, the concentration would have been 1.3 % by volume. Initially there is a spike in the readings which may be caused by electrical noise associated with the firing of the squib used to release the agent. Approximately 1 s after release the DIRRACS near the discharge recorded a peak concentration of about 4 %, while the DIRRACS near the exhaust required about 8 s to reach a 1 % concentration. At least 2 s after agent release is required before a noticeable increase in concentration is observed near the exhaust. This time far exceeds the desired 30 ms time to extinguish a dry-bay fire. If the test fires are suppressed by an agent released far from the fire, our results would suggest that the flame extinction is not a direct suppression effect of the agent on the fire.

We also show a second set of data where the DIRRACS probes were moved so that one was near the opening used to simulate the entry point of a projectile into the dry bay and the second was located directly above it nearer the discharges. In this case, the mass of agent released was increased by a factor of four to 0.9 kg (2 lb). It is seen in Figure 77 that there is a momentary 9 % spike in the concentration near the exhaust for about 100 ms and then a decrease to about 1 %; on the other hand, near the discharge the concentration builds up to about 40 % 2 s after the discharge. We suspect that the value of 40 % may be a factor of two higher than actually present based on the flow effect discussed in the previous section. It is noteworthy that these are the first time-resolved dry-bay measurements that have been made!

In the course of carrying out the tests we encountered several difficulties. There was a problem with false-trigger signals apparently arising from the high noise on the transmission line from the Wright-Patterson control system to the NIST data-acquisition system. We ran a total of six tests, but only two gave useful data. Secondly, there appeared to be electrical interference arising from the squib firing, which initiated the agent release. At the time, the DIRRACS was grounded to the instrument chassis; however, the squib is grounded to the dry bay, which is in physical contact with the instrument chassis. To correct the problem, we now have a separate instrument ground. The final problem was an apparent leak around the ZnS window on the light transmission tube for one of the DIRRACS, which was corrected back at NIST.

While no engine nacelle testing was performed, it was found that the DIRRACS was compatible with the opening in the engine nacelle test facility.

**11.3.9.2 Testing in the Turbulent Spray Burner Facility at NIST.** The turbulent spray burner facility (see Section 9 of this report) at NIST allows the release of a pulse of agent from a 6.5 cm diameter tube. Both the concentration and duration of the pulse can be controlled. A combination of radial injection ports for the agent into the air stream and two sets of screens ensured uniform mixing of the agent with the air. Typical test conditions were an agent release mole fraction of 0.08 for 200 ms. Both DIRRACS probes were placed in series just downstream of the flame stabilization disk. The air-flow velocity was on the order of 20 m/s. Figure 78 shows the peak-to-valley voltages recorded during one of these tests for HFC-125 with the agent first flowing through the "black" DIRRACS and then the "blue" DIRRACS. Using the appropriate calibration curves the data is converted into concentration versus time. The resulting curves are shown in Figure 79 and 29 point smoothed curves are shown in Figure 80. The solid horizontal line is the expected concentration based on the known amount of agent released during the test (0.088 mole fraction). It is seen that the blue DIRRACS result is about 33 % greater than the actual concentration while the black DIRRACS is about 90 % greater. The differences between the measured and predicted results are thought to result



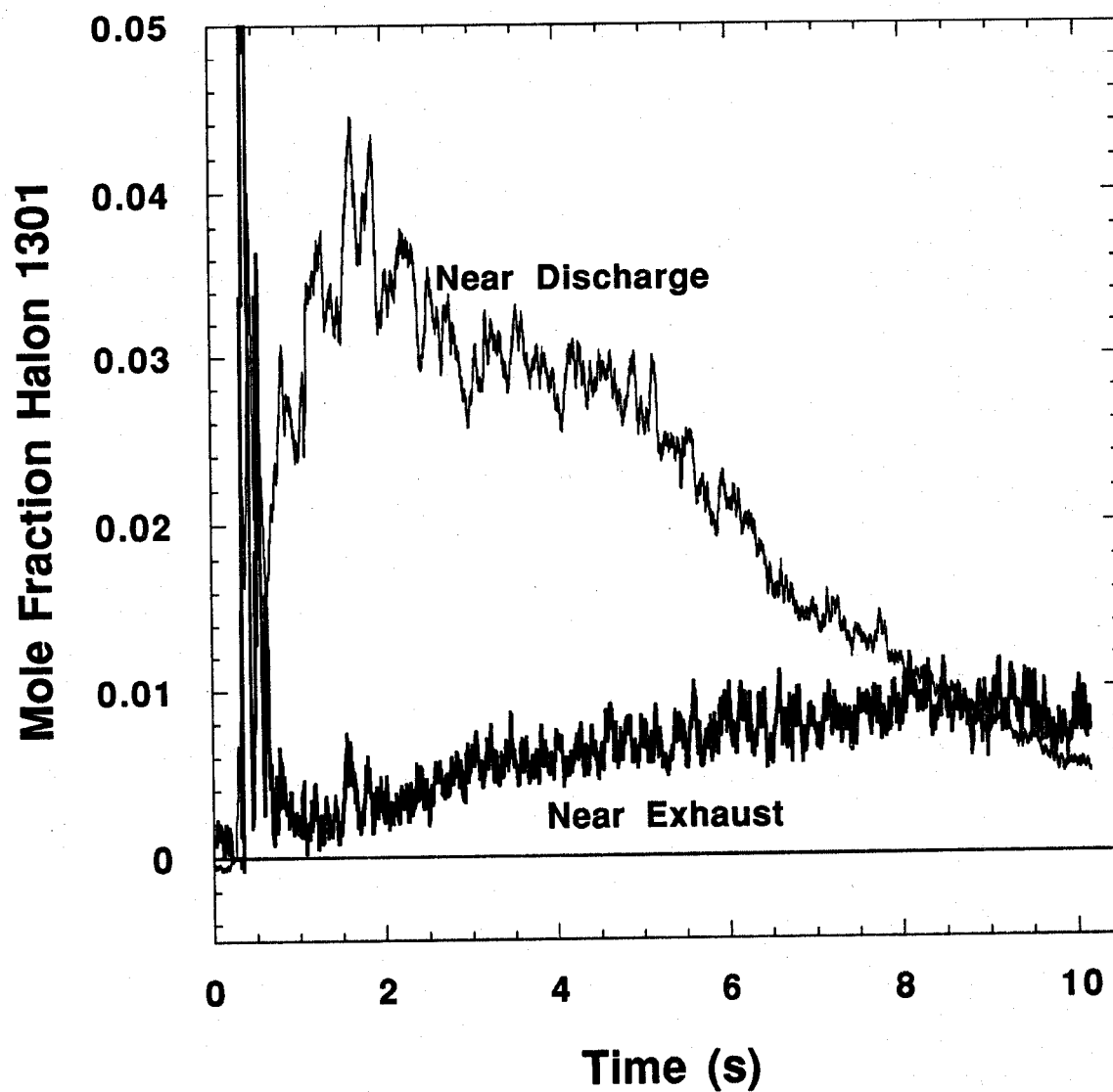


Figure 76. Concentration versus time for the total release of 0.23 kg (1/2 lb) of halon 1301. A 29 point smoothing of the data has been used. The exhaust position is at the far left side of the facility.

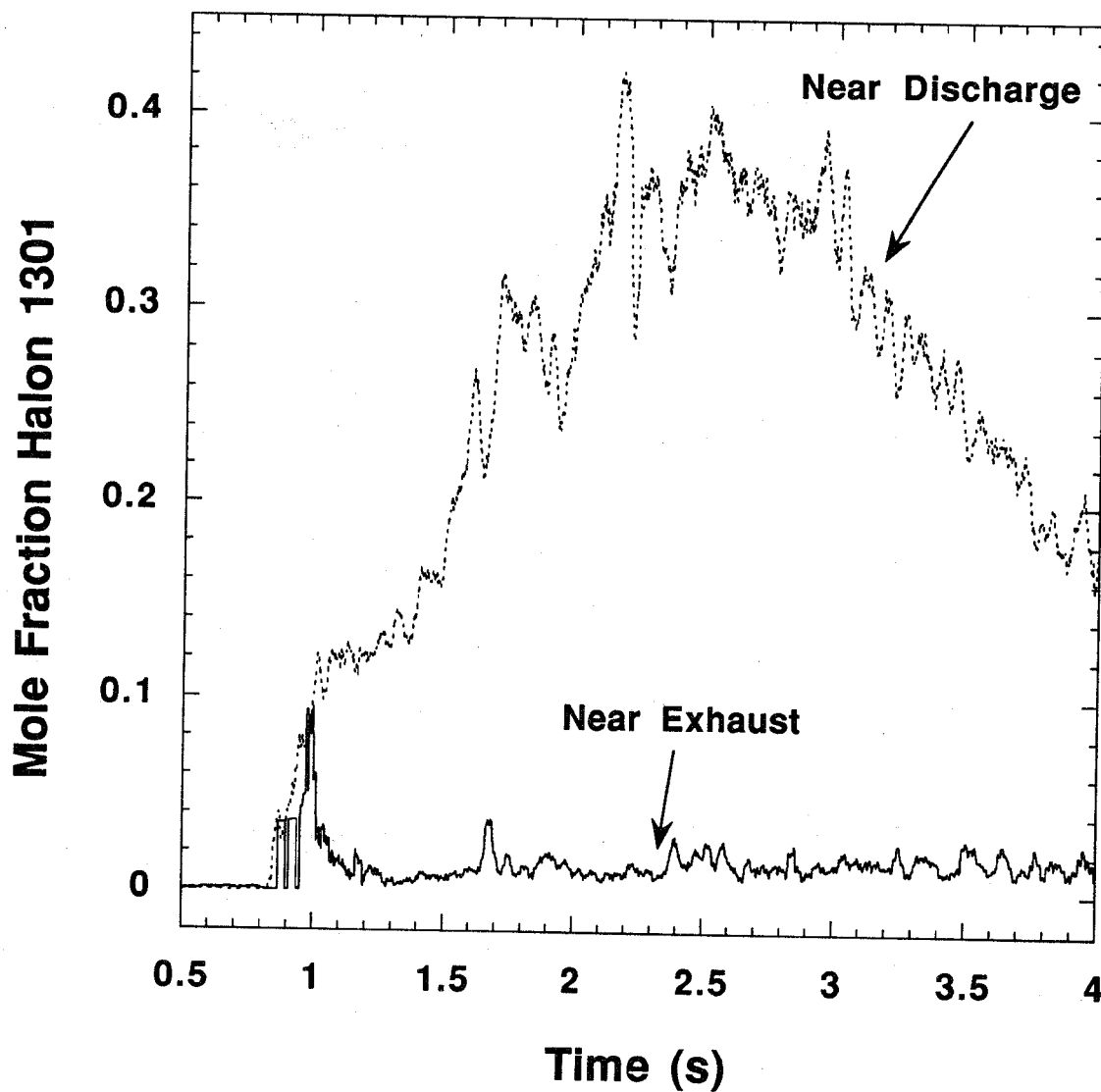


Figure 77. Concentration versus time for the total release of 0.9 kg (2 lb) of halon 1301. The exhaust position corresponds to the opening in the front center of the facility.

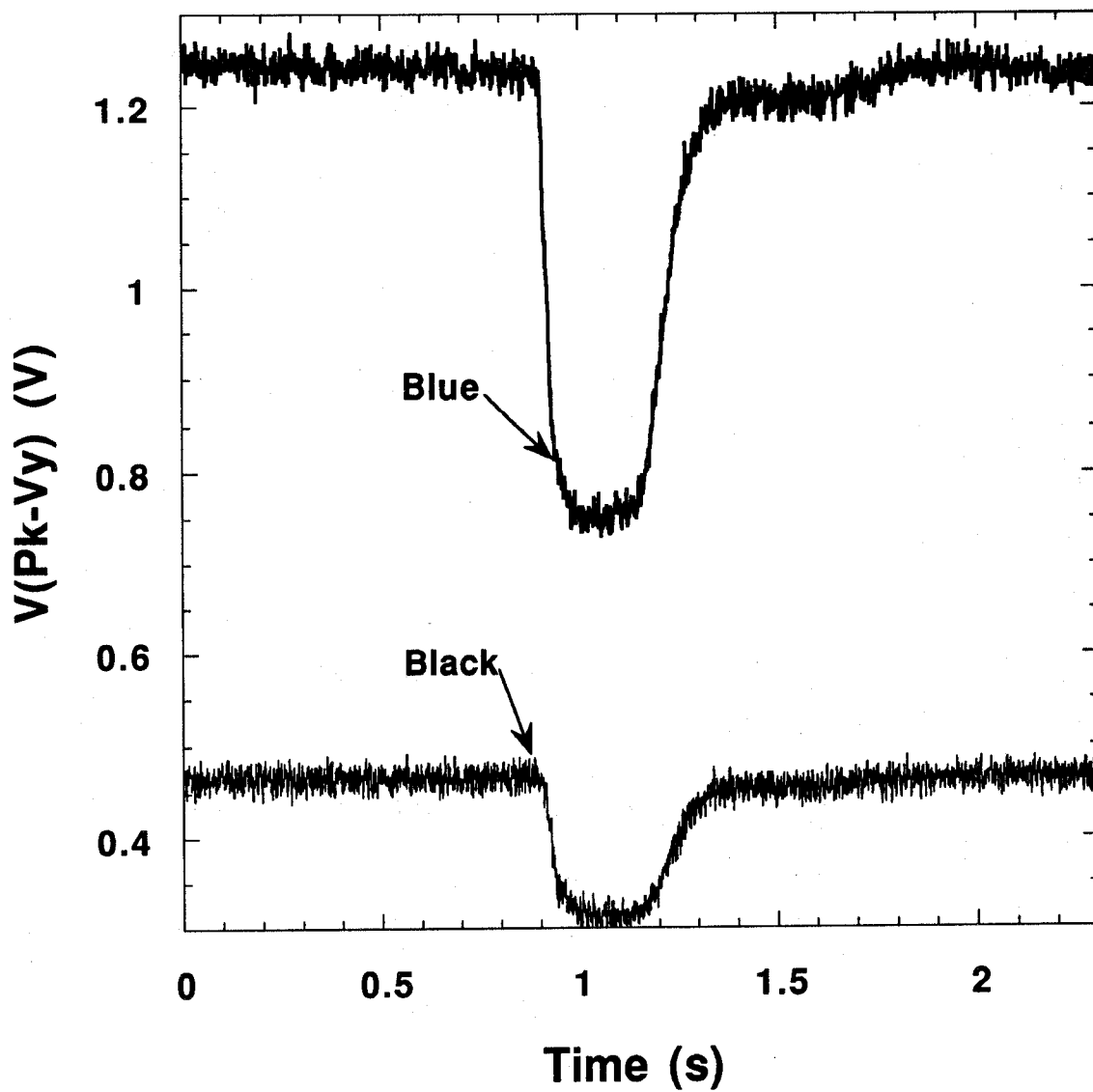


Figure 78. The Pk-Vy voltage is plotted versus time for a release of HFC-125/N<sub>2</sub> mixture from a 6.5 cm diameter pipe at a velocity of about 20 m/s.

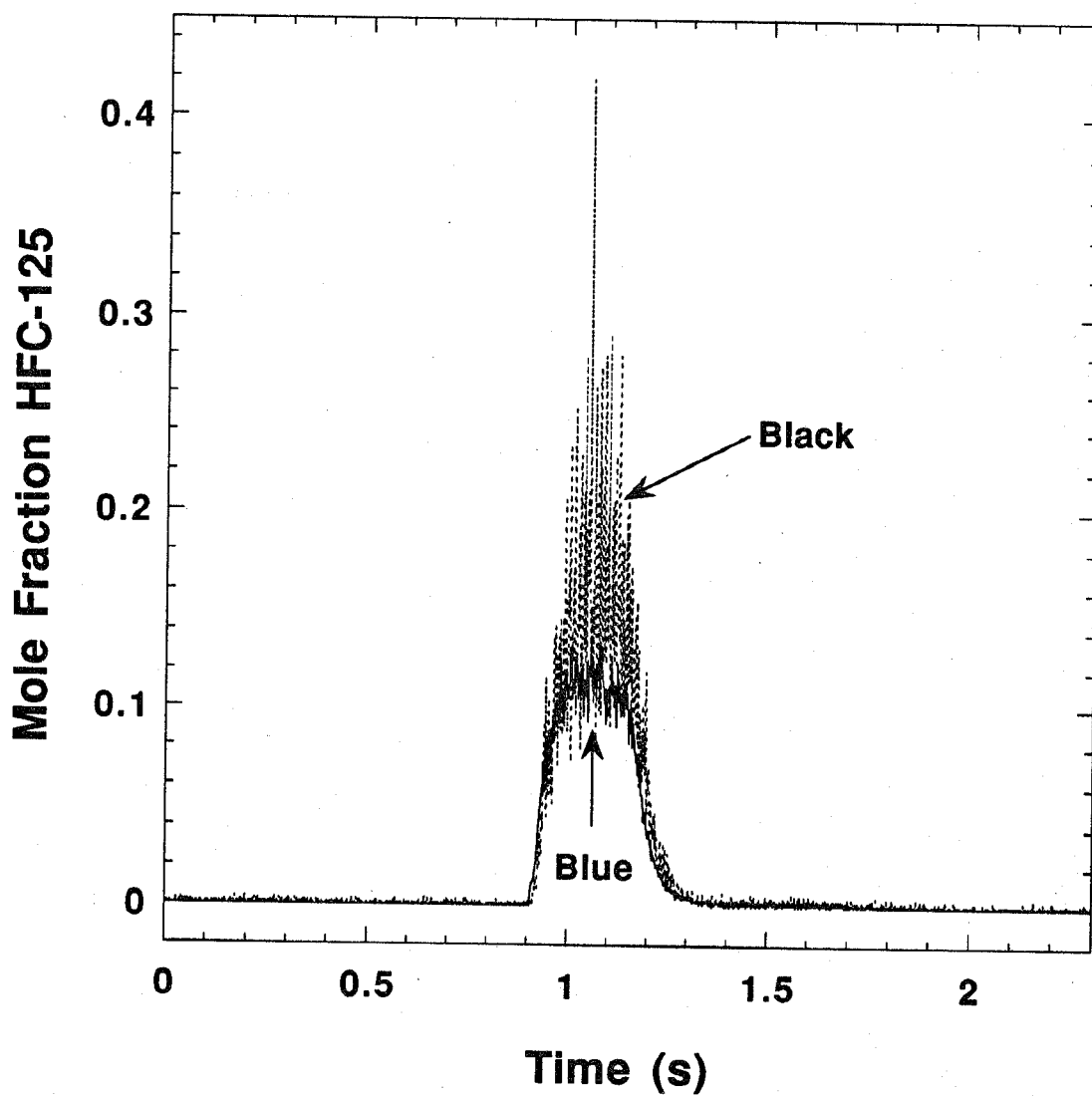


Figure 79. Concentration versus time for a HFC-125 release into the turbulent spray flame burner based on the analysis of the data in the previous figure. The data is not smoothed.

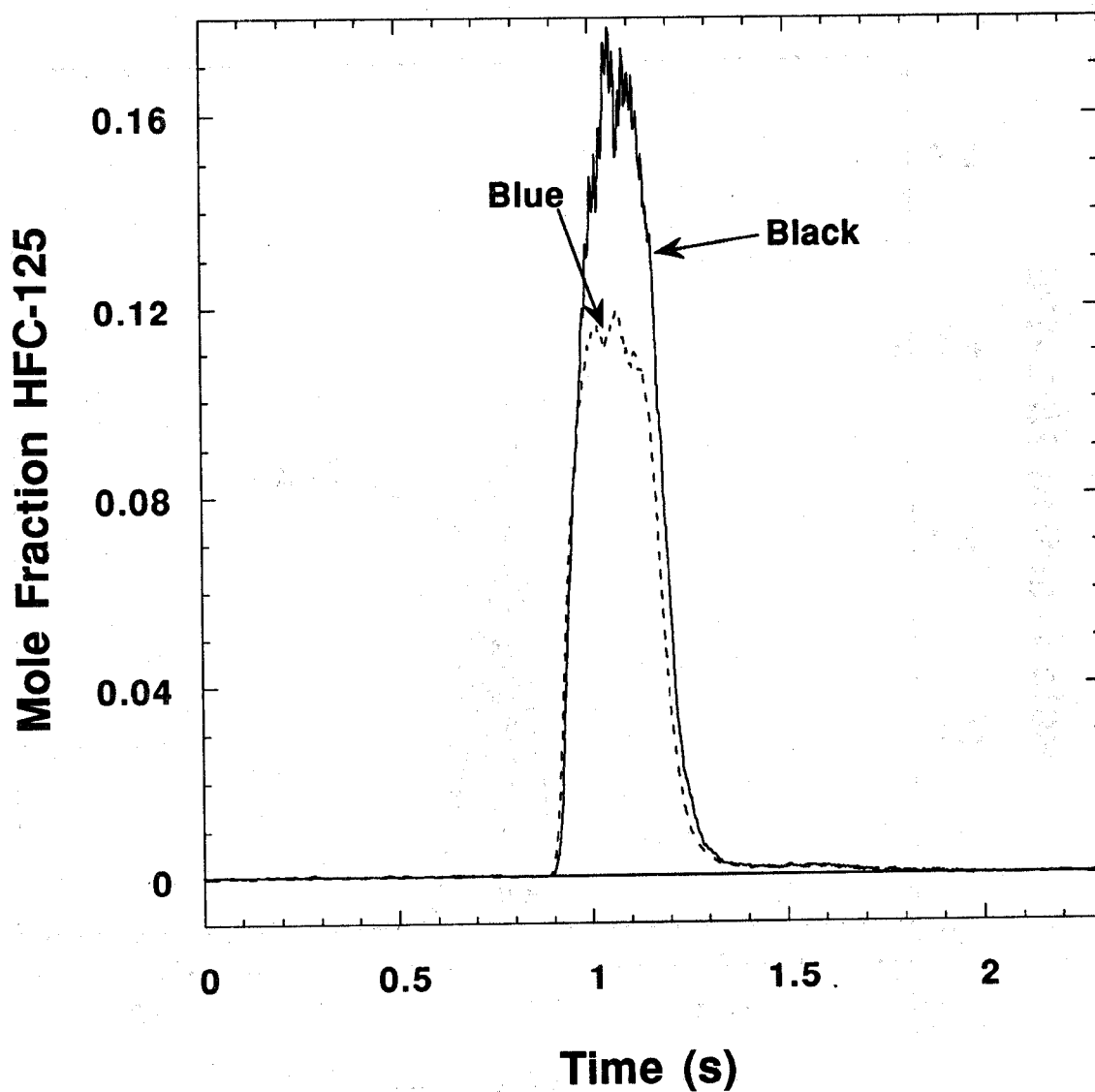


Figure 80. A 29 point smoothing of the data in the previous figure for a HFC-125 release. The solid line represents the nominal concentration for the release.

from the calibrations for the instruments being effected by the flow as discussed in the instrument calibration section.

While the absolute concentration is in error, the duration of the concentration pulse measured by the DIRRACS of 240 ms was in good agreement with both the predicted response time and the output of the combined aspirated hot-film/cold-wire agent concentration probe. Furthermore, this good agreement indicates that the low-band-pass filter used with the DIRRACS does not qualitatively distort the response for the conditions of this release. The peak for the DIRRACS concentration is rounded while the combined probe measured concentration has a trapezoidal shape with an extended flat section. We speculate that the difference is caused by the much larger probe volume of the DIRRACS compared to the combined sensor.

The value of  $\Delta C/C$  is 0.12 for the blue unit and 0.34 for the black unit based on 30 ms of unsmoothed data over the flat period. The value for the blue unit is about 3 times larger than the value of  $\Delta C/C$  obtained for the calibration curves, and the value for the black unit is about 6 times larger. The cause of this large decrease in performance during actual testing is not known. One possible factor is that the agent uniformly fills the sensing volume during the calibration but does not during the test release.

An effort was made to perform a final test with a cooled sensor, but the results were not conclusive. Components were used from both devices because the heating element burned out in the blue DIRRACS and the only wide-band-pass filter was mounted on the blue DIRRACS. The noise level was high, but the results indicated an instrument signal appreciably greater than the expected value. One possible reason is that the cooling coil is not adequate to fully cool the infrared source housing. The flow in the burner, which is faster than that present during the calibration measurements, may cause additional cooling of the source housing, thus affecting the output of the instrument.

**11.3.10 Summary and Recommendations.** The concept of using an incandescent source and a pyroelectric sensor for a millisecond time response fire-agent concentration measurement has been validated, even though the original instrument developed on this principle, the Fire Extinguishing Agent Sensor (FEAS), was found lacking in performance. The sensor output signal of the FEAS was dependent on frequency and had a low signal-to-noise ratio. Modelling of a modified FEAS with a flat frequency response indicated possible application as a qualitative probe.

An improved system, designated as the DIRRACS, was developed which has a stronger infrared source, larger area detector, and wider IR band-pass filter compared to the FEAS. The use of an optical chopper produces a millisecond time response, but the sample size can limit the effective time response for velocities less than 30 m/s. The total cost of the components is less than \$5,000. The DIRRACS is compatible with both dry-bay and engine-nacelle test facility at Wright-Patterson AFB.

The current design has an average uncertainty,  $\Delta C/C$ , in the repeatability of the concentration calibrations of 0.05 for the blue unit and 0.12 for the black unit at the 95 % confidence interval. However, data collected during an actual release indicated larger uncertainties of  $\Delta C/C$  of 0.15 and 0.40 respectively. A more comprehensive uncertainty analysis is not warranted until the large effect of flow on the instrument response is eliminated.

This study includes the first measurements of the dispersal time of an agent in the dry-bay test facility at Wright-Patterson AFB. The preliminary measurements indicate a relatively long time on the order of a few seconds for dispersal of the agent throughout the large dry bay. This information has important implications about the mechanism of extinguishment when the fire is far from the release point of the agent. If the fire is extinguished under these conditions, the mechanism must not involve a direct interaction of the agent with the fire if one assumes the presence of the fire does not affect the distribution of the agent. More research is needed to understand what the controlling mechanism is for flame extinction.

One major obstacle which must be overcome before the DIRRACS can be used for quantitative concentration measurements is the effect of the surrounding flow on the instrument response. Because of the large flow effect, the DIRRACS output could be in error by 50 % at high flow velocities for agent concentrations in the range 30 % - 100 %. We attempted to cool the source housing to minimize the effect of the flow velocity on the housing temperature. The results were encouraging, but not conclusive. Additional development of the cooling system may greatly reduce the flow effect on the instrument output.

A second desired improvement is to reduce the sampling volume of the instrument in order to improve the effective temporal resolution. Such a reduction is feasible, though a number of refinements may be needed to offset the reduction in signal. These include providing a constant temperature for the detector housing, improved acoustic isolation of the sensor, coated windows, polished light-transmission tube, and optimized collection cone. The first two of these refinements were crucial in the development of an accurate CO<sub>2</sub> gas monitor using a pyroelectric detector by Takeuchi *et al.* (1993).

Another issue to be resolved is the possible effect of the use of a low-band-pass filter on the temporal response of the DIRRACS.

## 11.4 Review of Statham and Halonyzer Extinguishing-Agent Concentration Recorders

Two instruments have been certified by the FAA for measuring halon 1301 concentrations within a nacelle during certification of fire-extinguishment systems. These are the Statham analyzer manufactured by Statham Laboratories of Los Angeles, CA under contract from the United States Air Force and the Halonyzer which is based on similar design principles as the Statham analyzer and was produced by the HTL Division of Pacific Scientific of Duarte, CA.

The early history of the development of these instruments can be traced through a 1947 Air Force report and a patent (Yanikoski, 1952) filed October 18, 1946 and issued on Feb. 26, 1952. In the original patent application the device was referred to as a "Gas Analysis Apparatus." The basic operating principles of these devices are straight forward. The patent application provides a good description of the basis for the devices in use today.

Figure 81 shows the drawings included in the patent filing. The gas to be analyzed is generally drawn through a tube into the instrument. The instrument inlet is denoted by "5" in drawing "Fig. 1" of Figure 81. The insulated instrument is maintained at a constant temperature using a thermostated heater. The flow enters a heat exchanger (denoted "6" in the drawing) which heats the gas flow rapidly to a predetermined temperature. Once the gas has been heated it enters a restriction made of porous material ("13" in the drawing) which ensures viscous flow and results in a pressure drop as a result of its resistance to flow. For these flow conditions the resulting pressure drop,  $\Delta P$ , is

$$\Delta P = c_2 \mu Q, \quad (54)$$

where  $\mu$  is the dynamic viscosity,  $Q$  is the volumetric flow rate and  $c_2$  is a constant. Fittings "17" and "18" are placed just before and just after the flow restriction to allow the pressure drop to be measured. Any device capable of differential pressure measurement may be used. In the drawing a manometer, "19", is shown.

A second restriction, marked "20" in the drawing, is placed in the flow downstream of the first restriction. This restriction is designed to be a sonic orifice which provides the maximum possible

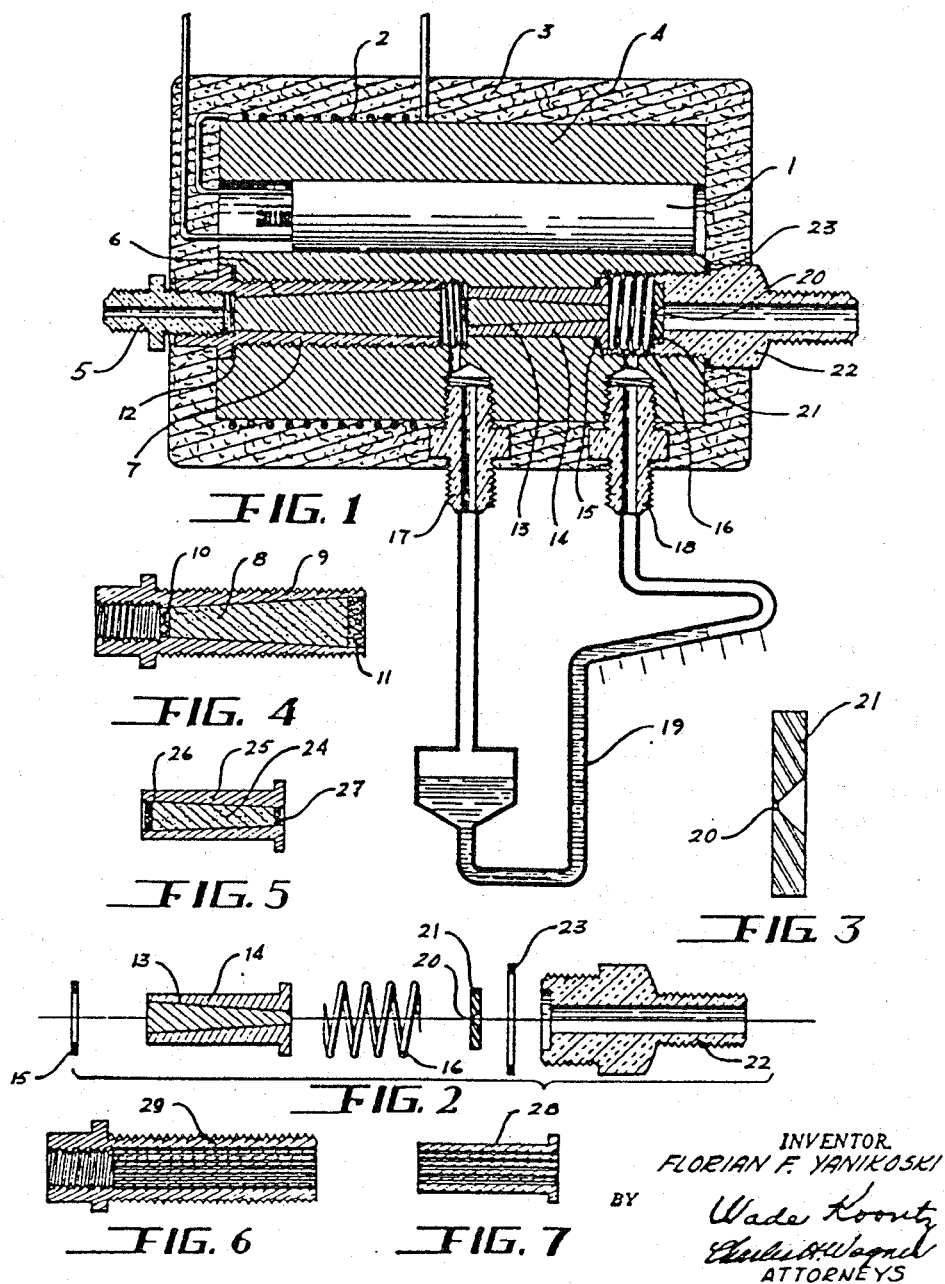


Figure 81. Schematic for a "Gas Analysis Apparatus" reproduced from the United States patent of Yanikoski (1952).



volume-flow rate when the flow is choked, which is generally true when the pressure downstream of the sonic orifice is maintained at less than one half the upstream pressure. The volume-flow rate through a choked orifice can be written as

$$Q = c_2 \frac{\pi d_{so}^2}{4} \sqrt{\frac{gTR}{MW} \gamma \left( \frac{2}{\gamma+1} \right)^{\frac{\gamma+1}{\gamma-1}}}, \quad (55)$$

where  $c_2$  is a constant,  $d_{so}$  is the diameter of the orifice,  $MW$  is the molecular weight of the gas,  $g$  is the gravitational constant,  $T$  is the temperature,  $R$  is the universal gas constant, and  $\gamma$  is the ratio of the constant pressure and constant volume heat capacities of the gas. Note that Equation (55) is a different form of Equation (11) introduced in Section 11.2.1.2 during the discussion of aspirated hot-film concentration probes.

Since the temperature is a constant, the volume flow rate through the sonic orifice is only a function of the square root of the product of the gas  $\gamma$  and the inverse molecular weight. The value of  $Q$  which appears in Equation (54) should therefore be a unique function of concentration for a given binary gas mixture. In general, values of  $\mu$  depend on molecular composition and will vary with concentration in binary gas mixtures. By substituting Equation (55), Equation (54) can be rewritten as

$$\Delta P = c_3 \frac{\mu}{\sqrt{MW}} \sqrt{\gamma \left( \frac{2}{\gamma+1} \right)^{\frac{\gamma+1}{\gamma-1}}}, \quad (56)$$

where  $MW$ ,  $\mu$ , and  $\gamma$  all depend on the concentration of species 1 in the binary mixture. Note that one or both of the components can actually be a well defined mixture of gases such as air.

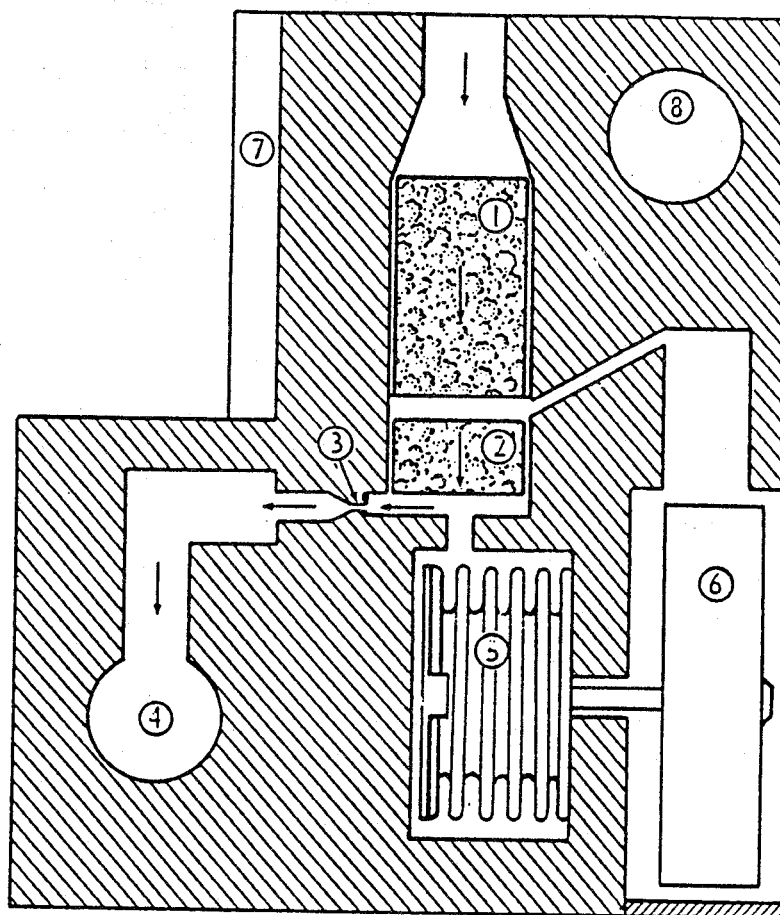
Equation (56) allows the expected variation in pressure drop across the first flow restriction to be predicted when the required molecular properties are known for the pure gases and mixtures. Note that the overall response is a function of a number of variables. In practice, it is common to calibrate the response of the analyzer by recording the measured pressure drop for the pure gases and assuming a linear dependence of pressure change on concentration (such a measurement is often referred to as "Relative Concentration") or by calibrating the pressure drops for a number of known mixtures and curve fitting the resulting pressure changes to the known concentrations.

A discussion concerning the response time of the instrument was not provided by Yanikoski, but it was stated that "One object of the invention is to provide a gas analysis apparatus capable of very high speeds in responding to a change in the composition of the sample."

New and Middlesworth (1953) reported extensive characterization tests of the first Statham analyzer (Model GA-1) delivered to the Air Force. They reported that the specifications for the instrument were:

1. An instrument capable of continuous recording of agent concentration for gases drawn from eighteen regions,
2. A response time of 0.1 s to a concentration change of 100 %,
3. A measurement error not to exceed  $\pm 3$  % over the full concentration range,
4. Accurate measurements over normal ranges of temperature and pressure, and
5. Capable of being operated on flying aircraft.

Figure 82 reproduces a schematic for a typical analyzer cell taken from the report. The primary features discussed in the patent can be seen. The flow enters the heated metal block of the cell as



- 1 - TEMPERATURE-REGULATING POROUS PLUG
  - 2 - PRESSURE-DROP POROUS PLUG
  - 3 - CRITICAL FLOW ORIFICE
  - 4 - VACUUM MANIFOLD
  - 5 - PRESSURE-SENSITIVE BELLOWS
  - 6 - STRAIN GAGE
  - 7 - HEATING ELEMENT
  - 8 - THERMOSTAT TEMPERATURE CONTROL
  - 9 - METAL BLOCK
- } TRANSDUCER A

Figure 82. Schematic for a single analyzer cell of a Statham gas analyzer reproduced from the report of New and Middlesworth (1953).

shown. The heat exchanger is a porous plug ("1" in the figure) which is followed by a second porous plug ("2") over which the pressure drop is measured. In this design the pressure change is measured using a pressure-sensitive bellows attached to a Statham strain gage which outputs an electrical signal proportional to the displacement of the bellows. The volume flow rate is controlled by a sonic orifice ("3"). Vacuum was applied through a manifold machined into the metal block. The voltage outputs of the strain gages were recorded using a remotely controlled oscillograph.

The overall analyzer unit consisted of eighteen analyzer cells assembled in two groups which allowed eighteen simultaneous measurements to be recorded. Samples were drawn into the analyzers through electrically heated 1.8 m lengths of copper tubing. New and Middlesworth reported that a period of 0.10 s was required for the instrument to respond (defined as the period required to attain 95 % of the maximum displacement) to an instantaneous increase of carbon dioxide concentration from 0 % to 100 % when the gas was introduced directly into the instrument. When the 1.8 m sample line was used the response time increased to 0.25 s. The increase in response time was attributed to molecular diffusion in the sample line during the period required for flow from the sampling point to the instrument.

The response of the instrument was analyzed using Equations (54) - (56). The expected response for a particular gas was characterized by calculating the expected pressure change ratio for the test gas relative to that for air using Equation (56). Unfortunately, the authors did not report the operating temperature of the analyzer. Three fire-fighting agents; carbon dioxide, methyl bromide, and bromochloromethane; were considered. Table 11 lists the predicted ratios of  $\Delta P$  for the three agents. Note that substantial differences in  $\Delta P$  are predicted on going from air to high concentrations of the agents.

By recording the instrument response for air and the agents, experimental values were determined for these ratios. The results are included in Table 11. It can be seen that while the theoretical predictions reproduce the general trends observed for changes in the ratios with agent, the quantitative agreement is poor. The reason for the poor agreement between the theoretical and actual response of the instrument was not determined, but it was speculated that it may have been due to departures from the ideal gas law.

The response of the instrument to changes in concentration was assumed to be linear. With this assumption, the percentage of agent in air could be calculated using

$$\% \text{ Agent} = 100 \frac{\Delta P_{\text{air}} - \Delta P_{\text{mix}}}{\Delta P_{\text{air}} - \Delta P_{\text{agent}}}, \quad (57)$$

where the subscripts refer to measurements for air, the agent, and the unknown mixture. In practice, the values which were used in Equation (57) were the displacements of the recorded response which should be proportional to  $\Delta P$ . A number of tests were run on known concentrations of carbon dioxide in air varying from 25 % to 75 %. Measured values were found to agree within 5 %.

The sensitivity of the instrument to variations in ambient pressure and relative humidity were discussed. In general, these parameters require small, but significant, corrections.

The instrument was tested during simulated fire testing on a B-45 nacelle using carbon dioxide. Reliable concentration measurements were obtained which allowed an evaluation of the extinguishing system. Measurements were also performed during actual flights and found to be satisfactory.

Hough (1959) considered the response of the Statham analyzer in more detail. His work was an outgrowth of an uncited study by the Federal Aeronautics Administration which indicated that the response of the instrument was not linear as assumed in deriving Equation (57). Both theoretical and experimental results are presented.

Table 11. Various Values of  $\Delta P_{\text{agent}}/\Delta P_{\text{air}}$  Reported in the Literature for the Statham Analyzer.

Agent	Predicted (New and Middlesworth)	Observed (New and Middlesworth)	Predicted (Hough)	Observed (Demaree and Dierdorf)
CO <sub>2</sub>	0.64	0.73	0.729	0.717
CH <sub>2</sub> BrCl	0.375	0.51	0.400	0.395
CH <sub>3</sub> Br	0.316	0.40	-	0.466
CF <sub>3</sub> Br	-	-	0.403	0.401
CF <sub>2</sub> Br <sub>2</sub>	-	-	0.328	0.319

The analyzer considered in this case was slightly different than the original system described by New and Middlesworth (1953). Instead of eighteen cells it contained twelve. The operating temperature of the instrument was reported to be 116 °C.

In order to understand the nonlinear behavior Hough started with Equation (56). He used known values of  $\mu$ ,  $\gamma$ , and MW to calculate expected values of  $\Delta P_{\text{agent}}/\Delta P_{\text{air}}$  for CF<sub>3</sub>Br, CF<sub>2</sub>Br<sub>2</sub>, CH<sub>2</sub>BrCl, and CO<sub>2</sub>. The results of the calculations are included in Table 11. Similar calculations were carried out for intermediate concentrations (10 %, 20 %, 40 %, 60 %, and 80 %) of the agents. The data were plotted in such a way that variations due to changes in  $\mu$  and  $\gamma$  with concentration were emphasized. The analysis showed that the variation of  $\mu$  introduced some nonlinearity into the expected response. The degree of nonlinearity was least for CO<sub>2</sub> and increased in the order CH<sub>2</sub>BrCl, CF<sub>3</sub>Br, and CF<sub>2</sub>Br<sub>2</sub>. Values of  $\gamma$  were assumed to vary linearly with concentration. When these values were incorporated into Equation (56) it was demonstrated that the dependence on  $\gamma$  also introduced nonlinear dependencies on concentration into the predicted response curves.

The deviation of the theoretical response from a linear dependence resulted in large errors when a linear response, which was the basis for Equation (57), was assumed. An indication of the large errors is obtained from the results listed in Table 12 taken from Hough (1959), where concentration values (in %) which were obtained using Equation (57) are listed as functions of the assumed actual concentrations for the four agents. In some cases the differences are greater than 100 %.

As part of the analysis, values of concentration for mixtures of air and CF<sub>3</sub>Br recorded using the Statham analyzer and Equation (57) were compared to the actual concentrations for the mixtures. The differences in actual and measured values were large, but the differences were well explained by the analysis discussed above. On this basis the author provided four charts which were used to convert measurements of an agent's relative concentration using Equation (57) to corrected values. The uncertainty in a concentration measurement following correction was estimated to be less than 1 %. A brief discussion indicated that the analysis also did a good job of predicting the nonlinear behaviors observed in the earlier FAA tests.

Demaree and Dierdorf (1959) have provided a detailed account of the operating and installation procedures for a Model GA-2A Statham Analyzer. This instrument is different than the earlier model discussed above in that it utilizes 12 cells arranged in three analyzer units. The theory and principles

Table 12. Predicted Relative Mole Per Cent (Assuming Linear Response of Statham Analyzer) as Function of Actual Mole Per Cent in Various Agent/Air Mixtures Based on the Calculations of Hough (1959)

Actual agent mole per cent	Prediction of indicated agent mole per cent			
	CF <sub>3</sub> Br	CF <sub>2</sub> Br <sub>2</sub>	CH <sub>2</sub> BrCl	CO <sub>2</sub>
0.00	0.00	0.00	0.00	0.00
10.0	27.3	31.9	22.5	14.8
20.0	45.6	50.0	38.3	23.6
40.0	67.5	70.7	60.8	45.8
60.0	82.3	83.5	76.8	65.7
80.0	91.8	92.7	89.4	83.4
100.0	100.0	100.0	100.0	0.319

for operation of the device are the same as discussed by New and Middlesworth (1953). Instructions were provided for mounting the equipment for flight tests. This included the use of 6.4 mm copper tubes for extracting samples. It was noted that, in order to prevent the analyzer cells from becoming clogged with fine suspensions carried by the gas, a filter was used to at the end of each sampling line to remove particles.

The initial data treatment was identical to that described above. Equation (57) was used to calculate relative concentrations for the agent. The authors noted that it was not necessary to calibrate the instrument for a given agent before a test. Experimental ratios of  $\Delta P_{agent}$  and  $\Delta P_{air}$  were deemed constant enough to be used. These values are included in Table 11. Note that these values differ somewhat from those recommended by Hough (1959). Once relative concentration values were available, it was necessary to use calibration curves for the various agents to convert the results to either volume or mass percentages. Calibration curves were provided for CO<sub>2</sub>, CH<sub>3</sub>Br, CH<sub>2</sub>BrCl, CF<sub>2</sub>Br<sub>2</sub>, and CF<sub>3</sub>Br. Comparison of the calibrations curves for CO<sub>2</sub>, CH<sub>2</sub>BrCl, CF<sub>2</sub>Br<sub>2</sub>, and CF<sub>3</sub>Br with those provided by Hough shows that they are qualitatively similar, but that there are significant quantitative differences. As above, the use of Equation (57) without correction would lead to large errors in concentration measurements.

The report lists the concentrations of the agents required for extinguishment of a nacelle fire. The criteria for a system to be considered adequate was that all twelve sampling positions maintain the minimum required concentration at the same time for not less than 0.5 s.

A later FAA report by Chamberlain (1970) deals primarily with installation and test procedures for the Statham analyzer under actual testing conditions, but it does provide some details concerning the instrumentation, as well as discussing a number of findings from earlier test series. The instrument utilized was the same Model GA-2A discussed by Demaree and Dierdorf (1959). The operating temperature of the analyzer was listed as 121 °C. A schematic of one of the individual cells is included in the report which is identical to Figure 82 reproduced from New and Middlesworth (1953)

for the Model GA-1 Statham Analyzer. This suggests that there had been very little change in the cell configuration on going from the Model GA-1 to the Model GA-2. At the time of the report, the later version of the instrument had been in use for over 10 years.

A useful plot included in the report shows the delay time in the response of the analyzer to a concentration change as a function of the length of tubing used for sampling. The increase with tube length was roughly linear with a delay of 4.4 s for a 9.1 m length of tubing. The results indicate that the flow velocity in the tube was roughly 2.1 m/s.

The data analysis procedure recommended by Chamberlain was the same as that discussed by Demaree and Dierdorf. A detailed description of the procedure is given. An important recommendation was that concentration values be determined manually from the continuous recordings at 0.5 s intervals. Note that such plots will have very poor temporal resolution.

These authors concluded that the Statham Analyzer was at the time "the most comprehensive and practical means available for the determination of aircraft fire-extinguishing system performance."

From 1959 to 1968 the Federal Aviation Administration was actively engaged in the evaluation of fire-extinguishment systems for nacelles. After this time, this function was turned over to private contractors. In 1977 (Ferrarese) an advisory circular was issued which summarized the measurement approach. In addition to a discussion of earlier reports, this document incorporated several useful tables and graphs. One of these tables included the required extinguishing concentrations in weight per cent, volume percent, and relative concentration percent. This table is reproduced as Table 13.

Since this time a revised Statham Analyzer had been designed and constructed by Pacific Scientific (1988a, 1988b). This newer instrument is known as the Halonyzer. Its design principles are similar to those of the Statham Analyzer, but several design modifications have been incorporated into the newer instrument. One of the more significant changes is the replacement of the porous plug used for the pressure drop measurement with a series of capillary tubes. Instead of recording the instrument response as an analog output, a computer data-acquisition system has been included which is capable of recording data at a rate as high as 100 Hz. Additionally, calibration curves have been incorporated into the data analysis, so it is possible to obtain the results directly as either volume or mass percents of agent. This is in contrast to the Statham Analyzer, where relative concentrations were corrected manually using calibration curves. Current FAA procedures recommend the use of volume fraction for testing of fire-fighting agents. The documentation for the instrument indicates that the system is only certified for use with halon 1301 (Pacific Scientific, 1988a).

Documentation for the Halonyzer (Pacific Scientific, 1988a) indicates the system is designed to respond to a change from 100 % air to 100 % halon 1301 in 250 ms. William Meserve and Duane Van Ostrand of Pacific Scientific were kind enough to provide the authors with the results of a test designed to characterize the experimental time-response behavior of the instrument. For this test, three of the inputs for the Halonyzer were connected through different lengths of tubing (0.91 m, 3.7 m, and 7.6 m) to a flow system which could be rapidly switched from air to halon 1301 using a quick-dump valve. In this way, it was possible to characterize crudely the time response of the instrument.

Two different aspects of the response of the Halonyzer are relevant. The first is the period required for the agent to flow from the source to the detector. The second, and more important, time period is that required for the sensor to respond to the assumed step function increase in concentration. For the purposes of the current discussion, this period will be characterized by the time required for the measured halon 1301 concentration to increase from zero to 95 % following its earliest detection by the Halonyzer. Figure 83 shows a plot of the measured time of first detection of halon 1301 as a function of tube length. The data lie roughly on a straight line. The result of a linear least-squares-curve fit of the data is included on the figure. Note that the plot indicates that the flow was initiated at 390 ms which is consistent with the manner in which the experiment was performed (*i.e.*, the Halonyzer data scan was initiated just prior to switching the quick-dump valve). The slope of the line

Table 13. Required Concentrations of Various Fire-Fighting Agents for Aircraft Nacelles Taken from Ferrarese (1977)

Agent	Weight percent	Volume percent	Relative concentration
CO <sub>2</sub>	49	37	40
CH <sub>3</sub> Br	30	11	15
CH <sub>2</sub> BrCl	36	11	25
CF <sub>2</sub> Br <sub>2</sub>	26.5	5	15
CF <sub>3</sub> Br	22	6	15

indicates that the delay time increases with tubing length at roughly 389 ms/m. This value is similar to the value of 480 ms/m which can be derived from the results of Chamberlain (1970) for a Statham Analyzer.

By subtracting the time for first detection from the actual time, it is possible to plot the Halonyzer response for different sampling-tube lengths on a normalized time plot. The results are shown in Figure 84. It is clear that the period required for the instrument to respond fully to the change in concentration is increasing with the tubing length. This is quantified in Figure 85 where the time required to reach 95 % of the actual concentration change is plotted as a function of the tubing length. This plot shows clearly that the response time increases with tubing length. This observation is consistent with the occurrence of molecular diffusion within the sample during the time required to flow from the sampling position to the instrument as first suggested by New and Middlesworth (1953). The response time reported in this earlier work is somewhat shorter than shown in Figure 85, for which the shortest response time is extrapolated to be on the order of 600 ms, but definite conclusions can not be made because it is not known how fast the valve could be closed in the Pacific Scientific experiments.

The experimental results shown in Figure 83 to Figure 85 confirm the literature findings that significant delay times are required for the agent to flow from the sampling point, and that the longer the sampling tubes used, the longer is the response time of the instrument to a step increase in concentration. Practical minimum response times are significantly longer than 100 ms.

### 11.5 Literature Search For Additional Diagnostics for High-Speed Alternative-Agent Concentration Measurement

As part of the overall program on alternative-agent concentration measurement, a literature search was performed to identify possible alternative approaches to the combined aspirated hot-film/cold-wire probe and the Differential Infrared Rapid Agent Concentration Sensor already discussed in this report. The preceding section summarizes the characteristics of Statham Analyzers and Halonyzers which are currently used for certifying halon 1301 fire-extinguishing systems in aircraft nacelles. It was concluded that these devices do not have sufficient time response to meet the design goals of the

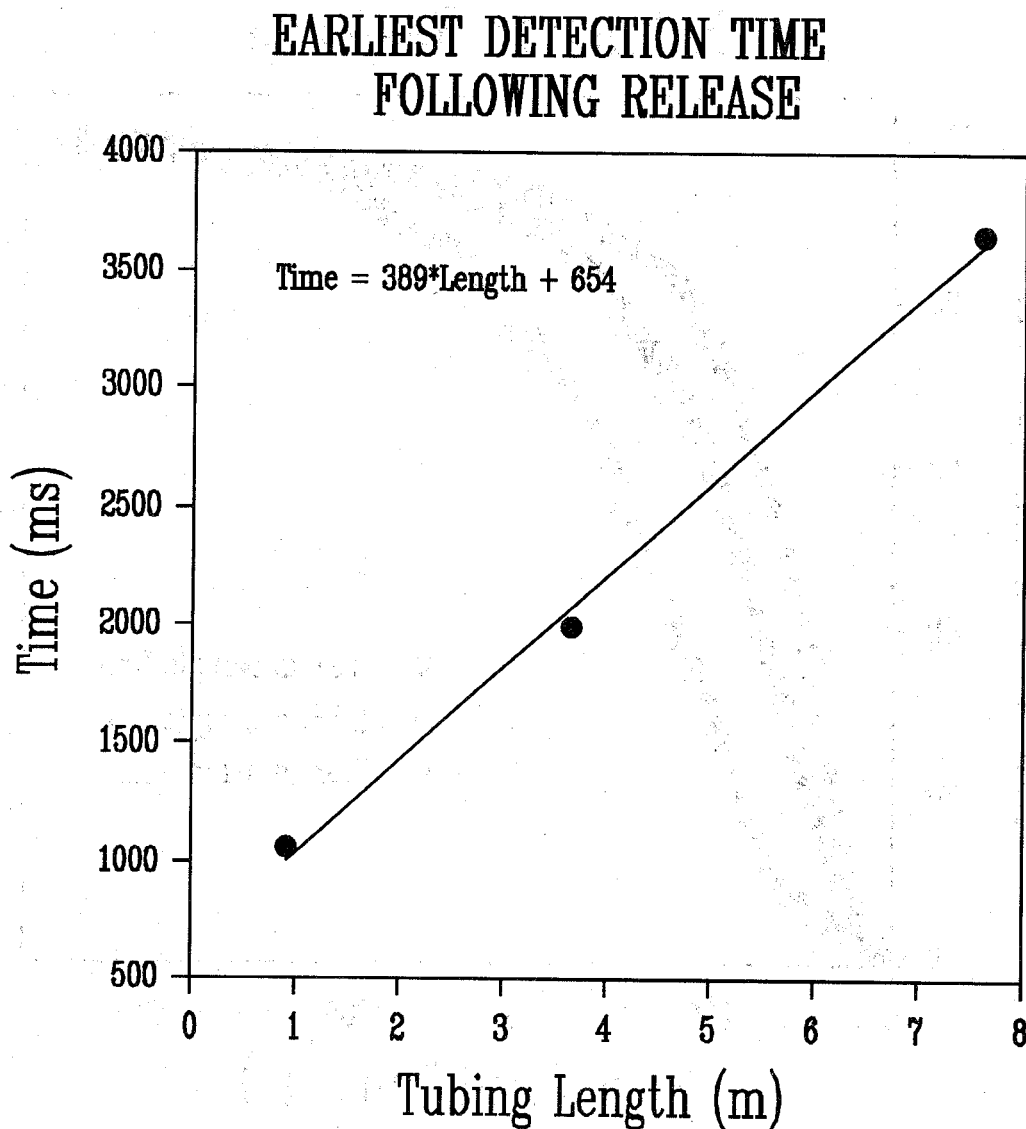


Figure 83. The period required for a Halonyzer to first respond to a step change in halon 1301 concentration from 0 to 100% as a function of sampling tube length. Data provided by W. Meserve and D. Van Ostrand of Pacific Scientific.



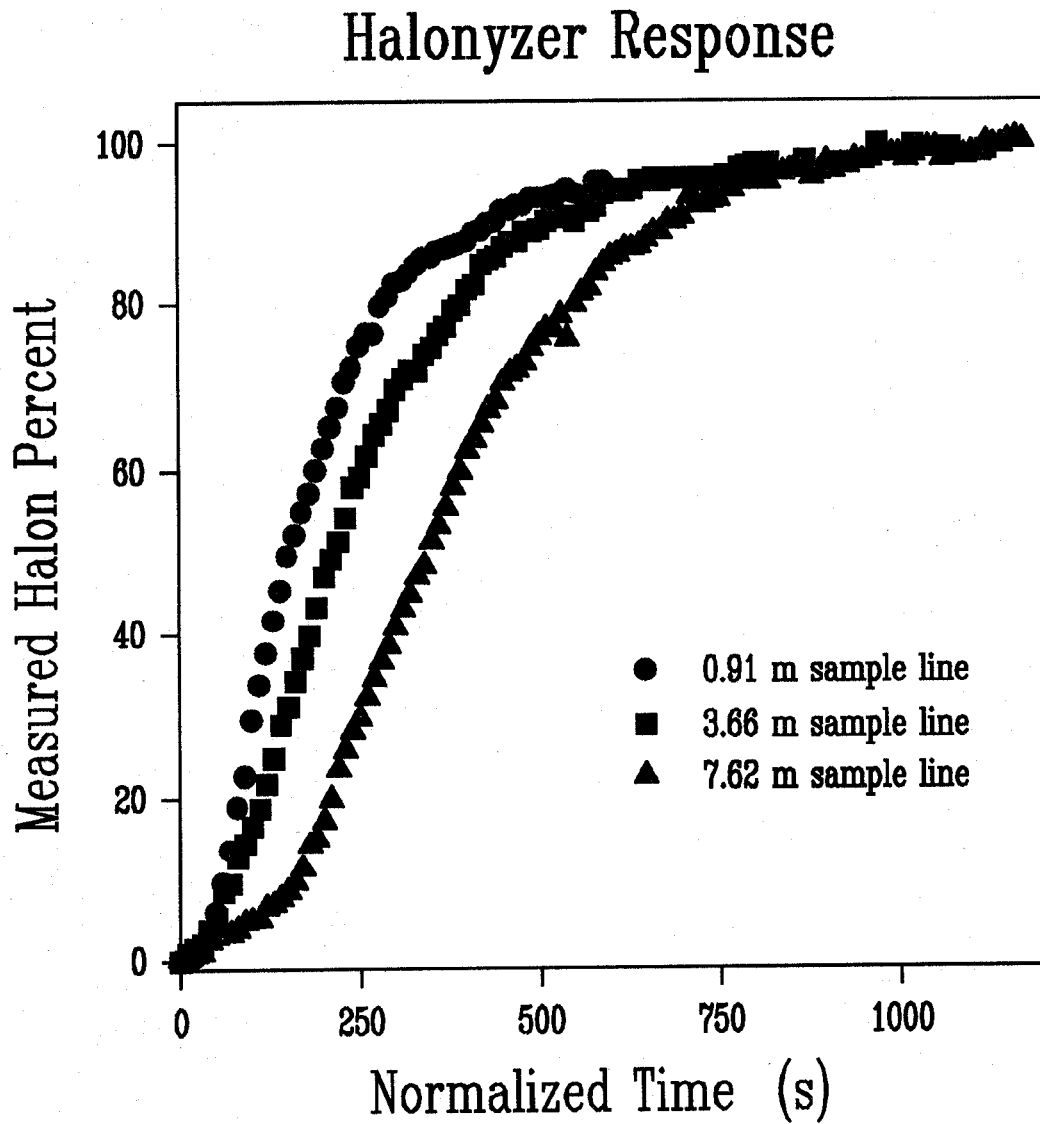


Figure 84. Measured halon 1301 mole percent as a function of normalized time for three different lengths of sampling tube. Data provided by W. Meserve and D. Van Ostrand of Pacific Scientific.

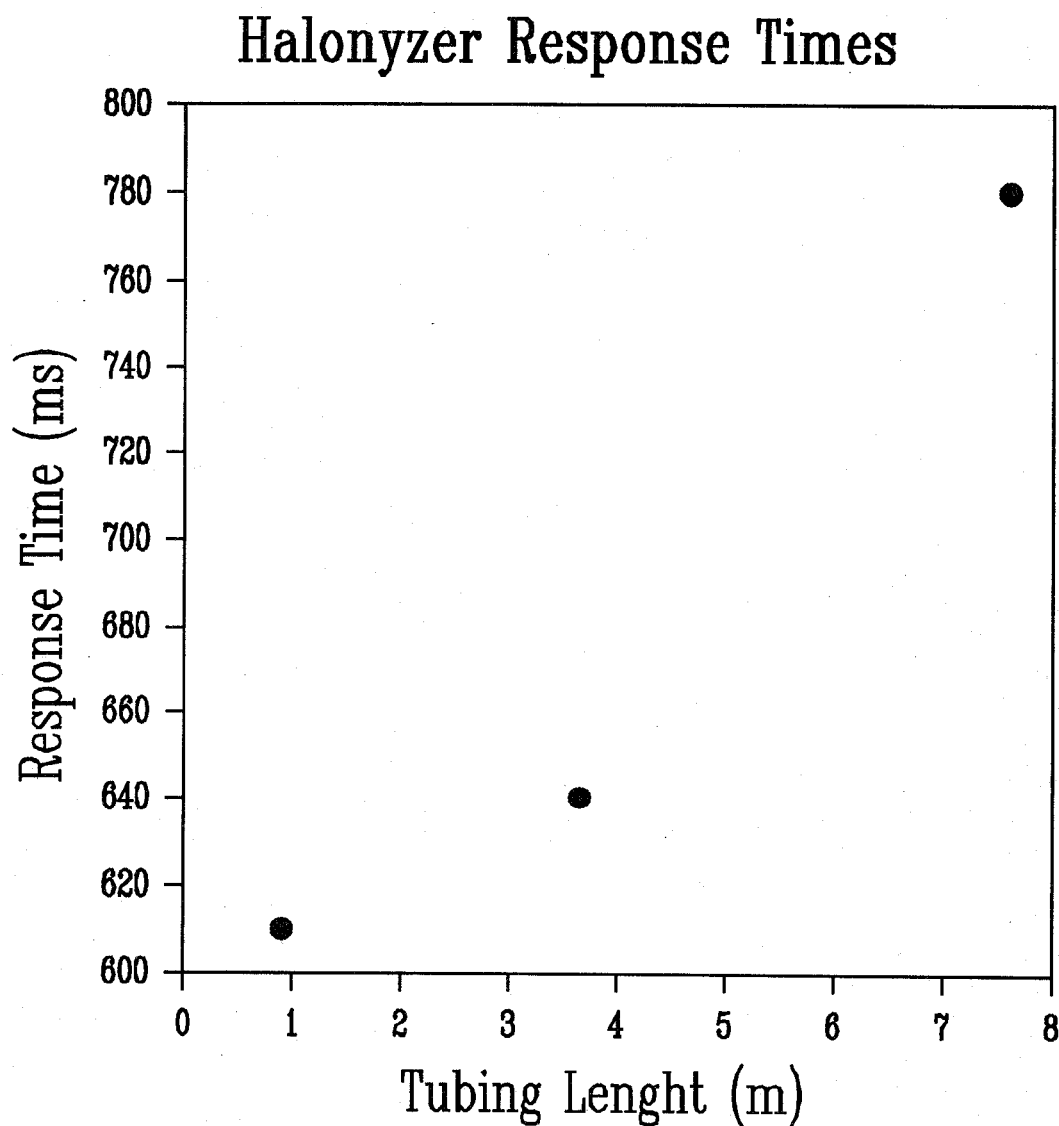


Figure 85. Response times for a Halonyzer concentration reading to change from 0 to 0.95 for a step increase in halon 1301 mole fraction to 1 as a function of sampling tube length. Data provided by W. Meserve and D. Van Ostrand of Pacific Scientific.

current effort. In this chapter other possible concentration measurement techniques are discussed and assessed as to their potential for making the required measurements.

Recall that accurate real-time measurements of the proposed halon 1301 alternatives--FC-218, HFC-227ea, HFC-125, and halon 1301--are desired with a time resolution of 1 ms. As discussed, this temporal resolution requirement places constraints on the sampling volume as well. Generally, sample volumes on the order  $1 \text{ mm}^3$  are desirable. These parameters severely limit the existing concentration diagnostics which might be applicable. This section summarizes the possible approaches which have been considered during the literature review.

**11.5.1 Introduction.** The development of measurement techniques for concentration is one of the most active areas in chemistry. Nearly an infinite number of techniques have been described for measurements in a wide variety of systems. Numerous monographs are available which describe chemical instrumentation and analysis methods. Clearly such a literature is too extensive to review in depth. For the purposes of this project we have chosen to limit ourselves to gas measurement techniques which may have applicability for the measurement of halon 1301 and its potential replacements.

A useful starting point for discussion is the monograph by Strobel and Heineman (1989). This book provides discussions of a wide range of instrumentation used for chemical characterization. Several of the methods are useful for measuring gas concentrations. These include widely used techniques such as absorption spectrometry, mass spectrometry, x-ray fluorescence spectrometry, and gas chromatography. Many of these techniques are discussed below.

It is interesting that many concentration-measurement techniques which are useful for binary mixtures are not included in this list. Such techniques include two instruments--the Statham analyzer and the combined aspirated hot-film/cold-wire probe--which have already been discussed. These probes function by sensing changes in physical properties such as viscosity, heat capacity, or thermal conductivity which are dependent on concentration. Such techniques will not generally be applicable to mixtures of multiple gases because insufficient information is available to fully characterize the concentration of each species.

The ability to follow concentration changes in time is often not a requirement in making chemical concentration measurements. The sample is available and it can be analyzed at one's leisure. However, there are a number of areas where time-resolved concentration measurements are required. Examples include studies of chemical kinetics where changes in concentration result from chemical reaction and turbulent flows and combustion systems where fluid-flow fluctuations lead to rapid changes in concentration at a given sampling point. Many of the techniques which are discussed below have been developed for these specialized applications. The time-scale range important in these applications is large, varying from femtoseconds for very fast chemical reactions to days or years for slowly changing processes. Clearly the technique chosen for a particular application must depend on the time resolution required.

Several characteristics of concentration measurements are relevant to the discussion. An "in situ" concentration measurement is one which is made within the system of interest while an extractive technique requires that a sample be removed for analysis. For instance, the Differential Infrared Rapid Agent Concentration Sensor can be considered an in-situ concentration probe because it was designed to operate within nacelles and dry bays. The Statham analyzer and Halonyzer are extractive techniques since the sample is removed to a remote location for measurement. Another important property of a measurement technique is whether it behaves intrusively or nonintrusively. If a measurement is made which does not modify the system under study it is said to be nonintrusive, while measurements which change, or have the potential to change, the system, are said to be intrusive. Any physical probe will generally be intrusive even though the perturbations to the system under study can be quite

small. On the other hand, many remote sensing optical techniques are characterized as nonintrusive because the measurement has minimal effects on the system.

In the following section the possible application of standard chemical analysis methods for the measurements of halon replacements will be considered. This will be followed by a discussion of several possible specialized techniques which have been developed primarily for measurements of concentration in turbulent flows of isothermal binary mixtures or chemically reacting species.

### 11.5.2 "Standard" Chemical-Analysis Techniques

**11.5.2.1 Gas-Solid and Gas-Liquid Chromatography.** Gas chromatography is a chemical-analysis technique which separates and quantitatively measures concentrations of gases (or liquids) in a sample. In its simplest form the sample to be analyzed is injected into a flow of "carrier gas" which then passes through a chromatographic column. The column contains either a solid substrate such as alumina (gas-solid) or a solid substrate coated with a high-boiling liquid (gas-liquid). As the sample passes along the column its components are absorbed or dissolved on the substrate and then released back into the gas flow repeatedly. As a result, their progress along the column is slowed. The relative amounts of time spent in the gas or attached to the substrate is temperature dependent, so the ability to vary the temperature of the column is generally provided. Different components of a mixture interact with the substrate differently, so as a mixture moves along the column the components begin to separate in space along the column. If the experimental conditions are chosen appropriately, by the time the various components reach the end of the column they will be well separated in time and space. The time required for a particular component to move along the column is known as its "retention time." For a given set of experimental conditions, each species in the mixture will have a characteristic retention time which can be quantified by injecting the individual gas onto the column. The last major component of a chromatograph is a suitable detector which can be any of a number capable of sensing the presence of small amounts of materials in a carrier gas. Flame-ionization, thermal-conductivity, and electron-capture detectors are three of the most common types.

This method of chemical analysis is intrusive and extractive since it is necessary to withdraw a sample from the region of interest. However, sample requirements are generally small and it should be possible to design probes which have minimal effects on the types of flows of current interest.

Chromatographic techniques are well developed and widely used. They are certainly capable of separating and quantifying fire-extinguishing agent concentrations in air. However, a major drawback with this approach for the current application is the time required to make an individual measurement. Normally a period of several seconds is required due to the need for flow through the column. This clearly prohibits real-time concentration measurements with the required temporal resolution. An approach which is sometimes used to improve the response time is to take a series of "grab bag" samples at selected times and analyze the samples at a later time. For the current application the number of samples required would be prohibitive, and the analysis would be very costly. On this basis, we conclude that chromatographic techniques are not a viable alternative for real-time measurement of fire-fighting agent concentration.

**11.5.2.2 Mass Spectrometry.** Mass spectrometry is a technique which is widely used for the identification and quantification of chemical species. In this method the gas-phase species to be analyzed are injected into a region of low pressure (on the order of  $10^{-2}$  Pa) and ionized. The resulting charged particles are then electrically accelerated and physically separated according to their mass-to-charge ratio by one of a number of possible approaches. The separated ionized species are then detected which can be very efficient since charged species are easily observed and quantified. The technique can be made quantitative by proper calibration. Mass spectrometry is capable of

identifying molecular components in a mixture since the mass-to-charge distributions of fragments formed from a particular species is generally unique. Interferences do occur when two or more species generate ions having the same mass-to-charge ratio.

A number of sources have been used to ionize molecular species. The most common is an electron beam generated by a heated filament. The energetic electrons interact with the low-pressure species and create positive ions which are then analyzed. A drawback of this approach is that the energetic electrons not only ionize a molecular species, but also tend to break up the species into smaller charged molecular fragments. As a result, a single molecular species may result in the formation of fragments having a number of mass-to-charge ratios. A second approach is chemical ionization in which a simple molecular species is first ionized by electron impact. The ionized species is then accelerated and interacts with the sampled gas where it results in ionization of the sample. This method generally results in less fragmentation than electron impact. Other methods which are used less frequently include laser desorption/ionization and photoionization.

Once the ions have been generated, they can be accelerated to a high velocity by application of an electric field. All of the accelerated ions are accelerated to the same energy. For singly charged species (generally the most common by far) the kinetic energy and electrical energy are equivalent, which can be written as

$$\frac{1}{2}mv^2 = eV, \quad (58)$$

where  $m$  is the mass of the ion,  $v$  is the velocity,  $e$  is the charge on an electron, and  $V$  is the electric-field applied potential. Accelerated ions having different  $m/e$  ratios can now be separated in a number of ways. One such mass selector is known as a magnetic-sector analyzer. This approach is based on the fact that a charged species in a magnetic field will follow a curved path having a radius which depends on the strength of magnetic field and the mass of the ion. By adjusting the magnetic field, it is possible to select the particular mass-to-charge-ratio ions which will reach a detector. A second type of analyzer uses a curved electric field to separate the ions. As for the magnetic-sector analyzer, the curvature of the ion path can be adjusted by varying the electric field strength and the spatial location of a particular mass ion can be selected.

Another type of analyzer known as the time-of-flight approach uses the time required for the accelerated ions to cover a known distance to infer the mass. From Equation (58), it is clear that if the ions are impulsively accelerated along a free path, the time required to reach a certain distance will be inversely proportional to ion velocity and therefore its mass. By recording the ion arrival times using a suitable detector, the mass can be measured accurately.

The approach most widely used today for mass separation is the quadrupole mass analyzer. The quadrupole analyzer consists of four metal rods which are arranged parallel to each other in the shape of a diamond. A combination of dc and ac radio-frequency electric fields are applied to the rods which cause ions moving between the rods to undergo a series of oscillations. These oscillations can grow to the point where the ions strike a rod and are lost. Whether or not this occurs depends on the magnitudes of the applied fields. For a given combination of fields only a narrow range of  $m/e$  ions can traverse the analyzer for detection at the end. For this type of analyzer, the velocity of the ions entering the analysis region is unimportant, and the ions do not need to be accelerated to the high velocities required for the other types of analyzers described above.

Several different detectors have been developed to detect the charged species. The two most common are briefly described here. A Faraday cup is a sloping plate electrode formed in the shape of a metal cup. When a charged species strikes the cup it generates secondary electrons which are collected and detected as a current. Most mass spectrometers today employ electron multipliers. These devices are similar to Faraday cups in that the energetic ions strike a metal surface to generate

electrons. The difference is that once the electrons are created, they are accelerated in an electric field and strike a second metal surface which generates still more electrons. This process can be repeated many times so that the detection of a single ion can lead to the generation of a large number of electrons. In other words, the device provides a great deal of amplification and a current which is easily measurable.

Most mass spectrometers are designed to perform mass analysis on molecular species. For all of the analyzers discussed above, except the time-of-flight system, the sample is usually introduced continuously into the spectrometer and the detected mass is swept by changing the applied magnetic or electric fields to generate a mass spectrum of the sample which consists of the detected ion signal as a function of  $m/e$ , or, assuming a charge of one electron, the mass of the ions. As mentioned above, the analysis is often complicated by the fact that an individual molecular species may fragment into a number of different ions. The mass spectrum for complicated chemical mixtures can be quite complex indeed. For this reason, it is common to perform chemical separation on a mixture before performing mass analysis. Mass spectrometry is often combined with the chromatographic techniques mentioned above. In this method it is necessary to record the mass spectrum fast enough to resolve the individual species which are leaving the chromatographic column. This has led to the development of mass spectrometers which can be swept quite rapidly. (White and Wood, 1986)

In its standard configuration a mass spectrometer is unlikely to be a suitable device for quantitative measurements of real-time fire-fighting agent concentration. The period required to scan the mass spectrum is simply too long. However, the instruments have been modified to allow on-line sampling of composition of particular species. This is done by setting the spectrometer to a particular  $m/e$  of interest and recording the resulting ion signal as a function of time. Since the mass does not need to be scanned, quite rapid measurements are possible. By using a mass analysis method which provides spatial separation of ions, it is possible to place multiple ion detectors in the instrument and monitor several species at once. (White and Wood, 1986; Whistler and Schaefer, 1983; Savin *et al.*, 1983)

Even though mass spectrometry has not been tested for the current application, it seems to offer possibilities for the real-time measurement of fire-fighting agent concentrations. Since very small samples are required, it should be possible to develop sampling systems which perturb the sampled system very little and which allow accurate measurements of concentration with good temporal resolution. Major drawbacks of using mass spectrometry for this application are its relative complexity and cost. The components and electronics of a mass spectrometer must be carefully designed and manufactured. The system generally requires a very good vacuum system capable of high pumping speeds. As a result, the systems tend to be fairly expensive (on the order of tens of thousands of dollars), bulky, and difficult to operate and maintain. These considerations should be carefully considered before designing a system to make the required measurements.

**11.5.2.3 Standard Optical Absorption Techniques.** Optical techniques are widely used in chemical analysis. The mostly frequently employed methods involve the absorption or emission of electromagnetic radiation by molecules. Interactions between matter and electromagnetic energy occur over a very wide energy range from low-energy radio waves to high-energy gamma rays. Various analytical techniques based on absorption or emission of electromagnetic energy have been developed which use different portions of the electromagnetic spectrum. Table 14 lists some of these techniques and includes the types of molecular energy transitions which are responsible.

Many of the spectroscopic methods listed in Table 14 are rarely used for quantitative measurements in the gas phase. These include nuclear magnetic resonance, electron spin resonance, microwave spectroscopy, x-ray spectroscopy, and gamma-ray spectroscopy. These techniques will not be discussed further here, but the reader should keep in mind that it is possible that quantitative analysis

Table 14. Various Types of Molecular Spectroscopies Are Listed Along With The Relevant Electromagnetic Spectrum Region and the Molecular Motion Responsible for the Transitions

Type of spectroscopy	Energy range	Molecular interaction
Nuclear magnetic resonance	Radio	Nuclear spin
Electron spin resonance	Radio	Electron spin
Rotational	Microwave	Rotational
Infrared absorption	Mid-infrared	Vibrational
Near-infrared absorption	Near infrared, Visible	Vibrational overtones
Raman	Visible, ultraviolet	Vibrational
Electronic absorption	Visible, ultraviolet	Electronic
Fluorescence	Visible, ultraviolet	Electronic
X ray	X ray	Inner-shell electronic
$\gamma$ ray	$\gamma$ ray	Nuclear

techniques for fire-fighting agents based on some of these approaches might be feasible following a significant development effort.

The remaining spectroscopic methods included in Table 14 have been used extensively for quantitative concentration measurements of gas-phase species. These techniques are discussed in more detail below.

Infrared absorption spectroscopy is widely used for chemical identification and concentration measurement. The technique normally refers to the absorption of infrared electromagnetic energy (usually defined as having wavelengths from 0.75  $\mu\text{m}$  to 400  $\mu\text{m}$ ) which lies in the mid-infrared range of 2.5  $\mu\text{m}$  to 16  $\mu\text{m}$ . In infrared work the positions of absorption bands are often reported in wavenumber units ( $\text{cm}^{-1}$ ) which are the inverse of the wavelength of light and are proportional to the energy of the light. The mid-infrared region extends from 4000  $\text{cm}^{-1}$  to 625  $\text{cm}^{-1}$ .

The reason for the great importance of infrared absorption techniques is that the vibrational energy-level separations of the vast majority of molecules lie in this energy range, and the molecules can absorb infrared energy during allowed transitions from a lower lying vibrational energy level to a higher lying level. A discussion of transition rules is beyond the scope of this discussion, but suffice it to say that most molecules which are not linear and symmetrical will have at least one allowed infrared absorption. The energy required for absorption is highly dependent on the atoms in the molecule as well as the molecular structure. It is this strong dependence on molecular structure which allows infrared spectroscopy to be such an excellent technique for molecular identification.

The concentration of an absorbing species can be quantified using Beer's law which states that the logarithm of the ratio of infrared power at a given wavelength transmitted through a space containing an absorbing species ( $P$ ) to the power transmitted in the absence of the species ( $P_0$ ) is equal to the product of the absorption coefficient of the absorbing species ( $\epsilon$ ), the pathlength over which the energy travels ( $\ell$ ), and the concentration of the species ( $c$ ),

$$\log \frac{P}{P_o} = \epsilon lc . \quad (59)$$

A variety of units may be used for the terms in Equation (59), and care must be used to ensure that the units are consistent. When the pathlength and absorption coefficient are known for a species, a measurement of the light transmission allows the concentration to be determined.

Infrared absorption measurements are normally recorded using either dispersive or Fourier transform spectrometers. The older of the two is the dispersive type. In this approach a narrow wavelength range of a continuous source of infrared radiation, such as a heated filament, is isolated with a dispersive element such as a prism or grating. The selected radiation is then passed through a cell containing the sample of interest. Following passage through the sample, the infrared energy strikes a detector which records the intensity of the transmitted light. It is common to use a second unabsorbed beam of light as a reference for  $I_o$ .

The Fourier transform infrared (FTIR) spectrometer is a more recent development. This instrument is typically formed from a Michaelson interferometer in which one of the optical legs is replaced by a mirror which can be scanned back and forth with time. The infrared radiation exiting the interferometer first passes through an absorption cell containing the sample, and the intensity is then measured with a suitable detector. Unlike a dispersive spectrometer, all wavelengths of interest are passed through the interferometer simultaneously. The detected light varies at the frequency of the scanned mirror, and the resulting interferogram includes information concerning frequency components of the absorption spectra. The normal infrared spectrum in terms of wavelength or energy is recovered by Fourier transforming using the fast Fourier transform (FFT) algorithm from the frequency space of the measurement to wavelength (energy) space. Additional details can be found in numerous textbooks (*e.g.*, Strobel and Heineman, 1989).

Dispersive infrared and FTIR spectrometers are similar in that both usually use absorption cells which are inserted into the instruments. For making time-resolved measurements, it is necessary to flow gases through the cell with a sufficient volume-flow rate that the volume is completely flushed at a rate equal to the required time resolution. Additionally, the instruments require finite times to record a resolved spectrum. Due to these requirements, commercial infrared spectrometers are generally not used to record concentrations having time resolutions on the order of 1 ms. As a result, commercial infrared spectrometers are not recommended for time-resolved agent concentration measurements.

As noted above, the energies of most vibrational bands in molecules result in strong allowed molecular absorptions which have energies corresponding to the mid-infrared portion of the electromagnetic spectrum. In reality, the vibrational energy levels of molecules are like a step ladder, with the energy separation increasing with the number of steps separating the levels. For most molecules, the probability of absorption of a photon is much higher for a step size of one (*i.e.*,  $\Delta v = 1$ , where  $v$  is known as the vibrational quantum number) than for larger steps. However, there are often small probabilities of electromagnetic absorption occurring for step sizes larger than one. Such transitions have a higher energy and often fall in an energy range known as the near-infrared which lies in the 0.75  $\mu\text{m}$  to 2.5  $\mu\text{m}$  wavelength range.

The near-infrared has been used very little for quantitative concentration measurement using standard spectrometers due to the weak absorption of molecules in this spectral range. However, as discussed below, there are potential advantages for making concentration measurements in this wavelength range. However, measurements using standard commercial spectrometers will be subject to the same limitations described above for mid-infrared measurements and, as a result, are unlikely to be applicable for high-speed applications.



As one moves to higher energy in the electromagnetic spectrum, one comes to the visible and ultraviolet regions where photons have energies sufficient to induce transitions between electronic states of a molecule. The actual wavelengths where these transitions occur depend strongly on the structure and symmetry of the particular molecule. Electronic transitions can be quite strong and, when they occur, are quite useful for analytical measurements.

For the purposes of the following discussion we will subdivide the visible and ultraviolet portions of the electromagnetic spectrum into three regions: the visible from 350 nm to 750 nm, the quartz ultraviolet from 200 nm to 350 nm, and the vacuum ultraviolet from 100 nm to 200 nm. The names are quite literal. The visible region corresponds roughly to wavelengths which can be detected by the human eye, the quartz ultraviolet corresponds to wavelengths which are transmitted by quartz, and the vacuum ultraviolet corresponds to a region of the spectrum which is strongly absorbed by oxygen in the air and therefore normally requires a vacuum for efficient transmission. This classification follows Pasto and Johnson (1969).

A review of the literature reveals that halon 1301 and the replacement agents are transparent at visible wavelengths (*i.e.*, absorption is either very weak or totally absent). On the other hand,  $\text{CF}_3\text{Br}$  and  $\text{CF}_3\text{I}$  have relatively strong absorptions in the quartz ultraviolet.  $\text{CF}_3\text{Br}$  has a broad absorption which begins in the vacuum ultraviolet and reaches a maximum at roughly 205 nm (Roxlo and Mandl, 1980; Molina *et al.*, 1982).  $\text{CF}_3\text{I}$  has a moderately weak, but broad absorption which peaks near 268 nm and extends out to 317 nm (Calvert and Pitts, 1966). This molecule also has a relatively sharp, strong absorption band with a maximum at 174 nm (Roxlo and Mandl, 1980). The absorption bands in the quartz ultraviolet offer possibilities for quantitative analysis. However, standard absorption spectrometers are too slow to allow highly time-resolved measurements (however, see the section on the Ultra-Violet Halonalyser below). On this basis, it is concluded that standard absorption spectrometry is not appropriate for the current application.

The remaining alternative agents, *i.e.*,  $\text{C}_2\text{F}_5\text{H}$ ,  $\text{C}_3\text{F}_8$ , and  $\text{C}_3\text{F}_7\text{H}$ , all have electronic absorption bands which lie in the vacuum ultraviolet and would be difficult to quantify in air using standard spectroscopic analysis.

**11.5.3 Fiber-Optic-Based Measurements of Concentration.** A variety of techniques have been demonstrated or are under development which utilize fiber-optic probes for concentration measurements. In some cases these probes are simple absorption techniques where the fiber optics are used to convey the light to and from an open-path sample volume. In other cases the chemical to be sensed is used to induce changes in the light transmission characteristics of the fiber, and concentration is monitored by changes in light transmitted by the fiber. Examples of each approach are discussed below.

**11.5.3.1 Introduction To Fiber Optics.** Simply speaking, an optical fiber is a long, thin filament of a transparent, dielectric material, such as glass or plastic, used for the transmission of light over long distances with very little loss. If the diameter of this fiber is large relative to the wavelength of the transmitted light, then simple geometrical optics may be used to describe the light transmission in the fiber. The key principle is that of total internal reflection. If the fiber is modeled as a cylinder of glass surrounded by air, then a ray of light within the fiber striking a wall will be totally internally reflected (that is, all of the light remains in the reflected ray with no refracted ray

escaping through the wall) when the incident angle (measured from the normal to the wall) is greater than a critical angle given by

$$\theta_c = \sin^{-1} \frac{n_o}{n_1}, \quad (60)$$

where  $n_o$  is the index of refraction for the fluid surrounding the fiber and  $n_1$  is the index of refraction for the fiber material (chosen such that  $n_1 > n_o$ ). Thus, rays of light coupled into an optical fiber may undergo many thousands of reflections per meter and still remain trapped within the fiber. However, one can easily see that if moisture, dust, or oils come into contact with the surface of the fiber, then the critical angle at the air/fiber interface is altered, and light may well leak through the fiber. Furthermore, if large numbers of fibers are packed together in a bundle, light may leak from one fiber to another (crosstalk). To prevent these rather common problems, currently manufactured optical fibers are equipped with a thin, transparent sheath of material with a lower index of refraction than the core material. This sheath is known as cladding. Typical index of refraction values are 1.62 for the core material and 1.52 for the cladding although other values are commonly available. A fiber with two discrete values for the index of refraction of the core and cladding is known as a step-index fiber. A graded-index fiber has a continuous distribution of values for the index of refraction proceeding from the centerline of the fiber to the boundary. The presence of cladding prevents many of the types of leakage described above, but it cannot prevent leakage resulting from sharp bends or kinks in the fiber. In general, fibers have a minimum bend radius specification on the order of 5 cm for glass and 2.5 cm for fused-silica fibers.

Light is coupled into the fiber by directing rays into one of the end faces. There exists a maximum for the incident angle (measured from the normal to the end face and denoted by  $\eta_{max}$ ) of these input rays in order for the ray to strike an interior wall of the fiber at an angle greater than the critical angle for total internal reflection. Rays entering the end face of the fiber with an incident angle greater than this maximum angle will be partially refracted at each encounter with the core-cladding interface and will quickly leak out of the fiber. Thus,  $\eta_{max}$  represents the half-angle of a cone centered on the fiber axis for which light within this acceptance cone will be transmitted through the fiber, whereas light outside of the cone will not. This maximum angle may be determined from

$$\sin \theta_{max} = \frac{(n_1^2 - n_2^2)^{1/2}}{n_o}, \quad (61)$$

where  $n_o$  is the index of refraction for the fluid surrounding the fiber (air),  $n_1$  is the index of refraction for the fiber core material, and  $n_2$  is the index of refraction for the fiber cladding. As with lenses, one may define a numerical aperture, the square of which is a measure of the light gathering power of the system,

$$NA = n_o \sin \theta_{max} = \frac{1}{2f\#}, \quad (62)$$

where  $f\#$  is the f-number of the system. For air ( $n_o \approx 1$ ), the numerical aperture cannot exceed 1 which corresponds to  $\theta_{max} = 90^\circ$  and a condition in which all light entering the end face of the fiber is transmitted through it. Commercially available fibers may be obtained with numerical apertures ranging from 0.2 up to and including 1.0.

In order to be flexible, single fibers must have a small diameter (typically 200  $\mu\text{m}$  to 1 mm); however this makes them inefficient for the collection of light from large, incoherent, non-laser sources. To overcome this limitation, fibers packed in a bundle may be obtained. These bundles provide both flexibility as well as a larger physical aperture (several millimeters) in which to focus the input beam. If no attempt is made to order the individual fibers within a bundle into some sort of ordered array, they are said to form an incoherent bundle and are useful only for the transmission of light from one location to another. On the other hand, when the fibers are carefully arranged such that their terminations occupy the same relative positions at both ends of the bundle, then this coherent fiber may be used for the transmission of images. In addition, bundles that are bifurcated or trifurcated are readily available, and they allow beam splitting to be performed without the aid of lenses. Although the transmittance through single fibers is nearly 100 %, the transmittance through a bundle is usually much less (50 % - 70 % for a length of about 0.3 m). This fiber-bundle transmittance is usually expressed in dimensionless form as the ratio of the bundle transmittance to the transmittance of a single fiber with the same physical aperture and is a function of the wavelength of the transmitted light and the length of the bundle. Single glass fibers are commonly available and transmit light over a range of wavelengths from 500 nm to about 1600 nm in the near-infrared. Single fused-silica fibers may also be obtained and can extend this range from about 300 nm in the UV range out to about 2000 nm. Bundles may be obtained in these wavelength ranges as well, but transmittances tend to fall off rapidly for lengths exceeding about 0.3 m.

Single fibers may be multimode or single mode. This refers to the number of axial laser modes (which comprise a single laser line) which a fiber can guide. The number of modes drops as the fiber core diameter or the numerical aperture is reduced. For small enough values of either, only one fiber mode exists, and the fiber is referred to as single mode. Single-mode fibers are generally more expensive, are more difficult to obtain, and are of very small diameter (4  $\mu\text{m}$  to 8  $\mu\text{m}$  with NAs of about 0.2). They are generally used for communication over long distances.

### 11.5.3.2 Spatially Resolved Absorption Concentration Measurements Using Fiber Optics.

Numerous systems have been developed which utilize fiber optics to allow absorption measurements over small regions of space and, therefore, allow spatially resolved concentration measurements. In order to provide the reader an understanding of such an approach, several early applications are described.

Batt (1977) has reported the use of a fiber-optic probe in his study of the turbulent structure and diffusive characteristics associated with the mixing of both a passive and reacting species in a two-dimensional free turbulent shear layer. Specifically, Batt used a vertically oriented recirculating wind tunnel to deliver the primary (core) flow which consisted of dry air that had been cooled to -20 °C by means of liquid-nitrogen injection and then seeded with dilute concentrations of nitrogen tetroxide ( $\text{N}_2\text{O}_4$ ). He then made use of the decomposition of nitrogen tetroxide to give nitrogen dioxide gas by the reaction



The primary flow was exhausted into the larger test section chamber of the tunnel containing a secondary source of dry air at room temperature and forming a two-dimensional free turbulent shear layer at the interface. Due to the mixing of  $\text{N}_2\text{O}_4$ -rich cold eddies in the mixing layer with the hot (ambient temperature) eddies of the secondary fluid, the dissociation of  $\text{N}_2\text{O}_4$  to generate  $\text{NO}_2$  was favored. Thus, this configuration allowed the study of the mixing of chemically reacting species. However, a unique feature of this reaction was the fact that when the temperature of the primary gas was increased from -20 °C to room temperature, the degree of dissociation varied from 0.3 to 0.96.

This required that the dissociation was essentially complete immediately after significant mixing into the primary flow, and with this configuration, the author could study the mixing of a passive species. The author made point measurements of velocity using constant-temperature hot wires, measurements of temperature using constant-current cold wires, and measurements of the concentration of  $\text{NO}_2$  gas with the fiber-optic probe.

The light-sensor probe was constructed by splitting the light from a tungsten-filament lamp into two beams which were then chopped at 1 Hz by a rotating chopper wheel. The resulting beams were directed through optical high-pass filters (with a cut-off wavelength at 380 nm) and then focused into two optical fibers. One fiber was routed to the measurement location in the mixing layer and the other to a reference location in the secondary ambient air. At each of these locations the fibers were terminated and fitted with a glass lens. A fixture was then employed to position a second fiber, also fitted with a glass lens, immediately adjacent to the first fiber with only a 2.5 mm gap separating them. The other end of this second fiber was directed to a photomultiplier tube. The idea, then, was that light from the lamp exited the fiber through the lens, was attenuated upon passing through eddies of dark-brown  $\text{NO}_2$  gas instantaneously present in the gap, then proceeded into the second fiber and terminated at the photomultiplier tube where the transmitted light was measured. Due to the fact that the nitrogen dioxide gas strongly absorbed at a wavelength of 400 nm, whereas the other species in the flow were transparent to this wavelength, the light attenuation in the gap was a measure of the gas concentration. To eliminate problems associated with stray light, the measurements were acquired in complete darkness. The relationship between the transmission of light in the gap and concentration of  $\text{NO}_2$  gas is described by the Beer-Lambert law,

$$\frac{I}{I_o} = \frac{E}{E_o} = 10^{-\beta l_f c}, \quad (64)$$

where  $I$  is the transmitted light intensity,  $E$  is the photomultiplier voltage, the subscript  $o$  refers to the transmitted light intensity or voltage with no absorption,  $\beta$  is the molar extinction coefficient for nitrogen dioxide gas in  $\text{cm}^2/\text{mole}$ ,  $l_f$  is the gap spacing, and  $c$  is the concentration of  $\text{NO}_2$  gas in  $\text{mole}/\text{cm}^3$ . Note that Equation (64) is simply another way to write Equation (59). Since only dilute concentrations were measured, Equation (64) could be simplified into the following linear relation as

$$\frac{\Delta E}{E_o} = -2.3\beta l_f c, \quad (65)$$

where  $\Delta E$  represents the difference in photomultiplier voltages resulting from the reference and attenuated light signals.

The purpose of the chopper wheel was to provide a means for monitoring the reference-signal strength and the extent of any drift in the source intensity that may have occurred during the course of the measurement. It was activated immediately before a concentration measurement, then turned off while the concentration data was obtained, then reactivated immediately afterward. This probe exhibited a sensitivity of 300 mV per percent of  $\text{NO}_2$  in  $\text{N}_2$ , had a bandwidth of approximately 2 kHz, and a signal-to-noise ratio of 70 dB. In addition to the mean and fluctuating values of concentration that could be obtained with this sensor, Batt reported simultaneous correlation measurements of concentration and velocity or temperature by positioning a hot-wire or cold-wire sensor in the gap of the light probe, but displaced a small amount from the gap center in a lateral direction to avoid disturbing the transmitted light signal.

The origins of the light sensor probe employed by Batt (1977) may be found in the earlier papers of Lee and Brodkey (1964) and Nye and Brodkey (1967a). The first paper describes the original light-

sensor probe developed for the specific case of the measurement of turbulent concentration fluctuations in high Schmidt-number flows. Recall that the Schmidt number is the ratio of momentum diffusivity to mass diffusivity, and a high Schmidt-number case corresponds to the mixing of mass in a liquid stream. The authors had pointed out that the existing hot-wire techniques for resolving concentration fluctuations in low Schmidt-number flows could not be adapted to the high Schmidt-number case, and this deficiency necessitated the development of a new experimental technique. The experimental configuration consisted of the axial injection of dye in the form of a turbulent jet on the centerline of a co-flowing water stream in a 7.8 cm pipe. Further details of the experimental apparatus may be found in Lee and Brodkey (1964).

The light probe of Lee and Brodkey (1963) consisted of a pair of optical fibers of diameter 0.75 mm which were separately encased in 1 mm diameter, thin-wall metal tubes for support. The two metal tubes were spaced 1 mm apart and rigidly housed inside a probe body constructed of a 6.3 mm diameter Monel tube with a length of 16.5 cm. At one end of the probe body, the Monel tube was tapered, and the metal tubes containing the optical fibers extended from the probe housing for a distance of about 12 mm. At the very end of the two metal tubes, small prisms were attached to the ends of the optical fibers such that the optical paths were directed inward by 90° to meet each other across the 1 mm gap. At the other end of the probe body, the optical fibers were directed into flexible, waterproof, plastic tubes of diameter 2.5 mm and with a length of over 1.5 m which allowed light to be transported into and out of the experimental facility. The spatial resolution was computed to be the volume obtained by extending the fiber optical cross-section of 0.56 mm<sup>2</sup> across the 1 mm gap for a probe volume of  $5.6 \times 10^{-4}$  cm<sup>3</sup>. The light source was an intense white light from a lamp. As in the paper by Batt, the principle is that of light attenuation in the gap due to the presence of dilute concentrations of gentian violet dye injected into the flow. The relationship between dye concentration and light attenuation is again governed by the Beer-Lambert law, Equation (64). Measurement of light intensity was accomplished by means of a 9-stage photomultiplier tube, and the frequency response of the probe was approximately 10 kHz.

The goal of the investigation was to report on the general shape of the concentration spectrum and to compare it to predictions from theory. The resulting measurements were generally inconclusive, which was deemed to be the result of deficiencies in the design of the light sensor. Improvements such as a smaller probe volume and increased light level resulting from a higher intensity light source and a reduction in the length of the 1.5 m optical fibers for transporting the beams were suggested as a means for increasing the signal-to-noise ratio. These improvements were the basis of a second-generation sensor described in the paper by Nye and Brodkey (1967a).

The second-generation light sensor was entirely revamped. It was constructed by bringing two optical fibers, of diameters 0.25 mm and 0.38 mm, enclosed in metal tubing and with small glass windows cemented to their ends, face to face across a gap of 0.25 mm. This was accomplished by means of a supporting mount which suspended the two optical fibers, encased in tubes, in a U-arrangement. The probe volume was calculated by using the cross-sectional area of the 0.25 mm fiber and extending it across the 0.25 mm gap to obtain  $1.2 \times 10^{-5}$  cm<sup>3</sup>. This was a reduction in volume relative to the previous sensor of about 46. A much stronger white light source was also employed. The dye was also changed, and higher concentrations were used. The net result of these changes to the probe and system was a signal-to-noise ratio ten times better than that obtained by Lee and Brodkey (1963). The concentration spectra obtained with the new probe were considered to be satisfactory, and full details of the data and the concomitant comparison to theory may be found in the paper of Nye and Brodkey (1967b).

The optical sensors discussed to this point have been able to acquire point measurements due to the relatively high concentrations of contaminant that were introduced. The method, however, can be extended to the measurement of extremely low, mean concentrations by increasing the gap spacing so

that a greater distance is traversed through the fluid to be measured. One then obtains an integrated line-of-sight measurement as opposed to a point measurement.

This approach finds application as an economical and safe way for the implementation of remote sensing of various dangerous, explosive, and toxic gases at strategic locations within enclosed environments such as factories, fuel-storage facilities, tunnels, ships and buildings. Since electrical sensors are inappropriate in these kinds of hostile environments, optical techniques based on absorption spectroscopy appear to be the most suitable. However, implementation of such an optical technique was hampered by the fact that most hydrocarbon gases have weak absorption coefficients in the near-infrared region where conventional fused silica optical fibers remain transparent. The use of light in the near-infrared requires long path lengths within the measured gas in order to obtain sufficient attenuation of the signal. Such a method was pursued by Chan *et al.* (1984) for the measurement of low levels of propane ( $C_3H_8$ ). They employed ultra-low-loss silica fibers transmitting light at  $1.68\ \mu m$ , but were required to have a path length through the gas of 0.5 m!

On the other hand, as discussed in Section 11.5.2.3, hydrocarbon gases display strong absorption bands in the mid-infrared, but conventional optical fibers exhibit large transmission losses in this region. Tai *et al.* (1987) employed standard silica fibers transmitting mid-infrared radiation at  $3.392\ \mu m$  for the detection of methane, but they were forced to keep the fiber length to less than 40 cm in order to avoid large transmission losses. (They used a very interesting arrangement, however, in which a portion of the fiber itself formed the transducer. We will return to this feature below.) Saito *et al.* (1988) seem to have found a better solution. They have developed a system exploiting the properties of novel optical fibers made from chalcogenide glasses such as arsenic sulphide ( $As_2S_3$ ) and arsenic selenide ( $As_2Se_3$ ).

Specifically, the optical fiber consisted of a 0.5 mm core of  $As_2S_3$  glass and a  $70\ \mu m$  thick cladding of Teflon FEP. The transmissivity of the fiber was a maximum (63 % to 67 %) at the  $3.39\ \mu m$  wavelength used in the study. Furthermore, the methane ( $CH_4$ ) gas examined in this investigation (as well as most hydrocarbon molecules) has a very strong absorption band in this part of the spectrum. The experimental configuration consisted of a 4 mW He-Ne laser as the light source. Light from this source was conveyed through an  $As_2S_3$  fiber (1.0 m to 1.5 m long) to a cell containing the gas to be measured. A second fiber routed the light transmitted through the cell to a liquid-nitrogen-cooled InSb detector which transduced the radiation into an electrical signal. This configuration, however, was sensitive to fluctuations or drift in the source intensity of the laser. Indeed, this was checked, and fluctuations as large as 10 % were found. To remove this effect from the system, a clever combination of a chopper wheel and interrupter wheel was used to alternately direct the beam from the laser through the fiber to the gas cell or to send the beam directly to the detector, bypassing the gas cell completely. This allowed the detector to produce a voltage instantaneously proportional to the source intensity immediately followed by a voltage quantifying the concentration of gas within the cell. Division of the latter quantity by the former had the effect of removing the dependence on source intensity from the system. The modified signal showed a small fluctuation level on the order of 2 % which was attributed to vibrations of the chopper disk and represented the noise floor of the system.

Saito *et al.* (1988) used this system to detect methane levels ranging from a predesigned maximum of 5700 ppm down to 300 ppm (which represents 0.6 % of the lower explosion limit) in a gas cell of length 100 mm. When using a shorter cell of only 50 mm in length, the lowest resolvable concentration was 700 ppm. The optical path lengths used in this study, 50 mm and 100 mm, are large compared to the point measurements made by Batt and by Brodkey and his coworkers. When these lengths are placed into the inverse exponential Beer-Lambert law, one can immediately see that the concentration levels that can be discerned with this technique are of much smaller magnitude and are therefore most appropriate for these leak detection studies.

Saito *et al.* (1992) reviewed the attractive features of chalcogenide glass fibers and recent applications in thermometry and gas monitoring using these fibers. Details from this paper include the fact that the fibers have large numerical apertures allowing them to accept a large amount of radiation from a large field of view. The  $\text{As}_2\text{S}_3$  fiber has a transmission wavelength range of  $1\text{ }\mu\text{m}$  -  $6\text{ }\mu\text{m}$  and a minimum optical loss of 0.06 dB/m, whereas the  $\text{As}_2\text{Se}_3$  has a wavelength range of  $1\text{ }\mu\text{m}$  -  $10\text{ }\mu\text{m}$  and a minimum loss of 0.3 dB/m. Furthermore, these fibers have a minimum bending radius less than 50 mm when the core diameter of the fiber is less than 0.7 mm, and this is primarily a mechanical specification as the transmissivity of the fibers is relatively unaffected by bending. The authors also describe a coherent  $\text{As}_2\text{S}_3$  fiber bundle containing 1000 individual fibers with cores of  $20\text{ }\mu\text{m}$  and an outer bundle diameter of 1 mm. This bundle was successfully utilized for thermal imaging applications during the monitoring of a Tokamak fusion reactor.

Gregory (1993) describes infrared fibers which are available commercially. For wavelengths longer than  $3\text{ }\mu\text{m}$  these include Fluoride ZBLAN ( $0.4\text{ }\mu\text{m}$  -  $5\text{ }\mu\text{m}$ ), chalcogenide ( $1\text{ }\mu\text{m}$  -  $11\text{ }\mu\text{m}$ ), polycrystalline ( $4\text{ }\mu\text{m}$  -  $15\text{ }\mu\text{m}$ ) and hollow glass ( $7\text{ }\mu\text{m}$  -  $9.4\text{ }\mu\text{m}$ ), metal ( $5\text{ }\mu\text{m}$  -  $5.5\text{ }\mu\text{m}$ ,  $10\text{ }\mu\text{m}$  -  $13\text{ }\mu\text{m}$ ) and sapphire ( $10\text{ }\mu\text{m}$  -  $17\text{ }\mu\text{m}$ ) fibers. With the exception of chalcogenide, losses are generally greater than 0.5 dB/m in this region. Work is continuing on the development of mid-infrared fibers. It has recently been reported (Laser Focus World, 1994) that tellurium-containing glass fibers with an attenuation of 0.11 dB/m at  $6.6\text{ }\mu\text{m}$  and less than 1 dB/m over a range of  $5.25\text{ }\mu\text{m}$  -  $9.5\text{ }\mu\text{m}$  have been fabricated.

The discussion above suggests that fiber-optic based diagnostics may be suitable for developing a high-speed probe for the measurement of replacement-agent and halon 1301 concentrations. Based on the discussion in Section 11.5.2.3, the mid-infrared and near-infrared regions of the spectrum seem to offer the best possibilities, even though the ultraviolet region is also feasible for halon 1301 and  $\text{CF}_3\text{I}$ . Here we will focus on the possibility of developing fiber-optic probes based on absorption of infrared radiation.

In many ways a fiber-optic-based concentration probe is similar to the DIRRACS system described earlier in that the absorption of an infrared band is monitored to infer concentration, and that the pathlength of the light beam is used to define the absorption volume. However, there are potentially several advantages for a fiber-based measurement technique. Fibers tend to have fairly small diameters (values less than 1 mm are common) so the sampling volume as well as the probe size itself can be quite small. As a result one would expect a fiber-optic-based probe to sample a smaller volume and to be less intrusive than the DIRRACS. Both the detector and light source can be isolated from the measurement volume so that heating problems such as those encountered during the current study can be eliminated.

Since the absorption of mid-infrared light is strongest and the most commonly used approach, fiber optic systems employing this wavelength range are discussed first. This is followed by a discussion of near-infrared methods.

As mentioned above, incoherent light sources are difficult to couple into single fiber optics. If available, lasers offer a much better alternative as a light source. There are a number of tunable lasers which operate in the mid-infrared region. Several of these are reviewed by Eng and Ku (1982). The best candidates which are currently available for the application under discussion are known as tunable lead-salt diode lasers (TDLs). Eng *et al.* (1980) list some of the unique features of TDLs as narrow linewidths ( $< 10^{-4}\text{ cm}^{-1}$ ), broad and continuous tunability, ease of rapid amplitude modulation and wavelength scanning, operation throughout the  $3\text{ }\mu\text{m}$  to  $30\text{ }\mu\text{m}$  spectral range, and extremely small emitting areas.

TDLs are formed from lead-salt semiconductors and their alloys with SnSe, SnTe, CdS, and other materials. Laser action is induced by optical transitions across the bandgap between the nearly empty conduction band and the nearly full valence band existing across a p-n junction. The laser wavelength

is dependent on a number of system parameters including composition, hydrostatic pressure, magnetic fields, operating temperature, and bias current. One major disadvantage of TDLs is that they require cryogenic cooling in order to operate. The requirement for cooling substantially complicates the operation of these devices.

TDLs have been used for spectroscopy measurements in a wide variety of molecules (Eng *et al.*, 1980; Eng and Ku, 1982). The devices have also been widely used for making line-of-sight measurements of concentrations for a range of molecules. As an example, Sell (1983) measured the concentration of CO in the exhaust of an operating engine by line-of-sight absorption of TDL laser light at 4.70  $\mu\text{m}$ . Measurements over a concentration range of 0.1 to 1.5 volume percent were discussed. Particularly significant was the ability to make accurate measurements of CO concentration in the presence of water vapor. The time response of the instrument was reported as 25 ms.

Hanson (1983) has summarized a series of TDL measurements in systems relevant to combustion. Due to the ability to compare on- and off-resonance signals, it was shown that molecular absorption measurements can be made in the presence of concentrated soot fields, which also strongly absorb the infrared light. Many of the measurements discussed were line-of-sight applications, but of particular relevance to the current discussion is the use of TDL absorption measurements for local time-resolved measurements of concentration. Schoenung and Hanson (1982a) demonstrated two techniques for making such measurements in nonreacting and combustng turbulent flows of CO. Absorption measurements were carried out in the region of the 4.6  $\mu\text{m}$  band center of CO. In one case, 8 mm diameter cooled hollow light pipes constructed from brass and aluminum were used to transport the IR laser beam to and from an open absorption path typically having a length of 5 mm. With this probe it was possible to make CO concentration measurements having a signal-to-noise ratio of 1 for a 0.1 mole percent concentration of CO. Response times for the measurements were estimated to be 0.5 ms.

In a second approach, Schoenung and Hanson (also discussed in 1982b) rapidly extracted a sample of the flow through a miniature water-cooled quartz sampling probe having a choked orifice of 0.04 cm diameter. The gases then passed into a room-temperature sample cell having a 1.4 cm pathlength. TDL absorption measurements were then carried out in the cell. With this configuration, it was possible to detect CO concentrations as low as mole fractions of 0.000001. Both experiments and modeling indicated that the response time for this probe was on the order of 0.5 ms with a sampling length of roughly 5 mm for room-temperature gases and 2.0 cm in the flame.

As an indication of the response times achievable using TDL absorption spectroscopy, consider the work of Hanson (1977) who reported a line-of-sight measurement of CO heated by a shock tube. It was reported that measurements could be recorded in less than 100  $\mu\text{s}$ .

Based on the above discussion, it would appear that a TDL system in conjunction with either a properly designed extractive probe or IR fiber optics could be used to make concentration measurements with the required temporal resolution. Kuznetsov *et al.* (1992) have demonstrated the feasibility of fiber-based measurements by coupling lead-salt diode lasers with infrared halide and chalcogenide fibers. The system for coupling the lasers and fiber optics is described. Measurements are reported for ammonia at 10  $\mu\text{m}$ , water at 7.3  $\mu\text{m}$ , and carbon monoxide at 4.7  $\mu\text{m}$ .

Given the ability of the technique to quantify small absorptions and the known strengths of absorption lines in halon 1301 (Baldacci *et al.* 1982), it should be possible to record halon 1301 concentration measurements for very short path lengths. Similar IR absorption strengths at slightly different spectral locations are to be expected for the other replacement agents. Based on these characteristics, the sampling volume for such a system could be made considerably smaller than the current version of the DIRRACS. As discussed earlier, there is a strong interaction between sampling volume, flow velocity, and the ability to time resolve concentration fluctuations. The capability of making concentration measurements in the presence of an absorbing and scattering medium suggests



that measurements should be possible in dirty environments and, perhaps, even in the presence of a two-phase flow of the agent.

It should be noted that the use of lead-salt TDLs does have some drawbacks. Significant complications are introduced by the need for cryogenic cooling. They are fairly complicated devices which require significant training to use appropriately. Additionally, their cost remains relatively high. Often it is necessary to calibrate the output wavelength using known absorptions. Wavelength scans can be nonlinear, and it is common to use a Fabry-Perot etalon to determine the scanning behavior. Occasionally, the frequency output is stabilized by passing part of the beam through a cell with a known absorber. These characteristics suggest that a concentration measurement system for halon alternatives is likely to be costly to construct and operate.

Development work on mid-infrared lasers is continuing. For example, Faist *et al.* (1994a; 1994b) have recently reported the development of a new type of semiconductor laser known as a quantum cascade laser. The laser demonstrated operated near 4.35  $\mu\text{m}$ , but the authors conclude that by varying the band structure of the semiconductor it should be possible to construct lasers having wavelengths throughout the mid-infrared and extending out to the submillimeter wave region. The new laser requires cooling, but operation has been demonstrated for temperatures above that of liquid nitrogen (77 K) suggesting that cooling of these lasers would be somewhat easier than for mid-infrared TDLs which generally must be cooled to substantially lower temperatures. The authors suggest that it may even be possible to operate quantum cascade lasers at higher temperatures.

It is clear that additional development of this new technology is required before a combination of mid-infrared lasers and fiber optics can be used for making concentration measurements in gas mixtures containing replacement halons. However, the advances made thus far in both fiber optics and lasers suggest that in the future it should be possible to quantitatively measure many molecular species, including replacement fire-fighting agents, with high spatial and temporal resolution using a fiber-optic based, mid-infrared absorption probe.

Until recently, the near-infrared has been used very little for quantitative concentration measurements due to the weak absorption of most molecules in this spectral range. However, there are potential advantages for making concentration measurements in this wavelength region. In the mid-infrared the number of lasers and sensitive detectors has been very limited. On the other hand, numerous tunable and nontunable lasers have been developed for near-infrared work, and quantum detectors capable of amplification exist for these wavelengths. The availability of a number of communication lasers operating in the spectral region has driven a great deal of development. These lasers are inexpensive, come in small packages, require low input power, can be efficiently modulated at high frequencies, and require little or no cooling.

Recent research has shown that it is possible to use near-IR absorption techniques for sensitive concentration measurements. A few of these studies are summarized here to give a flavor of the possibilities. One of the earliest studies was by Lenth (1983) who used a GaAlAs diode laser to detect a water-vapor absorption line at a wavelength of 0.8167  $\mu\text{m}$ . In order to increase the sensitivity, a technique known as optical heterodyne spectroscopy was employed. The details of this approach are beyond the scope of the current discussion. It will suffice to point out that the method involves rapid scanning of the laser wavelength over the spectral region of the transition under investigation. This turns out to be relatively simple since the GaAlAs laser can be scanned by varying either the operating temperature or "injection current" for the laser. Lenth used temperature to adjust the laser to operate at a wavelength of 0.8167  $\mu\text{m}$  and then modulated the injection current at a microwave frequency of 2.6 GHz. An absorption cell having a 1 m pathlength containing 2.4 kPa of water vapor was used to provide a 5 % absorption which was easily detected using the experimental configuration.

Later investigators have employed a frequency modulation technique in which two well defined, but closely spaced frequencies are superimposed on the injection current. This approach is known as

two-tone frequency modulation spectroscopy (TTFMS) and has been discussed in detail by Cooper and Warren (1987). Wang *et al.* (1989) applied the technique to record water concentration using overtone absorptions near  $0.8171\ \mu\text{m}$ . It was demonstrated that absorptions as small as  $3 \times 10^{-7}$  could be measured. Based on data provided in the paper, it can be shown that such high sensitivity is sufficient to accurately measure water vapor at pressures less than 1 kPa for a 1 mm pathlength. Stanton and Silver (1988) reported similar measurements using the third overtone absorption band of hydrogen chloride. A InGaAsP laser operating at  $1.2\ \mu\text{m}$  was used for these measurements. The minimum detectable absorption was  $4 \times 10^{-6}$ , but it was argued that relatively straight-forward modifications to the experimental system would be expected to lower this value below  $10^{-6}$ .

Very recently, Bomse (1994) has suggested that near-infrared diode laser spectroscopy could be used to measure a number of species relevant to fire extinguishment including hydrogen fluoride, hydrogen chloride, hydrogen bromide, hydrogen iodide, water, methane, carbon dioxide, carbon monoxide, hydrogen cyanide and oxygen. Furthermore, he speculated that the technique could be developed for measuring halon replacement concentrations. This manuscript also contains a good introduction of the technology which is used for these measurements.

Very efficient optical fibers have been developed for communication applications, and it was a natural extension to couple the newly developed sensitive near-infrared absorption techniques with optical-fiber transport of the laser beam. Carlisle and Cooper (1990) used TTFMS to record a  $10^{-4}$  absorption of water at  $1.3\ \mu\text{m}$  following transport of the laser beam through 100 m of optical fiber. After passing through the optical fiber, the laser beam was collimated with a lens, passed through a sample cell containing the water vapor, and was detected with a InGaAs photodiode. A two-beam method was employed in which a reference beam was split from the laser beam before entering the absorption cell. The signal levels indicated the minimum detectable absorption was  $5 \times 10^{-7}$ .

The use of fiber optics makes it possible to multiplex two or more laser beams into a single fiber. Arroyo *et al.* (1994) used two separate lasers operating at  $1.393\ \mu\text{m}$  and  $1.394\ \mu\text{m}$  to record two individual absorption lines of water vapor heated to 1293 K in a shock tube. Frequency modulation techniques were not used for this experiment. Instead, the two lasers were simply scanned at high rates at different times, and the absorption of each beam was measured by comparing transmitted light with a reference signal. The scans could be recorded at a 3 kHz rate. Since the two water transitions were for different rovibronic states, temperature measurements could be derived from the ratio of integrated intensities for the two transitions. The inferred temperature was within 4 % of the actual temperature.

Baer *et al.* (1994) extended the multiplexing technique further by demonstrating that three laser beams could be used to simultaneously measure water concentration, oxygen concentration, and temperature. In this case, two of the laser beams, operating at  $1.347\ \mu\text{m}$  and  $1.392\ \mu\text{m}$ , were used to measure water vapor temperature in the same way as above. The third laser was operated near  $0.76065\ \mu\text{m}$  and was used to measure the absorption of a weak electronic transition of oxygen. The multiplexed beams were transported to the observation region by the optical fiber and then allowed to pass through either a heated static cell or a 236 cm long room-temperature air path. After passing through the observation volume, the beams were separated using a diffraction grating and detected by three individual photodetectors. Note that since the beams were physically separated, it was not necessary to scan the lasers at different times. Absorption measurements of the water lines were made in a standard way using dual beam approaches, while the oxygen absorption was measured using TTFMS. All three measurements were recorded with a repetition rate of 2 kHz. Measurements showed that the concentration and temperature measurements could be made with good accuracy.

The near-infrared investigations discussed thus far would all be classified as line-of-sight experiments and therefore are not directly applicable to measurements having high spatial resolution. However, Bomse (1994) discusses two approaches which could be used to provide short pathlengths and, therefore, high spatial resolution. The first is referred to as "pitch and catch" in which a laser

beam is transported to the observation volume by a fiber optic, is then passed through the observation volume, and then enters a second fiber optic which transports the beam to a detector. He indicates that collection efficiencies of 25 % - 50 % are possible with this configuration. In the second arrangement, the transmitted laser beam is allowed to strike a detector directly after passing through the observation volume. This is the same approach used in the fiber-optic experiments discussed above. It may be possible to obtain high spatial resolution by reducing the separation between the fiber and detector.

Based on the above discussion, it is clear that fiber-optic-based infrared absorption methods in both the near- and mid-infrared have excellent potential for highly spatial and temporally resolved measurements of fire-fighting agents. Considerable research and development would be required to demonstrate the viability of these approaches and develop a system for field use.

**11.5.3.3 Other Fiber-Optic-Based Concentration Measurement Approaches.** As mentioned previously, simple geometrical optics may be used to describe the light transmission in an optical fiber if the diameter is large relative to the wavelength of the transmitted light. As the diameter becomes small, however, the transmission tends to behave according to wave-guide theory. In other words, the wave nature of light must be taken into account. Furthermore, for small diameter fibers, light propagates not only in the core but also in the cladding. This latter component is known as the evanescent wave, and it decays rapidly in a direction away from the axis of the fiber. If a fiber has no cladding, the evanescent wave penetrates into the fluid outside of the fiber, and, if the fluid strongly absorbs at the wavelength of the transmitted light, the power of the propagating light in the evanescent wave is decreased. Thus, if the fiber is of very small diameter, and the gas surrounding the fiber is a strong absorber, gas sensing can be performed by using an unclad portion of the optical fiber itself as the transducer and employing evanescent wave coupling.

On the other hand, as the fiber diameter gets larger, geometrical optics assumes increasing importance, and the transmission of light behaves according to total internal reflection. For this case, with a gas surrounding the fiber, the core index of refraction,  $n_1$ , is much greater than the index of refraction for the gas,  $n_2$ , and the fiber becomes highly guiding in the sensing region with a corresponding reduction in evanescent wave power and a resulting loss in detection sensitivity. For liquids, a larger fiber with the cladding stripped from a small sensing region performs better due to the relatively higher indices of refraction for liquids. This latter principle for the detection of chemical species is referred to as attenuated total internal reflection (ATR).

The former case of using a very small fiber and taking advantage of evanescent wave coupling to a gas was demonstrated by Tai *et al.* (1987) using fibers transmitting mid-infrared radiation at 3.392  $\mu\text{m}$  for the detection of methane. The authors used standard fused-silica fibers with a core of 50  $\mu\text{m}$  and a cladding thickness of 125  $\mu\text{m}$ . Then, by heating the fiber and drawing a portion of it to a much smaller diameter (1.8  $\mu\text{m}$ ), they fashioned a 10 mm long sensing region and were able to generate an evanescent wave of 5 % to 40 % of the total propagating power outside of the fiber. The minimum detectable concentration of methane using this configuration was reported to be about 1 %.

Expanding upon the idea of ATR, an optical fiber may incorporate fluorocarbon polymers or silicones as cladding materials. Due to their high refractive indices (weak guiding of the core light), the evanescent fields can penetrate deeply into the cladding. These cladding materials, however, are quite porous, and the evanescent field may interact with any gas present in the pores. A power loss at a particular wavelength can then be used to infer the concentration of gas present. Ruddy and Lardner (1993) have modeled the time-dependent attenuation of the optical power in a multimode, step-index fiber due to Fickian diffusion of a fluid through its porous cladding. They proceeded to derive sensor sensitivity, response time, and the product of minimum detectable concentration and sensing length in terms of the fiber parameters, the absorptivity of the fluid, and the diffusion coefficient in the cladding

material. A large number of results are reported in the form of a table listing many common gases. For each gas, an absorption coefficient at a particular wavelength is used to estimate the evanescent power attenuation for typical fiber parameters, and these data yield a value of the product of minimum detectable concentration and sensing length which is reported in the table for each gas. A disadvantage for a technique such as this is the fact that diffusion of the absorbing gas into the fiber is a slow process. Time-response estimates provided by the model are reported in the form of a parameter,  $t_{90}$ , which represents the time required for the attenuation to reach 90 % of the saturation value. Predicted  $t_{90}$  values for typical fiber dimensions were in the range of 20 s to 30 min. The paper also contains numerous references to other ATR and evanescent wave coupling investigations.

An interesting variation on the porous cladding technique was reported by Zhou *et al.* (1989) in which a copolymerization process was used to create a fully porous, plastic fiber with a pore size range from 5 nm to 10 nm and a surface area of 100 m<sup>2</sup>/g. A small 5 mm length of the porous fiber, representing the sensing area, was then spliced into a length of standard, nonporous, plastic fiber. A strongly absorbing gas was then allowed to permeate fully into the sensor core and direct in-line absorption occurred. The authors claim that this sort of sensor has much greater sensitivity than those based on evanescent wave coupling. Furthermore, they assert that the porous fiber exhibits high gas permeability as well as high liquid impermeability, making it particularly suitable for gas concentration measurements in aqueous samples (such as blood gas sensing, for example). An additional advantage was the high flexibility and ease of use for plastic fibers relative to glass fibers. Disadvantages for this technique include the fact that some light gets scattered out of the porous section of the fiber, the calibration curve is nonlinear, and response times are on the order of minutes.

Wenquan *et al.* (1992) describe the application of a tin oxide (SnO<sub>2</sub>) film to an optical fiber, and the resulting increase in transmission when the fiber is immersed in differing concentrations of such gases as methanol, acetone vapor, and ammonia vapor. They present data in the form of transmission spectra for various concentrations of these gases and show that the increases occur in the visible and near-infrared ranges.

The concentration-measurement approaches discussed in this section are under active development. It must be concluded, however, that they have not yet been developed sufficiently to allow real-time concentration measurements of halon replacements. However, as advances are made, it is possible that these techniques could become quite useful for this application.

**11.5.4 Additional Optical-Based Techniques.** There are a number of additional optical techniques beyond the standard absorption and fiber-optic-based approaches discussed thus far which have been used for rapid concentration measurement of gas-phase species. Several of these are discussed in the following sections.

**11.5.4.1 Raman Spectroscopy.** Raman light scattering refers to the nonresonant scattering of light by a molecule in which the energy of the scattered light is shifted by an amount corresponding to differences between the rotational, vibrational, or electronic energy levels of the molecule. When the scattered light has a longer wavelength (lower energy) than the light incident on the molecule it is known as Stokes scattering, and when the scattered wavelength is shorter (higher energy) it is known as anti-Stokes scattering. The most common form of Raman light scattering involves vibrational transitions, and this type will be the focus of the current discussion. Eckbreth (1988) provides a good discussion of Raman light scattering and its use for measurements in combustion environments.

The physical mechanisms responsible for Raman scattering are relatively weak, and very intense lasers are generally required to scatter sufficient radiation for easy detection. The intensity of scattering increases with the photon energy to the fourth power. As a result, visible and even ultraviolet lasers are commonly used to induce Raman scattering. Since the effect causes wavelength

shifts which are characteristic of a particular vibrational transition, it can be selective. As the shifts in wavelength are characteristic of vibrational transitions, they have energies which correspond to mid-infrared transitions. Such energy shifts are small compared to the initial energy of the photons for the light source. The light scattering process also generates light which is unshifted in wavelength from the light source (*i.e.*, resonance or Rayleigh scattering which will be discussed shortly) and which is generally many times more intense than the Raman scattering. As a result, it is typically necessary that the Raman scattered light be isolated from the Rayleigh light scattering in some manner (*e.g.*, by using a spectrograph or a narrow-band spectral filter). The need for spectral isolation complicates the experimental set up.

Raman light scattering can be used for concentration measurements since the intensity of the scattered light is proportional to the number of molecules in the scattering volume. Time-resolved measurements are generally made using high-power pulsed laser which generate sufficient scattered light intensities to provide accurate concentration measurement. A significant drawback of the use of pulsed lasers is that the repetition rates tend to be low ( $< 100$  Hz), and the pulse-to-pulse variations can be large requiring that the laser intensity be measured for each pulse. Copper vapor lasers have recently become available having pulse rates greater than 1000 Hz and sufficient power levels for Raman scattering studies.

It is our opinion that an experimental system could be developed using Raman light scattering for the measurement of halon-replacement concentrations at the required data rate. However, the system would be very expensive to construct and maintain, would require high levels of operator training, and would require that the system in which the measurements were to be made allow adequate optical access for the laser beam and the collection of scattered light. As a result, we conclude that Raman light scattering is not a practical approach for the current application.

**11.5.4.2 Coherent Anti-Stokes Raman Spectroscopy (CARS).** Coherent anti-Stokes Raman spectroscopy (CARS) is a complicated nonlinear optical effect which leads to the generation of an intense coherent beam when two laser beams are "mixed" with the proper phases in an appropriate medium. The effect occurs when two laser beams have a frequency difference ( $\omega_1 - \omega_2$ , with  $\omega_1 > \omega_2$ ) corresponding to a vibrational transition frequency of a molecule in the volume where the laser beams cross. The resulting coherent beam has a frequency,  $\omega_3$ , given by

$$\omega_3 = 2\omega_1 - \omega_2 . \quad (66)$$

The beam which is generated has a higher energy than either of the original laser beams which is why it is known as anti-Stokes scattering. Due to the phase-matching requirements of the technique, the coherent beam which is generated propagates in a different direction than either of the input laser beams.

Since the optical effect which leads to CARS is nonlinear, very high laser intensities are required to induce the effect, but once a threshold power is reached, the intensity of the generated beam increases rapidly. CARS has several advantages over the Raman scattering technique described in the last section. First, the coherent CARS beam can have an intensity many times higher than obtainable from simple incoherent Raman scattering. Second, the fact that the CARS beam is coherent means that it can be transported over a long distance before detection. As a result, it can be spatially separated from potential interferences such as the laser beams used to induce the effect. Third, due to the coherence of the generated beam, CARS measurements can be carried out in flows which are heavily laden with particles. Eckbreth (1988) and Goss (1993) provide excellent reviews of CARS techniques.

CARS has been widely employed for temperature measurements in combustion and other types of systems. In some laboratories it is used quite routinely, and systems have been developed which are sufficiently hardened that they can be used in quite harsh environments (*e.g.*, Eckbreth *et al.*, 1984). Proper calibration allows the technique to be used for concentration measurements as well. It is likely that CARS could be developed as a technique for monitoring suppression-agent concentrations. However, there are several drawbacks which could potentially limit the use of CARS for the current application. Perhaps the most detrimental problem is the complexity and cost of a CARS system. Normally a high powered pulsed Nd<sup>3+</sup>/YAG-pumped dye laser is combined with the doubled output of the solid-state laser at 532 nm to provide the two laser beams. Such a laser system with the associated hardware and detection equipment normally runs well in excess of a 100 000 dollars. In order to record multiple measurements multiple CARS systems would be required. Additionally, the use of a CARS system is far from turn-key, and a qualified professional is required to operate the system. Similar to the Raman measurements discussed earlier, the ability to record measurements every millisecond is likely to be limited by the maximum pulse rate of the laser system. Generally measurements are made at 10 Hz - 20 Hz. Apparently, no measurements have been made at 1000 Hz. Finally, optical access to the region of interest is required. Due to the coherent nature of the laser beams and the generated CARS beam, it would be possible to design systems with relatively small windows for optical access.

Due to the cost, complexity, and relatively low frequency of the CARS approach, we do not recommend this technique for routine concentration measurements of alternative agents. However, it could prove very effective for special measurements under certain circumstances. In particular, it would appear that CARS measurements could be performed during an actual fire-extinction event.

**11.5.4.3 Rayleigh Light Scattering.** As mentioned above, Rayleigh light scattering refers to light scattering by molecules in which the wavelength (energy) of the scattered light is unchanged from that of the light source. The intensity of scattered light is generally at least a 1000 times greater than observed for Raman scattering. As for Raman scattering, the intensity of scattering light increases as the inverse fourth power of light wavelength. Rayleigh light scattering can easily be observed using commercial high-power CW lasers such as argon ion lasers. Scattering can also be induced using pulsed lasers.

Rayleigh light scattering occurs as the result of the interaction of light with all atoms and molecules in a volume. However, the intensity of scattered light depends on the polarizability of the atom or molecule, and the intensity for different molecules varies widely. The rate of photon detection ( $R_p$ ) for Rayleigh scattered light can be written as

$$R_p = KN \sum_{j=1}^M \sigma_j X_j, \quad (67)$$

where  $K$  is a constant whose value depends on the laser intensity, the optics used, and the quantum efficiency of the detector,  $N$  is the total number of molecules in the observation region,  $\sigma_j$  is the Rayleigh light scattering cross section for species  $j$  which is a measure of the efficiency of the molecule for scattering light, and  $X_j$  is the mole fraction of species  $j$ .

For gas mixtures containing three or more species, Equation (67) alone does not provide sufficient information to determine values of  $X_j$ . However, in mixtures of two gases, *e.g.*, air and a halon replacement, the sum of the two mole fractions must equal 1, and it is possible to measure mole fractions for the two species. If calibrations are carried out for the pure gases, denoted as 1 and 2, Equation (67) can be rewritten as

$$X_2(t) = \frac{I(t) - I_1}{I_2 - I_1}, \quad (68)$$

with  $X_2(t)$  being the time-dependent concentration of species 2,  $I(t)$  the observed time-dependent Rayleigh light scattering intensity from the observation volume, and  $I_1$  and  $I_2$  the observed scattering intensities from pure gases 1 and 2.

Rayleigh light scattering has been widely used to record time-resolved concentration measurements in turbulent flows of binary gas mixtures (e.g., Pitts and Kashiwagi, 1984; Dowling and Dimotakis, 1990). It has been demonstrated that measurements are possible for a variety of gas pairs which have data rates in excess of 20 kHz and sampling volumes as small as  $0.0003 \text{ mm}^3$ . The technique has been applied to molecules such as  $\text{CF}_4$  and  $\text{SF}_6$  (Pitts, 1991) which are similar to the replacement agents in molecular structure. Concentrations of halon 1301 have been recorded during unpublished work at NIST. (Pitts, 1984)

There is no doubt that Rayleigh light scattering could be used to make accurate measurements of the replacement agent concentrations given the proper experimental conditions. In fact, Rayleigh light scattering was considered as a serious candidate for such measurements during the planning for the current project. It was ultimately rejected due to its sensitivity to stray scattered light. As discussed above, Rayleigh light scattering occurs at the same wavelength as the laser which induces it. Scattering from particles, known as Mie scattering, also occurs at this same wavelength. Unfortunately, unless special precautions are taken, particles are always present in air with sufficient size to induce Mie scattering from a single particle which is much stronger than the Rayleigh light scattering measured for all of the molecules in the observation volume. As a result, Rayleigh light scattering concentration measurements are nearly impossible unless these small particles are removed in some way. Additionally, any surfaces which are near the observation region can reflect or scatter stray laser light (known as glare) at the same wavelength. For the worst cases, glare can completely overwhelm the Rayleigh light-scattering signal.

A facility for the investigation of turbulent flows has been constructed at NIST which nearly totally eliminates problems associated with the presence of particles and glare. (Bryner *et al.*, 1992) However, such an approach was deemed impractical for field studies of agent releases and Rayleigh light scattering was eliminated from consideration for the current application.

**11.5.4.4 Fluorescence Concentration Measurements.** It was noted earlier that quite strong absorption of light is often observed for transitions between the electronic states of molecules and atoms. These strong absorptions are referred to as "allowed" transitions. The result of the absorption of light is that a molecule ends up in an excited state. The energy which is absorbed is eventually given up by the absorbing species, and the system returns to a lower energy state. There are a number of ways that an electronically excited species can lose energy. One of these is by the release of a photon. The resulting electromagnetic energy can either have the same energy as the photon which was absorbed (*i.e.*, it can return to the same lower energy state from which it came by a process known as resonance fluorescence), or it can result from a transition to a different lower lying state, in which case the emitted photon will be at a different energy than the absorbed photon. Unless absorption occurred from relatively high lying energy states, the transition is most likely to occur to energy states which lie higher than the state from which absorption occurred. As a result, the emitted photon will have a lower energy than the absorbed photon (*i.e.*, the emitted photon is red-shifted).

Fluorescence can be used for selective detection since the absorption and emission wavelengths for a particular molecule are determined by the electronic structure of the molecule which is generally unique. By careful selection of the absorption wavelength and spectral isolation of the emitted energy,

it is possible to isolate the fluorescence from an individual species in complicated mixtures. Generally, electronic transitions of molecules and atoms correspond to photon energies in the visible and ultraviolet portions of the electromagnetic spectrum. Very efficient light sources for absorption and detectors for observing fluorescence have been developed. As a result, species which strongly fluoresce can be detected and measured nonintrusively with good sensitivity using laser-induced fluorescence (LIF). Techniques based on LIF can have excellent temporal and spatial resolution.

The details of the fluorescence behavior of molecules and atoms is a complex subject which is beyond the scope of the current review. Excellent discussions are available in numerous monographs (e.g., Calvert and Pitts, 1966; Eckbreth, 1988). It is sufficient to point out that fluorescence techniques are widely used to measure species in very complicated systems including combustion (e.g., see Eckbreth, 1988). LIF is sufficiently sensitive that images can be recorded for two-dimensional sheets (Seitzman and Hanson, 1993).

As noted above, with the exception of  $\text{CF}_3\text{Br}$  and  $\text{CF}_3\text{I}$ , the agents considered in the current study do not have strong electronic absorptions at energies lower than those corresponding to the vacuum ultraviolet. As a result, it would be extremely difficult to apply fluorescence techniques to the direct measurements of these agents. However, there is another approach based on fluorescence detection which could be applicable.

For measurements of concentration for species which do not fluoresce, it is common to add small amounts of species which strongly fluoresce as tracers. Examples of species which might be added are acetone and iodine. If the tracer species is uniformly mixed with the molecule of interest, then a measure of the tracer species also provides a good approximation for the concentration of the desired species. Such measurements have not been reported for halon 1301 or its possible replacements considered in this study, but it is possible that a tracer fluorescing species could be dissolved in the agent at low concentrations and used to monitor the agent concentration.

The development of a LIF-based measurement approach for agent concentration measurements would require a large research and development effort. A successful conclusion could not be guaranteed. On this basis, it is suggested that this approach be utilized only if more well developed methods do not prove feasible.

**11.5.4.5 Mie Scattering Concentration Measurements.** A light scattering technique for the noninvasive point measurement of mean and fluctuating concentration fields within mixtures was pioneered by Rosensweig, Hottel and Williams (1961). A standard implementation of the technique calls for one of the components to be seeded with passive marker particles (or naturally occurring particles may be used, if appropriate) prior to entering the mixing region. An optical probe in the form of an incident light beam is then propagated into the mixture, and the colloidal suspension of particles in the path of the beam scatters light in all directions. Some of that light is collected by a lens outside of the measurement chamber and directed to a field stop (a slit) which passes light scattered from only a short segment of the incident beam. This defines a probe-measurement volume that is then imaged onto a photomultiplier tube where the collected photons are transduced into an electrical current. The current from the transducer is proportional to the number of particles instantaneously contained within the probe volume, in other words, to the particle concentration.

Strictly speaking, marker concentration is an accurate measure of the marked component concentration only when the diffusivity of the marker in the mixture is the same as the diffusivity of the marked species within the mixture. A measure of the two diffusivities can be obtained by comparing the marker Schmidt number with the Schmidt number of the marked component. Normally, the marker Schmidt number is substantially higher. This condition will not affect the measurement of mean concentration, but it will necessitate that caution be used in the interpretation of concentration fluctuations, particularly those that occur very rapidly. So, in addition to the rather



obvious requirement that the particles have light scattering properties, such as size, shape, and refractive index, that remain invariant from the point of introduction into the flow field to the measurement location, the method further requires that the marker particles faithfully follow the motion of the marked fluid.

The latter constraint leads to a choice of particle diameters typically in the range of 0.2  $\mu\text{m}$  to 2.0  $\mu\text{m}$ . The scattering of light from particles in this size range is described by the Mie equations, which are based on a general solution of Maxwell's equations, and, for this reason, the method is often referred to as an application of Mie scattering. However, H.A. Becker, one of the early pioneers of the procedure, combined the Greek word *nephelē* (meaning cloud) with meter and coined the alternate phrase "marker nephelometry" in his 1977 review paper describing the technique.

Indeed, the exhaustive introduction to marker nephelometry by Becker (1977) remains an excellent initial entry point into the literature for the reader unfamiliar with the procedure. This paper describes the state of the art of the marker-scattered-light technique prevailing at that time. Becker gives a rigorous and general treatment of the theory and reviews the experimental efforts up to the time of publication. In particular, he examines the suitability of using marker concentration as an accurate measure of marked component concentration, and he provides theoretical estimates that demonstrate the validity of the claim when a characteristic length scale of the probe measurement volume (the diameter of a sphere with the same volume, say) is much smaller than the largest length scale over which concentration fluctuations occur in the flow field. The author summarizes the following advantages of the technique: noninvasive, applicable in hostile environments, minimal need for calibration, inherent linearity, and good frequency response.

With the exception of a few key papers, no attempt will be made to repeat the extensive review of the literature prior to 1977 conducted by Becker. Instead, selected relevant papers, which serve to provide an overview of the progress in the field up to the present time, will be discussed. The reader is urged to consult Becker (1977) for earlier investigations.

The initial investigation using this technique was that of Rosensweig *et al.* (1961). The experimental configuration consisted of an air jet marked with smoke particles discharging from a 12.7 mm diameter round nozzle into ambient air. The probe measurement volume was defined by the cross section of the incident light beam and by the width of the slit positioned just in front of the photomultiplier tube. The beam diameter at the measurement location was 1.6 mm and the slit width was 1.8 mm. If we assume that the magnification of the collection optics was equal to one, a probe measurement volume of 3.62 mm<sup>3</sup> can be calculated. The frequency response of the system was reported to be flat out to 2.5 kHz. The authors noted that primary scattering was weak, and that the smoke concentration was dilute so that secondary scattering was negligible. Smoke particles with diameters of 1  $\mu\text{m}$  were used. These smoke particles must be small enough to follow the flow. A criterion for evaluating this condition may be found by evaluating the ratio of particle maximum velocity to fluid maximum velocity for a state of steady sinusoidal fluctuation. A brief analysis which yields this criterion follows.

Consider a spherical smoke particle suspended in an air flow of velocity  $u$  which is sinusoidally oscillating at frequency  $f$  with a maximum velocity  $U$ ,

$$u = U \sin(2\pi ft), \quad (69)$$

and acted on with a force ( $F$ ) given by Stokes' expression (modified by the Cunningham correction) for viscous drag in creeping flow, namely

$$F = \frac{3\pi\mu D_p u_{rel}}{1 + \frac{K_g l}{D_p}}, \quad (70)$$

where  $D_p$  is the particle diameter,  $\mu$  is the fluid kinematic viscosity,  $u_{rel}$  is the relative velocity between the particle and the fluid,  $K_g$  is the Cunningham correction factor ( $= 1.8$  for air),  $l$  is the molecular mean free path, and  $l/D_p$  is the Knudsen number. Note that the Cunningham correction assumes importance only when the particle diameter becomes small enough to approach the size of the molecular mean free path. If the weight of the particle is negligible relative to this drag force, then the equation of motion becomes

$$m_p \frac{dv}{dt} = \frac{3\pi\mu D_p (v - u)}{1 + \frac{K_g l}{D_p}}, \quad (71)$$

where  $m_p = (\pi/6)\rho_p D_p^3$  is the particle mass for particle density  $\rho_p$ ,  $v$  is the particle velocity, and  $u_{rel} = (v - u)$ . The solution of this equation is of the form

$$v = V \sin(2\pi f t + \theta), \quad (72)$$

and one can then form the ratio

$$\frac{V}{U} = \left[ 1 + \left( \frac{2\pi f}{a} \right)^2 \right]^{-1/2}, \quad (73)$$

where

$$a = \frac{18\mu}{\rho_p D_p^2 \left( 1 + \frac{K_g l}{D_p} \right)}. \quad (74)$$

For values of this ratio that are very nearly equal to one, the particle is considered to follow the fluid motion. Thus, upon specification of the fluid and the particle density, one may compute a frequency for a given particle size which yields a specified value of the ratio. For the  $1 \mu\text{m}$  diameter particles used by Rosensweig *et al.* (1961), the ratio was 0.997 at a frequency of 5 kHz. Note that the Stokes drag expression used above is valid only when the Reynolds number based on particle diameter is within the creeping flow regime (less than 1). The authors claimed that this condition was satisfied.

Rosensweig *et al.* (1961) used their experimental system to compute mean concentration, concentration intensity (concentration rms divided by mean concentration), frequency spectra,

autocorrelation functions, two-point spatial correlation functions, and integral length scales at various locations throughout the axisymmetric jet. The measurements established the feasibility of the technique and defined the capabilities and limitations of the system. Becker *et al.* (1967a, 1967b) established a large portion of the theory, refined the experimental technique, and carried out an extensive study of the round free jet configuration with the goal of characterizing its behavior as accurately as possible. Once again the authors measured mean concentration, rms concentration, concentration intermittency factor, spectra, and two-point spatial correlation functions at various locations throughout the jet. A general conclusion drawn from the study was that marker nephelometry applied to gas mixing yields a substantial amount of information in the convective region of the concentration fluctuation spectrum, but cannot give information for spatial scales where molecular diffusion is important because the marker particles do not mimic gas behavior at this level.

Grandmaison *et al.* (1982) repeated the earlier measurements of Becker *et al.* (1967a, 1967b) in the round, free turbulent jet configuration. They used a much larger jet, however. Because of the large scale of the jet, the ratio of turbulence integral length scale to probe measurement volume (a measure of spatial resolution) was quite large. The results were therefore used as a check of the accuracy of earlier measurements. In addition, the authors acquired measurements of the skewness and kurtosis of the concentration fluctuations, the probability density function and wave-number spectra extending into the viscous-convective subrange of the concentration fluctuation spectrum.

With the exception of the experiment by Grandmaison *et al.* (1982), all of the experiments reviewed to this point were conducted with systems employing conventional light sources. Shaughnessy and Morton (1977) appear to have been the first to introduce the use of a laser as the light source for the system. The 2 W argon-ion laser beam employed in this study reduced the electronic-shot-noise level in the detector to levels lower than previously attained. The resulting low detector-noise level allowed the study of another type of noise process: marker shot noise. This noise arises as the result of the random arrival in the control volume of the particles which mark the flow field and is usually referred to as ambiguity noise. The intent of the experiment was to explore the limitations imposed by ambiguity noise on the light scattering technique, and, therefore, the well-documented experimental configuration of a round turbulent jet of air marked with smoke particles and exhausting into a secondary air flow was chosen for the study. The authors detected ambiguity noise and determined that it provided a fundamental limitation on spectral measurements. They furnished theoretical estimates of the ambiguity noise spectrum and its dependence on the size of the control volume and on particle concentration. They also presented experimental measurements to support the theoretical predictions. This paper is also a good source for additional references to the literature before 1977.

Gad-el-Hak and Morton (1979) combined the techniques of laser-Doppler velocimetry (LDV) and marker nephelometry to obtain a probe capable of simultaneous measurement of both concentration and velocity fluctuations at a point. They employed this system for the study of the downstream evolution of smoke released in an isotropic, turbulent flow field. Specifically, the experimental configuration consisted of a biplanar grid of rods with diameter 2.4 mm and mesh size 12 mm mounted in the 20 cm  $\times$  30 cm test section of a wind tunnel. Air, flowing at a velocity of 4 m/s, created a nearly isotropic turbulent flow field after passing through the grid. Smoke was released upstream of the grid. The smoke had a mean particle diameter of 0.3  $\mu$ m and consisted of dioctyl phthalate polydispersed particles produced by a smoke generator. The probe consisted of a standard LDV arrangement in which two equal intensity beams from a laser were crossed in the flow field forming a fringe system at the intersection volume. Forward scattered light was collected and focused onto a 1 mm diameter pinhole (spatial filter) where it then passed to a photomultiplier tube. The output from the photomultiplier tube was amplified and low pass filtered at 5 kHz to yield a voltage that was directly proportional to the concentration of smoke, whereas for velocity measurements, the

tube output was band pass filtered between 300 kHz and 3 MHz, amplified, and then directed to a circuit which removed amplitude information. The resulting frequency modulated signal was passed through a phase-locked loop in order to demodulate the Doppler frequency shift and to convert it to a voltage directly proportional to the velocity component normal to the bisector of the two crossed beams. Note that velocity measurements were possible only when smoke was present. The spatial resolution of the system was about 2 mm, and the signal-to-noise ratio was about 100 for the axial velocity component and 200 for the concentration signal. The system was used for the acquisition of mean and rms velocity and concentration profiles, concentration autocorrelation functions, spectra, scales, intermittencies, probability density functions and concentration-velocity cross correlations. These data were obtained for a selection of downstream locations. An earlier note by Catalano *et al.* (1976) describes similar measurements using the same techniques for an examination of the development of an axisymmetric jet exhausting into a co-flowing airstream.

The work of Long *et al.* (1981) dramatically extended the application of marker nephelometry by simultaneously acquiring the instantaneous concentration field at 10 000 spatial locations in a plane intersecting a turbulent jet flow. The output beam from a 2.5 W argon-ion laser was first focused using a long-focal-length spherical lens (in order to minimize the thickness of the sheet produced in the next step) and then diverged by means of a cylindrical lens. The resulting laser sheet was 0.15 mm thick. The sheet was directed into the seeded jet, and scattered light was collected and imaged onto the active area of a computer-controlled, low-light-level TV camera. In order to freeze the motion, the camera was gated on for a period of 10  $\mu$ s after which the image was digitized and the values transferred to computer memory and then onto magnetic tape. The digitization was performed on a  $100 \times 100$  array so that the scattered light intensity as a function of position was recorded at 10 000 locations. The lenses were selected such that the area imaged onto the camera corresponded to a  $2 \text{ cm} \times 2 \text{ cm}$  region of the jet with each pixel of the image corresponding to a volume given by  $0.2 \text{ mm} \times 0.2 \text{ mm} \times 0.15 \text{ mm}$ . The smallest resolvable length scale was therefore 0.2 mm. The frequency corresponding to this smallest scale at the Reynolds numbers typically used was 7.5 kHz resulting in a minimum resolvable time scale of about 130  $\mu$ s, which was much longer than the 10  $\mu$ s time during which the camera was gated on. Thus, each image was essentially a realization of the instantaneous concentration distribution within the flow. The time required to digitize the 10 000 point array and transfer the results to tape was about 1 s, which was much longer than the longest characteristic time scale of the flow. This implied that successive images were independent events and that statistical quantities could be calculated by means of ensemble averaging. The results included plots of mean and rms concentration surfaces varying in two space dimensions over a longitudinal plane passing through the axis of the jet and covering a region extending from three to eight diameters downstream of the jet. Furthermore, a rotation of the laser sheet also allowed data to be acquired for a plane oriented normal to the jet flow. Further results included spatial covariance information and temporal information along a line in the flow field which resulted from an interesting variation on the technique. Additional discussion of the mixing mechanism and the structure of the jet mixing layer as revealed by these measurements was provided by Long and Chu (1981). An earlier paper by Long *et al.* (1979) gives an initial brief introduction to the experimental technique.

Marker nephelometry provides an accurate and sensitive means for measuring concentration in time-varying flows. It is generally considered nonintrusive. Optical access is required, but the experimental configuration is relatively simple. The required lasers and optics are relatively inexpensive and simple to operate. With regard to the current application, however, a major drawback is the need to seed the flow with a uniform concentration of small particles. We have identified no investigations in the literature where a released superheated liquid has been seeded with particles, such that the vaporized liquid has a uniform distribution of particles. A possible alternative would be to seed the air flow. However, this approach would be very difficult to implement in the full-scale dry-

bay and nacelle test facilities at Wright-Patterson AFB. On this basis, marker nephelometry is not recommended for measurements of agent concentration.

**11.5.4.6 Specialized Concentration Measurements Based on Optical Absorption.** In this section two techniques are discussed which can be utilized for concentration measurements of specific species or for binary mixtures which are known to consist of only two gases such as the halon 1301 and replacement-agent mixtures in air discussed in this report.

An infrared absorption technique known as the nondispersive infrared (NDIR) approach is widely used for quantitative concentration measurements. Various configurations are used, but the most relevant is the Luft-type NDIR analyzer. (Strobel and Heineman, 1989) These devices are often employed for measurements of carbon dioxide and carbon monoxide. In this approach two heated nichrome wires are used as IR sources, and their output is chopped so that light passes first through a sample cell and then a reference cell. Light transmitted by the cells falls on a Golay detector formed by placing the gas of interest in a volume containing a flexible membrane. When radiation is absorbed by the gas in the detector, the volume changes and causes movement of the membrane which can be detected optically or by changes in capacitance. The resulting alternating signal has an amplitude which can be related to the concentration of the gas in the sample cell. Proper calibration results in an instrument which has low noise levels and very little drift. A major drawback of these instruments for the current application is that their time response is on the order of 3 s to 5 s and that gas samples must be extracted and passed through the sample cell. Significant engineering would be required to produce an instrument based on this principle having a millisecond time response.

Kidde-Graviner company (1992) has developed an instrument, named the Ultra-Violet Halonyser, for measuring concentrations of halon 1211 and 1301 based on ultraviolet absorption. It consists of a sensing head having dimensions of 18 cm  $\times$  12.5 cm  $\times$  8.5 cm which is placed in the flow of interest. The sensing head contains two ultraviolet sources which are transmitted over a pathlength of roughly one cm. One source falls in a wavelength range which is absorbed by the species of interest, while the second is not absorbed. The transmitted beams are then detected by solar blind (one which does not respond to visible wavelengths) detectors. By comparing the two transmitted beam intensities, the concentration of absorbing species can be determined. The presence of the second beam allows the measurement to be corrected for the presence of dust or condensed water.

The specifications for the instrument indicate that it has excellent accuracy, stability, linearity, and temperature insensitivity. The response time is listed as 1 ms. Note that this instrument will be subject to the same geometric constraints as the DIRRACS which were discussed earlier. A 1 ms response time will only be possible if the detection volume is swept out during this period.

The operating wavelengths are not given, but it is certain that the ultraviolet radiation must have longer wavelengths than the vacuum ultraviolet which is strongly absorbed by air. Of the replacement agents, only  $\text{CF}_3\text{I}$  has strong absorption in this region. For this reason, this instrument could not be used for  $\text{C}_2\text{F}_5\text{H}$ ,  $\text{C}_3\text{F}_8$ , or  $\text{C}_3\text{F}_7\text{H}$ . Measurements could be made by mixing a species such as halon 1301 into the agent which would act as a tracer. (Hillman, 1994)

The Ultra-Violet Halonyser seems to offer potential for the direct measurement of halon 1301 and  $\text{CF}_3\text{I}$ . Drawbacks of the current system include the large size of the sampling head, the large sampling volume, and limitations on the number of agents which can be sampled. It would be worthwhile to consider further development of this approach to see if these limitations could be overcome.

**11.5.4.7 Optical Speckle Technique.** An optical speckle technique was utilized by Oberste-Lehn and Merzkirch (1993) for the indirect measurement of density fluctuations which can then be related to temperature fluctuations by assuming a constant pressure, ideal-gas flow. Because the method directly measures the deflection of light caused by gas density fluctuations, it is also suitable

for the measurement of concentration fluctuations. Recall that speckle refers to the granular appearance that arises when laser light is reflected from a diffuse surface. Because of the rough texture of the diffusely reflecting surface, two wavelets arriving at a point in space that are scattered from different bumps on the surface undergo an optical path length difference. For most light sources, the coherence length is so small that overlapping wave trains change rapidly and randomly, thereby have washing out any interference pattern that might have been set up. Conversely, most lasers enjoy a relatively large coherence length (at least much greater than the height of the surface imperfections) such that when the two wavelets meet at a point in space as described above, a constant phase difference is maintained and a large-scale interference pattern can be sustained. In other words, the spatially coherent light scattered from a diffuse surface fills the surrounding region with a stationary interference pattern.

Oberste-Lehn and Merzkirch made use of this technique to study the turbulent temperature field developed downstream of a turbulence generating grid through which a heated mixture of methane and air was passed. Specifically, methane was injected into the air flow at the grid location by passing the methane gas through injection holes in the tubes which formed the structure of the grid. The gas mixture was then stably burned at the grid location. The grid itself served as the flame holder producing a nearly planar and stable flame front. The investigators determined that a homogeneous turbulent scalar field was produced as a result of this technique beginning at a distance of 15 mesh lengths downstream from the grid. Furthermore, rms values of temperature fluctuations as high as 33 K were produced which were an order of magnitude higher than any achieved by earlier investigations. This fact allowed the experimenters to investigate the question of whether or not a turbulent scalar field remains passive (*i.e.*, it does not affect the turbulence dynamics) at such high fluctuation amplitudes. This question was the motivation for the experiment.

The experimental arrangement for the optical speckle technique employed the light from a pulsed ruby laser. The beam was expanded to a diameter of 90 mm and was then transmitted as a parallel beam through the test section downstream of the grid. After exiting from the test section, the beam passed through a lens which formed a half-size image of a vertical plane in the test section on a ground glass plate placed after the lens. The ground glass served as the diffusely reflecting surface for the generation of a speckle pattern. The light exiting the ground glass plate was then imaged onto a photographic plate. The experimental procedure required that a double exposure be recorded on the photographic plate: the first exposure resulted from a 50 ns pulse transmitted through the test section with no flow, and the second exposure was acquired after passing the pulsed beam through a flow with density variations. The density variation in the turbulent temperature field deflected light resulted in a displaced speckle pattern with respect to the first reference pattern. The local displacement  $\Delta$  at a point furnished a measure of the light deflection angle  $\varepsilon$  at a point in the flow field. Subsequent point-by-point interrogation of the double exposure (the specklegram) with a thin laser beam produced a Young's fringe pattern at each location. Evaluation of the fringe pattern permitted the recovery of the local displacement  $\Delta$  at each point, and thus the light deflection angle  $\varepsilon$  at each point in the field of view. Finally, this information was used to recover such information as the spatial correlation of the density fluctuations  $r_{pp}$ , macro and micro integral length scales  $\Lambda_p$  and  $\lambda_p$ , as well as one-dimensional energy spectra of the density and temperature fields. By comparing the experimental data with the theoretical models of Rotta (1972) and of Driscoll and Kennedy (1985), the authors determined that even at very large fluctuation magnitudes, the turbulent temperature field could still be regarded as a passive scalar field.

This technique is very interesting because it allows the entire flow field to be analyzed simultaneously. However, we feel that the technique is not appropriate for the current application since it requires significant optical access and a very high degree of experimental sophistication. It would be difficult to record data in real time.

**11.5.4.8 Miniature Mach-Zehnder Interferometer.** Fabricius *et al.* (1992) discuss the use of a miniature gas sensing system for the measurement of gas concentrations as small as 0.000001 mole fraction. The centerpiece of this system is a small chip (4 cm x 1 cm) which, by employing integrated optics, incorporates a miniature Mach-Zehnder interferometer. As with most interferometry techniques, the input light path is split into two arms (paths) and then brought back together. If the optical path lengths of the two arms are not identical, then the coherent light will form an interference pattern, thereby altering the intensity of the output beam. Light is directed through the chip by means of surface wave guides which are single-mode structures on the order of 4  $\mu\text{m}$ . Now, if one of the arms of the interferometer is coated with a gas-sensitive polymer layer (polysiloxane) which is sensitive to the vapors of organic solvents, then the presence of one of these gases will produce a continuous change in the refractive index of the polymer layer and, in turn, alter the optical path length of one arm of the interferometer. Thus, the phase shift imparted to the signal in one arm induces an interference pattern, and the output intensity of the signal is reduced. The phase shift of the signal is a function of the type of gas and the concentration. To complete the miniature sensor system, light at 788 nm from a semiconductor laser was coupled into the interferometer chip, and the output light was guided by a 50  $\mu\text{m}$  multimode optical fiber to a diode array detector. The authors investigated the response of the system to the presence of various hydrocarbons, chlorohydrocarbons and aromatic compounds. They found the calibration curve (phase shift versus concentration) to be linear, and the response time to be on the order of seconds. Possible drawbacks could include: a lack of reproducibility resulting from difficulties in controlling the thickness and adhesion of the polymer layer and a sensitivity issue due to the fact that light must penetrate a short distance into the polymer layer from within the wave guide and therefore light interaction with the gas-sensitive material is limited.

**11.5.5 Acoustic Absorption.** A review of the literature indicates that the measurement of concentration of a contaminant within a binary gas mixture can be made by means of acoustic techniques by taking advantage of the direct dependence of sound absorption in gas mixtures on mole fraction. When a sound wave propagates through a fluid or solid medium, it loses some of its energy due to losses in the medium and at the boundaries of the medium. More specifically, following Temkin (1981), the passage of an acoustic wave serves to drive individual fluid particles into oscillation about their mean positions, and because of this motion, the pressure, density, temperature and entropy vary for each fluid particle. The sound wave performs a net amount of work on each fluid particle at the expense of the acoustic energy. In other words, the loss of acoustic energy of the wave becomes an increase in the internal energy of the fluid particles. In general, attenuation within the medium is a result of many factors: viscous losses, heat conduction effects, and diffusive processes, as well as losses associated with molecular exchanges of energy. If the medium is bounded, then losses at the boundaries can also occur as a result of the combination of the effects of reflection, refraction, diffraction and scattering. For the measurement of concentration, the basic experimental arrangement would require an acoustic source which transmits a signal which is attenuated upon passage through the fluid medium of variable concentration to a receiver where the intensity of the signal would be monitored. This basic setup could then be improved with the addition of a second transmitter-receiver pair which propagates a reference signal through a portion of the same fluid medium, but for which the concentration is held constant. Division of the attenuated signal by the reference signal would serve to remove the effects of drift resulting from changes in source intensity as well as variations in the fluid medium itself due to effects other than a changing concentration (humidity variations, *etc.*). Furthermore, techniques based upon the propagation of an acoustic beam vis a vis the transmission of an optical beam enjoy the additional advantage that the fluid medium may be optically opaque. A

brief review of pertinent theory and experiments will be followed by a probative calculation serving to illustrate the feasibility of the method.

The subject of acoustic wave propagation in fluids has been treated by many authors over a period of 150 years. An exhaustive history of the oldest work may be found in Truesdell (1953). In addition, Truesdell develops, with considerable detail and rigor, the classical viscothermal theory describing the propagation of a plane acoustic wave into a Newtonian viscous fluid obeying Fourier's law of heat conduction. The extension of the theory to nonreacting, binary mixtures undergoing various diffusive processes may be found in the papers by Kohler (1949), Huang (1973), and Margulies and Schwarz (1985). In addition, the latter authors extend the theory further by discussing the case of a nondiffusive, equilibrium mixture with coupled chemical reactions as well as the case of a single component viscoelastic material. Bass *et al.* (1984) discuss the classical theory, but augment it with a lengthy discourse on molecular relaxation processes which are of importance for the general case of absorption of sound by the atmosphere. For further information on relaxation processes and their relation to sound propagation in fluids, the interested reader is referred to Lindsay (1982). Several experimental investigations are available which serve to gage the range and validity of the theory. Angona (1953) measured absorption in  $\text{CO}_2$ ,  $\text{CS}_2$ ,  $\text{C}_2\text{H}_4\text{O}$  and in mixtures of  $\text{CS}_2$  and  $\text{C}_2\text{H}_4\text{O}$  for frequencies ranging from 2 kHz to 10 kHz. He reported that differences between theory and the observed attenuation were less than 5 %. Greenspan (1956) performed measurements of sound absorption in monatomic gases such as He, Ne, Ar, Kr, and Xe and Greenspan (1959) extended the measurements to such polyatomic gases as  $\text{N}_2$ ,  $\text{O}_2$  and dry air. He reports that the classical theory is verified for monatomic gases, but differences between theory and observed attenuation are somewhat larger in the case of diatomic gases. He provides an extensive review of theory and experiment in Greenspan (1965). Law *et al.* (1966) examined the behavior of sound absorption in mixtures of He in Ar and He in Kr at a single frequency of 70 kHz. They plotted the variation in the absorption coefficient versus mole fraction of He and showed excellent agreement with theory over the entire range. Prangma *et al.* (1970) performed measurements of sound absorption in mixtures of Ar in He for frequencies ranging from 108 Hz to 1010 Hz. Their data is in good agreement with theory over the lower half of their frequency range. Finally, in the area of detection of acoustic waves in fluids, Bucaro *et al.* (1982) review the state of the art in the use of optical fibers for the purpose of creating acoustic sensors as well as the related issues of acoustic modulation of optical field parameters such as phase, intensity, and polarization. In order to illustrate the nature of the theory and to lay the groundwork for the calculation to follow, the classical viscothermal case will be reviewed below.

The simplest one-dimensional problem concerns the forced propagation of planar, infinitesimal, acoustic waves into a semi-infinite, single component, homogeneous fluid, otherwise at rest. The variables in this perturbed system will be considered to consist of an equilibrium value ( $I_o$ ) and an acoustic contribution ( $I^a$ ). The decomposition is represented by

$$I = I_o + I^a \quad (75)$$

where  $I$  represents any of the system variables such as velocity, pressure, temperature, *etc.* If one positions a reference coordinate system such that the  $x$ -axis points in the propagation direction, then the acoustic contribution oscillates the  $yz$ -plane of fluid at  $x = 0$  according to



$$I^a = \Re[I_o^a e^{i\omega t}] , \quad (76)$$

where  $\omega$  is the radian frequency of the oscillation,  $t$  is time, and  $\Re$  indicates the real part of the expression. This disturbance then propagates in the  $x$ -direction as a damped harmonic oscillation governed by the complex propagation constant

$$\chi = -(\alpha + ik) = -\left(\alpha + i\frac{\omega}{c}\right) , \quad (77)$$

where the imaginary part, the wave number  $k$ , describes the spatial variation in the propagation direction, and the real part, the absorption coefficient  $\alpha$ , is a measure of the change in amplitude with distance.  $c$  is the phase speed of the wave. The full description of the damped longitudinal wave is, therefore, given by

$$I^a = \Re[I_o^a e^{\chi x + i\omega t}] . \quad (78)$$

The attenuation and dispersion (variation of phase speed with wavelength) of this acoustic wave are found by solving the balance equations for the fluid such as: conservation of mass, momentum and energy, and with the use of such constitutive relations as: Newton's law (the linear relationship between stress and rate of strain) and Fourier's law, for example. Considerable simplification of the problem follows from the linearization of the field equations that results from the introduction of the infinitesimal acoustic contributions as described by Equation (75) for each variable and then neglecting products of acoustic quantities. Into this set of linear partial differential equations, one substitutes the acoustic disturbance (Equation (78)) for each variable to obtain a set of algebraic equations in terms of the acoustic amplitude variables  $\chi$ . In order to obtain a nontrivial solution, the determinant of the coefficients of the equations is set to zero. This process yields a biquadratic characteristic equation in the dimensionless variable  $\chi/k_o$ , where  $k_o = \omega/c_o$ . Note that  $c_o$  is a fixed, reference sound speed which is conventionally obtained by neglecting the effects of viscosity and heat conduction. For this case, fluid pressure is a function of density alone, and  $(c_o)^2 = (\partial p / \partial \rho)_s$  (constant entropy). Expressed in dimensionless form, this equation is referred to as the Kirchhoff-Langevin equation and is given by

$$[(i - \gamma X)XY] \left(\frac{\chi}{k_o}\right)^4 + [1 + iX(1 + \gamma Y)] \left(\frac{\chi}{k_o}\right)^2 + 1 = 0 , \quad (79)$$

where the dimensionless variables are

$$X = StVi = \frac{\omega \eta_o Vi}{\rho_o c_o^2} \quad (\text{Frequency Number}) , \quad (80)$$

$$Y = \frac{1}{PrVi} = \frac{k_\theta}{\eta_o C_p Vi} \quad (\text{Thermoviscous Number}) , \quad (81)$$

$$\gamma = \frac{C_p}{C_v} \quad (\text{Specific Heat Ratio}) , \quad (82)$$

$$St = \frac{\omega \eta_o}{\rho_o c_o^2} \quad (\text{Stokes Number}) , \quad (83)$$

$$Vi = \frac{4}{3} + \frac{\kappa_o}{\eta_o} \quad (\text{Viscosity Number}) , \quad (84)$$

and

$$Pr = \frac{\eta_o / \rho_o}{k_o / \rho_o C_p} = \frac{\eta_o C_p}{k_o} \quad (\text{Prandtl Number}) . \quad (85)$$

Additional quantities referred to in the dimensionless groups are radian frequency,  $\omega$ , dynamic viscosity,  $\eta$ , density,  $\rho_o$ , reference phase speed,  $c_o$ , thermal conductivity,  $k_o$ , specific heat at constant pressure,  $C_p$ , specific heat at constant volume,  $C_v$ , and bulk viscosity,  $\kappa_o$ .

The roots of the Kirchhoff-Langevin equation are found by means of the quadratic formula. The simplest expressions are obtained by solving for the alternative quantity  $(k_o/\chi)^2$  yielding the two pairs of roots:

$$\begin{aligned} \left(\frac{k_o}{\chi}\right)^2 &= \frac{-[1+iX(1+\gamma Y)] - \{1-X^2(1-\gamma Y)^2 + 2iX[1-(2-\gamma)Y]\}^{1/2}}{2} \\ &\quad \text{and} \\ \left(\frac{k_o}{\chi}\right)^2 &= \frac{-[1+iX(1+\gamma Y)] + \{1-X^2(1-\gamma Y)^2 + 2iX[1-(2-\gamma)Y]\}^{1/2}}{2} . \end{aligned} \quad (86)$$

Note that in this expression, of the two possible values for the square root of the complex quantity within the braces, one uses the principal value, that is, the value for which the argument of the complex number expressed in polar form lies between  $-\pi \leq \theta \leq \pi$ . Furthermore, of the two pairs of roots in Equation (86), only one root from each pair may be retained, namely the root for which a positive value is obtained for  $\alpha$  corresponding to real attenuation. This analysis yields two solutions. The first, referred to as type I waves, corresponds to typical compressional sound waves and is obtained from the first equation in Equation (86), whereas the second is denoted as type II waves, commonly referred to as thermal waves, and derived from the latter expression in Equation (86). Unfortunately, due to the complexity of the expressions in Equation (86), one cannot easily interpret the behavior of  $\alpha$  and  $c$ . However, for fluids such that  $Y < 1/(2 - \gamma)$  and for low frequencies  $X \ll 1$ , one may employ a power series expansion to yield an approximation to the solutions in Equation (86). For this approximation, only the pressure wave solution survives (the attenuation of the type II waves is very large at low frequencies) and one obtains

$$\frac{\alpha}{k_o} = \frac{X}{2} [1 + (\gamma - 1)Y] \quad \text{and} \quad c = c_o. \quad (87)$$

This approximation predicts no dispersion and a simple form for the absorption coefficient due to Kirchhoff (1868). In dimensional form, the absorption coefficient becomes

$$\alpha = \frac{2\pi^2 f^2}{c_o^3} \left[ \frac{\kappa_o + \frac{4}{3}\eta_o}{\rho} + \frac{\gamma - 1}{\gamma} \frac{k_o}{\rho} C_v \right], \quad (88)$$

where  $f$  is the frequency of the acoustic wave in Hz. Unfortunately, due to the many assumptions and approximations employed in its derivation, this expression has only limited utility and is most accurate only for low frequencies where the absorption is proportion to  $f^2$ .

The extension of the derivation to binary mixtures undergoing various diffusive processes requires the generalization of the balance and constitutive equations used. For example, Fick's equation describing diffusion due to a concentration gradient (Fick, 1855) must be added to the derivation and should, for low frequency number, be extended to include, at the very least, terms describing pressure diffusion and thermo-diffusion (the Soret effect). The pressure diffusion effect describes the tendency for a preferential diffusion of the component with the greater molecular weight toward the region of higher pressure in a local pressure gradient. The thermo-diffusion or Soret effect occurs with a local temperature gradient and describes the tendency for heavier molecules to diffuse toward regions of low temperature. In other words, following Bass *et al.* (1984), when there is a local pressure or temperature gradient, less massive molecules with their higher thermal speeds move toward a condition of equilibrium more rapidly than heavier molecules. The diffusion due to the pressure gradient is accompanied by preferential diffusion of the lighter molecules due to the thermal gradient. Fourier's law must also be supplemented with a term which yields additional heat transfer as a result of diffusion. This effect, called the diffusion-thermo effect, tends to have the opposite effect to that of thermo-diffusion. This sort of generalized Fick's law was developed in the dissertation of Huang (1973) and allows for finite propagation of concentrations at large distances from a diffusing source.

Now, following the more complete derivation of Margulies and Schwarz (1985), the constitutive equations along with the balance equations for the fluid such as conservation of mass, momentum, and energy, are once again combined and linearized as before. A solution in the form of Equation (78) is again assumed and substituted into the equations to yield a set of algebraic equations in the variable  $\chi$ . The resulting characteristic equation for the determinant of the coefficients becomes a sixth-order polynomial and admits three pairs of roots. Retaining the root from each pair that yields a positive value for  $\alpha$  (real attenuation) produces three possible solutions, types I, II and III waves. Once again employing a power series expansion valid for  $X \ll 1$ , we can obtain explicit expressions for  $\alpha$  and  $c$  for the sole surviving type I wave. The form obtained when one assumes a binary mixture of perfect, monatomic gases is given by

$$\alpha = \frac{2\pi^2 f^2}{c_o^3} \left[ \frac{k_o + \frac{4}{3}\eta_o}{\rho} + \frac{\gamma-1}{\gamma} \frac{k_o}{\rho C_v} + D_{AB} x_A x_B \gamma \left( \frac{M_B - M_A}{M} + \frac{\kappa_T(\gamma-1)}{x_A x_B \gamma} \right)^2 \right] \quad (89)$$

and  
 $c = c_o$ ,

where the undefined variables in the equation are the diffusion coefficient due to a concentration gradient,  $D_{AB}$ , mole fractions of components A and B,  $x_A$  and  $x_B$ , molecular weights for components A and B,  $M_A$  and  $M_B$ , molecular weight for the mixture,  $M = x_A M_A + x_B M_B$ , and the thermodiffusion coefficient,  $\kappa_T$ . This approximation also predicts no dispersion, and the classical form for the absorption coefficient is extended to include diffusion effects. This form of the equation was also found by Kohler (1949).

The absorption coefficient  $\alpha$  is more precisely termed an amplitude attenuation coefficient and has units of nepers per meter. Note that a neper (Np) is a dimensionless unit of *level* often used in the acoustics community. More specifically, the American Institute of Physics Handbook defines the level of a quantity as the logarithm of the ratio of that quantity to a reference quantity of the same kind. The neper, then, is a unit of level when the logarithm is to the napierian base  $e$ . This attenuation coefficient is not to be confused with the *energy attenuation coefficient*. The latter is related to  $\alpha$  because the acoustic energy is proportional to the square of the wave's amplitude. Thus, the energy of the wave will decay with an exponential constant, the energy attenuation coefficient, equal to  $2\alpha$ . We can express this precisely in terms of the acoustic intensity  $I$  which is defined as the average rate of flow of energy through a unit area normal to the direction of propagation and has units of  $W/m^2$ . The difference in intensity level as the wave propagates from 0 to  $x$  is given by

$$\begin{aligned} I(x) &= I(0)e^{-2\alpha x} \\ \text{or} \\ 2\alpha x &= \ln \frac{I(0)}{I(x)}. \end{aligned} \quad (90)$$

This quantity, also in nepers per meter, can be expressed in the more conveniently measured units of dB per m by calculating the quantity (see Kleppe, 1989)

$$\begin{aligned} 10 \log_{10} \left( \frac{I(0)}{I(x)} \right) &= 10 \log_{10}(e^{2\alpha x}) \\ &= 10 \log_{10}(e) \ln(e^{2\alpha x}) \\ &= 10 \log_{10}(e)(2\alpha x) \\ &= 8.686 \alpha x. \end{aligned} \quad (91)$$

Summarizing, then,  $\alpha$  expressed in Np/m can be converted to the more easily measured units of dB/m by multiplying by 8.686.

Some experimental data is available to document the range of validity of Equation (89). Specifically, the experiments of Prangma *et al.* (1970), Law *et al.* (1966), and Greenspan (1956) are particularly useful. The mixture data of Prangma *et al.* (1970) and Law *et al.* (1966) show good agreement with theory for relatively low frequencies, and the data of Greenspan (1956) in monatomic

gases displays excellent agreement with Equation (89) up to a frequency number of about  $X = 0.1$ . Furthermore, in a plot revealing the relative contributions to the absorption coefficient from the effects of viscosity, heat conduction, and diffusion effects, Law *et al.* (1966) showed that for  $x_{He} > 0.25$  (He in Ar) and for  $x_{He} > 0.15$  (He in Kr), concentration dependent diffusive effects dominate the relative contributions to the absorption coefficient and were attributed to the large differences in molecular weights for the two components. Equation (89), therefore, appears to be a good predictor of the behavior of the absorption coefficient for acoustic waves in a binary mixture of gases with frequency numbers  $X < 0.1$ .

With this in mind, a probative calculation using Equation (89) was performed to determine the variation in the absorption coefficient of a planar acoustic wave propagating through mixtures of halon replacement agents and air. Although these agents are not monatomic, nor do they follow a perfect gas equation of state, the calculation should, nevertheless, reveal the nature of the variation of the absorption coefficient with mole fraction and should serve as a reasonable guide for the determination of the feasibility of a potential acoustic absorption experiment. The bulk viscosity  $\kappa_o$  and the thermodiffusion coefficient  $\kappa_T$  were both assumed to be zero for the purposes of this calculation. All other material parameters for the fluid were taken to be those for dry air at 20 °C. The acoustic wave was chosen to have a frequency of 1 MHz corresponding to a frequency number  $X = 0.001$ . The precise diffusivity value to use was unknown. However an examination of experimental diffusivities for various gas mixtures found in such texts as Bird *et al.* (1960) shows that a value of  $D_{AB} = 1 \times 10^{-5} \text{ m}^2\text{s}^{-1}$  is reasonable. Note that the various fluid parameters such as  $\eta_o$ ,  $k_\theta$ , and  $D_{AB}$  should actually be values calculated for the mixture and should thus be a function of mole fraction. The functional behavior with mole fraction for these values can, with some difficulty, be calculated from the Chapman-Enskog theory described in Hirschfelder *et al.* (1964) or from the more complete two-fluid theory of Goldman and Sirovich (1967, 1969). However, simply using constant values for dry air at 20 °C will provide a relatively accurate first approximation. Finally, the result from Equation (89) was multiplied by 8.686 as explained above in order to obtain units of dB/m. The results are shown in Figure 86, and the program used for the calculation may be found in Appendix M. The figure shows that for each agent, the absorption  $\alpha(x_{agent})$  rises to a maximum for  $0.1 \leq x_{agent} \leq 0.3$  and then slowly decays back to its starting level. The inverse function  $x(\alpha)$  is double valued. It is very sensitive for small mole fractions and less sensitive for larger mole fractions. Except for mole fractions close to the maximum value where some ambiguity could arise, determining the mole fraction based upon sound absorption appears to be quite feasible. Topics which will need to be investigated further include the effects of humidity and the presence of particles on the absorption coefficient.

Even though the analysis provided here suggests that sound absorption has the potential to measure concentration in binary mixtures of air and fire-fighting agents, we have not identified examples where such measurements have been made. For this reason, it is concluded that a great deal of development would be required before this technique would be available for the current application. On this basis, it is recommended that this approach not be developed until other, more developed approaches have been tried.

**11.5.6 Summary and Recommendations.** During the course of the literature review summarized above we have identified no analytical techniques which could be used to record agent concentrations with high temporal and spatial resolution without a significant development and testing effort. This is true despite the fact that a large and wide variety of possibilities were considered. In fact, none of the techniques surveyed appear to be more promising than the two approaches (combined aspirated hot-film/cold-wire probe and DIRRACS) considered during the current effort.

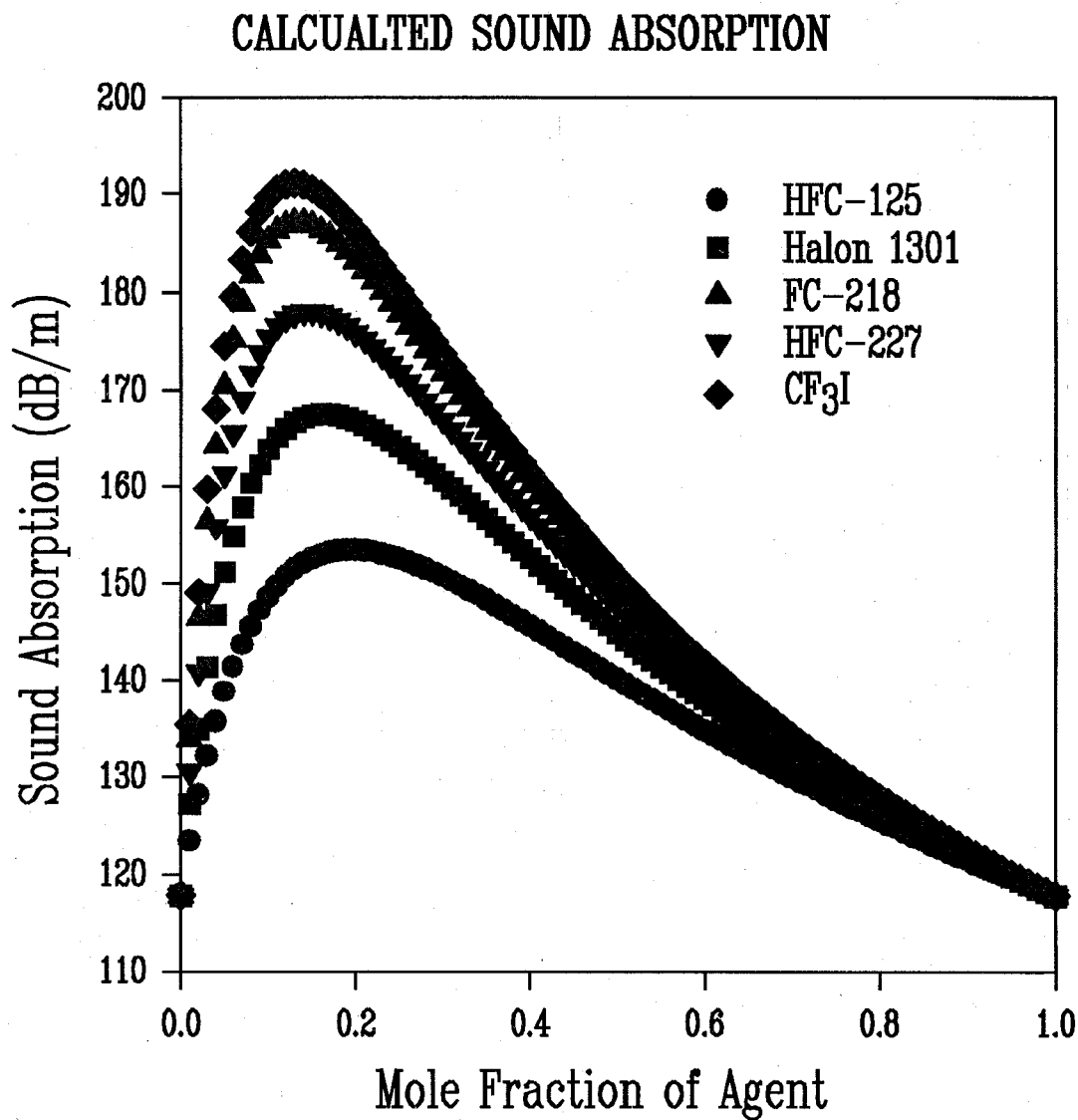


Figure 86. Values of sound absorption (dB/m) as a function of mixture fraction for HFC-125, halon 1301, FC-218, HFC-227ea, and CF<sub>3</sub>I in air calculated using Equation (89).

On the other hand, it is also clear that some of the techniques surveyed are more promising than others. In particular, we have concluded that time-resolved mass spectrometry, and mid- and near-infrared absorption used in conjunction with fiber optics (to provide easy access and spatial resolution) are the most promising approaches considered during our literature search. If it is necessary to expand the search for suitable diagnostics, these approaches should be assessed very early in the effort.

## 11.6 Acknowledgments

This project was supported by the Air Force, Navy, Army, and the Federal Aviation Administration. A large number of people made contributions to our efforts by providing guidance, data, advice, and information. We are very grateful to all for the help we received. Lt. Gretchen Brockfeld of Wright-Patterson AFB served as the project manager. Her advice and support was very much appreciated. Our specifications of the combined aspirated hot-film/cold-wire probe was greatly aided by our discussions with Jagadish Buddhavarapu, Skip Kiland, and Steve Hoff of TSI, Inc. George Kluoda, Jim Norris, and Bill Dorko of the Chemical Science and Technology Laboratory at NIST provided advice for the design of the calibration system. Dr. Dean Ripple, George Burns, and Dr. Billy Mangum of the Physics Laboratory at NIST provided guidance in the calibration and use of thermocouples. Dr. Calvin Stainback of NASA Langley provided understanding of compressible flow through a nozzle. Dr. George Mattingly of the Chemical Science and Technology Laboratory suggested the use of a soap bubble meter for calibrating our mass-flow controllers and helped with the calibration of the soap-bubble meter. Dick Jacobs of MKS Instruments, Inc. helped with details concerning the mass flow controllers and the use of gas correction factors. Dr. Jiann Yang of BFRL at NIST was very helpful with regard to the computer work sheets used in calibration and data acquisition. Professor Ronald So of Arizona State University and Anthony Birch of the British Gas Corporation provided useful information concerning the response of aspirated hot-films to velocity fluctuations. We are grateful for the efforts of Mike Glover in assembling the DIRRACS, Yonas Makai for assembling an amplifier and assisting with the optical design of the DIRRACS, Darren Lowe for design and electronics assistance, Mike Smith for his testing of the FEAS, and Zhuomin Zhang for characterizing various optical components of the DIRRACS. We are appreciative of the capable and timely support we received at Wright Patterson AFB under the direction of Captain Gregg Caggianelli during experiments in the dry-bay test facility; including set up and testing support by Russ Cornetet, William Humphries, and Frank Feldman from Systems Research Laboratory, and the availability of Ron Britton's laboratory for calibration work. Several experts provided information concerning the Statham analyzer and the Halonyzer. These included William Meserve and Duane Van Ostrand of Pacific Scientific, Paul Boris of the Federal Aviation Administration, Steve Lamb of Walter Kidde Aerospace, and Joe Petkus of Boeing Aerospace Corporation. Special thanks go to William Meserve and Duane Van Ostrand who provided experimental results for the time response of the Halonyzer. Tom C. Hillman of Walter Kidde Aerospace provided insights concerning the Ultra-Violet Halonyzer. Dr. Tim Margulies of the Environmental Protection Agency suggested the acoustical technique for concentration measurements and provided many helpful discussions.

## 11.7 References

Adler, D., "A Hot Wire Technique for Continuous Measurement in Unsteady Concentration Fields of Binary Gaseous Mixtures," *J. Phys. E. Scientific Ins.* 5, 163 (1972).

- Ahmed, S.A., and So, R.M.C., "Concentration Distributions in a Model Combustor," *Exp. Fluids* 4, 107 (1986).
- Aihara, Y., Koyama, H., and Morishita, E., "Effects of an Air Stream on Turbulent Diffusion of a Helium Jet from a Small Nozzle," *Phys. Fluids* 17, 665 (1974).
- Angona, F.A., 1953 "The Absorption of Sound in Gas Mixtures," *J. Acoustical Soc. Am.* 25, 1116 (1953).
- Antonia, R.A., Browne, L.W.B., and Chambers, A.J., "Determination of Time Constants of Cold Wires," *Rev. Sci. Instrum.* 52, 1382 (1981).
- Arroyo, M.P., Birbeck, T.P., Baer, D.S., and Hanson, R.K., "Dual Diode-Laser Fiber-Optic Diagnostic for Water-Vapor Measurements," *Optics Lett.* 19, 1091 (1994).
- Bass, H.E., Sutherland, L.C., Piercy, J., and Evans, L., "Absorption of Sound by the Atmosphere," *Physical Acoustics XVII*, 145 (1984).
- Baer, D.S., Hanson, R.K., Newfield, M.E., and Gopaul, N.K.J.M., "Multiplexed Diode-Laser Sensor System for Simultaneous H<sub>2</sub>O, O<sub>2</sub>, and Temperature Measurements," *Optics Lett.* 19, 1900 (1994).
- Baldacci, A., Passerini, A., and Ghersetti, S., "Infrared Absorption Studies in the Vapor Phase of CF<sub>3</sub>Br: Spectra Between 1800 and 400 cm<sup>-1</sup>," *J. Mol. Spectros.* 91, 103 (1982).
- Batt, R.G., "Turbulent Mixing of Passive and Chemically Reacting Species in a Low-Speed Shear Layer," *J. Fluid Mech.* 82, 53 (1977).
- Becker, H.A., Hottel, H.C., and Williams, G.C., "On the Light-Scatter Technique for the Study of Turbulence and Mixing," *J. Fluid Mech.* 30, 259 (1967a).
- Becker, H.A., Hottel, H.C., and Williams, G.C., "The Nozzle-Fluid Concentration Field of the Round, Turbulent, Free Jet," *J. Fluid Mech.* 30, 284 (1967b).
- Becker, H.A., "Mixing, Concentration Fluctuations, and Marker Nephelometry," in *Studies in Convection: Theory, Measurement, and Applications, Volume 2*, Launder, B.E., Ed., pp. 45-139, Academic, New York, 1977.
- Birch, A.D., Brown, D.R., Dodson, M.G., and Thomas, J.R., "The Turbulent Concentration Field of a Methane Jet," *J. Fluid Mech.* 88, 431 (1978).
- Birch, A.D., Brown, D.R., Dodson, M.G., and Swaffield, F., "Aspects of Design and Calibration of Hot-Film Aspirating Probes Used for the Measurement of Gas Concentration," *J. Phys. E. Scientific Ins.* 19, 59 (1986).
- Bird, R.B., Stewart, W.E., and Lightfoot, E.N., *Transport Phenomena*, Wiley, New York, 1960.
- Blackshear, Jr., P.L. and Fingerson, L., "Rapid-Response Heat Flux Probe for High Temperature Gases," *ARS J.* 32, 1709 (1962).
- Bomse, D.S., *Real Time Detection of Halon Replacement Decomposition Products Using Near-Infrared Diode Laser Spectroscopy*, A White Paper for the Halon Replacement RDT&E Community, Southwest Sciences, Inc., September 19, 1994.
- Bradshaw, P., *An Introduction to Turbulence and Its Measurement*, Pergamon, New York, 1971.
- Brown, G.L., and Rebollo, M.R., "A Small, Fast-Response Probe to Measure Composition of a Binary Gas Mixture," *AIAA J.* 10, 649 (1972).
- Brown, J.A., and DeStefano, R.J., "Fire Extinguishing Agent Sensor (FEAS)," Wright Laboratories, Wright-Patterson AFB., Ohio 45433-6553, 1992.
- Bryner, N., Richards, C.D., and Pitts, W.M., "A Rayleigh Light Scattering Facility for the Investigation of Free Jets and Plumes," *Rev. Sci. Instrum.* 63, 3629 (1992).
- Bucaro, J.A., Lagakos, N., Cole, J.H., and Giallorenzi, T.G., "Fiber Optic Acoustic Transduction," *Physical Acoustics XVI*, 385 (1982).
- Calvert, J.G., and Pitts, J.N., *Photochemistry*, Wiley, New York, 1966.



Carlisle, C.B., and Cooper, D.E., "Tunable Diode Laser Frequency Modulation Spectroscopy Through an Optical Fiber: High-Sensitivity Detection of Water Vapor," *Appl. Phys. Lett.* 56, 805 (1990).

Catalano, G.D., Morton, J.B., and Humphris, R.R., "Experimental Investigation of an Axisymmetric Jet in a Coflowing Airstream," *AIAA J.* 14, 1157 (1976).

Chamberlain, G., *Criteria for Aircraft Installation and Utilization of an Extinguishing Agent Concentration Recorder*, Federal Aviation Administration Report No. FAA-DS-70-3, March, 1970.

Chan, K., Ito, H., and Inaba, H., "All-Optical Remote Monitoring of Propane Gas Using a 5-km-Long, Low-Loss Optical Fiber Link and an InGaP Light-Emitting Diode in the 1.68  $\mu\text{m}$  Region," *Appl. Phys. Letters* 45, 220 (1984).

Comte-Bellot, G., "Hot-Wire Anemometry," *Annual Review of Fluid Mechanics* 8, 209 (1976).

Cooper, D.E., and Warren, R.E., "Two-Tone Optical Heterodyne Spectroscopy with Diode Lasers: Theory of Line Shapes and Experimental Results," *J. Opt. Soc. Am. B* 4, 470 (1987).

Corrsin, S., "Turbulence: Experimental Methods," in *Handbook der Physik*, Vol. 8/2, Flugge, S., and Truesdell, C., Eds., pp. 523-590, Springer Verlag, Berlin, 1963.

Demaree, J.E., and Dierdorf, P.R., *Aircraft Installation and Operation of an Extinguishing-Agent Concentration Recorder*, National Aviation Facilities Experimental Center Technical Development Report No. 403, September 25, 1959.

Dereniak, E.L., and Crowe, D.G., *Optical Radiation Detectors*, Wiley, New York, 1984. The expression given in the book is for the spectral radiant emittance which is  $\pi$  times the spectral radiance.

Dowling, D.R., and Dimotakis, P.E., "Similarity of the Concentration Field of Gas-Phase Turbulent Jets," *J. Fluid Mech.* 218, 109 (1990).

Driscoll, R.J., and Kennedy, L.A., "A Model for the Spectrum of Passive Scalars in an Isotropic Turbulence Field," *Phys. Fluids* 28, 72 (1985).

Eckbreth, A.C., Dobbs, G.M., Stufflebeam, J.H., and Tellex, P.A., "CARS Temperature and Species Measurements in Augmented Jet Engine Exhausts," *Appl. Optics* 23, 1328 (1984).

Eckbreth, A.C., *Laser Diagnostics for Combustion Temperature and Species*, Abacus, Cambridge, MA, 1988.

Edgell, W.F. and May, C.E., "Raman and Infrared Spectra of  $\text{CF}_3\text{Br}$  and  $\text{CF}_3\text{I}$ ," *J. Chem. Phys.* 22 1808 (1953).

Eng, R.S., Butler, J.F., and Linden, K.J., "Tunable Diode Laser Spectroscopy: An Invited Review," *Opt. Eng.* 19, 945 (1980).

Eng, R.S., and Ku, R.T., "High Resolution Linear Laser Absorption Spectroscopy-A Review," *Spectros. Letters* 15, 803 (1982).

Fabricius, N., Gauglitz, G., and Ingenhoff, J., "A Gas Sensor Based on an Integrated Optical Mach-Zehnder Interferometer," *Sensors and Actuators B* 7, 672 (1992).

Faist, J., Capasso, F., Sivco, D.L., Sirtori, C., Hutchinson, A.L., and Cho, A.Y., "Quantum Cascade Laser," *Science* 264, 553 (1994a).

Faist, J., Capasso, F., Sivco, D.L., Sirtori, C., Hutchinson, A.L., and Cho, A.Y., "Quantum Cascade Laser: An Intersub-band Semiconductor Laser Operating Above Liquid Nitrogen Temperature," *Electron. Letters* 30, 865 (1994b).

Fedyayev, A.A., Mironov, A.K., and Sergievskiy, E.D., "An Experimental Investigation of Binary Turbulent Boundary Layer Structures," *Dantec Information* 9, 13 (September, 1990).

Ferrarese, J.A., *General Guidelines for Measuring Fire-Extinguishing Agent Concentrations in Powerplant Compartments*, Federal Aviation Administration Advisory Circular AC No. 20-100, September 21, 1977.

- Fick, A., "Über Diffusion," *Annalen Phys. Chem.* 94, 59 (1855).
- Fingerson, L.M., and Freymuth, P., "Thermal Anemometers," in *Fluid Mechanics Measurements*, Goldstein, R.J., Ed., pp. 99-154, Hemisphere, Washington, 1983.
- Gad-el-Hak, M., and Morton, J.B., "Experiments on the Diffusion of Smoke in Isotropic Turbulent Flow," *AIAA J.* 17, 558 (1979).
- Goldman, E., and Sirovich, L., "Equations for Gas Mixtures," *Phys. Fluids* 10, 1928 (1967).
- Goldman, E., and Sirovich, L., "Equations for Gas Mixtures II," *Phys. Fluids* 12, 245 (1969).
- Goss, L.P., "CARS Instrumentation for Combustion Applications," in *Instrumentation for Flows with Combustion*, Taylor, A.M.K.P., Ed., pp. 251-322, Academic, New York, 1993.
- Grandmaison, E.W., Rathgeber, D.E., and Becker, H.A., "Some Characteristics of Concentration Fluctuations in Free Turbulent Jets," *Can. J. Chem. Eng.* 60, 212 (1982).
- Greenspan, M., "Propagation of Sound in Five Monatomic Gases," *J. Acoustical Soc. Am.* 28, 644 (1956).
- Greenspan, M., "Rotational Relaxation in Nitrogen, Oxygen and Air," *J. Acoustical Soc. Am.* 31, 155 (1959).
- Greenspan, M., 1965 "Transmission of Sound Waves in Gases at Very Low Pressures," *Phys. Acoustics II*, 1 (1965).
- Gregory, C.C., "IR Fibers Shed Poor Reputation at Longer Wavelengths," *Photonics Spectra* 27(7), 103 (July, 1993).
- Grosshandler, W.L., Gann, R.G., and Pitts, W.M., *Evaluation of Alternative In-Flight Fire Suppressants for Full-Scale Testing in Simulated Aircraft Engine Nacelles and Dry Bays*, National Institute of Standards and Technology Special Publication SP-861, April, 1994.
- Hamins, A., Gmurczyk, G., Grosshandler, W., Presser, C., and Seshadri, K., "Flame Suppression Effectiveness," in *Evaluation of Alternative In-Flight Fire Suppressants for Full-Scale Testing in Simulated Aircraft Engine Nacelles and Dry Bays*, Grosshandler, W.L., Gann, R.G., and Pitts, W.M., Eds., pp. 345-465, National Institute of Standards and Technology Special Publication SP-861, April, 1994.
- Hanson, R.K., "Shock Tube Spectroscopy: Advanced Instrumentation with a Tunable Diode Laser," *Appl. Optics* 16, 1479 (1977).
- Hanson, R.K., "Tunable Diode Laser Measurements in Combustion Gases," in *Tunable Diode Laser Development and Spectroscopy Applications, Proceedings of SPIE, Volume 438*, Lo, W., Ed., pp. 75-83, The Society of Photo-Optical Instrumentation Engineers, Bellingham, WA, 1983.
- Hillman, T.C., Walter Kidde Aerospace, Personal Communication, February, 1994.
- Hinze, J.O., *Turbulence Second Edition*, McGraw-Hill, New York, 1975.
- Hirschfelder, J.O., Curtiss, C.F., and Bird, R.B., *Molecular Theory of Gases and Liquids*, Wiley, New York, 1964.
- Hough, R.L., *Critical Analysis of the Statham Gas Analyzer Method*, Wright Air Development Center Technical Memorandum WCLE-TM-59-14, March 18, 1959.
- Huang, M.-N., *Ultrasound and Light Scattering in a Diffusing and Chemically Reacting Binary Mixture of Fluids*, Ph.D. Dissertation, The John Hopkins University, 1973.
- Jones, B.G., and Wilson, R.J., "Gas Concentration Measurements with a Temperature Compensated Aspirating Probe," in *Symposium on Turbulence*, Patterson, G.K., and Zakin, J.L., Eds., pp. 205-210, Science Press, Princeton, 1979.
- Kleppe, J.A., *Engineering Applications of Acoustics*, Artech House Acoustics Library, Artech House, Norwood, MA, 1989.
- Kidde-Graviner, Ltd., *Ultra-Violet Haloniser*, Data Sheet, September, 1992.

King, L.V., "On the Convection of Heat from Small Cylinders in a Stream of Fluid: Determination of the Convection Constants of Small Platinum Wires with Applications to Hot-Wire Anemometry," *Phil. Trans. R. Soc. London* A214, 373 (1914).

Kirchhoff, G.R., "Über den Einfluß der Wärmeleitung in einem Gase auf die Schallbewegung," *Annalen Phys. Chem.* 134, 177 (1868).

Kohler, M., "Schallabsorption in Binären Gasmischungen," *Zeits. Physik* 127, 41 (1949).

Kuznetsov, A.I., Nadezhdinskii, A.I., and Stepanov, E.V., "Tunable Diode Laser Spectroscopy Accessories Based on Middle IR Halide and Chalcogenide Fibers," in *Tunable Diode Laser Applications*, Nadezhdinskii, A.I., and Prokhorov, A.M., Eds., pp. 104-118, The Society of Photo-Optical Instrumentation Engineers, Bellingham, WA (1992).

Lang, S.B., *Sourcebook of Pyroelectricity*, Gordon and Breach, New York, 1974.

*Laser Focus World* 30(9), 13 (September, 1994), "Purification Lowers IR-Fiber Loss to 0.11 db/m."

LaRue, J.C., Deaton, T., and Gibson, C.H., "Measurement of High-Frequency Turbulent Temperature," *Rev. Sci. Instrum.* 46, 757 (1975).

Law, A.K., Koronaios, N., and Lindsay, R.B., "Effect of Diffusion on Ultrasonic Attenuation in Mixtures of the Rare Gases," *J. Acoustical Soc. Am.* 41, 93 (1966).

Lee, J., and Brodkey, R.S., "Light Probe for the Measurement of Turbulent Concentration Fluctuations," *Rev. Sci. Instrum.* 34, 1086 (1963).

Lee, J., and Brodkey, R.S., "Turbulent Motion and Mixing in a Pipe," *A.I.Ch.E. J.* 10, 187 (1964).

Lenth, W., "Optical Heterodyne Spectroscopy with Frequency- and Amplitude-Modulated Semiconductor Lasers," *Optics Lett.* 8, 575 (1983).

Lindsay, R.B., "Relaxation Processes in Sound Propagation in Fluids: A Historical Survey," *Physical Acoustics XVI*, 1 (1982).

Long, M.B., and Chu, B.T., "Mixing Mechanism and Structure of an Axisymmetric Turbulent Mixing Layer," *AIAA J.* 19, 1158 (1981).

Long, M.B., Webber, B.F., and Chang, R.K., "Instantaneous Two-Dimensional Concentration Measurements in a Jet Flow by Mie Scattering," *Appl. Phys. Letters* 34, 22 (1979).

Long, M.B., Chu, B.T., and Chang, R.K., "Instantaneous Two-Dimensional Gas Concentration Measurements by Light Scattering," *AIAA J.* 19, 1151 (1981).

Margulies, T.S., and Schwarz, W.H., 1985 "Acoustic Wave Propagation in Fluids," in *Frontiers in Fluid Mechanics, A Collection of Research Papers Written in Commemoration of the 65th Birthday of Stanley Corrsin*, Davis, S.H., and Lumley, J.L., Eds., pp. 219-280, Springer-Verlag, New York (1985).

McGee, P.R., Cleveland, F.F., and Miller, S.I., "Infrared Spectral Data and Tentative Assignments for  $\text{CF}_3\text{Br}$  and  $\text{CF}_3\text{I}$ ," *J. Chem. Phys.* 20, 1044 (1952).

McQuaid, J., and Wright, W., "The Response of a Hot-Wire Anemometer in Flows of Gas Mixtures," *Int. J. Heat Mass Transfer* 16, 819 (1973).

McQuaid, J., and Wright, W., "Turbulence Measurements with Hot-Wire Anemometry in Non-Homogeneous Jets," *Int. J. Heat Mass Transfer* 17, 341 (1974).

Molelectron Application Note, *P1-Series Pyroelectric Detector/Amplifier*, Molelectron Detector Incorporated, Portland, OR, 1994.

Molina, L.T., Molina, M.J., and Rowland, F.S., "Ultraviolet Absorption Cross Sections of Several Brominated Methanes and Ethanes of Atmospheric Interest," *J. Phys. Chem.* 86, 2672 (1982).

New, J.D., and Middlesworth, C.M., *Aircraft Fire Extinguishment. Part III. An Instrument for Evaluating Extinguishing Systems*, Civil Aeronautics Administration Technical Development and Evaluation Center Technical Development Report No. 206, Indianapolis, IN, June, 1953.

- Ng, W.F., and Epstein, A.H., "High-Frequency Temperature and Pressure Probe for Unsteady Compressible Flows," *Rev. Sci. Instrum.* 54, 1678 (1983).
- Ninnemann, T.A., and Ng, W.F., "A Concentration Probe for the Study of Mixing in Supersonic Shear Flows," *Exp. Fluids* 13, 98 (1992).
- Nye, J.O., and Brodkey, R.S., "Light Probe for Measurement of Turbulent Concentration Fluctuations," *Rev. Sci. Instrum.* 38, 26 (1967a).
- Nye, J.O., and Brodkey, R.S., "The Scalar Spectrum in the Viscous-Convective Subrange," *J. Fluid Mech.* 29, 151 (1967b).
- Oberste-Lehn, K., and Merzkirch, W., "Speckle Optical Measurement of a Turbulent Scalar Field With High Fluctuation Amplitudes," *Expts. Fluids* 14, 217 (1993).
- Pacific Scientific HTL Division, *Halonyzer II Operation/Maintenance*, Document No. 57180001, September, 1988a.
- Pacific Scientific HTL Division, *Calibration Certification Plan for HTL P/N 60000009-2 Model Halonyzer II with Halon 1301 Extinguishant*, Document No. 57710001, September, 1988b.
- Pasto, D.J., and Johnson, C.R., *Organic Structure Determination*, Prentice-Hall, Englewood Cliffs, NJ, 1969.
- Perry, A.E., *Hot-Wire Anemometry*, Oxford University Press, Oxford, 1982.
- Perry, A.E., "The Time Response of an Aspirating Probe in Gas Sampling," *J. Phys. E. Scientific Ins.* 10, 898 (1977).
- Pitts, D.R., and Sissom, L.E., *Schaum's Outline of Theory and Problems of Heat Transfer*, McGraw-Hill, New York, 1977.
- Pitts, W.M., "Effects of Global Density Ratio on the Centerline Mixing Behavior of Axisymmetric Turbulent Jets," *Expts. Fluids* 11, 125 (1991).
- Pitts, W.M., and Kashiwagi, T., "The Application of Laser-Induced Rayleigh Light Scattering to the Study of Turbulent Mixing," *J. Fluid Mech.* 141, 391 (1984).
- Pitts, W.M., and McCaffrey, B.J., "Response Behaviour of Hot Wires and Films to Flows of Different Gases," *J. Fluid Mech.* 169, 169 (1986).
- Pitts, W.M., unpublished work (1984).
- Pitts, W.M., Yang, J.C., Gmurczyk, G., Copper, L.Y., Grosshandler, W.L., Cleveland, W.G., and Presser, W.G., "Section 3. Fluid Dynamics of Agent Discharge" in *Evaluation of Alternative In-Flight Fire Suppressants for Full-Scale Testing in Simulated Aircraft Engine Nacelles and Dry Bays*, Grosshandler, W.L., Gann, R.G., and Pitts, W.M., Eds., pp. 37-343, National Institute of Standards and Technology Special Publication SP-861, April, 1994.
- Prangma, G.J., Jonkman, R.M., and Beenakker, J.J.M., "Sound-Absorption Measurement in Helium-Argon Mixtures in the 'Burnett Region'" *Physica* 48, 323 (1970).
- Putley, E.H., "The Pyroelectric Detector," In *Semiconductors and Semimetals*, Vol. 5, Willardson, R.K., and Beers, A.C., Eds., pp. 259-285, Academic Press, New York, 1970.
- Rosensweig, R.E., Hottel, H.C., and Williams, G.C., "Smoke-Scattered Light Measurement of Turbulent Concentration Fluctuations," *Chem. Eng. Science* 15, 111 (1961).
- Rotta, J.C., *Turbulente Strömungen*, B. G. Teubner, Stuttgart, 1972.
- Roxlo, C., and Mandl, A., "Vacuum Ultraviolet Absorption Cross Sections for Halogen Containing Molecules," *J. Appl. Phys.* 51, 2969 (1980).
- Ruddy, V., and Lardner, K., "Porous Clad Fibres as Sensor Probes," *Int. J. Optoelect.* 8, 87 (1993).
- Saito, M., Takizawa, M., Ikegawa, K., and Takami, H., "Optical Remote Sensing System for Hydrocarbon Gases Using Infrared Fibers," *J. Appl. Phys.* 63, 269 (1988).

Saito, M., Miyagi, M., Kuritani, T., and Tanei, F., "Radiation Thermometry and Gas Sensor Using Chalcogenide Glass Fibres," *Int. J. Optoelect.* 7, 375 (1992).

Savin, O.R., Shkurdoda, V.F., and Simonovsky, V.I., "Mass Spectrometers for Technological Control in Industry," *Int. J. Mass Spect. Ion Phys.* 46, 163 (1983).

Schoenung, S.M., and Hanson, R.K., "Laser Absorption Sampling Probe for Temporally and Spatially Resolved Combustion Measurement," *Appl. Optics* 21, 1767 (1982a).

Schoenung, S.M., and Hanson, R.K., "Temporally and Spatially Resolved Measurements of Fuel Mole Fraction in a Turbulent CO Diffusion Flame," *Nineteenth Symposium (International) on Combustion*, pp. 449-458, Combustion Institute, Pittsburgh, 1982b.

Seitzman, J.M., and Hanson, R.K., "Planar Fluorescence Imaging in Gases," in *Instrumentation for Flows with Combustion*, Taylor, A.M.K.P., Ed., pp. 405-466, Academic, New York, 1993.

Sell, J.A., "Tunable Diode Laser Measurements of Carbon Monoxide in Engine Exhaust," in *Tunable Diode Laser Development and Spectroscopy Applications, Proceedings of SPIE, Volume 438*, Lo, W., Ed., pp. 67-74, The Society of Photo-Optical Instrumentation Engineers, Bellingham, WA, 1983.

Shaughnessy, E.J., and Morton, J.B., "Laser Light-Scattering Measurements of Particle Concentration in a Turbulent Jet," *J. Fluid Mech* 80, 129 (1977).

So, R.M.C., and Ahmed, S.A., "Helium Jets Discharging Normally into a Swirling Air Flow," *Expts. Fluids* 5, 255 (1987).

So, R.M.C., Zhu, J.Y., Ötügen, M.V., and Hwang, B.C., "Some Measurements in a Binary Gas Jet," *Exp. Fluids* 9, 272 (1990).

So, R.M.C., Zhu, J.Y., Ötügen, M.V., and Hwang, B.C., "Behavior of Probability Density Functions in a Binary Gas Jet," *Exp. Fluids* 11, 227 (1991).

Stanton, A.C., and Silver, J.A., "Measurements in the HCl 3  $\leftarrow$  0 Band Using a Near-IR InGaAsP Diode Laser," *Appl. Optics* 27, 5009 (1988).

Strobel, H.A., and Heineman, W.R., *Chemical Instrumentation: A Systematic Approach, Third Edition*, Wiley, New York, 1989.

Tai, H., Tanaka, H., and Yoshino, T., "Fiber-Optic Evanescent-Wave Methane-Gas Sensor Using Optical Absorption for the 3.392- $\mu$ m line of a He-Ne Laser," *Opt. Letters* 12, 437 (1987).

Takeuchi, K., Tanaka, T., Ikeda, M., Shibata, K., Sakauchi, Y., Yamada, Y., and Nakano, S., "Highly Accurate CO<sub>2</sub> Gas Sensor Using a Modulation-Type Pyroelectric Infrared Detector," *Jpn. J. Appl. Phys.* 32, 221 (1993).

Temkin, S., *Elements of Acoustics*, Wiley, New York, 1981.

Truesdell, C., "Precise Theory of the Absorption and Dispersion of Forced Plane Infinitesimal Waves According to the Navier-Stokes Equations," *J. Rational Mech. Analysis* 2, 643 (1953).

Wang, L.-G., Tate, D.A., Riris, H., and Gallagher, T.F., "High-Sensitivity Frequency-Modulation Spectroscopy with a GaAlAs Diode Laser," *J. Opt. Soc. Am B* 6, 871 (1989).

Way, J., and Libby, P.A., "Hot-Wire Probes for Measuring Velocity and Concentration in Helium-Air Mixtures," *AIAA J.* 8, 976 (1970).

Way, J. and Libby, P.A., "Application of Hot-Wire Anemometry and Digital Techniques to Measurements in a Turbulent Helium Jet," *AIAA J.* 9, 1567 (1971).

Wenquan, L., Sigan, G., and Shunxuan, Z., "Study of Optical Characteristics of SnO<sub>2</sub> as Optical Fiber Sensing Material," *Chinese Phys. Lasers* 19, 215 (1992).

Whistler, W.J., and Schaefer, K., "Design Considerations and Applications of Mass Spectrometers for Process Measurement and Control," *Int. J. Mass Spect. Ion Phys.* 46, 159 (1983).

White, F.A., and Wood, G.M., *Mass Spectrometry Application in Science and Engineering*, Wiley, New York, 1986.

Wilson, D.J., and Netterville, D.D.J., "A Fast-Response, Heated-Element Concentration Detector for Wind-Tunnel Applications," *J. Wind Eng. Ind. Aerodynamics* 7, 55 (1981).

Yanikoski, F.F., *Gas Analysis Apparatus*, United States Patent Office Patent Number 2,586,899, February, 26, 1952.

Zhou, Q., Kritz, D., Bonnell, L., and Sigel, Jr., G.H., "Porous Plastic Optical Fiber Sensor for Ammonia Measurement," *Appl. Optics* 28, 2022 (1989).

Zhu, J.Y., So, R.M.C., and Ötügen, M.V., "Turbulent Mass Flux Measurements Using a Laser/Hot-Wire Technique," *Int. J. Heat Mass Transfer* 31, 819 (1988).

Zhu, J.Y., So, R.M.C., and Ötügen, M.V., "Mass Transfer in a Binary Gas Jet," *AIAA J.* 27, 1131 (1989).

## Appendix A. FORTRAN Program NOZZLE.FOR to Estimate Volume-Flow Rates of Agents and Air Extracted By Aspirating Hot-Film Probe

```

*   Isentropic flow through a nozzle. (NOZZLE.FOR)

*   David E. Hess
*   Fluid Flow Group - Process Measurements Division
*   Chemical Science and Technology Laboratory
*   National Institute of Standards and Technology
*   January 31, 1994
*   Updated on May 21, 1994 - incorporates calibration data.

*   This routine computes various data corresponding to the
*   sonic nozzle contained within the TSI Model 1440 Aspirating
*   probe for the measurement of concentration or temperature.
*   Three modes of operation are provided :

*       1. The full set of conditions are computed and displayed
*          to the screen for stagnation pressure set to 1 atm
*          and a user-selected temperature.

*       2. The variation in a subset of nozzle parameters is
*          computed for stagnation pressure set to 1 atm and
*          a user-selected range of temperatures. The data
*          are written to a data file [.PRN].

*       3. The variation in a subset of nozzle parameters is
*          computed for stagnation temperature set to 20 °C and
*          a user-selected range of pressures. The data
*          are written to a data file [.PRN].

IMPLICIT  REAL*8 (A-H,M,O-Z), INTEGER*2 (I-L,N)
PARAMETER (NUMO=2)
LOGICAL*1 ST
CHARACTER*1 INP
CHARACTER*4 FEXT
CHARACTER*10 GAS
CHARACTER*12 FNAMO

COMMON /GPROP/ MW,RHOSTAND,GAMMA,GCF,RUNIV
COMMON /AREA/  A,ASTAR,ARAT
COMMON /STAG/  RHOZERO
COMMON /ENTR/  P,T,RHO,M,C,U,MRATE1,QRATE1,QN1
COMMON /THROAT/ PSTAR,TSTAR,RHOSTAR,MSTAR,CSTAR,
+             USTAR,MRATE2,QRATE2,QN2,PSTPSI,PSTMM

```

```
DATA      D1,D2 / 1.2192D-3, 0.508D-3 / ! meters
DATA      FEXT /'.PRN'/
```

\* Initialization.

```
PI=2.0D0*DASIN(1.0D0) ! Formula for pi
RUNIV=8314.36D0       ! Universal gas constant - J / kmol K
ARAT=D1**2/D2**2 ! Area ratio
A=PI*D1**2/4.0D0
ASTAR=PI*D2**2/4.0D0
```

\* Display list of gases.

```
5  WRITE (*,'(/16X,A/16X,A)') 'ISENTROPIC, ADIABATIC FLOW OF A',
+    ' PERFECT GAS THROUGH A NOZZLE'
WRITE (*,'(/16X,A)') 'Choose from the following gases : '
WRITE (*,'(/16X,A)') '      1. AIR'
WRITE (*,'(16X,A)') '      2. CF3I'
WRITE (*,'(16X,A)') '      3. HFC-227'
WRITE (*,'(16X,A)') '      4. FC-218'
WRITE (*,'(16X,A)') '      5. HFC-125'
WRITE (*,'(16X,A)') '      6. HALON-1301'
WRITE (*,'(/16X,A)') 'Enter choice (1-6) : '
READ (*,*) IGAS
WRITE (*,'( )')

GO TO (10,20,30,40,50,60) IGAS
GO TO 5
```

\* Get gas properties. (SI Units)

\* \*\*\*\*\* AIR \*\*\*\*\*

```
10 MW=28.966D0      ! Molecular weight - kg / kmol
RHOSTAND=1.29304D0  ! Density (at 273 K and 1 atm) - kg / m3
GAMMA=1.4D0        ! Specific heat ratio
GCF=1.0D0          ! Gas correction factor (from MKS)
GAS='AIR'
GO TO 70
```

\* \*\*\*\*\* CF3I \*\*\*\*\*

```
20 MW=195.911D0     ! kg / kmol
RHOSTAND=9.0439D0   ! kg / m3
GAMMA=1.149D0       ! Specific heat ratio
GCF=0.34D0          ! Gas correction factor (from MKS)
GAS='CF3I'
GO TO 70
```



\* \*\*\*\*\* HFC-227 \*\*\*\*\*

```
30  MW=170.03D0      ! kg / kmol
    RHOSTAND=7.92544D0 ! kg / m3
    GAMMA=1.075D0     ! Specific heat ratio
    GCF=0.19D0        ! Gas correction factor (from cal)
    GAS='HFC-227'
    GO TO 70
```

\* \*\*\*\*\* FC-218 \*\*\*\*\*

```
40  MW=188.017D0     ! kg / kmol
    RHOSTAND=8.68268D0 ! kg / m3
    GAMMA=1.068D0     ! Specific heat ratio
    GCF=0.176D0       ! Gas correction factor (from cal)
    GAS='FC-218'
    GO TO 70
```

\* \*\*\*\*\* HFC-125 \*\*\*\*\*

```
50  MW=120.02D0      ! kg / kmol
    RHOSTAND=5.47635D0 ! kg / m3
    GAMMA=1.103D0     ! Specific heat ratio
    GCF=0.275D0       ! Gas correction factor (from cal)
    GAS='HFC-125'
    GO TO 70
```

\* \*\*\*\*\* HALON 1301 \*\*\*\*\*

```
60  MW=148.91D0      ! kg / kmol
    RHOSTAND=6.77643D0 ! kg / m3
    GAMMA=1.145D0     ! Specific heat ratio
    GCF=0.38D0        ! Gas correction factor (from cal)
    GAS='HALON-1301'
```

\* This section of code calculates the variation in nozzle  
 \* parameters as a function of stagnation pressure (barometric  
 \* pressure) for a single temperature (20 °C). I allow for a  
 \* worst case variation of 29.0 to 31.0 in Hg which corresponds  
 \* to a variation of 98.0 k Pa to 104.8 kPa or 14.2 psia to 15.2 psia.

```
70  WRITE (*, '(10X,A)')
    + 'Enter (A)tmospheric press or (M)any pressures : '
    READ (*, '(A)') INP
    WRITE (*, '( )')
    GO TO (70,72) ILET(INP, 'MA')
```

\* Compute data for SINGLE pressure.

```
PZERO=101300.0D0 ! Stagnation pressure - Pa
GO TO 75
```

```
* Compute data for MANY pressures.
```

```
72 WRITE (*,'(16X,A,A,A)')
+ 'Enter name of output file [',FEXT,']:'
READ (*,'(A)') FNAMEO
WRITE (*,'( )')
```

```
* Concatenate file extension to FNAMEO (if necessary)
* and then open the file.
```

```
IPD=INDEX(FNAMEO,'.')
IF (IPD .GT. 9) GO TO 80
IF (IPD .EQ. 0) THEN
  IEND=LEN_TRIM(FNAMEO)
  FNAMEO(IEND+1:IEND+4)=FEXT
ENDIF
```

```
OPEN (NUMO,FILE=FNAMEO,STATUS='UNKNOWN')
```

```
TEMPC=20.0D0 ! Room temp (°C)
TZERO=TEMPC+273.15D0 ! Kelvin
```

```
WRITE (*,'(16X,A)') 'Enter Pstart, Pstop, Pstep (in Hg) : '
READ (*,*) PSTART,PSTOP,PSTEP
WRITE (*,'( )')
```

```
NVAL=NINT((PSTOP-PSTART)/PSTEP)+1
PSTART=PSTART*3379.978D0 ! Pa
PSTOP=PSTOP*3379.978D0 ! Pa
PSTEP=PSTEP*3379.978D0 ! Pa
PZERO=PSTART-PSTEP
```

```
IEND=LEN_TRIM(GAS)
WRITE (NUMO,'(21X,A,A,A)')
+ 'NOZZLE CONDITIONS FOR ',GAS(IEND), ' : '
WRITE (NUMO,'(5X,A,A)')
+ 'P0 (inHg) T0 (°C) U (m/s) P* (psi) T* (°C) Q (slmN)',
+ ' m (kg/s)'
WRITE (NUMO,'(5X,A,A)')
+ '-----',
+ '-----'
```

```
DO I=1,NVAL
  PZERO=PZERO+PSTEP
  CALL NOZCALC (PZERO,TZERO)
```

```

WRITE (NUMO,'(5X,6(F8.3,2X),1P,E9.3)')
+   PZERO/3379.978D0,TZERO-273.15D0,U,PSTPSI,
+   TSTAR-273.15D0,QN1,MRATE1
ENDDO
CLOSE (NUMO)
STOP ' '

```

\* Compute data for single temperature or many temperatures.

```

75 WRITE (*,'(16X,A)') 'Enter (S)ingle temp or (M)any temps : '
READ (*,'(A)') INP
WRITE (*,'( )')
GO TO (75,80) ILET(INP,'MS')

```

\* Get SINGLE stagnation temperature.

```

WRITE (*,'(16X,A)')
+ 'Enter the stagnation temperature (in °C) : '
READ (*,*) TEMPC
WRITE (*,'( )')
NVAL=1
TSTEP=1.0D0
TZERO=TEMPC-TSTEP+273.15D0 ! Kelvin
ST=.TRUE.
GO TO 90

```

\* Get data to compute for MANY stagnation temperatures.

```

80 WRITE (*,'(16X,A,A,A)')
+ 'Enter name of output file [',FEXT,'] : '
READ (*,'(A)') FNAMO
WRITE (*,'( )')

```

\* Concatenate file extension to FNAMO (if necessary)  
 \* and then open the file.

```

IPD=INDEX(FNAMO,'.')
IF (IPD .GT. 9) GO TO 80
IF (IPD .EQ. 0) THEN
  IEND=LEN_TRIM(FNAMO)
  FNAMO(IEND+1:IEND+4)=FEXT
ENDIF

```

```

OPEN (NUMO,FILE=FNAMO,STATUS='UNKNOWN')

```

```

WRITE (*,'(16X,A)') 'Enter Tstart, Tstop, Tstep (in °C) : '
READ (*,*) TSTART,TSTOP,TSTEP
WRITE (*,'( )')

```

```

NVAL=NINT((TSTOP-TSTART)/TSTEP)+1
TZERO=TSTART-TSTEP+273.15D0      ! Kelvin
ST=.FALSE.

IEND=LEN_TRIM(GAS)
WRITE (NUMO,'(21X,A,A,A/A)')
+   'NOZZLE CONDITIONS FOR ',GAS(:IEND), ' : '
WRITE (NUMO,'(5X,A,A)')
+   'P0 (kPa)  T0 (°C)  U (m/s)  P* (psi)  T* (°C)  Q (slmN)',
+   '  m (kg/s)'
WRITE (NUMO,'(5X,A,A)')
+   '-----',
+   '-----'

```

```

90 DO I=1,NVAL
    TZERO=TZERO+TSTEP
    CALL NOZCALC (PZERO,TZERO)
    IF (.NOT. ST) WRITE (NUMO,'(5X,6(F8.3,2X),1P,E9.3)')
+   PZERO/1000.0D0,TZERO-273.15D0,U,PSTPSI,
+   TSTAR-273.15D0,QN1,MRATE1
    ENDDO
    IF (.NOT. ST) CLOSE (NUMO)

```

\* Display results.

```

IF (ST) THEN
    WRITE (*,'(25(/))')
    IEND=LEN_TRIM(GAS)
    WRITE (*,'(26X,A,A,A/A)')
+   'NOZZLE CONDITIONS FOR ',GAS(:IEND), ' : '

    WRITE (*,'(16X,A,8X,A)')
+   'Stagnation Properties : ', 'Gas Properties : '
    WRITE (*,'(16X,A,F8.3,A,12X,A,F8.3)')
+   'P0 = ',PZERO/1000.0D0,' kPa', 'Γ = ',GAMMA
    WRITE (*,'(16X,A,F8.3,A,13X,A,F8.3)')
+   'T0 = ',TZERO-273.15D0,' °C', 'MW = ',MW
    WRITE (*,'(16X,A,F8.3,A,10X,A,F8.3,A)')
+   'Rho0 = ',RHOZERO,' kg/m3', 'RhoS = ',RHOSTAND,' kg/m3'
    WRITE (*,'(48X,A,F8.3/)') 'GCF = ',GCF

    WRITE (*,'(16X,A,10X,A)')
+   'Entrance Properties : ', 'Throat Properties : '
    WRITE (*,'(16X,A,F8.3,A,12X,A,F8.3,A)')
+   'P = ',P/1000.0D0,' kPa', 'P* = ',PSTAR/1000.0D0,' kPa'
    WRITE (*,'(16X,A,F8.3,A,13X,A,F8.3,A)')
+   'T = ',T-273.15D0,' °C', 'T* = ',TSTAR-273.15D0,' °C'
    WRITE (*,'(16X,A,F8.3,A,10X,A,F8.3,A)')

```

```

+   'Rho = ',RHO,' kg/m3',   'Rho* = ',RHOSTAR,' kg/m3'
  WRITE (*,'(16X,A,F8.3,A,12X,A,F8.3,A)')
+   'M   = ',M,' m/s',       'M*   = ',MSTAR,' m/s'
  WRITE (*,'(16X,A,F8.3,A,12X,A,F8.3,A)')
+   'C   = ',C,' m/s',       'C*   = ',CSTAR,' m/s'
  WRITE (*,'(16X,A,F8.3,A,12X,A,F8.3,A)')
+   'U   = ',U,' m/s',       'U*   = ',USTAR,' m/s'
  WRITE (*,'(16X,A,1P,E9.3,A,11X,A,E9.3,A)')
+   'mdot = ',MRATE1,' kg/s',  'mdot = ',MRATE2,' kg/s'
  WRITE (*,'(16X,A,F8.3,A,12X,A,F8.3,A)')
+   'Qdot = ',QRATE1,' slm',   'Qdot = ',QRATE2,' slm'
  WRITE (*,'(16X,A,F8.3,A,10X,A,F8.3,A)')
+   'Qdot = ',QN1,' slm-N',    'Qdot = ',QN2,' slm-N'
  WRITE (*,'(16X,A,F5.3,A/16X,A,F6.3,A,F5.3,A,F6.2,A)')
+   'The vacuum pump must draw at least ',QN1,' slm-N at ',
+   'a pressure ≤ ',PSTAR/1000.0D0,' kPa = ',PSTPSI,
+   ' psia = ',PSTMM,' mm Hg abs.'
ENDIF

```

END

SUBROUTINE NOZCALC (PZERO,TZERO)

IMPLICIT REAL\*8 (A-H,M,O-Z), INTEGER\*2 (I-L,N)  
 PARAMETER (ITMAX=99, EPS=1.0D-6)

```

COMMON /GPROP/ MW,RHOSTAND,GAMMA,GCF,RUNIV
COMMON /AREA/  A,ASTAR,ARAT
COMMON /STAG/  RHOZERO
COMMON /ENTR/  P,T,RHO,M,C,U,MRATE1,QRATE1,QN1
COMMON /THROAT/ PSTAR,TSTAR,RHOSTAR,MSTAR,CSTAR,
+              USTAR,MRATE2,QRATE2,QN2,PSTPSI,PSTMM

```

- \* The entrance and throat diameters of the nozzle are known.
- \* Solve for the Mach number (M) by iteration.

```

M=0.1D0
MDIFF=1.0D0
ITER=0
EX=(GAMMA+1.0D0)/(GAMMA-1.0D0)/2.0D0

```

DO WHILE (MDIFF .GT. EPS .AND. ITER .LE. ITMAX)

```

  ITER=ITER+1
  MGUESS=( 2.0D0/(GAMMA+1.0D0) *
+ (1.0D0+(GAMMA-1.0D0)/2.0D0*M**2) )**EX / ARAT
  MDIFF=DABS(MGUESS-M)
  M=MGUESS
ENDDO

```

- \* Compute stagnation density from Perfect Gas equation of state.
- \* This gives densities which are in error by 1% to 3%.

```

R=RUNIV/MW          ! Gas constant - J / kg K
RHOZERO=PZERO/(R*TZERO)  ! Stagnation density - kg / m3

```

- \* Compute properties at entrance to nozzle.

```

T=TZERO/(1.0D0+(GAMMA-1.0D0)/2.0D0*M**2)
TRAT=T/TZERO
P=PZERO*TRAT**(GAMMA/(GAMMA-1.0D0))
RHO=RHOZERO*TRAT**(1.0D0/(GAMMA-1.0D0))
C=DSQRT(GAMMA*R*T)
U=M*C
MRATE1=RHO*U*A          ! kg / s
QRATE1=MRATE1/RHOSTAND*60000.0D0  ! slm of agent
QN1=QRATE1/GCF          ! slm of nitrogen

```

- \* Compute properties at throat of nozzle.

```

FACTOR=2.0D0/(GAMMA+1.0D0)
TSTAR=TZERO*FACTOR
PSTAR=PZERO*FACTOR**(GAMMA/(GAMMA-1.0D0))
PSTPSI=PSTAR/6894.76D0      ! PSTAR in psi
PSTMM=PSTAR/133.07D0       ! PSTAR in mm Hg
RHOSTAR=RHOZERO*FACTOR**(1.0D0/(GAMMA-1.0D0))
CSTAR=DSQRT(GAMMA*R*TSTAR)
USTAR=CSTAR
MSTAR=1.0D0
MRATE2=RHOSTAR*USTAR*ASTAR    ! kg / s
QRATE2=MRATE2/RHOSTAND*60000.0D0  ! slm of agent
QN2=QRATE2/GCF              ! slm of nitrogen

```

```

RETURN
END

```

```

FUNCTION ILET (INP,STRING) ! (ILET.FOR)

```

```

IMPLICIT  INTEGER*2 (I-N)
CHARACTER*1 INP
CHARACTER*(*)  STRING

```

- \* First, convert INP to uppercase if it is lowercase. If it
- \* is uppercase, leave it unchanged.

```

IF (ICHAR(INP) .GE. 97 .AND. ICHAR(INP) .LE. 122) THEN
  IHOLD=ICHAR(INP)-32

```

```
    INP=CHAR(IHOLD)
ENDIF
```

- \* Determine the position of INP in STRING, then add one to get
- \* ILET which determines label to use in computed GO TO statement.

```
IPOS=INDEX(STRING,INP)
ILET=IPOS+1
```

```
RETURN
END
```

## Appendix B. FORTRAN Program COIL.FOR to Estimate Length of Pipe Required For Laminar and Turbulent Flows in Pipes to Achieve Pipe-Wall Temperature

\* Laminar and Turbulent Heat Transfer in a Pipe (COIL.FOR)

\* David E. Hess

\* Fluid Flow Group - Process Measurements Division

\* Chemical Science and Technology Laboratory

\* National Institute of Standards and Technology

\* February 3, 1994

```
IMPLICIT      REAL*8 (A-H,O-Z), INTEGER*2 (I-N)
REAL*8        MOUT
```

```
DATA          MOUT / 2.1D-4 /
```

\* Display list of gases.

```
10  WRITE (*, '(//16X,A//16X,A)') 'LAMINAR AND TURBULENT HEAT',
+      ' TRANSFER IN A PIPE FLOW'
```

```
WRITE (*, '(//16X,A)') 'Enter pipe diameter (in) : '
```

```
READ (*,*) D
```

```
WRITE (*, '( )')
```

```
D=D*25.4D0/1.0D3      ! Convert from inches to meters
```

```
WRITE (*, '(//16X,A)') 'Choose from the following gases : '
```

```
WRITE (*, '(//16X,A)') '      1. AIR'
```

```
WRITE (*, '(//16X,A)') '      2. CF3I'
```

```
WRITE (*, '(//16X,A)') '      3. HFC-227'
```

```
WRITE (*, '(//16X,A)') '      4. FC-218'
```

```
WRITE (*, '(//16X,A)') '      5. HFC-125'
```

```
WRITE (*, '(//16X,A)') '      6. HALON-1301'
```

```
WRITE (*, '(//16X,A)') '      7. ALL OF THE ABOVE'
```

```
WRITE (*, '(//16X,A)') 'Enter choice (1-7) : '
```

```
READ (*,*) ICHOICE
```

```
WRITE (*, '( )')
```

```
IF (ICHOICE .GE. 1 .AND. ICHOICE .LE. 6) THEN
```

```
    CALL COILCALC (ICHOICE, MOUT, D)
```

```
ELSEIF (ICHOICE .EQ. 7) THEN
```

```
    DO I=1,6
```



```

CALL COILCALC (I,MOUT,D)
WRITE (*,'( )')
ENDDO

```

```

ELSE

```

```

GO TO 10

```

```

ENDIF

```

```

STOP ' '
END

```

```

SUBROUTINE COILCALC (IGAS,MOUT,D)

```

```

IMPLICIT      REAL*8 (A-H,O-Z), INTEGER*2 (I-N)
PARAMETER      (ITMAX=99, EPS=1.0D-8)
REAL*8         MW,K,MUB,MUW,MURAT,NU,L,LDIFF,LGUESS
REAL*8         K1,K2,N,MOUT,NUINF,LT
CHARACTER*10   GAS

```

```

COMMON /GPROP/ MW,GAMMA,GCF,RHO,RHOI,RHOO,RHOS,CP,K,
+           MUB,MUW,NU,TB,TW,TBI,TBO,GAS

```

```

EXTERNAL      GASPROP

```

```

DATA  NUINF,K1,K2,N / 3.656D0,0.0668D0,0.04D0,0.6667D0 /

```

\* Get the gas properties.

```

CALL GASPROP(IGAS)

```

\* Calculate average velocity.

```

PI=2.0D0*DASIN(1.0D0) ! Formula for pi
A=PI*D**2/4.0D0       ! Pipe cross-sectional area - m2
CTOK=273.15D0         ! Convert °C to K
UOUT=MOUT/(RHOO*A)
UIN=MOUT/(RHOI*A)
UM=(UIN+UOUT)/2.0D0

```

\* Calculate various dimensionless parameters.

```

RE=UM*D/NU           ! Reynolds number
ALPHA=K/(RHO*CP)     ! Thermal diffusivity
PR=NU/ALPHA          ! Prandtl number
PE=RE*PR             ! Peclet number
MURAT=(MUB/MUW)**0.14D0 ! Viscosity ratio

```

- \* Calculate length for laminar heat transfer.

```
TWK=TW+CTOK
TBK=TB+CTOK
TBOK=TBO+CTOK
TBIK=TBI+CTOK
F1=RHO*UM*CP*D*(TBOK-TBIK)/(4.0D0*(TWK-TBK))
F2=NUINF*K/D
F3=K1*MURAT*K*PE
L=1.0D0
LDIFF=1.0D0
ITER=0
```

```
DO WHILE (LDIFF .GT. EPS .AND. ITER .LE. ITMAX)
  ITER=ITER+1
  DENOM=1.0D0+K2*(PE*D/L)**N
  LGUESS=F1/(F2+F3/L/DENOM)
  LDIFF=DABS(LGUESS-L)
  L=LGUESS
ENDDO
```

- \* Calculate length for laminar heat transfer.

```
H=0.023D0*MURAT*K/D*RE**0.8D0*PR**0.333D0
LT=F1/H
```

- \* Calculate the pressure drop for turbulent flow.

```
P=PDROP (UM,1.0D0,D)
```

- \* Display the results.

```
IEND=LEN_TRIM(GAS)
WRITE (*,'(16X,A,A,A)')
+ 'COMPUTED COIL LENGTHS FOR ',GAS(:IEND), ' :'
```

```
WRITE (*,'(16X,A,1PE9.3,A)') 'Mout = ',MOUT,' kg / s'
```

```
WRITE (*,'(16X,A,F6.3,A,F5.4,A)')
```

```
+ 'D   = ',D*1.0D3,' mm = 0',D*1.0D3/25.4D0,' in'
```

```
WRITE (*,'(16X,A,F6.3,A,5X,A,F6.0)')
```

```
+ 'Uin = ',UIN,' m / s', 'RE = ',RE
```

```
WRITE (*,'(16X,A,F6.3,A,5X,A,F4.3)')
```

```
+ 'Uout = ',UOUT,' m / s', 'PR = 0',PR
```

```
WRITE (*,'(16X,A,F6.3,A,5X,A,F6.0)')
```

```
+ 'Uavg = ',UM,' m / s', 'PE = ',PE
```

```
WRITE (*,'(16X,A,F8.5,A)') 'Laminar : L = ',L,' m'
```

```
WRITE (*,'(16X,A,F8.5,A)') 'Turbulent : L = ',LT,' m'
```

```

WRITE (*,'(/16X,A,F8.3,A,F7.3,A/16X,A)')
+ 'Pdrip = ',P/1.0D3,' kPa = ',P/6894.76D0,' psi',
+ '(based on a length of 1 m of coiled tubing)'

```

```

RETURN
END

```

```

FUNCTION PDROP (U,L,D)

```

```

IMPLICIT      REAL*8 (A-H,O-Z), INTEGER*2 (I-N)
REAL*8        MW,K,MUB,MUW,NU,L,L2
CHARACTER*10   GAS

```

```

COMMON /GPROP/ MW,GAMMA,GCF,RHO,RHOI,RHOO,RHOS,CP,K,
+           MUB,MUW,NU,TB,TW,TBI,TBO,GAS

```

\* Calculate the friction factor for turbulent flow through a pipe.

```

RE=U*D/NU
F=0.184D0/RE**0.2D0

```

\* Compute the pressure drop. Double (?) the pipe length used  
 \* in the calculation because the pipe is coiled, not straight.

```

L2=2.0D0*L
PDROP=F*L2*RHO*U**2/(2.0D0*D)  ! Result in Pa

```

```

RETURN
END

```

```

SUBROUTINE GASPROP (IGAS)

```

```

IMPLICIT      REAL*8 (A-H,O-Z), INTEGER*2 (I-N)
REAL*8        MW,K,MUB,MUW,NU
CHARACTER*10   GAS

```

```

COMMON /GPROP/ MW,GAMMA,GCF,RHO,RHOI,RHOO,RHOS,CP,K,
+           MUB,MUW,NU,TB,TW,TBI,TBO,GAS

```

```

GO TO (10,20,30,40,50,60) IGAS

```

\* Get gas properties. (SI Units)

\* \*\*\*\*\* AIR \*\*\*\*\*

```

10  MW   = 28.966000D+0 ! Molecular weight - kg / kmol
    GAMMA = 1.400000D+0 ! Specific heat ratio
    GCF   = 1.000000D+0 ! Gas correction factor (from MKS)

```

RHO = 1.397970D+0 ! Density (at TB and 1 atm) - kg / m3  
 RHOI = 1.209650D+0 ! Density (at TBI and 1 atm) - kg / m3  
 RHOO = 1.745990D+0 ! Density (at TBO and 1 atm) - kg / m3  
 RHOS = 1.293040D+0 ! Density (at 273 K and 1 atm) - kg / m3  
 CP = 1.005300D+0 ! Specific heat - kJ / kg·K  
 K = 2.252000D-5 ! Thermal conductivity - kJ / s·m·K  
 MUB = 1.519000D-5 ! Dynamic viscosity - (kg / m·s)  
 MUW = 1.338900D-5 ! Dynamic viscosity - (kg / m·s)  
 TB = -20.000000D+0 ! Bulk temperature - (°C)  
 TW = -60.000000D+0 ! Wall temperature - (°C)  
 TBI = 20.000000D+0 ! Inlet bulk temperature - (°C)  
 TBO = -60.000000D+0 ! Outlet bulk temperature - (°C)  
 GAS = 'AIR'  
 GO TO 70

\* \*\*\*\*\* CF3I \*\*\*\*\*

20 MW = 195.911000D+0 ! Molecular weight - kg / kmol  
 GAMMA = 1.149000D+0 ! Specific heat ratio  
 GCF = 0.340000D+0 ! Gas correction factor (from MKS)  
 RHO = 9.059290D+0 ! Density (at TB and 1 atm) - kg / m3  
 RHOI = 8.339090D+0 ! Density (at TBI and 1 atm) - kg / m3  
 RHOO = 9.943630D+0 ! Density (at TBO and 1 atm) - kg / m3  
 RHOS = 9.043900D+0 ! Density (at 273 K and 1 atm) - kg / m3  
 CP = 0.363263D+0 ! Specific heat - kJ / kg·K  
 K = 6.524410D-6 ! Thermal conductivity - kJ / s·m·K  
 MUB = 1.371780D-5 ! Dynamic viscosity - (kg / m·s)  
 MUW = 1.266080D-5 ! Dynamic viscosity - (kg / m·s)  
 TB = -1.000000D+0 ! Bulk temperature - (°C)  
 TW = -22.000000D+0 ! Wall temperature - (°C)  
 TBI = 20.000000D+0 ! Inlet bulk temperature - (°C)  
 TBO = -22.000000D+0 ! Outlet bulk temperature - (°C)  
 GAS = 'CF3I'  
 GO TO 70

\* \*\*\*\*\* HFC-227 \*\*\*\*\*

30 MW = 170.030000D+0 ! Molecular weight - kg / kmol  
 GAMMA = 1.075000D+0 ! Specific heat ratio  
 GCF = 0.180000D+0 ! Gas correction factor (from MKS)  
 RHO = 7.837960D+0 ! Density (at TB and 1 atm) - kg / m3  
 RHOI = 7.260000D+0 ! Density (at TBI and 1 atm) - kg / m3  
 RHOO = 8.509880D+0 ! Density (at TBO and 1 atm) - kg / m3  
 RHOS = 7.925440D+0 ! Density (at 273 K and 1 atm) - kg / m3  
 CP = 0.793461D+0 ! Specific heat - kJ / kg·K  
 K = 1.128140D-5 ! Thermal conductivity - kJ / s·m·K  
 MUB = 1.093770D-5 ! Dynamic viscosity - (kg / m·s)  
 MUW = 1.014750D-5 ! Dynamic viscosity - (kg / m·s)

TB = 2.000000D+0 ! Bulk temperature - (°C)  
 TW = -16.000000D+0 ! Wall temperature - (°C)  
 TBI = 20.000000D+0 ! Inlet bulk temperature - (°C)  
 TBO = -16.000000D+0 ! Outlet bulk temperature - (°C)  
 GAS = 'HFC-227'  
 GO TO 70

\* \*\*\*\*\* FC-218 \*\*\*\*\*

40 MW = 188.017000D+0 ! Molecular weight - kg / kmol  
 GAMMA = 1.068000D+0 ! Specific heat ratio  
 GCF = 0.170000D+0 ! Gas correction factor (from MKS)  
 RHO = 8.962690D+0 ! Density (at TB and 1 atm) - kg / m3  
 RHOI = 7.987000D+0 ! Density (at TBI and 1 atm) - kg / m3  
 RHOO = 10.257900D+0 ! Density (at TBO and 1 atm) - kg / m3  
 RHOS = 8.682680D+0 ! Density (at 273 K and 1 atm) - kg / m3  
 CP = 0.752860D+0 ! Specific heat - kJ / kg·K  
 K = 1.111450D-5 ! Thermal conductivity - kJ / s·m·K  
 MUB = 1.131740D-5 ! Dynamic viscosity - (kg / m·s)  
 MUW = 1.005830D-5 ! Dynamic viscosity - (kg / m·s)  
 TB = -8.000000D+0 ! Bulk temperature - (°C)  
 TW = -36.000000D+0 ! Wall temperature - (°C)  
 TBI = 20.000000D+0 ! Inlet bulk temperature - (°C)  
 TBO = -36.000000D+0 ! Outlet bulk temperature - (°C)  
 GAS = 'FC-218'  
 GO TO 70

\* \*\*\*\*\* HFC-125 \*\*\*\*\*

50 MW = 120.020000D+0 ! Molecular weight - kg / kmol  
 GAMMA = 1.103000D+0 ! Specific heat ratio  
 GCF = 0.300000D+0 ! Gas correction factor (from MKS)  
 RHO = 5.788080D+0 ! Density (at TB and 1 atm) - kg / m3  
 RHOI = 5.057000D+0 ! Density (at TBI and 1 atm) - kg / m3  
 RHOO = 6.807060D+0 ! Density (at TBO and 1 atm) - kg / m3  
 RHOS = 5.476350D+0 ! Density (at 273 K and 1 atm) - kg / m3  
 CP = 0.753624D+0 ! Specific heat - kJ / kg·K  
 K = 1.127550D-5 ! Thermal conductivity - kJ / s·m·K  
 MUB = 1.137060D-5 ! Dynamic viscosity - (kg / m·s)  
 MUW = 9.828150D-6 ! Dynamic viscosity - (kg / m·s)  
 TB = -14.000000D+0 ! Bulk temperature - (°C)  
 TW = -48.000000D+0 ! Wall temperature - (°C)  
 TBI = 20.000000D+0 ! Inlet bulk temperature - (°C)  
 TBO = -48.000000D+0 ! Outlet bulk temperature - (°C)  
 GAS = 'HFC-125'  
 GO TO 70

\* \*\*\*\*\* HALON1301 \*\*\*\*\*

```
60  MW  = 148.910000D+0 ! Molecular weight - kg / kmol
    GAMMA = 1.145000D+0 ! Specific heat ratio
    GCF  = 0.370000D+0 ! Gas correction factor (from MKS)
    RHO  = 7.309030D+0 ! Density (at TB and 1 atm) - kg / m3
    RHOI = 6.263000D+0 ! Density (at TBI and 1 atm) - kg / m3
    RHOO = 8.829990D+0 ! Density (at TBO and 1 atm) - kg / m3
    RHOS = 6.776430D+0 ! Density (at 273 K and 1 atm) - kg / m3
    CP   = 0.443921D+0 ! Specific heat - kJ / kg·K
    K    = 7.729630D-6 ! Thermal conductivity - kJ / s·m·K
    MUB  = 1.312610D-5 ! Dynamic viscosity - (kg / m·s)
    MUW  = 1.110830D-5 ! Dynamic viscosity - (kg / m·s)
    TB   = -19.000000D+0 ! Bulk temperature - (°C)
    TW   = -58.000000D+0 ! Wall temperature - (°C)
    TBI  = 20.000000D+0 ! Inlet bulk temperature - (°C)
    TBO  = -58.000000D+0 ! Outlet bulk temperature - (°C)
    GAS  = 'HALON 1301'

70  NU  = MUB / RHO    ! Kinematic viscosity - m2 / s
```

```
RETURN
END
```

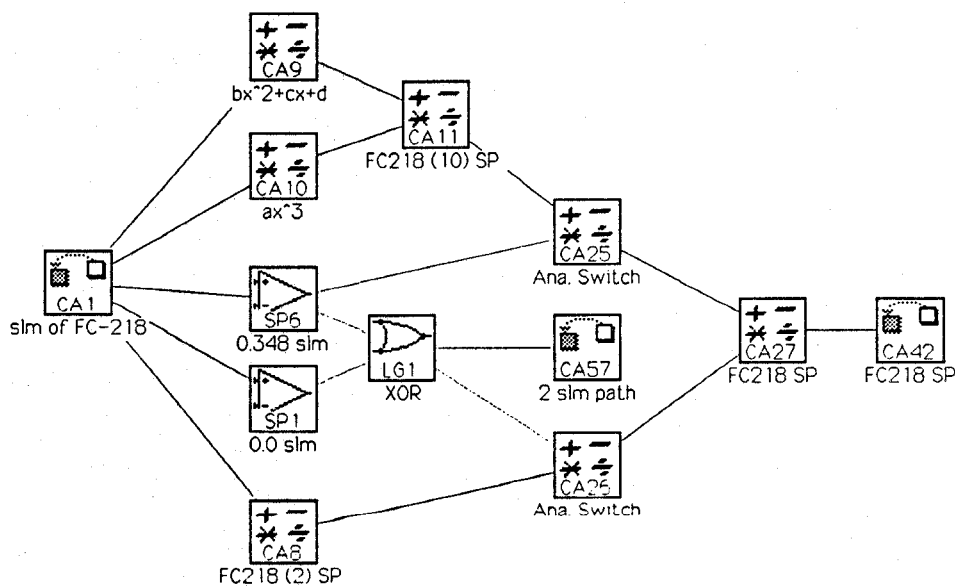
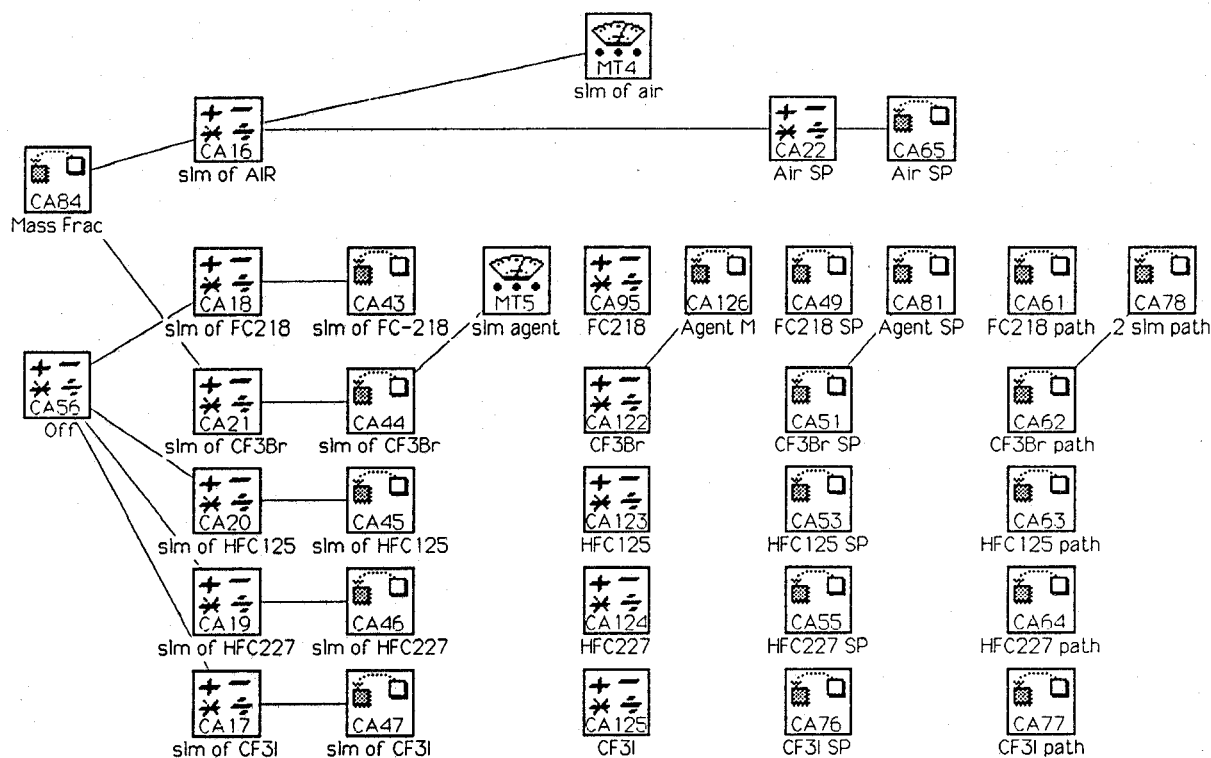
## Appendix C. Electrical Connections of Interface Boards and Components of Flow Calibration System

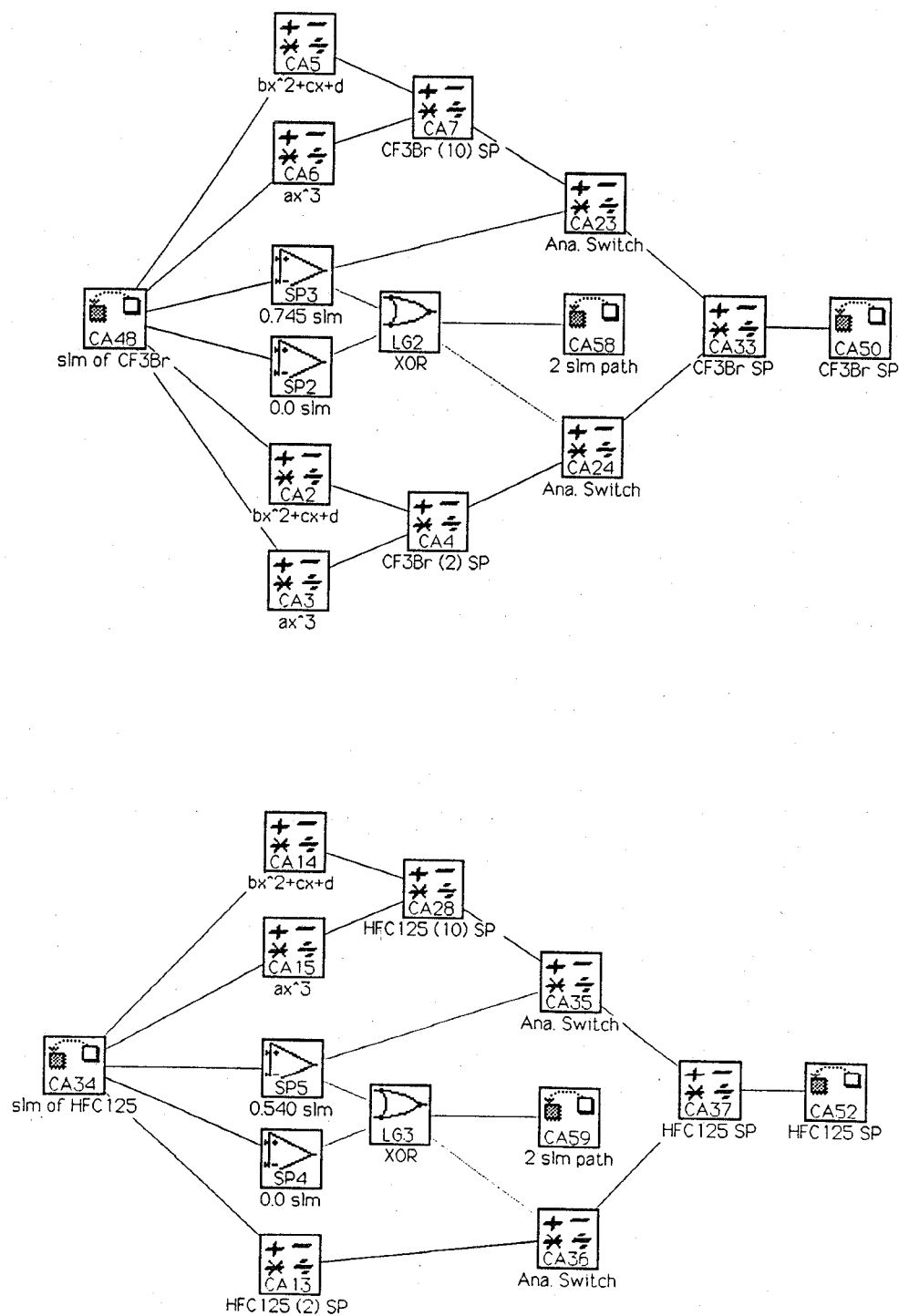
Signal Type	Computer Module Connection	Connections for Calibration System
ACAO-12 Interface Board		
Analog Output	Analog Output 1 (#1 on ACAO-12)	Set Point for Agent 10 slmn Mass-Flow Controller (Channel 3, Pin 6)
Flash-12 Interface Board		
Analog Output	Analog Output 3 (#1 on Flash-12)	Set Point for Air 10 slmn Mass-Flow Controller (Channel 1, Pin 4)
Analog Output	Analog Output 4 (#2 on Flash-12)	Set Point for Agent 2 slmn Mass-Flow Controller (Channel 2, Pin 5)
Digital Output	Digital Output 9 (#1 on Flash-12)	Enable to Switch Two-Way Electro-Pneumatic Valve and Light for Flow of Agent to Agent 2 slmn Mass-Flow Controller
Digital Output	Digital Output 10 (#2 on Flash-12)	Enable for Air 10 slmn Electro-Pneumatic Valve and Light
Digital Output	Digital Output 11 (#3 on Flash-12)	Enable for Agent 2 slmn Electro-Pneumatic Valve and Light
Digital Output	Digital Output 12 (#4 on Flash-12)	Enable for Agent 10 slmn Electro-Pneumatic Valve and Light
Digital Output	Digital Output 13 (#5 on Flash-12)	Enable for Vent/Test Electro-Pneumatic Valve and Light
Digital Output	Digital Output 14 (#6 on Flash-12)	Enable for 10 slmn Air Mass-Flow Controller (Channel 1, pin 12)
Digital Output	Digital Output 15 (#7 on Flash-12)	Enable for Agent 2 slmn Mass-Flow Controller (Channel 2, pin 10)
Digital Output	Digital Output 16 (#8 on Flash-12)	Enable for Agent 10 slmn Mass-Flow Controller (Channel 3, pin 11)
Analog Input	Analog-to-Digital Input #1	Thermocouple for Pump Temperature Measurement
Analog Input	Analog-to-Digital Input #2	Voltage Output for Air Mass-Flow Controller (Channel 1, pin 2)

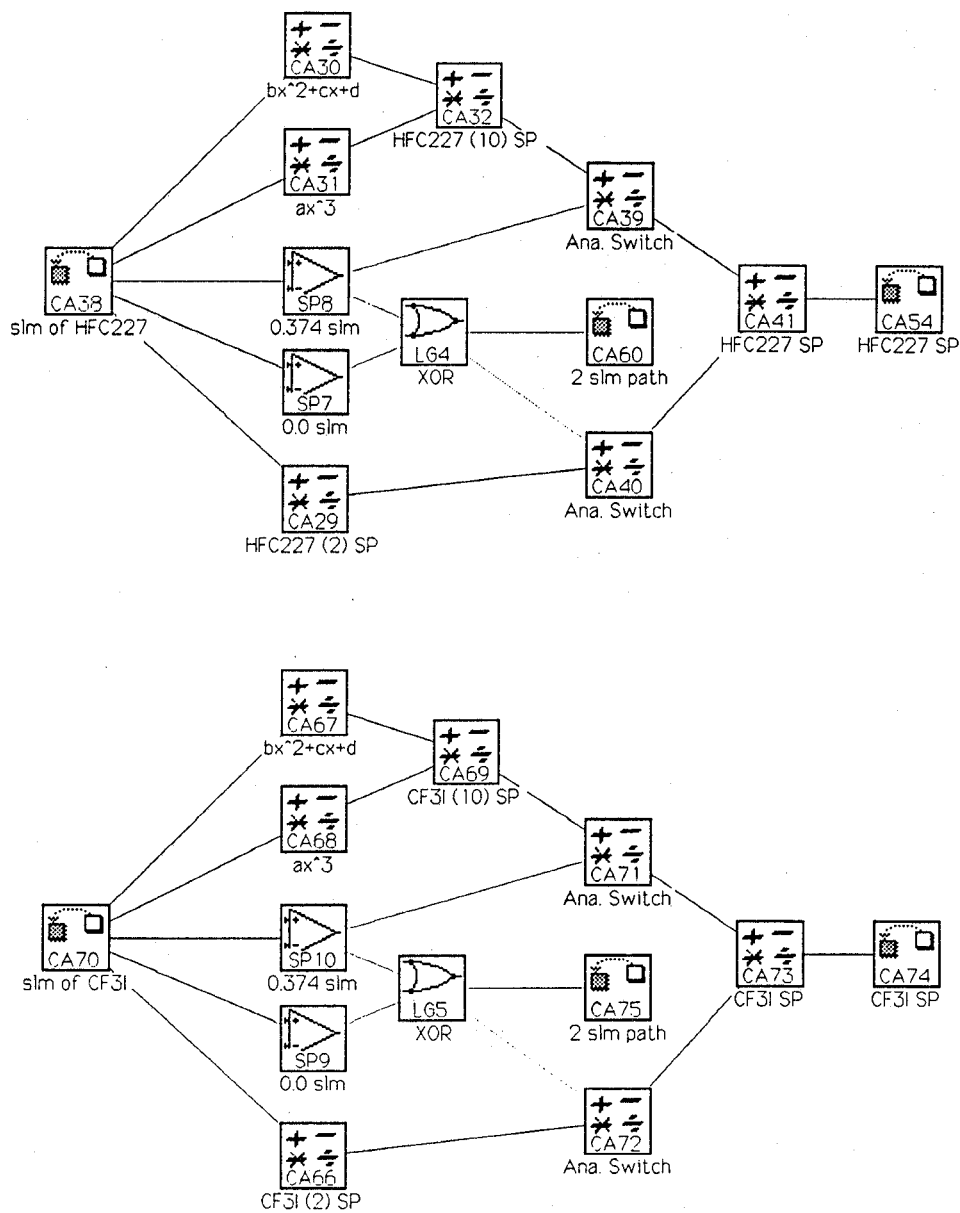
Analog Input	Analog-to-Digital Input #3	Voltage Output for Agent 2 slmn Mass-Flow Controller (Channel 2, pin 14)
Analog Input	Analog-to-Digital Input #4	Voltage Output for Agent 10 slmn Mass-Flow Controller (Channel 2, pin 16)
Analog Input	Analog-to-Digital Input #5	Thermocouple for Coil Temperature Measurement
Analog Input	Analog-to-Digital Input #6	Voltage Output for Constant-Tempera- ture Aspirated Hot Film
Analog Input	Analog-to-Digital Input #7	Voltage Output for Constant-Current Cold Wire

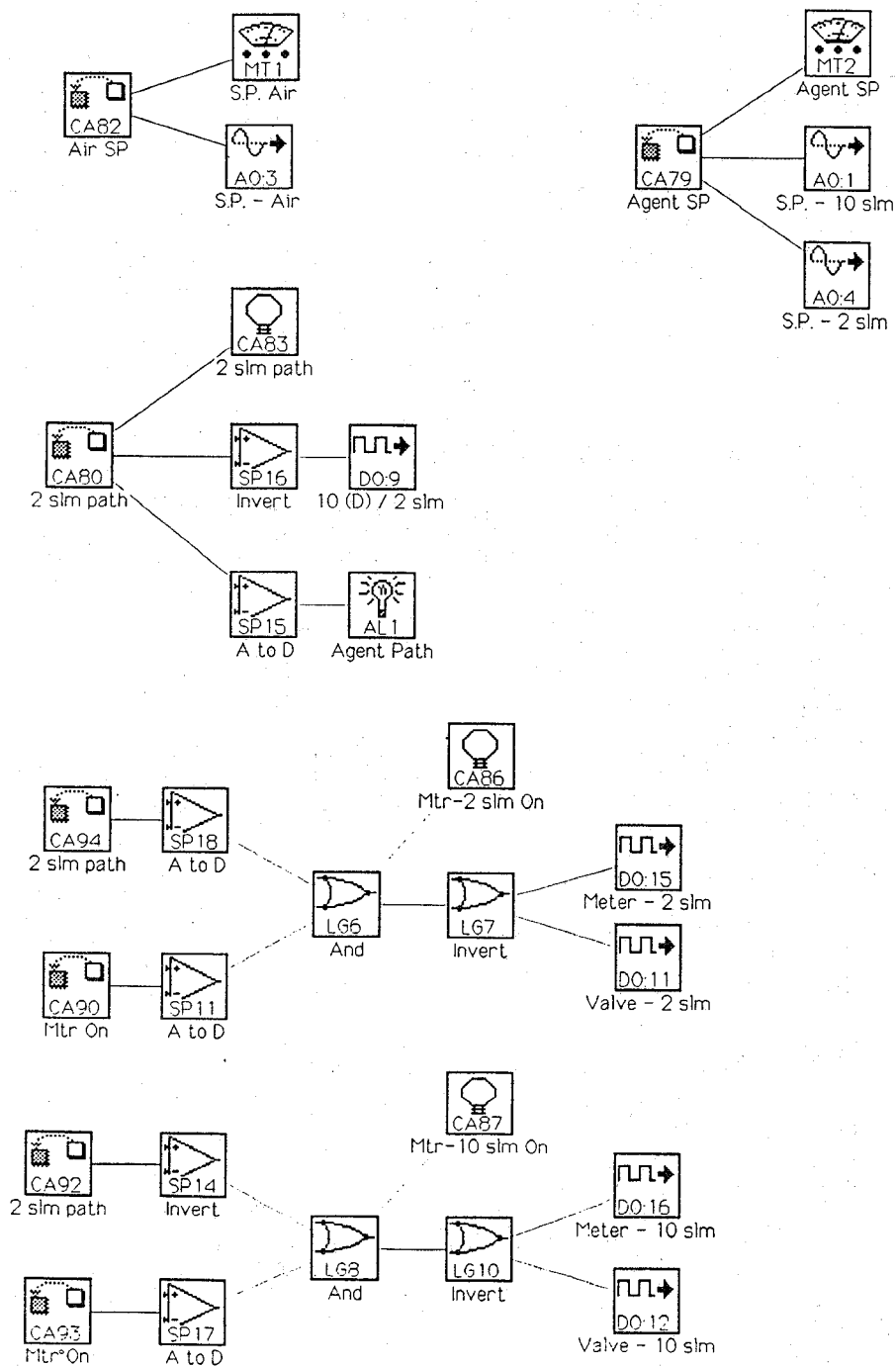


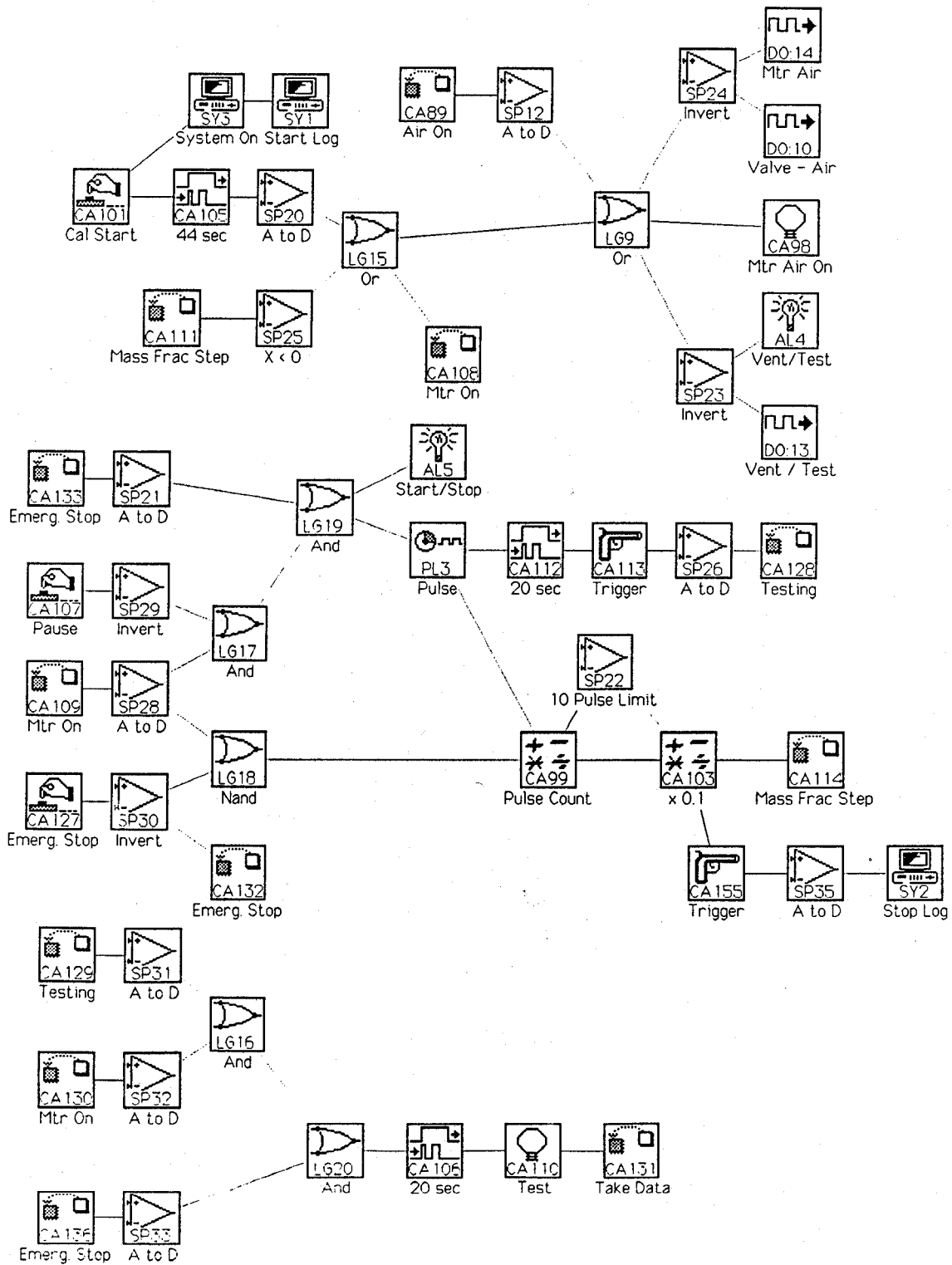
## Appendix D. Workbench PC Icon-Based Worksheet ACTRL3.WBB for Controlling Calibration System, Digitizing Voltages During Calibrations, and Storing Results to Files

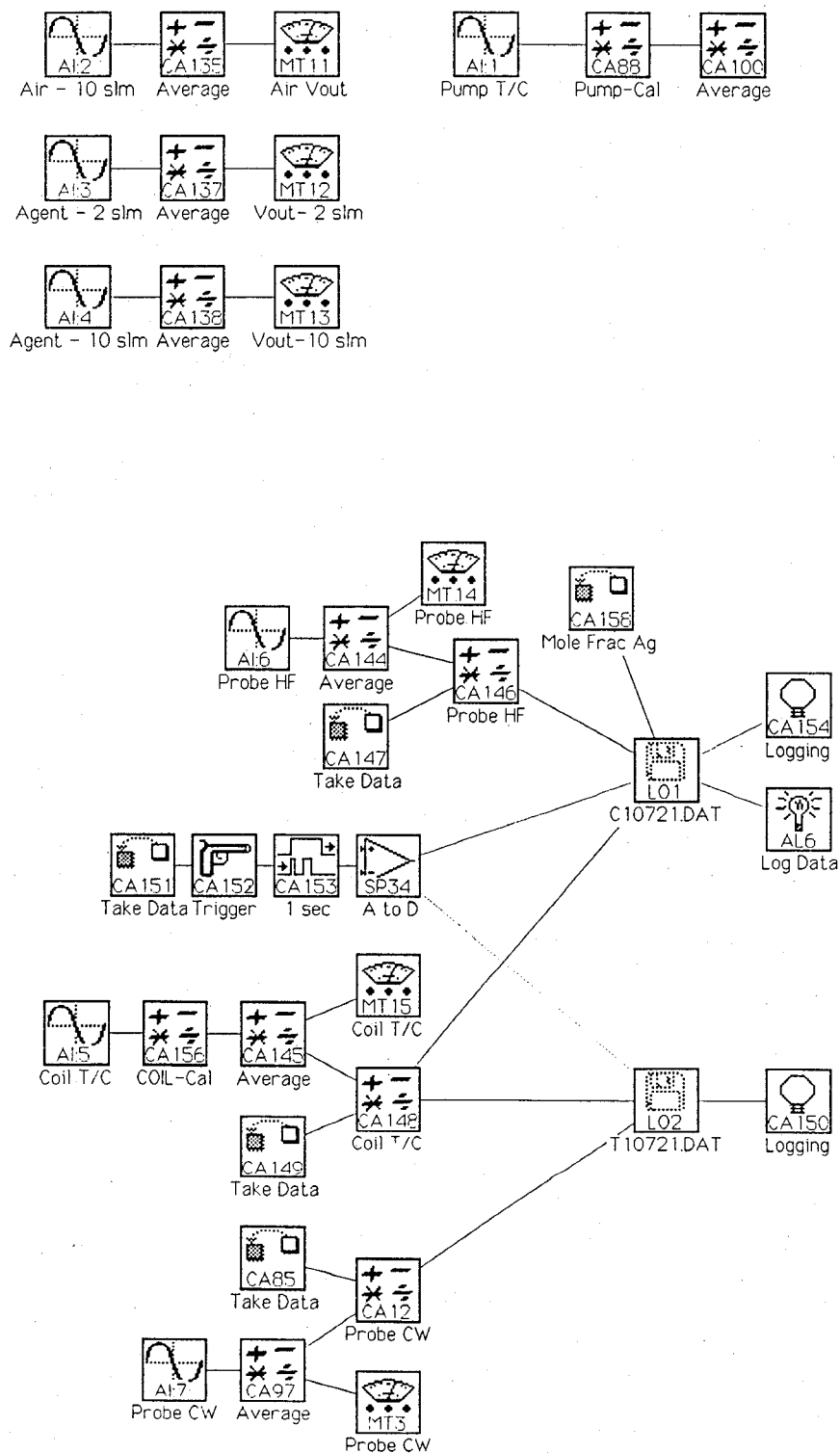


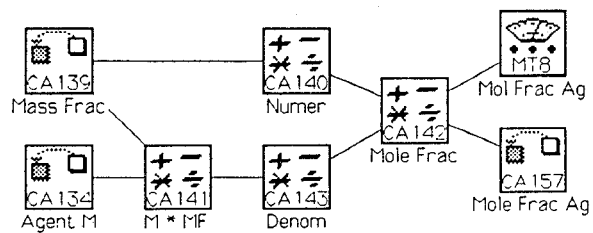
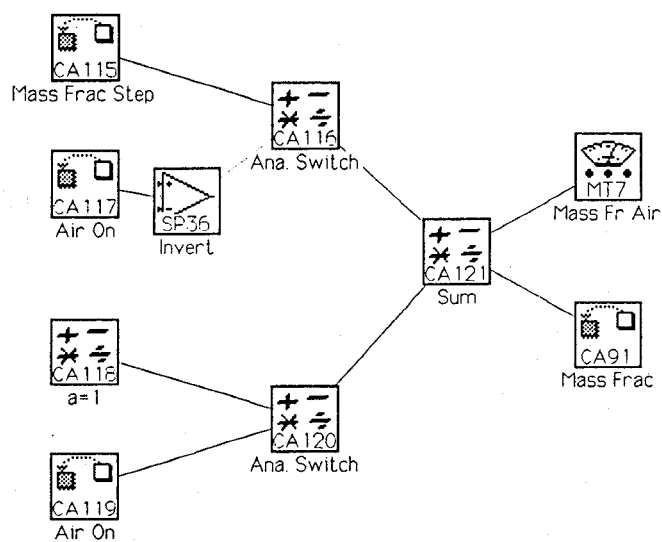
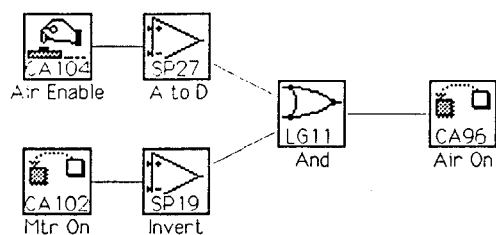
















**Appendix E. Workbench PC Computer-Control Panel for Calibration System. Panel Is Controlled By worksheet ACTRL3.WBB Shown in Appendix D**

<input type="checkbox"/> 104:  Air Enable	<input type="checkbox"/> 101:  Cal Start	<input type="checkbox"/> 107:  Pause	<input type="checkbox"/> 127:  Emerg. Stop	<input type="checkbox"/> MT7 • Mass Fr Air 0.00
				<input type="checkbox"/> MT8 • Mol Frac Ag 1.00000
<input type="checkbox"/> AL5 • Start/Stop Not Running	<input type="checkbox"/> AL4 • Vent/Test Vent		<input type="checkbox"/> AL6 • Log Data Off	
<input type="checkbox"/> MT4 • slm of air 0.000 slm	<input type="checkbox"/> MT5 • slm agent 1.859 slm		<input type="checkbox"/> MT15 • Coil T/C 2140064.92* C	
<input type="checkbox"/> MT1 • S.P. Air 0.000 V	<input type="checkbox"/> MT2 • Agent SP 2.508 V		<input type="checkbox"/> AL1 • Agent Path 10 slm path	
<input type="checkbox"/> MT11 • Air Uout 0.000 V	<input type="checkbox"/> MT13 • Uout-10 slm 0.000 V		<input type="checkbox"/> MT12 • Uout- 2 slm 0.000 V	
<input type="checkbox"/> MT14 • Probe HF 0.008 V	<input type="checkbox"/> MT3 • Probe CW - 6.698 V			



## Appendix F. Detailed Operating Procedures for Calibration of Combined Aspirated Hot-Film/Cold-Wire Probe

### TURN ON AND OPERATING PROCEDURE FOR CALIBRATION FACILITY

1. Turn on light in hood.
2. Check Syltherm level and fill if necessary. The fill line is located where the contraction of the nozzle straightens out.
3. Turn on the computer.
4. Turn on the power strip for the board, mixer, Agitainer, Exatrol, pump, and heaters. At this point do not plug in the pump.
5. Set up the IFA 100 anemometer.
  - a. Refer to TSI Reference Manual
  - b. Set up operating resistance
  - c. Perform frequency response tuning.
6. Position aspirating probe
  - a. Attach aspirating probe to drill press mount such that the end of the probe is approximately two inches from the steel block.
  - b. Tighten the screws uniformly.
  - c. Make sure the aspirating probe does not bend.
  - d. Mount the drill press holder on the vertical steel rod.
  - e. Locate the tip of the probe just above the exit of the nozzle. (This was done to reduce the chance of hitting the probe against the walls of the nozzle.
  - f. Locate the tip near the center of the nozzle. The X-Y translation stage provides an adjustment to center the probe.
  - g. Connect pump to aspirating probe.
  - h. Move drill press handle to lower the aspirating probe into the nozzle.
  - i. Place U-shaped bracket so that the drill press remains in the down position. We typically used the longest bracket.
7. Check that the set point on the Exatrol for the heater is below the lowest desired temperature. This will prevent overheating the liquid. **Note:** Do not connect the cooler to an outlet on the power strip described in 4 because the outlet will become overloaded.
8. While the fluid is transparent, check the operation of the magnetic stirrer.
9. Turn on the motor-driven stirrer. Set to approximately 60 to ensure smooth operation.
10. Turn on 100 psi air to valves.

11. Check the following on the Model 247C Readout:
  - a. All the toggle switches except for the power switch are in the down position.
  - b. Cables to flow meters:
    - Channel 1-10 slmn Air
    - Channel 2-2 slmn Agent
    - Channel 3-10 slmn Agent
    - Channel 4-Not used
  - c. Ribbon cable connects "Interface Channel 1-4" to box containing A/D boards (blue connector).
12. After warm-up time of 1/2 hr., zero the outputs on the Model 247C 4-Channel Readout. This is accomplished by adjusting the pot labelled Z.
13. Call up the appropriate worksheet (ACTRL3.WBB).
14. Enter the filename for the data into the log icon.
15. Set up worksheet for gas to be tested.
  - a. Connect global feedback CA84 to appropriate agent box CA17, CA18, CA19, CA20, or CA21.
  - b. Connect appropriate calculation icon CA43, CA44, CA45, CA46, or CA47 to MT5.
  - c. Connect appropriate global feedback icon CA49, CA51, CA53, CA55, or CA76 to global-feedback icon CA81.
  - d. Connect appropriate global-feedback icon CA61, CA62, CA63, CA64, or CA77 to global-feedback icon CA78.
16. Pressurize air and agent flow lines. Set pressures to 20 psig.
17. Turn on cooler.
18. Turn on dry air to prevent condensation. To do this press "air enabled" on the worksheet.
19. Check that Fenwall unit which controls the temperature of the plate is set to 28 °C.
20. Start all logs (This is automatically done in ACTRL3.WBB).
21. Wait for the Syltherm fluid to attain set-point temperature and stabilize.
22. Turn on pump.
23. Check pressure gauge to ensure that the probe is choked.
24. Set IFA 100 to "Run."
25. Press "Cal Start" on the worksheet.
27. Adjust the set point on the Exatrol to the next temperature setting. The 700 W heater can be used in addition to the 250 W heater during this period to accelerate heating of the liquid. Do not

leave the 700 W heater on for long periods because it heats quickly. Be careful!!! Do not leave the 700 Watt heater on.

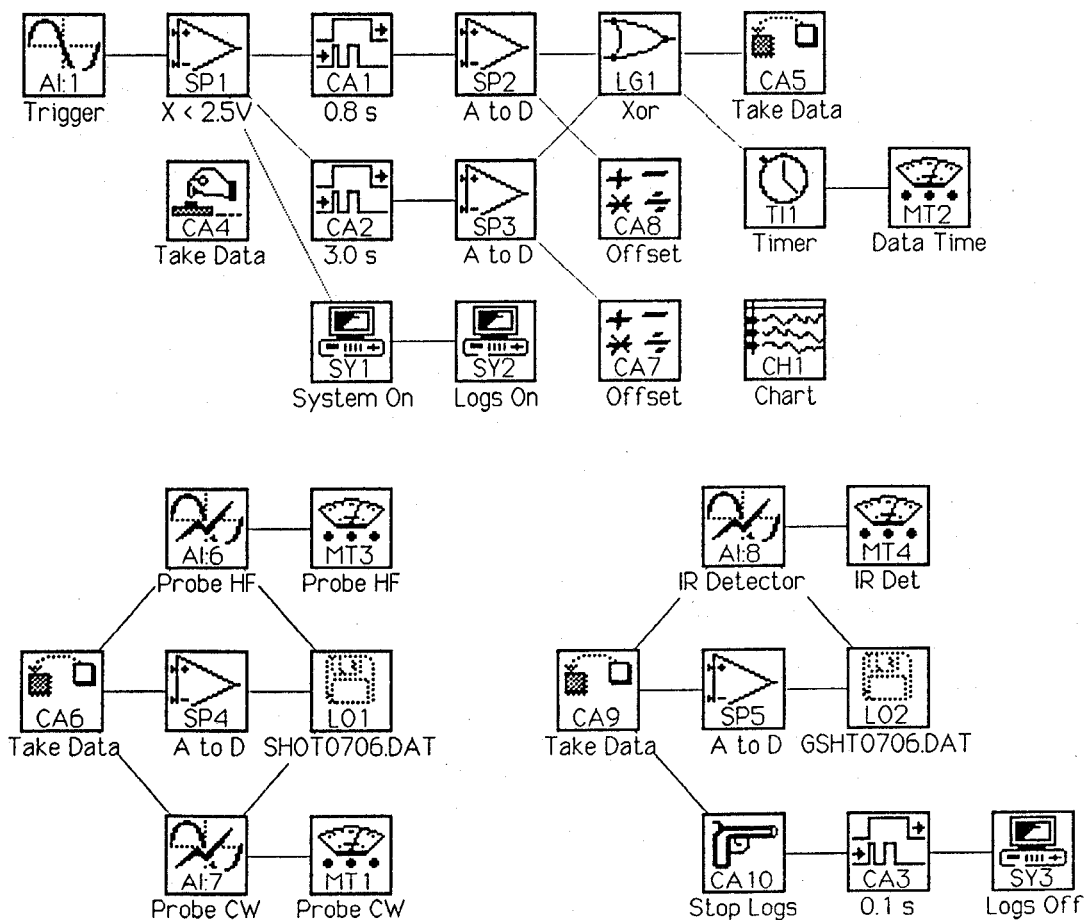
28. When the temperature has stabilized to 0.1 °C press "Cal Start."
29. Check to make sure that the software is operating properly.
  - a. Make sure MT1 "S.P. Air" and MT11 "Air Vout" are approximately the same for a specified mass fraction.
  - b. Make sure MT2 "Ag S.P." and MT13 "Vout slm" or MT12 "Vout 2slm" are the same for a specified mass fraction.
30. Then heat Syltherm up to next temperature and proceed as before.
31. When the calibration is completed begin the shut down procedure.

#### SHUT DOWN PROCEDURE

1. Set IFA 100 Anemometer to "standby."
2. Unplug pump.
3. Turn off cooler.
4. Adjust set point on Exatrol to a low temperature. This will avoid heating when the exatrol is turned on again.
5. Make sure the 700 W heater is off.
6. Turn off the motor-driven stirrer.
7. Turn off agent flow. Get MCTRL2.WBB worksheet, set mass fraction on slider to 0.0 and press "MTR ON" to bleed agent out of the lines.
8. Flush system with air.
  - a. Turn off black knob on air tank.
  - b. Hook up air line to agent line.
  - c. Set mass fraction on slider to 0.0, turn black knob on air tank on. Turn "MTR ON." This flushes out the 10 slmn path.
  - d. Set mass fraction to 0.78 to flush out the 2 slmn path.
  - e. Shut off air. The pressure will drop. Turn off meter.
9. Turn off 100 psi air supply. Flip vent on and off a few times. This will remove the air pressure from the line.
10. Turn off power strip.
11. Return air line to air pipe and agent line to agent pipe.

12. Turn off light in hood.
13. Turn off computer.

## Appendix G. Workbench PC Icon-Based Worksheet SHOT.WBB for Triggering Data Acquisition, Digitizing Hot-Film and Cold-Wire Voltages and Output of DIRRACS, and Storing Results to Files



## Appendix H. FORTRAN Program SURFFIT.FOR to Calculate Least Squares Fit to Surface of Order m Representing Agent Concentration. Surface is Fit of Agent Concentrations As Function of Temperature and Aspirated Hot-Film Voltage

- \* Fit a surface to calibration data. (SURFFIT.FOR)
- \* David E. Hess
- \* Fluid Flow Group - Process Measurements Division
- \* Chemical Science and Technology Laboratory
- \* National Institute of Standards and Technology
- \* June 8, 1994
- \* This routine is designed to accept three quantities:
- \* X(k), Y(k) and Z(k) for k = 1 to N.
- \* The data may be typed in at the keyboard or read from a file.
- \* The filename must be of the form :
- \* C // 1 digit test number // 4 digit date // .DAT (appended)
- \* There is no specific limit to the number of values N except
- \* that imposed by memory constraints. Note that the parameter
- \* NMAX must be greater than the largest anticipated value of N
- \* when reading data from a file.
- \* The program then uses a least square fit analysis to
- \* determine the Mth order surface: Z(X,Y). The (M+1)\*\*2
- \* coefficients for the fit are stored in A. An error analysis
- \* for the fit is performed, and the output is stored in a file.

```

IMPLICIT REAL*8 (A-H,O-Z), INTEGER*2 (I-N)
PARAMETER (NMAX=150)
PARAMETER (NUMI=1,NUMO=2)
INTEGER*2 DAT,TN
INTEGER*4 BYTES
CHARACTER*1 INP,FILKEY
CHARACTER*4 FEXT,FEXT2,FEXT3
CHARACTER*10 FNAMI,FNAME,FNAMA

```

```

REAL*8 Z [ALLOCATABLE] (:), ZTEMP [ALLOCATABLE] (:)
REAL*8 X [ALLOCATABLE] (:), Y [ALLOCATABLE] (:)
REAL*8 XTEMP [ALLOCATABLE] (:), YTEMP [ALLOCATABLE] (:)
REAL*8 XY [ALLOCATABLE] (:,:), XYT [ALLOCATABLE] (:,:)
REAL*8 XYTX [ALLOCATABLE] (:,:), XYTZ [ALLOCATABLE] (:,:)
REAL*8 ZEQS [ALLOCATABLE] (:,:), A [ALLOCATABLE] (:)
REAL*8 ZEST [ALLOCATABLE] (:), ZFEST [ALLOCATABLE] (:)

```

```
REAL*8      ZDEL [ALLOCATABLE] (:) , ZREL [ALLOCATABLE] (:)
```

```
DATA      EPS, INDIC / 1.0D-10, 1 /
DATA      FEXT, FEXT2, FEXT3 / '.DAT', '.ERR', '.COE' /
```

\* Title of routine.

```
WRITE (*,'(25(/))')
WRITE (*,'(18X,A//18X,A)')
+ '      LEAST SQUARES',
+ 'SURFACE FITTING ROUTINE'
WRITE (*,'(11(/))')
```

\* Get the order of the surface to fit.

```
WRITE (*,'( )')
WRITE (*,'(16X,A\\')') 'Enter order of surface M : '
READ (*,*) M
WRITE (*,'( )')
```

```
MP1=M+INT2(1)
MP1SQ=(MP1)**2
MP1SQP1=MP1SQ+INT2(1)
```

\* Read in X, Y and Z from a file or from the keyboard ?

```
10 WRITE (*,'(16X,A\\')') 'Enter (F)ile input or (K)eyboard input: '
READ (*,'(A)') FILKEY
WRITE (*,'( )')
GO TO (10,40) ILET(FILKEY,'FK')
```

\* Keyboard input section \*\*\*\*\*

\* Get values of X, Y and Z from keyboard.

```
20 WRITE (*,'(16X,A\\')') 'Enter # of calibration values (N) : '
READ (*,*) N
WRITE (*,'( )')
```

\* Estimate space required for arrays for this choice of M and N.

```
SPACE=DBLE(BYTES(M,N))/1024.0D0
```

```
WRITE (*,'(13X,A,F7.2,A/)')
+ 'Amount of space required for arrays = ',SPACE,' kB.'
PAUSE
+ '      Press enter to allocate arrays and continue.'
```

\* Allocate space for the necessary arrays.

```
ALLOCATE (X(N), Y(N), Z(N), STAT=IERR)
IF (IERR .NE. 0) STOP 'Can't allocate input arrays in main.'
```

```
ALLOCATE (XY(N,MP1SQ), XYT(MP1SQ,N), STAT=IERR)
IF (IERR .NE. 0) STOP 'Can't allocate XY & XYT arrays in main.'
```

```
ALLOCATE (XYTXY(MP1SQ,MP1SQ), STAT=IERR)
IF (IERR .NE. 0) STOP 'Can't allocate XYTXY array in main.'
```

```
ALLOCATE (XYTZ(MP1SQ,1), STAT=IERR)
IF (IERR .NE. 0) STOP 'Can't allocate RHS array in main.'
```

```
ALLOCATE (ZEQS(MP1SQP1,MP1SQP1), STAT=IERR)
IF (IERR .NE. 0) STOP 'Can't allocate ZEQS array in main.'
```

```
ALLOCATE (A(MP1SQ), STAT=IERR)
IF (IERR .NE. 0) STOP 'Can't allocate coeff arrays in main.'
```

```
ALLOCATE (ZEST(N),ZFEST(N),ZDEL(N),ZREL(N), STAT=IERR)
IF (IERR .NE. 0) STOP 'Can't allocate error arrays in main.'
```

\* Now, get the data.

```
DO I=1,N
  WRITE (*,30) I,I,I
30  FORMAT (16X,'Enter X(',I2,') , Y(',I2,') and Z(',I2,') : '\)
  READ (*,*) X(I),Y(I),Z(I)
ENDDO
WRITE (*,')
GO TO 70
```

\* File input section \*\*\*\*\*

```
40  WRITE (*,'(16X,A,I3,A)')
+    'Program will read up to ',NMAX,' points.'
50  WRITE (*,'(16X,A,A,A)')
+    'Enter name of input file [',FEXT,']:'
  READ (*,'(A)') FNAMI
  WRITE (*,')')
```

\* Concatenate file extension to FNAMI.

```
IPD=INDEX(FNAMI,')')
IF (IPD .GT. 9) GO TO 50
IF (IPD .EQ. 0) THEN
  IEND=LEN_TRIM(FNAMI)
  FNAMI(IEND+1:IEND+4)=FEXT
```



ENDIF

- \* Create the other filenames.

```
IPD=INDEX(FNAMI, '.')
FNAME = FNAMI(IPD-1) // FEXT2
FNAMA = FNAMI(IPD-1) // FEXT3
```

- \* Get the input file.

```
OPEN (NUMI, FILE=FNAMI, STATUS='OLD')
```

- \* First determine # of values of X, Y and Z in the file.

```
DO I=1, NMAX
  READ (NUMI, *, END=60) XTST, YTST, ZTST
ENDDO
```

```
60 N=I-1
  REWIND(NUMI)
```

- \* Estimate space required for arrays for this choice of M and N.

```
SPACE=DBLE(BYTES(M,N))/1024.0D0
```

```
WRITE (*, '(13X,A,F7.2,A)')
```

```
+ 'Amount of space required for arrays = ', SPACE, ' kB.'
```

```
PAUSE
```

```
+ '          Press enter to allocate arrays and continue.'
```

- \* Allocate space for the necessary arrays.

```
ALLOCATE (X(N), Y(N), Z(N), STAT=IERR)
IF (IERR .NE. 0) STOP 'Can't allocate input arrays in main.'
```

```
ALLOCATE (XY(N,MP1SQ), XYT(MP1SQ,N), STAT=IERR)
IF (IERR .NE. 0) STOP 'Can't allocate XY & XYT arrays in main.'
```

```
ALLOCATE (XYTXY(MP1SQ,MP1SQ), STAT=IERR)
IF (IERR .NE. 0) STOP 'Can't allocate XYTXY array in main.'
```

```
ALLOCATE (XYTZ(MP1SQ,1), STAT=IERR)
IF (IERR .NE. 0) STOP 'Can't allocate RHS array in main.'
```

```
ALLOCATE (ZEQS(MP1SQP1,MP1SQP1), STAT=IERR)
IF (IERR .NE. 0) STOP 'Can't allocate ZEQS array in main.'
```

```
ALLOCATE (A(MP1SQ), STAT=IERR)
IF (IERR .NE. 0) STOP 'Can't allocate coeff arrays in main.'
```

```

ALLOCATE (ZEST(N),ZFEST(N),ZDEL(N),ZREL(N), STAT=IERR)
IF (IERR .NE. 0) STOP 'Can't allocate error arrays in main.'

```

\* Get values of X, Y and Z from file.

```

DO I=1,N
  READ (NUMI,*) X(I),Y(I),Z(I)
ENDDO
CLOSE (NUMI)

```

\* Display these values on the screen for verification.

```

70 CALL DISPLAY_CALDATA (X,Y,Z,N,*130)

```

\* Fix, Insert, Delete an entry or Continue.

```

80 WRITE (*,'(16X,A)\') '(F)ix, (I)nsert, (D)elete '
  WRITE (*,'(A)\') 'an entry or (C)ontinue? '
  READ (*,'(A)\') INP
  WRITE (*,'( )')
  GO TO (80,90,110,130) ILET(INP,'IDCF')

```

\* Routine to fix bad keyboard entry \*\*\*\*\*

```

WRITE (*,'(16X,A)\') 'Enter array subscript of bad value: '
READ (*,*) I
WRITE (*,30) I,I,I
READ (*,*) X(I),Y(I),Z(I)
GO TO 70

```

\* Insert an entry \*\*\*\*\*

\* First, create some temporary space.

```

90 ALLOCATE (XTEMP(N+1), YTEMP(N+1), ZTEMP(N+1), STAT=IERR)
IF (IERR .NE. 0)
+ STOP 'Can't allocate XTEMP, YTEMP and ZTEMP in INSERT.'

```

\* Copy old values into temporary area.

```

DO I=1,N
  XTEMP(I)=X(I)
  YTEMP(I)=Y(I)
  ZTEMP(I)=Z(I)
ENDDO

```

\* Throw away old arrays.

```

DEALLOCATE (X,Y,Z, STAT=IERR)
IF (IERR .NE. 0)
+   STOP 'Can't deallocate X, Y and Z in INSERT.'

```

```

100  WRITE (*,'(16X,A)\') 'Insert after which array subscript? '
      READ (*,*) J
      IF (J .LT. 0 .OR. J .GT. N) GO TO 100
      N=N+1
      JP2=J+2
      DO I=N,JP2,-1
        IM1=I-1
        XTEMP(I)=XTEMP(IM1)
        YTEMP(I)=YTEMP(IM1)
        ZTEMP(I)=ZTEMP(IM1)
      ENDDO
      JP1=J+1
      WRITE (*,30) JP1,JP1,JP1
      READ (*,*) XTEMP(JP1),YTEMP(JP1),ZTEMP(JP1)

```

\* Create space for X, Y and Z arrays.

```

ALLOCATE (X(N), Y(N), Z(N), STAT=IERR)
IF (IERR .NE. 0)
+   STOP 'Can't allocate X, Y and Z in INSERT.'

```

\* Copy X, Y and Z values into permanent arrays.

```

DO I=1,N
  X(I)=XTEMP(I)
  Y(I)=YTEMP(I)
  Z(I)=ZTEMP(I)
ENDDO

```

\* Delete temporary space and display values.

```

DEALLOCATE (XTEMP,YTEMP,ZTEMP, STAT=IERR)
IF (IERR .NE. 0) STOP
+   'Can't deallocate XTEMP, YTEMP and ZTEMP in INSERT.'

```

```

GO TO 70

```

\* Delete an entry \*\*\*\*\*

\* First, create some temporary space.

```

110  ALLOCATE (XTEMP(N), YTEMP(N), ZTEMP(N), STAT=IERR)
      IF (IERR .NE. 0)
+   STOP 'Can't allocate XTEMP, YTEMP and ZTEMP in DELETE.'

```

\* Copy old values into temporary area.

```
DO I=1,N
  XTEMP(I)=X(I)
  YTEMP(I)=Y(I)
  ZTEMP(I)=Z(I)
ENDDO
```

\* Throw away old arrays.

```
DEALLOCATE (X,Y,Z, STAT=IERR)
IF (IERR .NE. 0)
+ STOP 'Can't deallocate X, Y and Z in DELETE.'
```

```
120 WRITE (*,'(16X,A\)' ) 'Delete which subscript? '
READ (*,*) J
IF (J .LT. 1 .OR. J .GT. N) GO TO 120
NM1=N-1
DO I=J,NM1
  IP1=I+1
  XTEMP(I)=XTEMP(IP1)
  YTEMP(I)=YTEMP(IP1)
  ZTEMP(I)=ZTEMP(IP1)
ENDDO
N=N-1
```

\* Create space for X, Y and Z arrays.

```
ALLOCATE (X(N), Y(N), Z(N), STAT=IERR)
IF (IERR .NE. 0)
+ STOP 'Can't allocate X, Y and Z in DELETE.'
```

\* Copy X, Y and Z values into permanent arrays.

```
DO I=1,N
  X(I)=XTEMP(I)
  Y(I)=YTEMP(I)
  Z(I)=ZTEMP(I)
ENDDO
```

\* Delete temporary space and display values.

```
DEALLOCATE (XTEMP,YTEMP,ZTEMP, STAT=IERR)
IF (IERR .NE. 0) STOP
+ 'Can't deallocate XTEMP, YTEMP and ZTEMP in DELETE.'
```

GO TO 70

\* Create an input file \*\*\*\*\*

```
130 WRITE (*,'(16X,A)') 'Create an input file? (Y/N) : '
    READ (*,'(A)') INP
    WRITE (*,'( )')
    GO TO (130,140) ILET(INP,'NY')
    CALL PRINT2 (N,X,Y,Z,FEXT)
```

\* Calculate all possible products of X and Y.

```
140 CALL COEFF (X,Y,XY,N,M)
```

\* Compute the transpose XYT of the XY array.

```
DO K=1,N
  DO J=1,MP1SQ
    XYT(J,K)=XY(K,J)
  ENDDO
ENDDO
```

\* Compute coefficient array:  $XYTXY = XYT * XY$

\* Compute right hand sides :  $XYTZ = XYT * Z$

```
CALL MATMLT (XYT,XY,XYTXY,MP1SQ,N, MP1SQ)
CALL MATMLT (XYT, Z, XYTZ,MP1SQ,N,INT2(1))
```

\* Create the augmented matrix ZEQS.

```
DO I=1,MP1SQP1
  DO J=1,MP1SQP1
    ZEQS(I,J)=0.0D0
  ENDDO
ENDDO
```

```
DO I=1,MP1SQ
  DO J=1,MP1SQ
    ZEQS(I,J)=XYTXY(I,J)
  ENDDO
ENDDO
```

```
DO I=1,MP1SQ
  ZEQS(I,MP1SQP1)=XYTZ(I,1)
ENDDO
```

\* Solve the set of MP1SQ eqs in MP1SQ unknowns for A.

```
DETERZ=SIMUL(MP1SQ,ZEQS,A,EPS,INDIC,MP1SQP1)
WRITE (*,'(16X,A,D16.5/)') 'Deter for Z = ',DETERZ
```

```

IF (DETERZ .EQ. 0.0D0) THEN
  WRITE (*,'(16X,A)') 'Z matrix is singular, no solution.'
  GO TO 160
ENDIF

```

\* Store the coefficients in a file.

```

OPEN (NUMO,FILE=FNAMA,STATUS='UNKNOWN')
  WRITE (NUMO,'(D25.15)') (A(I),I=1,MP1SQ)
CLOSE (NUMO)

```

\* Perform error analysis on Z.

```

160 IF (DETERZ .EQ. 0.0D0) GO TO 180
  CALL ERRANAL (X,Y,Z,XY,A,N,M,
+    ZEST,ZFEST,ZDEL,ZREL,ZMAX,ZAV,ZDEV,ZAVR,ZDEVVR,SZXY,R)

```

\* Generate filenames if keyboard option was selected.

```

IF (FILKEY .EQ. 'K') THEN

```

\* Get date and generate filenames.

```

  WRITE (*,'( )')
  WRITE (*,'(1X,A)') 'Enter date (mmdd) : '
  READ (*,*) DAT
  WRITE (*,'( )')

  WRITE (*,'(1X,A)') 'Enter test number (#) : '
  READ (*,*) TN
  WRITE (*,'( )')

```

```

  WRITE (FNAMI,'(A1,I1,I4.4,A4)') 'C',TN,DAT,FEXT
  WRITE (FNAME,'(A1,I1,I4.4,A4)') 'C',TN,DAT,FEXT2
  WRITE (FNAMA,'(A1,I1,I4.4,A4)') 'C',TN,DAT,FEXT3
ENDIF

```

\* Save data in a file.

```

  CALL STORE_ERRDATA ('Z',Z,FNAME,M,N,DETERZ,
+    ZEST,ZFEST,ZDEL,ZREL,ZMAX,ZAV,ZDEV,ZAVR,ZDEVVR,SZXY,R)

```

```

180 STOP ' '
END

```

```

FUNCTION ILET (INP,STRING) ! (ILET.FOR)

```

```

IMPLICIT INTEGER*2 (I-N)

```

```

CHARACTER*1 INP
CHARACTER*(*) STRING

```

- \* First, convert INP to uppercase if it is lowercase. If it
- \* is uppercase, leave it unchanged.

```

IF (ICHAR(INP) .GE. 97 .AND. ICHAR(INP) .LE. 122) THEN
  IHOLD=ICHAR(INP)-32
  INP=CHAR(IHOLD)
ENDIF

```

- \* Determine the position of INP in STRING, then add one to get
- \* ILET which determines label to use in computed GO TO statement.

```

IPOS=INDEX(STRING,INP)
ILET=IPOS+1

```

```

RETURN
END

```

```

FUNCTION BYTES (M,N)

```

```

IMPLICIT INTEGER*2 (A-Z)
INTEGER*4 BYTES

```

```

MP1=M+1
MP1SQ=(MP1)**2
MP1SQP1=MP1SQ+1

```

```

BYTES=3*8*N           ! X, Y, Z
BYTES=BYTES+2*8*N*MP1SQ ! XY, XYT
BYTES=BYTES+8*MP1SQ*MP1SQ ! XYTXY
BYTES=BYTES+8*MP1SQ      ! XYTZ
BYTES=BYTES+8*MP1SQP1*MP1SQP1 ! ZEQS
BYTES=BYTES+8*MP1SQ      ! A
BYTES=BYTES+4*8*N        ! ZEST, ZFEST, ZDEL, ZREL
BYTES=BYTES+8*MP1        ! C in F
BYTES=BYTES+3*2*N        ! IROW,JCOL,JORD in SIMUL
BYTES=BYTES+8*N          ! Y in SIMUL

```

```

RETURN
END

```

```

SUBROUTINE DISPLAY_CALDATA (X,Y,Z,N,*)

```

```

IMPLICIT REAL*8 (A-H,O-Z), INTEGER*2 (I-N)
REAL*8 X(N), Y(N), Z(N)

```

```

WRITE (*,'( )')
WRITE (*,10) 'I','X(I)','Y(I)','Z(I)'
WRITE (*,10) '-','----','----','----'
10  FORMAT (10X,A1,9X,A4,12X,A4,11X,A4)
    KOUNT=0
    KTST=18
    DO I=1,N
        WRITE (*,20) I,X(I),Y(I),Z(I)
20  FORMAT (8X,I3,4(F14.5,2X))
    KOUNT=KOUNT+1
    IF (KOUNT .EQ. KTST) THEN
        KOUNT=0
        KTST=20
        IF (N .EQ. I) CYCLE
        WRITE (*,'( )')
        WRITE (*,'(/16X,A,A)') 'Press Enter for next page',
+          ' or (C)ontinue : '
        READ (*,'(A)') INP
        WRITE (*,'( )')
        IF (INP .EQ. 'C' .OR. INP .EQ. 'c') RETURN 1
        WRITE (*,10) 'I','X(I)','Y(I)','Z(I)'
        WRITE (*,10) '-','----','----','----'
    ENDIF
ENDDO
IF (KOUNT .LT. KTST) THEN
    DO I=KOUNT-1,KTST
        WRITE (*,'( )')
    ENDDO
ENDIF

RETURN
END

SUBROUTINE STORE_ERRDATA (LETTER,Z,FNAM,M,N,DETERZ,
+   ZEST,ZFEST,ZDEL,ZREL,ZMAX,ZAV,ZDEV,ZAVR,ZDEVZ,SZXY,R)

IMPLICIT   REAL*8 (A-H,O-Z), INTEGER*2 (I-N)

PARAMETER   (NUM=1)
REAL*8      Z(N),ZEST(N),ZFEST(N),ZDEL(N),ZREL(N)
CHARACTER*1 LETTER
CHARACTER*10 FNAM

OPEN (NUM,FILE=FNAM,STATUS='UNKNOWN')
    WRITE (NUM,'(35X,A)') FNAM
    WRITE (NUM,'(8X,A,6X,A,8X,A,8X,A,8X,A)')
+   'M','N','Deter','Std Err','R'
    WRITE (NUM,'(8X,A,6X,A,8X,A,8X,A,8X,A)')

```



```

+      '-','-',',-----','-----','-'
  WRITE (NUM,'(8X,I1,4X,I3,D15.5,2X,D12.5,2X,G12.5)')
+      M,N,DETERZ,SZXY,R
  WRITE (NUM,'( )')
  WRITE (NUM,'(8X,A,7X,A,7X,A,6X,A,8X,A)')
+      'Max Err','Avg Err','S.D. Err','Avg %','S.D. %'
  WRITE (NUM,'(8X,A,7X,A,7X,A,6X,A,8X,A)')
+      '-----','-----','-----','-----','-----'
  WRITE (NUM,'(5X,5(G12.5,2X))')
+      ZMAX,ZAV,ZDEV,ZAVR,ZDEV
  WRITE (NUM,'( )')
  WRITE (NUM,'(4X,A,5X,A,9X,A,8X,A,10X,A,8X,A)')
+      'I',LETTER // '-act',LETTER // '-fit',
+      LETTER // '-func',LETTER // '-diff','Err (%)'
  WRITE (NUM,'(4X,A,5X,A,9X,A,8X,A,10X,A,8X,A)')
+      '-','-',',-----','-----','-----','-----','-----'
  WRITE (NUM,'(2X,I3,2X,G12.5,2X,G12.5,2X,
+      G12.5,2X,G12.5,2X,G12.5)')
+      (I,Z(I),ZEST(I),ZFEST(I),ZDEL(I),ZREL(I),I=1,N)
  CLOSE (NUM)

```

```

RETURN
END

```

```

SUBROUTINE COEFF (X,Y,XY,N,M)      ! (COEFF.FOR)

```

\* Inputs:

```

*      X - array containing X
*      Y - array containing Y
*      N - # of elements = (# of Q's) * (# of Alphas)
*      M - order of surface used in fit (most often 3 or 4)

```

\* Outputs:

```

*      XY - array containing all possible X * Y products

```

```

IMPLICIT  REAL*8 (A-H,O-Z), INTEGER*2 (I-N)
REAL*8    X(N),Y(N)
REAL*8    XY(N,(M+1)**2)

```

\* Initialization.

```

MP1=M+INT2(1)
MP1SQ=(MP1)**2

```

```

DO K=1,N

```

- \* Calculate first MP1 elements which have X's and no Y's.

```

XY(K,1)=1.0D0
DO J=2,MP1
  XY(K,J)=X(K)*XY(K,J-1)
ENDDO

```

- \* Calculate remaining elements which have X's and Y's.

```

DO J=MP1+1,MP1SQ
  I=J-MP1
  XY(K,J)=Y(K)*XY(K,I)
ENDDO

```

```

ENDDO

```

```

RETURN
END

```

```

SUBROUTINE MATMLT (A,B,C,M,N,P)  ! (MATMLT.FOR)

```

- \* Ref: Carnahan, B., Luther, H.A., Wilkes, J.O., Applied
- \* Numerical Methods, Wiley, New York, 1969, pp.210-217.

- \* Inputs:

- \* A - first input array
- \* B - second input array
- \* M,N,P - #'s of elements in various arrays
- \* A (M x N), B (N x P), C (M x P)

- \* Outputs:

- \* C - resultant array is product of A and B

- \* 
$$C_{ij} = \sum_{k=1}^N (A_{ik} B_{kj})$$
- \* Formula:
- \* 
$$C_{ij} = \sum_{k=1}^N (A_{ik} B_{kj})$$

```

IMPLICIT REAL*8 (A-H,O-Z), INTEGER*2 (I-N)
INTEGER*2 P
REAL*8 A(M,N),B(N,P),C(M,P)

```

- \* Zero the C array.

```

DO I=1,M
  DO J=1,P
    C(I,J)=0.0D0
  
```

```

      ENDDO
    ENDDO

```

\* Perform the multiplication.

```

      DO I=1,M
        DO J=1,P
          DO K=1,N
            C(I,J)=C(I,J)+A(I,K)*B(K,J)
          ENDDO
        ENDDO
      ENDDO

```

```

      RETURN
    END

```

```

      SUBROUTINE ERRANAL (X,Y,Z,XY,A,N,M,
+      ZEST,ZFEST,ZDEL,ZREL,ZMAX,ZAV,ZDEV,ZAVR,ZDEVR,SZXY,R)

```

\* Inputs:

```

*      X - array containing X
*      Y - array containing Y
*      Z - array containing Z
*      XY - array containing all possible X * Y products
*      A - array containing fit coeffs A (for Z)
*      N - # of elements = (# of Q's) * (# of Alphas)
*      M - order of surface used in fit (most often 3 or 4)

```

\* Outputs:

```

*      ZEST - array containing Z estimated
*             from fit coeffs * X * Y products
*      ZFEST - array containing Z estimated
*             from function subroutines.
*      ZDEL - array containing differences between Z and ZEST
*      ZREL - array containing percent errors between Z and ZEST
*      ZMAX - maximum absolute value of ZDEL array
*      ZAV - average ZDEL value
*      ZDEV - standard deviation of ZDEL array.

```

```

      IMPLICIT REAL*8 (A-H,O-Z), INTEGER*2 (I-N)
      REAL*8      X(N),Y(N),Z(N),A((M+1)**2)
      REAL*8      XY(N,(M+1)**2)
      REAL*8      ZEST(N),ZFEST(N),ZDEL(N),ZREL(N)

```

\* Initialization.

```

MP1=M+INT2(1)
MP1SQ=(MP1)**2
E2=0.0D0
ZM=0.0D0
ZSUM=0.0D0
ZRSUM=0.0D0
ZVARSUM=0.0D0
ZVARSUMR=0.0D0

```

\* Calculate various arrays.

```
DO K=1,N
```

```
  ZFEST(K)=F(X(K),Y(K),A,M) ! Calculate u's from function
```

```
  ZEST(K)=0.0D0
```

```
  DO J=1,MP1SQ          ! Calculate u's from fit coeffs
```

```
    ZEST(K)=ZEST(K)+A(J)*XY(K,J)
```

```
  ENDDO
```

```
  ZDEL(K)=Z(K)-ZEST(K)    ! Calculate differences
```

```
  E2=E2+ZDEL(K)*ZDEL(K)   ! Calculate sum of squared diffs.
```

```
  ZM=ZM+Z(K)             ! Calculate avg Z
```

```
  IF (Z(K) .EQ. 0.0) THEN ! Don't divide by zero
```

```
    ZREL(K)=0.0D0
```

```
  ELSE
```

```
    ZREL(K)=ZDEL(K)/Z(K)*100.0D0 ! Calculate percents
```

```
  ENDIF
```

```
  IF (K .EQ. 1) ZMAX=DABS(ZDEL(K))
```

```
  ZMAX=DMAX1(DABS(ZDEL(K)),ZMAX) ! Calculate largest ZDEL value
```

```
  ZSUM=ZSUM+DABS(ZDEL(K))
```

```
  ZRSUM=ZRSUM+DABS(ZREL(K))
```

```
ENDDO
```

\* Calculate standard error and mean value of Z(K).

```
IF (N .LE. 2) THEN
```

```
  SZXY=DSQRT(E2)
```

```
ELSE
```

```
  SZXY=DSQRT(E2/DBLE(N-2))
```

```
ENDIF
```

```
ZM=ZM/DBLE(N)
```

- \* Calculate unbiased std. dev. of Z(I). (N-1 Method)

```

SZ=0.0D0
DO K=1,N
  SZ=SZ+(Z(K)-ZM)**2
ENDDO

IF (N .EQ. 1) THEN
  SZ=DSQRT(SZ)
ELSE
  SZ=DSQRT(SZ/DBLE(N-1))
ENDIF

```

- \* Calculate the correlation coefficient as  $R = \sqrt{1 - SZ_{XY}^2 / SZ^2}$ .

- \* This is given in Ref. 2.

```

IF (SZ .LE. 0.0D0) THEN
  WRITE (*,'(16X,A)') 'Note SZ = 0. Forced R = 1.'
  PAUSE
  R=1.0D0
  RETURN
ENDIF

```

```

R=DSQRT(1.0D0-SZXY**2/SZ**2)

```

- \* Calculate the average ZDEL and ZREL values.

```

ZAV=ZSUM/DBLE(N)      ! Average of ABS(ZDEL)
ZAVR=ZRSUM/DBLE(N)    ! Average of ABS(ZREL)

```

- \* Calculate the standard deviation of ZDEL and ZREL.

```

DO K=1,N
  ZVARSUM=ZVARSUM+(DABS(ZDEL(K))-ZAV)**2
  ZVARSUMR=ZVARSUMR+(DABS(ZREL(K))-ZAVR)**2
ENDDO
ZDEV=DSQRT(ZVARSUM/DBLE(N))  ! Std. Dev. of ABS(ZDEL)
ZDEVR=DSQRT(ZVARSUMR/DBLE(N)) ! Std. Dev. of ABS(ZREL)

RETURN
END

```

```

FUNCTION F(X,Y,A,M) ! (F.FOR)

```

- \* Inputs:

- \* X - X value
- \* Y - Y value

- \* A - array containing fit coeffs A (for Z)
- \* M - order of surface used in fit (most often 3 or 4)

\* Output:

- \* F - value of Z

```
IMPLICIT REAL*8 (A-H,O-Z), INTEGER*2 (I-N)
REAL*8      A((M+1)**2)
REAL*8      C[ALLOCATABLE](:)
```

- \* Initialization.

```
MP1=M+INT2(1)
MP1SQ=(MP1)**2
```

```
ALLOCATE (C(MP1), STAT=IERR)
IF (IERR .NE. 0) STOP 'Can't allocate C in F function.'
```

- \* Note: C's (collections of A's and X's) multiply Y's
- \* and A's multiply X's. Calculate first C "coefficient."

```
C(MP1)=A(MP1SQ)
DO K=MP1SQ-1,M*MP1+1,-1
  C(MP1)=C(MP1)*X+A(K)
ENDDO
F=C(MP1)
```

- \* Enter double loop multiplying X's and Y's.

```
DO J=M,1,-1
  C(J)=A(J*MP1)
  DO K=J*MP1-1,(J-1)*MP1+1,-1
    C(J)=C(J)*X+A(K)
  ENDDO
  F=F*Y+C(J)
ENDDO
```

```
DEALLOCATE (C, STAT=IERR)
IF (IERR .NE. 0) STOP 'Can't deallocate C in F function.'
```

```
RETURN
END
```

\*\*\*\*\*

\*

```
SUBROUTINE PRINT2 (N,X,Y,Z,FEXT)
```

\*

\*

\*

```

*      David E. Hess                      *
*      August 17, 1992                    *
*                                          *
*      This subroutine stores the input data in a new sequential      *
*      formatted .PRN file for easy access by LOTUS and LSFIT.        *
*                                          *
*****
IMPLICIT  REAL*8 (A-H,O-Z), INTEGER*2 (I-N)
PARAMETER (NUM=2)
REAL*8    X(N),Y(N),Z(N)
CHARACTER*4 FEXT
CHARACTER*12 FILNAM

*      Get name of input file.

10 WRITE (*,'(16X,A,A,A)')
+   'Enter name of input file [',FEXT,']:'
READ (*,'(A)') FILNAM
WRITE (*,'( )')

*      Concatenate file extension to FILNAM.

IPD=INDEX(FILNAM,'.')
IF (IPD .GT. 9) GO TO 10
IF (IPD .EQ. 0) THEN
    IEND=LEN_TRIM(FILNAM)
    FILNAM(IEND+1:IEND+4)=FEXT
ENDIF

OPEN (NUM,FILE=FILNAM,STATUS='UNKNOWN')

*      Write results to file.

DO I=1,N
    WRITE (NUM,*) X(I),Y(I),Z(I)
ENDDO

CLOSE (NUM)
RETURN
END

*****
*                                          *
*      FUNCTION SIMUL (N,A,X,EPS,INDIC,NRC)          *
*                                          *
*      Ref: Carnahan, B., Luther, H.A., Wilkes, J.O., Applied      *
*      Numerical Methods, Wiley, New York, 1969, pp.290-291.      *

```

```

*
*
*      When INDIC is negative, SIMUL computes the inverse of the N
*      by N matrix A in place. When INDIC is zero, SIMUL computes
*      the N solutions X(1)...X(N) corresponding to the set of
*      linear equations with augmented matrix of coefficients in
*      the N by N+1 array A and in addition computes the inverse of
*      the coefficient matrix in place as above. If INDIC is
*      positive, the set of linear equations is solved but the
*      inverse is not computed in place. The Gauss-Jordan complete
*      elimination method is employed with the maximum pivot
*      strategy. Row and column subscripts of successive pivot
*      elements are saved in order in the IROW and JCOL arrays
*      respectively. K is the pivot counter, PIVOT the algebraic
*      value of the pivot element, MAX is the number of columns in
*      A and DETER the determinant of the coefficient matrix. The
*      solutions are computed in the (N+1)st column of A and then
*      unscrambled and put in proper order in X(1)...X(N) using the
*      pivot subscript information available in the IROW and JCOL
*      arrays. The sign of the determinant is adjusted, if
*      necessary, by determining if an odd or even number of
*      pairwise interchanges is required to put the elements of the
*      JORD array in ascending sequence where JORD(IROW(I))=JCOL(I).
*      If the inverse is required, it is unscrambled in place using
*      Y(1)...Y(N) as temporary storage. The value of the deter-
*      minant is returned as the value of the function. Should the
*      potential pivot of largest magnitude be smaller in magnitude
*      than EPS, the matrix is considered to be singular and a true
*      zero is returned as the value of the function.
*
*****

```

```

IMPLICIT REAL*8 (A-H,O-Z), INTEGER*2 (I-N)

```

```

INTEGER*2 IROW[ALLOCATABLE](:)

```

```

INTEGER*2 JCOL[ALLOCATABLE](:)

```

```

INTEGER*2 JORD[ALLOCATABLE](:)

```

```

REAL*8 Y[ALLOCATABLE](:)

```

```

REAL*8 A(NRC,NRC),X(N)

```

```

*      Set up space for arrays used only in SIMUL.

```

```

ALLOCATE (IROW(N), JCOL(N), JORD(N), Y(N), STAT=IERR)

```

```

IF (IERR .NE. 0) STOP 'Can't allocate arrays in SIMUL.'

```

```

*      Initialization.

```

```

MAX=N

```

```

IF (INDIC .GE. 0) MAX=N+1

```



\* Begin elimination procedure.

```
DETER=1.0D0
DO 40 K=1,N
  KM1=K-1
```

\* Search for the pivot element.

```
PIVOT=0.0D0
DO 30 I=1,N
  DO 20 J=1,N
```

\* Scan IROW and JCOL arrays for invalid pivot subscripts.

```
IF (K .EQ. 1) GO TO 10
```

```
DO ISCAN=1,KM1
  DO JSCAN=1,KM1
    IF (I .EQ. IROW(ISCAN)) GO TO 20
    IF (J .EQ. JCOL(JSCAN)) GO TO 20
  ENDDO
ENDDO
```

```
10 IF (DABS(A(I,J)) .GT. DABS(PIVOT)) THEN
  PIVOT=A(I,J)
  IROW(K)=I
  JCOL(K)=J
ENDIF
```

```
20 CONTINUE
```

```
30 CONTINUE
```

\* Ensure that selected pivot is larger than EPS.

```
IF (DABS(PIVOT) .LE. EPS) THEN
  SIMUL=0.0D0
  DEALLOCATE (IROW, JCOL, JORD, Y, STAT=IERR)
  IF (IERR .NE. 0) STOP 'Can't deallocate arrays in SIMUL.'
  RETURN
ENDIF
```

\* Update the determinant value.

```
IROWK=IROW(K)
JCOLK=JCOL(K)
DETER=DETER*PIVOT
```

\* Normalize pivot row elements.

```
DO J=1,MAX
  A(IROWK,J)=A(IROWK,J)/PIVOT
ENDDO
```

\* Carry out elimination and develop inverse.

```
A(IROWK,JCOLK)=1.0D0/PIVOT
```

```
DO 40 I=1,N
  AIJCK=A(I,JCOLK)
  IF (I .EQ. IROWK) GO TO 40
  A(I,JCOLK)=-AIJCK/PIVOT
```

```
DO J=1,MAX
  IF (J .NE. JCOLK) A(I,J)=A(I,J)-AIJCK*A(IROWK,J)
ENDDO
```

40 CONTINUE

\* Order solution values (if any) and create JORD array.

```
DO I=1,N
  IROWI=IROW(I)
  JCOLI=JCOL(I)
  JORD(IROWI)=JCOLI
  IF (INDIC .GE. 0) X(JCOLI)=A(IROWI,MAX)
ENDDO
```

\* Adjust sign of determinant.

```
INTCH=0
NM1=N-1
DO I=1,NM1
  IP1=I+1
  DO J=IP1,N
    IF (JORD(J) .GE. JORD(I)) CYCLE
    JTEMP=JORD(J)
    JORD(J)=JORD(I)
    JORD(I)=JTEMP
  INTCH=INTCH+1
ENDDO
ENDDO
```

```
IF (INTCH/2*2 .NE. INTCH) DETER=-DETER
```

\* If INDIC is positive, return with results.

```
IF (INDIC .GT. 0) THEN
```

```
SIMUL=DETER  
DEALLOCATE (IROW, JCOL, JORD, Y, STAT=IERR)  
IF (IERR .NE. 0) STOP 'Can't deallocate arrays in SIMUL.'  
RETURN  
ENDIF
```

- \* If INDIC is negative or zero, unscramble the inverse.
- \* ..... First by rows .....

```
DO J=1,N  
  
  DO I=1,N  
    IROWI=IROW(I)  
    JCOLI=JCOL(I)  
    Y(JCOLI)=A(IROWI,J)  
  ENDDO
```

```
  DO I=1,N  
    A(I,J)=Y(I)  
  ENDDO
```

```
ENDDO
```

- \* ..... then by columns.....

```
DO I=1,N  
  
  DO J=1,N  
    IROWJ=IROW(J)  
    JCOLJ=JCOL(J)  
    Y(IROWJ)=A(I,JCOLJ)  
  ENDDO
```

```
  DO J=1,N  
    A(I,J)=Y(J)  
  ENDDO
```

```
ENDDO
```

- \* Return for INDIC negative or zero.

```
SIMUL=DETER  
DEALLOCATE (IROW, JCOL, JORD, Y, STAT=IERR)  
IF (IERR .NE. 0) STOP 'Can't deallocate arrays in SIMUL.'  
RETURN  
END
```

## Appendix I. FORTRAN Program CONCEN.FOR Used to Calculate Time Records of Concentration and Temperature From Digitized Records of Cold-Wire and Aspirated Hot-Film Voltages

\* Convert voltage traces into concentration. (CONCEN.FOR)

\* David E. Hess

\* Fluid Flow Group - Process Measurements Division

\* Chemical Science and Technology Laboratory

\* National Institute of Standards and Technology

\* July 7, 1994

```
IMPLICIT REAL*8 (A-H,O-Z), INTEGER*2 (I-N)
```

```
INTEGER*4 I,N,NMAX
```

```
REAL*8 A [ALLOCATABLE] (:), B(2)
```

```
REAL*8 HF (8192), CW (8192)
```

```
REAL*8 TIME (8192), T (8192), C (8192)
```

```
CHARACTER*1 INP
```

```
CHARACTER*4 FEXT,FEXT2,FEXT3
```

```
CHARACTER*12 COEF1,COEF2,FNAMI,FNAMO
```

```
PARAMETER (NUMI=1,NUMO=2,NMAX=1000000)
```

```
DATA FEXT, FEXT2, FEXT3 / '.DAT', '.COE', '.OUT' /
```

\* Title of routine.

```
WRITE (*,'(25(/))')
```

```
WRITE (*,'(10X,A,A)')
```

```
+ 'Convert Voltage Traces to Temperature',
```

```
+ ' and Concentration Traces'
```

```
WRITE (*,'(11(/))')
```

\* Get the order of the fitted surface.

```
WRITE (*,'( )')
```

```
WRITE (*,'(16X,A)\') 'Enter order M of fitted surface : '
```

```
READ (*,*) M
```

```
WRITE (*,'( )')
```

```
MP1SQ=(M+1)**2
```

\* Get the sampling rate.

```
WRITE (*,'(16X,A)\') 'Enter data sampling rate (sps) : '
```

```
READ (*,*) SAMPRATE
```

```
WRITE (*,'( )')
```

```
DELT=1.0D0/SAMPRATE
```

\* Allocate coefficient array.

```
ALLOCATE (A(MP1SQ), STAT=IERR)
IF (IERR .NE. 0) STOP 'Can't allocate coeff array in MAIN.'
```

\* Get the surface fit coefficient data file.

```
5  WRITE (*,'(1X,A,A,A)')
+   'Enter name of surface fit coefficient file [',FEXT2,']: '
  READ (*,'(A)') COEF1
  WRITE (*,'( )')
```

\* Concatenate file extension to COEF1.

```
IPD=INDEX(COEF1, '.')
IF (IPD .GT. 9) GO TO 5
IF (IPD .EQ. 0) THEN
  IEND=LEN_TRIM(COEF1)
  COEF1(IEND+1:IEND+4)=FEXT2
ENDIF
```

\* Get the surface fit coefficient data.

```
OPEN (NUM1,FILE=COEF1,STATUS='OLD')
  READ (NUM1,*) (A(I), I=1,MP1SQ)
CLOSE (NUM1)
```

\* Get the temperature fit coefficient data file.

```
6  WRITE (*,'(1X,A,A,A)')
+   'Enter name of temperature fit coefficient file [',FEXT2,']: '
  READ (*,'(A)') COEF2
  WRITE (*,'( )')
```

\* Concatenate file extension to COEF2.

```
IPD=INDEX(COEF2, '.')
IF (IPD .GT. 9) GO TO 6
IF (IPD .EQ. 0) THEN
  IEND=LEN_TRIM(COEF2)
  COEF2(IEND+1:IEND+4)=FEXT2
ENDIF
```

\* Get the temperature fit coefficient data.

```
OPEN (NUM1,FILE=COEF2,STATUS='OLD')
  READ (NUM1,*) (B(I), I=1,2)
CLOSE (NUM1)
```

\* Get the input data file.

```

WRITE (*,'(1X,A,I7,A)')
+   'Program will read up to ',NMAX,' points.'
10 WRITE (*,'(1X,A,A,A)')
+   'Enter name of input data file [',FEXT,']:'
READ (*,'(A)') FNAMI
WRITE (*,'( )')
```

\* Concatenate file extension to FNAMI.

```

IPD=INDEX(FNAMI,'.')
IF (IPD .GT. 9) GO TO 10
IF (IPD .EQ. 0) THEN
    IEND=LEN_TRIM(FNAMI)
    FNAMI(IEND+1:IEND+4)=FEXT
ENDIF
```

\* Create the other filename.

```

IPD=INDEX(FNAMI,'.')
FNAMO = FNAMI(:IPD-1) // FEXT3
```

\* Open the input and output files.

```

OPEN (NUMI,FILE=FNAMI,STATUS='OLD')
OPEN (NUMO,FILE=FNAMO,STATUS='UNKNOWN')
```

\* Enter # of data points or determine from file.

```

20 WRITE (*,'(1X,A)')
+   '(E)nter # of data points or (R)ead from file : '
READ (*,'(A)') INP
WRITE (*,'( )')
GO TO (20,30,45) ILET(INP,'RE')
```

\* First determine # of values of X in the ascii file.

```

30 DO I=1,NMAX
    READ (NUMI,*,END=40) XTST
ENDDO
40 N=I-1
REWIND(NUMI)
WRITE (*,'(1X,A,I7,A)')
+   'Read ',N,' data values from file.'
GO TO 50
```

\* Enter the number of data points.

```
45  WRITE (*,'(1X,A)\') 'Enter the number of data points : '  
    READ (*,*) N  
    WRITE (*,'( )')
```

\* Divide N into sets 8192 REAL\*4 values and calculate remainder.

```
50  IFULL=N/8192  
    IPART=N-IFULL*8192
```

\* Loop over full sets of 8192 data points.

```
DO J=1,IFULL
```

\* Get values of hot-film voltage and  
\* cold-wire voltage from file.

```
    READ (NUMI,*) (HF(I), CW(I), I=1,8192)
```

\* Convert cold-wire voltages into temperatures using straight  
\* line fit. Then, use surface fit to get concentrations from  
\* temperature and hot-film voltage data.

```
    DO I=1,8192  
        TIME(I)=((J-1)*8192+I-1)*DELT  
        T(I)=B(1)+B(2)*CW(I)  
        C(I)=F(T(I),HF(I),A,M)  
    ENDDO
```

\* Store the data to the output file.

```
    WRITE (NUMO,'(3(G17.7,2X))')  
+    (TIME(I), T(I), C(I), I=1,8192)
```

```
ENDDO
```

\* Now do the remaining partial set of points.

```
IF (IPART .NE. 0) THEN
```

\* Get values of hot-film voltage and  
\* cold-wire voltage from file.

```
    READ (NUMI,*) (HF(I), CW(I), I=1,IPART)
```

\* Convert cold-wire voltages into temperatures using straight  
\* line fit. Then, use surface fit to get concentrations from  
\* temperature and hot-film voltage data.

```

DO I=1,IPART
  TIME(I)=(IFULL*8192+I-1)*DELT
  T(I)=B(1)+B(2)*CW(I)
  C(I)=F(T(I),HF(I),A,M)
ENDDO

```

\* Store the data to the output file.

```

WRITE (NUMO,'(3(G17.7,2X))')
+ (TIME(I), T(I), C(I), I=1,IPART)

```

```

ENDIF

```

```

CLOSE (NUMI)
CLOSE (NUMO)

```

\* Deallocate array.

```

DEALLOCATE (A, STAT=IERR)
IF (IERR .NE. 0) STOP 'Can't deallocate coeff array in MAIN.'

```

```

STOP ' '
END

```

```

FUNCTION ILET (INP,STRING) ! (ILET.FOR)

```

```

IMPLICIT INTEGER*2 (I-N)
CHARACTER*1 INP
CHARACTER*(*) STRING

```

\* First, convert INP to uppercase if it is lowercase. If it  
 \* is uppercase, leave it unchanged.

```

IF (ICHAR(INP) .GE. 97 .AND. ICHAR(INP) .LE. 122) THEN
  IHOLD=ICHAR(INP)-32
  INP=CHAR(IHOLD)
ENDIF

```

\* Determine the position of INP in STRING, then add one to get  
 \* ILET which determines label to use in computed GO TO statement.

```

IPOS=INDEX(STRING,INP)
ILET=IPOS+1

```

```

RETURN
END

```

```

FUNCTION F(X,Y,A,M) ! (F.FOR)

```



\* Inputs:

- \* X - X value
- \* Y - Y value
- \* A - array containing fit coeffs A (for Z)
- \* M - order of surface used in fit (most often 3 or 4)

\* Output:

- \* F - value of Z

```
IMPLICIT REAL*8 (A-H,O-Z), INTEGER*2 (I-N)
REAL*8      A((M+1)**2)
REAL*8      C[ALLOCATABLE](:)
```

\* Initialization.

```
MP1=M+INT2(1)
MP1SQ=(MP1)**2
```

```
ALLOCATE (C(MP1), STAT=IERR)
IF (IERR .NE. 0) STOP 'Can't allocate C in F function.'
```

- \* Note: C's (collections of A's and X's) multiply Y's
- \* and A's multiply X's. Calculate first C "coefficient".

```
C(MP1)=A(MP1SQ)
DO K=MP1SQ-1,M*MP1+1,-1
  C(MP1)=C(MP1)*X+A(K)
ENDDO
F=C(MP1)
```

- \* Enter double loop multiplying X's and Y's.

```
DO J=M,1,-1
  C(J)=A(J*MP1)
  DO K=J*MP1-1,(J-1)*MP1+1,-1
    C(J)=C(J)*X+A(K)
  ENDDO
  F=F*Y+C(J)
ENDDO
```

```
DEALLOCATE (C, STAT=IERR)
IF (IERR .NE. 0) STOP 'Can't deallocate C in F function.'
```

```
RETURN
END
```

## Appendix J. Components of DIRRACS

IR Source: Cable heater from Watlow, 120 V, 240 W, 1.57 mm diameter, 61 cm long; coiled with elliptical cross section to fit within tube.

### Optical Components:

Narrow bandpass filter from Optical Coating Laboratory, Inc. with center wavelength 8.654  $\mu\text{m}$ , half-power points 8.396 and 8.913  $\mu\text{m}$ , peak transmission 86%, 2.54 cm diameter, 1 mm thick. Attached at entrance of conical collector.

Wide-bandpass filter from Optical Coating Laboratory, Inc. with center wavelength 9.191  $\mu\text{m}$ , half power points 7.853  $\mu\text{m}$  and 10.529  $\mu\text{m}$ , peak transmission 95.4%, less than 0.1 % transmission out to 15.75  $\mu\text{m}$ , 2.54 cm diameter, 1 mm thick. Attached at exit of IR transmission tube.

ZnSe window, 2.80 cm diameter, 3.1 mm thick. Attached to IR source housing.

ZnS window, 2.54 cm diameter, 1 mm thick. Attached to entrance of IR transmission tube.

Detector: 5 mm diameter pyroelectric detector/FET Preamplifier from Moletron (P1-55) made from  $\text{LiTaO}_3$  with 5 mm diameter. Specifications for two units: Voltage responsivity 27.3 and 29.1 V/W, voltage noise  $1.1 \times 10^{-6}$  and  $1.2 \times 10^{-6}$ , and noise equivalent power  $40 \times 10^{-9}$  and  $41 \times 10^{-9}$  all measured at 15 Hz. Attached to far end of IR collection cone.

Optical Chopper: Chopper with controller from Stanford Research Systems (Model SR 540), 10.2 cm diameter, six slot blade with 2.13 cm aperture (5 slot portion taped over), operated at 500 Hz.

### Power Supplies:

15 V DC power supply (low power) for the pyroelectric detectors.

0-50 V, 100 W Sorensen DC power supply for the heater.

### Electronics:

100 $\times$  amplifier (see Figure 50 for schematic).

High bandpass filter operated at 300 Hz (Ithaco 4302 Dual 24 db/Octave filter).

### Hardware Components:

15.2 cm long cubical steel chassis box enclosing the chopper, collection cone, detector and electronics.

3.18 cm diameter, 1.6 mm thick, 20 cm long brass tube containing the source, the open area where the agent flows through, and IR transmission section. The end of tube where source is located was machined out to an ID of 3.02 mm and an end cap was silver soldered to the tube.

1 1/4 NPT soldered to the brass tube for connecting to the dry bay and the engine nacelle facilities at Wright Patterson AFB.

1.6 mm diameter flexible stainless steel tubing for N<sub>2</sub> purge line.

14 cm long, 7.5 cm wide, 6.4 thick brass support plate for rigid mounting of brass tube.

lens mounting plates: rings soldered into tube for mounting the ZnSe and ZnS windows; a plastic mounting was used for the wide-bandpass filter.

## Appendix K. Infrared Detector Model

```

*****
*
* PROGRAM:      INFRARED DETECTOR MODEL
*                IR.FOR/EXE
*
* PROGRAMMER:   RIK JOHNSON
*                SMOKE DYNAMICS RESEARCH GROUP
*                ROOM B256 BLDG 224 NIST
*                GAITHERSBURG, MD 20899
*
* DATE:        5/12/94
*
* PROJECT:      HALON REPLACEMENT
*
* VARIABLE DEFINITIONS:
*
* A( )          - ABSORBANCE
* AC            - AGENT CONCENTRATION
* AF            - AGENT ABSORBANCE COEFFICIENT
* AL( ) -      - ABSORBANCE WAVELENGTH
* ALTMP( )      - TEMPORARY VARIABLE FOR AL
* ATMP          - TEMPORARY VARIABLE FOR A
* C             - SPEED OF LIGHT
* DENSUM        - DENOMINATOR INTEGRATED SUM
* ENDF2         - LAST RECORD NUMBER OF FILE 2
* EX            - EXPONENTIAL TERM
* EX1           - LOWER WAVELENGTH PART OF EXPONENTIAL TERM
* EX2           - HIGHER WAVELENGTH PART OF EXPONENTIAL TERM
* F( )          - FILTER TRANSMITTANCE FUNCTION
* FF            - FILTER FUNCTION TERM
* FL( )         - FILTER TRANSMITTANCE WAVELENGTH
* H             - PLANCK'S CONSTANT
* I             - DUMMY VARIABLE
* IL            - INTENSITY TERM
* IL1           - LOWER WAVELENGTH PART OF INTENSITY TERM
* IL2           - HIGHER WAVELENGTH PART OF INTENSITY TERM
* J             - DUMMY VARIABLE
* KB            - BOLTZMAN CONSTANT
* L             - DUMMY VARIABLE
* M             - DUMMY VARIABLE
* NUMSUM        - NUMERATOR INTEGRATED SUM
* PI            - CONSTANT PI
* PL            - PATH LENGTH
* T             - TEMPERATURE

```

\* TRAT - RATIO TRANSMITTED INTENSITY TO BACKGROUND \*

\*\*\*\*\*

C  
C VARIABLE TYPE DEFINITIONS AND DIMENSIONING OF ARRAYS

C  
CHARACTER FNAME\*12,TNAME\*12  
REAL C,KB,H,PI,AC,T,PL,AL(2000),A(2000),AFF(344),FL(344),EX,EX1  
+,EX2,IL,IL1,IL2,FF,NUMSUM,DENSUM,TRAT,ATMP(2000),ALTMP(2000)  
INTEGER IL,M,ENDF2

C  
C VARIABLE INITIALIZATION

C  
ENDF2=0.  
EX1=0.  
EX2=0.  
EX=0.  
IL1=0.  
IL2=0.  
IL=0.  
FF=0.  
F(0)=0.  
M=1  
NUMSUM=0.  
DENSUM=0.

C  
C CONSTANT ASSIGNMENTS

C  
C=3.0E+8  
KB=1.38E-23  
H=6.626E-34  
PI=3.1415926

C  
C INPUT OF EXPERIMENTAL PARAMETERS

C  
C WRITE(\*,105)  
C READ(\*,110)FNAME  
C WRITE(\*,115)  
C READ(\*,\*)AC  
C WRITE(\*,120)  
C READ(\*,\*)T  
C WRITE(\*,125)  
C READ(\*,\*)PL  
C WRITE(\*,130)  
C READ(\*,\*)AF  
C WRITE(\*,132)  
C FNAME='C3.DAT'  
C FNAME='C13.DAT'

```
C  FNAME='CF3I.DAT'
FNAME='FC125MAC.DAT'
C  WRITE(*,101)
C  READ(*,102)TNAME
C  AC=2.
C  T=800.
  PL=0.028
C  AF=94.7
C  AF=56.79
C  AF=98.75
  AF=36.45
C
C READING OF FILTER FUNCTION
C
  WRITE(*,*)'THE FILTER FUNCTION'
  WRITE(*,*)'WAVELENGTH TRANSMITTANCE'
  OPEN (UNIT=1,FILE='FILWIN.15')
10  READ (1,135,END=11)(FL(I),F(I),I=1,344)
11  WRITE(*,*)I
    DO 12, I=1,344
12  FL(I)=FL(I)/1000000.
C  WRITE(*,140)(FL(I),F(I),I=1,344)
  CLOSE (1)
C
C READING OF ABSORBANCE DATA
C
  OPEN (UNIT=2,FILE=FNAME)
  DO 20 J=1,2000
    READ (2,145,END=21)AL(J),A(J)
C
C CONVERSION OF INVERSE CM TO M
C
20  AL(J)=1./(AL(J)+.00000001)/100.
21  WRITE(*,*)
    ENDF2=J-1
    WRITE(*,*)
    WRITE(*,*)ENDF2
  CLOSE (2)
C
C INVERSION OF DATA FOR INCREASING WAVELENGTH
C
  DO 30 I=1,ENDF2
    J=ENDF2-I+1
    ALTMP(J)=AL(I)
30  ATMP(J)=A(I)
  DO 40 I=1,ENDF2
    AL(I)=ALTMP(I)
40  A(I)=ATMP(I)
```

```

WRITE(*,*)
WRITE(*,*)'DATA'
WRITE(*,*)'WAVELENGTH ABSORBANCE'
C  WRITE(*,150)(AL(J),A(J),J=1,ENDF2)
C
C INTEGRATION LOOP
C
  WRITE(*,*)' RECORD   WAVELENGTH   NUMERATOR   DENOMINATO
+R'
  DO 50 L=1,ENDF2-1
C
C EXPONENTIAL TERM CALCULATION
C
  EX1=EXP(-AC*PL*AF*A(L))
  EX2=EXP(-AC*PL*AF*A(L+1))
  EX=(EX1+EX2)/2.
C
C INTENSITY TERM CALCULATION
C
  IL1=H*C**2./AL(L)**5./(EXP(H*C/AL(L)/KB/T)-1.)
  IL2=H*C**2./AL(L+1)**5./(EXP(H*C/AL(L+1)/KB/T)-1.)
  IL=(IL1+IL2)/2.
  IF(AL(L).GE.FL(M+1))M=M+1
C  IF(FL(M).GE.10./1000000.)THEN
C    F(M)=0.
C    F(M+1)=0.
C  ENDIF
C
C FILTER FUNCTION TERM CALCULATION
C
  FF=(F(M)+F(M+1))/2.
  IF(FL(M).GT.15./1000000.)FF=0.
C
C SUMMING OF NUMERATOR AND DENOMENATOR
C
  NUMSUM=NUMSUM+(EX*IL*FF)*(AL(L+1)-AL(L))
  DENSUM=DENSUM+(IL*FF)*(AL(L+1)-AL(L))
  AL(L)=10**6*AL(L)
C  OPEN(3,FILE=TNAME)
C  WRITE(3,154)AL(L),IL
  R=L-10.*INT(L/10.)
50  IF(R.EQ.0.)WRITE(*,155)L,AL(L),NUMSUM,DENSUM
C  CLOSE (3)
C
C CALCULATION OF RATIO OF TRANSMITTED INTENSITY TO BACKGROUND
C
  TRAT=NUMSUM/DENSUM
  WRITE(*,*)

```

```
WRITE(*,160)TRAT
101  FORMAT(/'INPUT THE BLACKBODY FILE NAME AS filename.ext',1X)
102  FORMAT(A12)
105  FORMAT(/'INPUT THE DATA FILE NAME AS filename.ext',1X)
110  FORMAT(A12)
115  FORMAT(/'INPUT THE AGENT CONCENTRATION IN moles/m^3',1X)
120  FORMAT(/'INPUT THE TEMPERATURE IN K',1X)
125  FORMAT(/'INPUT THE PATH LENGTH IN m',1X)
130  FORMAT(/'INPUT THE ABSORBANCE COEFFICIENT IN m^2/mole',1X)
132  FORMAT(/'INPUT THE ABSORBANCE DECREASE',1X)
135  FORMAT(F7.4,1X,F7.5)
140  FORMAT(F11.9,4X,F5.3)
145  FORMAT(F7.2,1X,F6.4)
150  FORMAT(E10.4,3X,F6.4)
154  FORMAT(F9.6,2X,E12.7)
155  FORMAT(I4,6X,F9.4,1X,F15.5,4X,F15.5)
160  FORMAT(/,'THE RATIO OF THE TRANSMITTED INTENSITY THROUGH THE GAS'
+/, 'SAMPLE TO THE INTENSITY THROUGH AIR IS',2X,F8.6,1X,',' )
END
```



## Appendix L. DIRRACS Data Reduction Program

\*\*\*\*\*

```

*
* PROGRAM:      DIRRACS DATA REDUCTION PROGRAM      *
*              SIG.FOR/EXE                          *
*
* PROGRAMMER:   RIK JOHNSON                          *
*              SMOKE DYNAMICS RESEARCH GROUP        *
*              ROOM B256 BLDG 224 NIST               *
*              GAITHERSBURG, MD 20899               *
*
* DATE:         JUNE 1994                            *
*
* REVISED:      DR. DAVID HESS, JULY 1994            *
*
* PROJECT:      HALON REPLACEMENT                    *
*
* VARIABLE DEFINITIONS:
*
* BLACK      - LOGICAL STATE FOR BLACK DETECTOR
* BLKLOW     - LOWER VOLTAGE LIMIT FOR BLACK DETECTOR
* BLUE       - LOGICAL STATE FOR BLUE DETECTOR
* BLUELOW    - LOWER VOLTAGE LIMIT FOR BLUE DETECTOR
* BOX        - DETECTOR IDENTITY
* C          - CONCENTRATION
* CHFR       - CHOPPER FREQUENCY
* DBLCYC     - NUMBER OF HALF CYCLES
* FEXT       - INPUT FILE EXTENSION
* FEXT2      - OUTPUT FILE EXTENSION
* FNAMEI     - INPUT FILE NAME
* FNAMEO     - OUTPUT FILE NAME
* I          - DO LOOP COUNTER FOR DATA
* IEND -     - LENGTH OF FILENAME BEFORE EXTENSION
* IPD        - INDEX OF FILENAME
* J          - CYCLE COUNTER
* K          - HALF-CYCLE COUNTER
* LIMIT      - LOWER VOLTAGE LIMIT OF DETECTOR
* NMAX       - MAXIMUM NUMBER OF DATA POINTS ALLOWED
* NOCYC      - NUMBER OF CYCLES
* NUMI       - INPUT FILE NUMBER
* NUMO       - OUTPUT FILE NUMBER
* PKPK       - DIFFERENCE OF HALF CYCLE MAX & MIN VOLTAGES
* PT         - CYCLE POINT COUNTER
* PTSCYC     - NUMBER OF POINTS PER CYCLE
* SMPFR      - SAMPLING FREQUENCY
* TMIN       - TIME MINIMUM VOLTAGE OCCURS FOR A CYCLE

```

```

*   TMAX   -   TIME MAXIMUM VOLTAGE OCCURS FOR A CYCLE   *
*   TOTPTS -   TOTAL NUMBER OF DATA POINTS             *
*   TV     -   TIME ASSIGNED TO CYCLE                   *
*   V      -   VOLTAGE FOR SPECIFIC DATA POINT          *
*   V0     -   PEAK-TO-PEAK VOLTAGE FOR AIR              *
*   VMAX   -   MAXIMUM VOLTAGE FOR A CYCLE               *
*   VMIN   -   MINIMUM VOLTAGE FOR A CYCLE               *
*   VOLD   -   PREVIOUS DATA POINT VOLTAGE VALUE        *
*   VV0    -   NORMALIZED PEAK-TO-PEAK VOLTAGE          *
*

```

```

*****

```

```

C
C VARIABLE TYPE DEFINITIONS AND DIMENSIONING OF ARRAYS
C

```

```

PARAMETER      (SIZE=12000)
INTEGER        I,J,TOTPTS,DBLCYC
REAL*4         V,NOCYC,LIMIT
REAL*4         VMAX [HUGE] (SIZE/2.0) , VMIN [HUGE] (SIZE/2.0)
REAL*4         PKPK [HUGE] (SIZE) , VV0 [HUGE] (SIZE)
REAL*4         TMIN [HUGE] (SIZE) , TMAX [HUGE] (SIZE)
REAL*4         TV [HUGE] (SIZE) , C [HUGE] (SIZE)
REAL*4         PT [HUGE] (SIZE/10.0)
LOGICAL*1      BLACK,BLUE
CHARACTER*1    BOX
CHARACTER*4    FEXT,FEXT2
CHARACTER*12   FNAMEI,FNAMEO

```

```

C
PARAMETER      (NUMI=1,NUMO=2,NMAX=1048576)
PARAMETER      (BLKLOW=0.6000,BLUELOW=0.5000)
DATA           FEXT, FEXT2 / '.DAT', '.OUT' /

```

```

C
C TITLE OF ROUTINE
C

```

```

WRITE (*,'(25(/))')
WRITE (*,'(24X,A)')
+ 'Infrared Halon Detection Routine'
WRITE (*,'(12(/))')

```

```

C
C GET THE INPUT FILENAME
C

```

```

WRITE (*,'(1X,A,I7,A)')
+ 'Program will read up to ',NMAX,' points.'
10 WRITE (*,'(1X,A,A,A)')
+ 'Type the input data file name [',FEXT,'] : '
READ (*,'(A)') FNAMEI
WRITE (*,'( )')

```

```

C
C CONCATENATE FILE EXTENSION TO FNAMEI

```

```

C
  IPD=INDEX(FNAMEI, '.')
  IF (IPD .GT. 8) GO TO 10
  IF (IPD .EQ. 0) THEN
    IEND=LEN_TRIM(FNAMEI)
    FNAMEI(IEND+1:IEND+4)=FEXT
  ENDIF
C
C GET THE OUPUT FILENAME
C
20  WRITE (*, '(1X,A,A,A)')
    + 'Type the output data file name [', FEXT2, ']' : '
    READ (*, '(A)') FNAMEO
    WRITE (*, '( )')
C
C CONCATENATE FILE EXTENSION TO FNAMEO
C
  IPD=INDEX(FNAMEO, '.')
  IF (IPD .GT. 8) GO TO 20
  IF (IPD .EQ. 0) THEN
    IEND=LEN_TRIM(FNAMEO)
    FNAMEO(IEND+1:IEND+4)=FEXT2
  ENDIF
C
C GET NEEDED INPUT PARAMETERS
C
  WRITE (*, '(1X,A)')
  + 'Enter the chopping frequency (Hz) : '
  READ (*, *) CHFR
  WRITE (*, '( )')
C
  WRITE (*, '(1X,A)')
  + 'Enter the sampling frequency (Hz) : '
  READ (*, *) SMPFR
  WRITE (*, '( )')
C
  WRITE (*, '(1X,A)')
  + 'Enter the zero concentration PK-PK voltage (V) : '
  READ (*, *) V0
  WRITE (*, '( )')
C
  WRITE (*, '(1X,A)')
  + '(B)lack or B(L)ue detector box : '
  READ (*, '(A)') BOX
  WRITE (*, '( )')
  IF (BOX .EQ. 'b') BOX='B'
  IF (BOX .EQ. 'l') BOX='L'
  IF (BOX .EQ. 'B') THEN

```

```

BLACK=.TRUE.
BLUE=.FALSE.
ENDIF
IF (BOX .EQ. 'L') THEN
BLACK=.FALSE.
BLUE=.TRUE.
ENDIF
C
C GET THE INPUT DATA
C
WRITE (*,'(1X,A)') 'Counting data points...'
OPEN (NUMI,FILE=FNAMEI,STATUS='OLD')
OPEN (NUMO,FILE=FNAMEO,STATUS='UNKNOWN')
DO I=1,NMAX
READ (NUMI,*,END=30) XTST
ENDDO
30 TOTPTS=I-1
REWIND (NUMI)
WRITE (*,'(1X,A,I7,A)')
+ 'Read ',TOTPTS, ' data values from file.'
C
PTSCYC=SMPFR/CHFR
NOCYC=TOTPTS/PTSCYC
C
J=0
VMAX(1)=0.
VMIN(1)=0.
V=0.
PT(J)=0
C
C LOOP TO READ VOLTAGE, FIND MAX, MIN PER CYCLE
C
WRITE(*,'(1X,A)') 'Finding cycle peak-to-peaks...'
DO I=0,TOTPTS-1
VOLD=V
READ(1,*)V
PT(J)=PT(J)+1
IF(V.GT.VMAX(J))THEN
VMAX(J)=V
TMAX(J)=I/SMPFR
ENDIF
IF(V.LT.VMIN(J))THEN
VMIN(J)=V
TMIN(J)=I/SMPFR
ENDIF
C
C FINDS BEGINNING OF A NEW CYCLE
C

```

```
IF(V.GT.0..AND.VOLD.LT.0..AND.PT(J).GT.INT(PTSCYC-3.))THEN
```

```
  J=J+1
```

```
  PT(J)=0
```

```
  VMAX(J)=0.
```

```
  VMIN(J)=0.
```

```
C
```

```
C IN CASE OF NO SIGN CHANGE INITIATES NEW CYCLE
```

```
C
```

```
  ELSEIF(PT(J).GT.INT(PTSCYC))THEN
```

```
    TMAX(J)=TMAX(J-1)+PTSCYC/SMPFR
```

```
    TMIN(J)=TMIN(J-1)+PTSCYC/SMPFR
```

```
    J=J+1
```

```
    PT(J)=0
```

```
    VMAX(J)=0.
```

```
    VMIN(J)=0.
```

```
    VOLD=0.
```

```
  ELSE
```

```
    CONTINUE
```

```
  ENDIF
```

```
ENDDO
```

```
C
```

```
C CALCULATION OF CONCENTRATIONS
```

```
C
```

```
  WRITE(*, '(1X,A/)' )'Calculating concentrations...'
```

```
  DBLCYC=2*(J-1)
```

```
C
```

```
  DO 23 K=1,DBLCYC-1,2
```

```
    L=(K+1)/2
```

```
    PKPK(K)=VMAX(L)-VMIN(L)
```

```
    VV0(K)=PKPK(K)/V0
```

```
    TV(K)=(TMAX(L)+TMIN(L))/2.
```

```
C
```

```
  IF (BLACK) LIMIT=BLKLOW
```

```
  IF (BLUE) LIMIT=BLUELOW
```

```
C
```

```
  IF (VV0(K) .LT. LIMIT) THEN
```

```
    C(K)=100.0
```

```
    GOTO 21
```

```
  ENDIF
```

```
C
```

```
  IF(VV0(K).GT.1.0001)THEN
```

```
    C(K)=0.0
```

```
    GOTO 21
```

```
  ENDIF
```

```
C
```

```
  IF (BLACK) C(K)=.42531+.13956/(.010587+VV0(K))**.31119
```

```
  IF (BLUE) C(K)=.26614+.16948/(.011903+VV0(K))**.33076
```

```
C
```

```

21  CONTINUE
C
  PKPK(K+1)=VMAX(L+1)-VMIN(L)
  VV0(K+1)=PKPK(K+1)/V0
  TV(K+1)=(TMAX(L+1)+TMIN(L))/2.
C
  IF (VV0(K+1) .LT. LIMIT) THEN
    C(K+1)=100.0
    GOTO 22
  ENDIF
C
  IF(VV0(K+1).GT.1.0001)THEN
    C(K)=0.0
    GOTO 22
  ENDIF
C
  IF (BLACK) C(K)=.42531+.13956/(.010587+VV0(K+1))**.31119
  IF (BLUE) C(K)=.26614+.16948/(.011903+VV0(K+1))**.33076
C
22  CONTINUE
C
C WRITING OUTPUT TO FILE
C
  IF(K.EQ.DBLCYC-1)WRITE(*,'(/1X,A)')'Saving to file...'
  WRITE(NUMO,140)TV(K),PKPK(K),VV0(K),C(K)
  WRITE(NUMO,140)TV(K+1),PKPK(K+1),VV0(K+1),C(K+1)
C
23  CONTINUE
C
  CLOSE (NUMI)
  CLOSE (NUMO)
C
  WRITE(*,'(/1X,A,1X,A)')'The output is in column form in this order
+:', 'TIME PEAK V/Vo CONCENTRATION'
C
101  FORMAT(25(/)1X'TYPE THE DATA INPUT FILE NAME AS filename.ext',1X)
111  FORMAT(A12)
102  FORMAT(/1X'TYPE THE DATA OUTPUT FILE NAME AS filename.ext',1X)
103  FORMAT(/1X'ENTER THE TOTAL NUMBER OF POINTS',1X)
104  FORMAT(/1X'ENTER THE SAMPLING FREQUENCY (Hz)',1X)
105  FORMAT(/1X'ENTER THE CHOPPING FREQUENCY (Hz)',1X)
106  FORMAT(/1X'ENTER THE ZERO CONCENTRATION PK-PK VOLTAGE (V)',1X)
135  FORMAT(F8.6)
140  FORMAT(F8.5,2X,F7.4,1X,F7.4,1X,F9.3)
141  FORMAT(1X' TIME MIN MAX PEAK V/Vo CONC')
END

```

## Appendix M. FORTRAN Program SOUND.FOR Used to Calculate Sound Attenuation As a Function of Fire-Fighting Agent Concentration in Air

```

*   Computes absorption coefficient versus (SOUND.FOR)
*   a user-specified abscissa.

*   David E. Hess
*   Submarine Dynamics Branch - Code 564
*   Ship Dynamics Department, Hydromechanics Directorate
*   David Taylor Model Basin
*   Naval Surface Warfare Center - Carderock
*   May 15, 1995

*   The following variables must be defined in an external ASCII
*   file. I have provided an example of the file; it has the file
*   extension [.NML] because it is a NAMELIST. All of these
*   variables are for dry air at 20 °C. A nice feature of namelists
*   is that the values of variables may be changed without having
*   to recompile the source code. The name of this first namelist
*   is AIR_PROP.

*   RHO  kg / m^3  density
*   GAMMA  dim'less  ratio of specific heats (Cp / Cv)
*   C  m / s      speed of sound
*   ETA0  Pa - s   dynamic viscosity
*   MW  dim'less  molecular weight of air
*   K  W / m - K   thermal conductivity
*   CP  kJ / kg - K  specific heat at constant pressure (air)

*   A second namelist entitled OTHER_PROP contains quantities which
*   may be used as the abscissa of a graph. The user selects the
*   chosen abscissa in the code below, then, the quantities NOT
*   chosen as the abscissa are defined with the values in this
*   namelist.

*   F  Hz      acoustic frequency
*   D  m^2 / s   mass diffusivity of agent in air
*   X  dim'less  mole fraction of agent in air

IMPLICIT  REAL*8 (A-H,O-Z), INTEGER*2 (I-N)

PARAMETER  (NUMI=1, NUMO=2)

REAL*8      MW_AGENT, MW_AIR, K
LOGICAL*1 EXISTS

```

```
CHARACTER*12 FILNAM
```

```
NAMelist /AIR_PROP/ RHO, GAMMA, C, ETA0,  
+ MW_AIR, K, CP
```

```
NAMelist /OTHER_PROP/ F, D, X
```

```
COMMON /AIR/ RHO, GAMMA, C, ETA0, MW_AIR, K, CP, MW_AGENT
```

\* Initialization.

```
PI=2.0D0*DASIN(1.0D0)
```

\* Check for existence of namelist file.

```
INQUIRE (FILE='PROPS.NML', EXIST=EXISTS)  
IF (.NOT. EXISTS) THEN  
  WRITE (*,'( )')  
  STOP 'Namelist file PROPS.NML not present in root directory.'  
ENDIF
```

\* Open the namelist file and read in data.

```
OPEN (NUM1, FILE='PROPS.NML')  
  READ (NUM1, NML=AIR_PROP, IOSTAT=IERR)  
  READ (NUM1, NML=OTHER_PROP, IOSTAT=IERR)  
  IF (IERR .NE. 0) THEN  
    WRITE (*,'( )')  
    STOP 'Error reading the namelist file.'  
  ENDIF  
CLOSE (NUM1)
```

\* Display list of gases.

```
5 WRITE (*,'(16X,A)') 'Calculation of Absorption Coefficient'  
  WRITE (*,'(16X,A)') 'Choose from the following gases : '  
  WRITE (*,'(16X,A)') '      1. CF3I'  
  WRITE (*,'(16X,A)') '      2. HFC-227'  
  WRITE (*,'(16X,A)') '      3. FC-218'  
  WRITE (*,'(16X,A)') '      4. HFC-125'  
  WRITE (*,'(16X,A)') '      5. HALON-1301'  
  WRITE (*,'(16X,A)') 'Enter choice (1-5) : '  
  READ (*,*) IGAS  
  WRITE (*,'( )')
```

\* Initialize MW\_AGENT with appropriate number.

```
SELECT CASE (IGAS)
```



```

CASE (1)
MW_AGENT = 195.91D0      ! CF3I

CASE (2)
MW_AGENT = 170.03D0      ! HFC-227

CASE (3)
MW_AGENT = 188.02D0      ! FC-218

CASE (4)
MW_AGENT = 120.02D0      ! HFC-125

CASE (5)
MW_AGENT = 148.91D0      ! HALON-1301

CASE DEFAULT
WRITE (*,'(16X,A)') 'Using HFC-125.'
MW_AGENT = 120.02D0      ! HFC-125

END SELECT

```

\* Select data to plot.

```

WRITE (*,'(16X,A)') 'Choose from the following: '
WRITE (*,'(16X,A)') ' 1. Alpha views F'
WRITE (*,'(16X,A)') ' 2. Alpha views D'
WRITE (*,'(16X,A)') ' 3. Alpha views X'
WRITE (*,'(16X,A)') ' 4. Single value'
WRITE (*,'(16X,A)') 'Enter choice (1-4) : '
READ (*,*) IPLOT
WRITE (*,'( )')

```

\* Get output filename.

```

IF (IPLOT .EQ. 1 .OR. IPLOT .EQ. 2 .OR. IPLOT .EQ. 3) THEN
  WRITE (*,'(16X,A)') 'Enter output filename: '
  READ (*,'(A)') FILNAM
  WRITE (*,'( )')
  OPEN (NUMO, FILE=FILNAM, STATUS='UNKNOWN')
ENDIF

```

\* Perform selected task.

```

SELECT CASE (IPLOT)

```

```

CASE (1) ! Alpha views F

```

\* Get Fstart, Fstop and Fstep.

```
WRITE (*,'(16X,A)\') 'Enter Fstart, Fstop and Fstep: '
READ (*,*) FSTART, FSTOP, FSTEP
WRITE (*,'( )')
```

\* Calculate alphas for this range of frequencies.

```
IMAX=NINT((FSTOP-FSTART)/FSTEP)+1
F=FSTART-FSTEP
DO I=1,IMAX
  F=F+FSTEP
  A=ALPHA(F,D,X)
  XNUM = 8.0D0 / 3.0D0 * PI * F * ETA0 / (RHO * C**2)
  WRITE (NUMO,*) F,A,XNUM
ENDDO
CLOSE (NUMO)
STOP ' '
```

CASE (2) ! Alpha views D

\* Get Dstart, Dstop and Dstep.

```
WRITE (*,'(16X,A)\') 'Enter Dstart, Dstop and Dstep: '
READ (*,*) DSTART, DSTOP, DSTEP
WRITE (*,'( )')
```

\* Calculate alphas for this range of frequencies.

```
IMAX=NINT((DSTOP-DSTART)/DSTEP)+1
D=DSTART-DSTEP
XNUM = 8.0D0 / 3.0D0 * PI * F * ETA0 / (RHO * C**2)
WRITE (NUMO,*) XNUM
DO I=1,IMAX
  D=D+DSTEP
  A=ALPHA(F,D,X)
  WRITE (NUMO,*) D,A
ENDDO
CLOSE (NUMO)
STOP ' '
```

CASE (3) ! Alpha views X

\* Get Xstart, Xstop and Xstep.

```
WRITE (*,'(16X,A)\') 'Enter Xstart, Xstop and Xstep: '
READ (*,*) XSTART, XSTOP, XSTEP
WRITE (*,'( )')
```

\* Calculate alphas for this range of frequencies.

```

IMAX=NINT((XSTOP-XSTART)/XSTEP)+1
X=XSTART-XSTEP
XNUM = 8.0D0 / 3.0D0 * PI * F * ETA0 / (RHO * C**2)
WRITE (NUMO,*) XNUM
DO I=1,IMAX
  X=X+XSTEP
  A=ALPHA(F,D,X)
  WRITE (NUMO,*) X,A
ENDDO
CLOSE (NUMO)
STOP ' '

```

CASE (4) ! Single value

```

A=ALPHA(F,D,X)
XNUM = 8.0D0 / 3.0D0 * PI * F * ETA0 / (RHO * C**2)
WRITE (*,'(16X,A,G17.8,A/)' ) 'Alpha = ', A, ' dB / m.'
WRITE (*,'(16X,A,G17.8,A/)' ) 'Xnum = ', XNUM, '.'
STOP ' '

```

CASE DEFAULT ! Single value

```

A=ALPHA(F,D,X)
XNUM = 8.0D0 / 3.0D0 * PI * F * ETA0 / (RHO * C**2)
WRITE (*,'(16X,A,G17.8,A/)' ) 'Alpha = ', A, ' dB / m.'
WRITE (*,'(16X,A,G17.8,A/)' ) 'Xnum = ', XNUM, '.'
STOP ' '

```

END SELECT

END

FUNCTION ALPHA (F, D, X)

```

IMPLICIT REAL*8 (A-H,O-Z), INTEGER*2 (I-N)
REAL*8      MW_AGENT, MW_AIR, MW_MIX, K, KNEW

```

```

COMMON /AIR/  RHO, GAMMA, C, ETA0, MW_AIR, K, CP, MW_AGENT

```

\* Initialization.

```

PI = 3.141592653589793D0
MW_MIX = X * MW_AGENT + (1.0D0-X) * MW_AIR

```

\* Convert K from (W / m - K) to (kW / m - K) = (kJ / m - s - K)  
 \* in order to have consistent units with Cp.

```

KNEW = K / 1000.0D0

```

\* Compute various parts of governing equation.

```
SCALE = 2.0D0 * PI**2 * F**2 / C**3
TERM1 = ETA0 * 4.0D0 / 3.0D0 / RHO
TERM2 = (GAMMA - 1.0D0) * KNEW / RHO / CP
TERM3 = D * X * (1.0D0 - X) * GAMMA
+      * ((MW_AIR - MW_AGENT) / MW_MIX)**2
ALPHA = SCALE * (TERM1 + TERM2 + TERM3)
```

\* Convert alpha from (nepers / m) to (dB / m).

```
ALPHA = 8.7 * ALPHA
```

\* Debug code.

```
* WRITE (*,'(16X,A,1P,E17.8)') 'Scale   = ', SCALE
* WRITE (*,'(16X,A,1P,E17.8)') 'Term1   = ', TERM1
* WRITE (*,'(16X,A,1P,E17.8)') 'Term2   = ', TERM2
* WRITE (*,'(16X,A,1P,E17.8)') 'Term3   = ', TERM3

* WRITE (*,'(16X,A,1P,E17.8)') 'Rho     = ', RHO
* WRITE (*,'(16X,A,1P,E17.8)') 'Gamma   = ', GAMMA
* WRITE (*,'(16X,A,1P,E17.8)') 'C       = ', C
* WRITE (*,'(16X,A,1P,E17.8)') 'Eta0    = ', ETA0
* WRITE (*,'(16X,A,1P,E17.8)') 'K       = ', K
* WRITE (*,'(16X,A,1P,E17.8)') 'Cp      = ', CP
* WRITE (*,'(16X,A,1P,E17.8)') 'MW_agent = ', MW_AGENT
* WRITE (*,'(16X,A,1P,E17.8)') 'MW_air  = ', MW_AIR
* WRITE (*,'(16X,A,1P,E17.8)') 'MW_mix  = ', MW_MIX

* WRITE (*,'(16X,A,1P,E17.8)') 'F = ', F
* WRITE (*,'(16X,A,1P,E17.8)') 'D = ', D
* WRITE (*,'(16X,A,1P,E17.8)') 'X = ', X
* WRITE (*,'(16X,A,1P,E17.8)') 'A = ', ALPHA
* PAUSE '          Press enter to continue.'
```

```
RETURN
END
```